

Teferi Dejene Demissie

# **The vertical structure and source regions of large and small scale waves in the middle atmosphere**

Thesis for the degree of Philosophiae Doctor

Trondheim, August 2013

Norwegian University of Science and Technology  
Faculty of Natural Sciences and Technology  
Department of Physics



**NTNU – Trondheim**  
Norwegian University of  
Science and Technology



## **Abstract**

The vertical phase structure of atmospheric waves of various scales in the middle atmosphere and their source regions have been investigated using a range of instruments. The methodology of this thesis involved the analysis of ozone mixing ratio data obtained from the British Antarctic Survey (BAS) ground-based microwave radiometer located at Troll station (72.0°S, 2.5°E) along with the nightly averaged mesospheric temperature derived from the hydroxyl nightglow at Rothera station (67.6°S, 68.1°W) and PMSE extracted from the near-range measurements of the Sanae (71.7°S, 2.8°W) Super Dual Auroral Radar (SuperDARN). Noctilucent cloud (NLC) images from digital camera in Trondheim and output from Gravity Wave Regional or Global Ray Tracer (GROGRAT) are also used in an attempt to identify the characteristics and source regions of gravity waves. A number of data processing methods are involved in this study, such as a digital filtering, fast Fourier transform (FFT), cross-spectral analysis, image projection and analysis.

Oscillations associated with 16-day wave are present in mesosphere and stratosphere during wintertime in Antarctica, but with large phase shifts and diminished amplitude around 55km. The 16-day oscillation is found to have vertical phase fronts consistent with a normal-mode structure, but interacts with the background wind near 55 m where it deposits some of its energy. The ozone mixing ratio variations were used to trace the phase variation of the quasi-periodic fluctuations in PMSE during the Antarctic summer. The results indicate that the modulation of PMSE occurrence frequency is the result of two planetary waves (5- and 6.5-days) with similar zonal structure, but with different vertical phase structures.

The parameters of 34 short-period gravity-wave events during summer were extracted from NLC images between 64° and 74°N and have been analyzed and compared with previous NLC and airglow imaging studies at different latitudes. The results of the NLC studies are consistent, with the waves found to be moving north and north-eastward in both studies.

The ray tracing analysis shows that waves propagating from the tropopause are more likely to be the sources of the prominent wave structures observed in the NLC, and the coastal region of Norway along the latitude of 70°N is identified as the primary source region of the waves.



## **Acknowledgements**

I would like to express my praises and thanks to the Almighty God for His blessings and favor that enabled me to complete this thesis.

Debts of gratitude are owed to many people who have made this thesis and my study a reality. Indeed, no amount of writing can precisely measure the contribution of the people who have been with me all the way at all times.

Foremost, I would like to express my deepest and sincere gratitude to my Supervisor Professor Patrick Joseph Espy for his immense support, motivation, patience and persistent guidance throughout the study. His deep knowledge of the subject matter, invested time, problem-solving skill and encouraging ability added considerably to my research experience and the overall tone of this thesis. I couldn't have imagined completing this thesis without his all-round assistance and his witty sense of humor that brought light in the distressing days.

I also would like to express my thanks to Prof. Robert Hibbins who always provide relentless support, motivation and helpful comments and suggestions in shaping my research.

Although many of my friends have their footprints in my studies and hard work, one way or the other, the support and motivation of Nora, Marianne, Corinne, Amund and Roos were exceptional. I depended a lot on their ingenious opinions, discussion and advice during the long years of hard work and difficult times.

My studies at the Norwegian University of Science and Technology and this thesis would have remained dream without the funding of Research Council of Norway, the Norwegian Polar Institute and Birkeland Centre of Excellence for Space Science for which I am extremely indebted to.

May my greatest gratitude also go to my wife Sewnet (Nunu) Gelaw whose relentless care, prayer and understanding I have been granted without fail. If I have succeeded in my studies it is because you have been there to me for that cause.

My studies were only possible because my parents were there for me at all times. If I have to single out one of them, it is my mom, Tirsit Assefa, whose love and support I have been blessed without fail. My sisters Mestawet and her husband Belayneh, Yeshe, Meseret and

brothers Mulugeta, Yonas and Fasil also deserve special thanks for their support and love that I have benefited greatly. I am also grateful to in-laws Segenet, Addis, Abiy, Endalk, Kidus, Seni, Misrak and Ashebir, Sabek and Ermias for their full support through this study.

It would be a gross mistake if I have not thanked close friends who have made my time in Trondheim enjoyable and unforgettable. It is literally impossible to mention all the names but your friendship and the great times we spent together remains in my heart forever. I thank you all for the good times we shared. The social gathering and the discussions on current issues with Mulugeta and Samrawit, Samson, Asmamaw and Haimanot and many of you was refreshing.

Last but not the least, my sincere thanks goes to Ebenezer church in Trondheim for your prayers and support in diverse forms.

August 2013, Trondheim

Teferi Dejene Demissie

## List of papers

The present thesis is based on the following papers, which will be referred in the text by their Roman numerals.

**I. Quasi-16 day period oscillations observed in middle atmospheric ozone and temperature in Antarctica**

**T. D. Demissie<sup>1</sup>, N. H. Kleinknecht<sup>1</sup>, R. E. Hibbins<sup>1,2</sup>, P. J. Espy<sup>1,2</sup>, C. Straub<sup>1</sup>**  
*Ann. Geophys.*, 31, 1279-1284, doi: 10.5194/angeo-31-1279-2013, 2013.

**II. Planetary wave oscillations observed in ozone and PMSE data from Antarctica**

**T. D. Demissie, K. Hosokawa, N. H. Kleinknecht, P. J. Espy, R. E. Hibbins**  
*In review at journal of Atmospheric and Solar-Terrestrial Physics (JASTP)*

**III. Characteristics and sources of gravity waves observed in NLC over Norway**

**T. D. Demissie, P. J. Espy, R. E. Hibbins**  
*Submitted to the journal of Atmospheric Chemistry and Physics (ACP)*

## Other papers

**1.** B. U. E. Brändström, C. -F. Enell, O. Widell, T. Hansson, D. Whiter, S. Mäkinen, D. Mikhaylova, K. Axelsson, F. Sigernes, N. Gulbrandsen, N. M. Schlatter, A. G. Gjendem, L. Cai, J. P. Reistad, M. Daae, T. Dejene Demissie, Y. L. Andalsvik, O. Roberts, S. Poluyanov, and S. Chernouss, 2012: **Results from the intercalibration of optical low-light calibration sources 2011**. *Geosci. Instrum. Method. Data Syst.*, 1, 91-107

**2.** Fuentes J. D, B. Geerts, T. Dejene, P. D'Odorico, and E Joseph, 2007: **Vertical attributes of precipitation in West Africa and adjacent ocean. Theoretical and Applied Climatology.**, 000, 1-13 (2007) DOI 10.1007/s00704 – 007-0318-0

**3.** Geerts, B., and T. Dejene, 2005: **Regional and diurnal variability of the vertical structure of precipitation systems in Africa based on space-borne radar data.** *J. Climate*, 18, 893-916

In papers I, II and III, I was responsible for the analyses and writing of the papers. The co-authors have contributed ideas, advice and feedback during the work. Paper II in this thesis is currently undergoing minor revision for the Journal of Atmospheric and Solar-Terrestrial Physics (JASTP), and paper III is submitted to Atmospheric Chemistry and Physics (ACP).

Included in the appendix are three papers on which I have worked but which do not directly address the theme of this thesis. The first paper represents work I did as part of a calibration project at the University Center on Svalbard, where my measurements and part of my report were included in the final publication. The last two papers are based upon my master's thesis at the University of Wyoming. The observations and data analysis from that thesis were later submitted for publications.

## Contents

Abstracts .....	iii
Acknowledgement .....	v
List of publications .....	vii
Content .....	ix
1. Introduction .....	10
2. Background .....	12
2.1. Thermal structure and atmospheric dynamics in the MLT region .....	12
2.2. Atmospheric waves .....	15
2.3. Planetary waves .....	16
2.4. Temperature-ozone relationship in the mesosphere .....	19
2.5. Gravity waves .....	21
3. Data sources and measurement .....	23
3.1. Ozone measurement and analysis .....	23
3.2. Michelson interferometer .....	25
3.3. SuperDARN radar and extraction of PMSE .....	26
3.4. NLC camera .....	27
4. Analysis and results .....	28
4.1 Quasi-16 day period oscillations observed in middle atmospheric ozone and temperature in Antarctica .....	29
4.2. Planetary wave oscillations observed in ozone and PMSE data from Antarctica .....	30
4.3. Characteristics and sources of gravity waves observed in NLC over Norway .....	31
5. Conclusions .....	32
References .....	33
Papers .....	38



## 1. Introduction

Atmospheric waves can have spatial sizes from a few kilometers to planetary scales, and temporal variations from days to minutes. They are typically generated in the lower atmosphere by topographic lifting of air masses, the action of weather systems (tropospheric eddies) or by land-sea heating contrasts, and propagate upward transporting energy and momentum. Indeed, waves are the primary way in which the atmosphere exchanges energy and momentum vertically. The main objective of this PhD thesis is to investigate the vertical phase structure of atmospheric waves of various scales in the middle atmosphere (30-90 km) so as to identify their source regions and where they deposit their energy and momentum.

As waves propagate upward, they interact with the strong thermally driven geostrophic winds. As a result of this interaction, they can reach critical layers, or grow in amplitude and become unstable, dissipating their energy and depositing their momentum. The energy and momentum from planetary waves (PW) are responsible for disturbing the strong stratospheric polar vortex winds that play a role in ozone depletion. Not only are they responsible for the vortex erosion, but also play an important role in the transport of trace gases in and out of the vortex (Plumb, 2002; Shepherd, 2007). The shorter scale gravity waves (GW) deposit their energy and momentum in the mesosphere, where they decelerate the winds, and drive the mesospheric winds and temperatures far from radiative equilibrium to create a global ageostrophic (meridional) circulation.

Since atmospheric waves play a key role in regulating global circulation and thermal balance, they are an important element of global circulation models (GCMs). However, due to the coarse resolution, topography and prescribed sea-surface temperatures of most GCMs, the source distributions of waves, as well as their propagation and dissipation, are not well represented or resolved in current GCMs. Hence, they require proper specification of wave sources and their geographical distribution to effectively simulate the wave-driven circulation effects. This is of particularly high importance in the Antarctic regions where information is scarce.

Measurements of PW in the upper stratosphere and lower mesosphere are very limited. This is partly because the altitude is too high for radiosondes, aircraft and stratospheric-tropospheric radars. Similarly, middle atmospheric radars do not cover the full altitude

range, and satellite remote-sensing measurements alias spatial and temporal coverage due to their orbital parameters. In this study we use continuous ground based measurements of ozone mixing ratio profiles from ~30 km to ~75 km that were recorded with a microwave radiometer located at Troll station, Antarctica (72.0°S, 2.5°E). Due to the temperature dependent ozone chemistry, it is possible to use variations in the ozone to trace and characterize the vertical phase structure of temperature perturbations caused by PWs. These studies focus on combining the planetary wave oscillations observed in middle atmospheric ozone with concurrent ground-based mesopause (~87 km) airglow temperature data recorded at Rothera station Antarctica (67.6°S, 68.1°W), and PMSE observations, which are used as a proxy for mesopause temperatures near 85 km, derived from the SuperDARN radar at Sanae, Antarctica (71.7°S, 2.8°W). Using these combined data sets it is possible to determine the PW source altitude regions, their propagation characteristics, and their interaction with the background wind throughout the middle atmosphere during the Antarctic winter and summer.

In a further study, the characteristics and sources of gravity waves are estimated from Noctilucent Cloud (NLC) images collected using an automated camera system in Trondheim. Typically such studies have been conducted using the perturbation of the night airglow chemistry and density caused by gravity waves to determine the wavelength, direction and phase speed of the waves. The use of the thin (~1 km) NLC provides the opportunity to extend such climatological studies to the sunlit polar summer. In addition, since the NLC perturbations are primarily density rather than chemically induced variations, the wave amplitudes can be determined and used to infer the altitude of their source regions for the first time. Ray-tracing can then be used to estimate the geographical distribution of these source regions.

The choice of scientific questions that are to be addressed in this thesis depended on the importance of the study in understanding the vertical phase structure of waves in the middle atmosphere, determining their source and energy-deposition regions and the unique datasets now available. The study greatly benefited from using the high temporal resolution ozone mixing ratio observations from the British Antarctic Survey (BAS), and the high resolution NLC images from the Leibniz-Institute of Atmospheric Physics, Kühlungsborn Germany (IAP).

## 2. Background

### 2.1. Thermal structure and atmospheric dynamics in the MLT region

The thermal structure of the atmosphere can be understood by the distribution of chemical species in the atmosphere such as  $\text{CO}_2$ ,  $\text{H}_2\text{O}$ ,  $\text{O}_3$  and  $\text{O}_2$ , their interaction with solar irradiance, radiative transfer within the atmosphere, and the turbulent heating driven by convection or wave motion. The radiative cooling and heating rates in the atmosphere are determined by the distribution of these chemical species. Figure 1 show that  $\text{O}_3$  is the main radiative heating species up to 80 km, while above that height,  $\text{O}_2$  is larger. On the other hand,  $\text{CO}_2$  is the major radiative cooling species throughout the atmosphere.

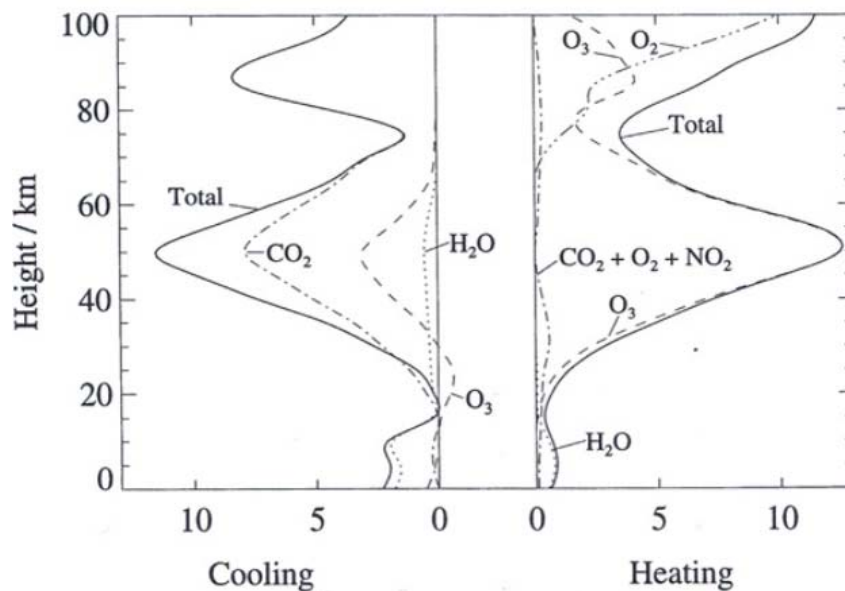


Figure 1: Global-mean vertical profiles of heating and cooling rate in K/day, from contributions of the chemical species in the atmosphere (London, 1980).

Under radiative equilibrium alone, without including the effects of convection or wave motions, the zonal average temperature of the atmosphere has been calculated by Geller [1983] and this is shown in Figure 2a. The corresponding geostrophic mean zonal winds under radiative equilibrium alone are shown in Figure 2b.

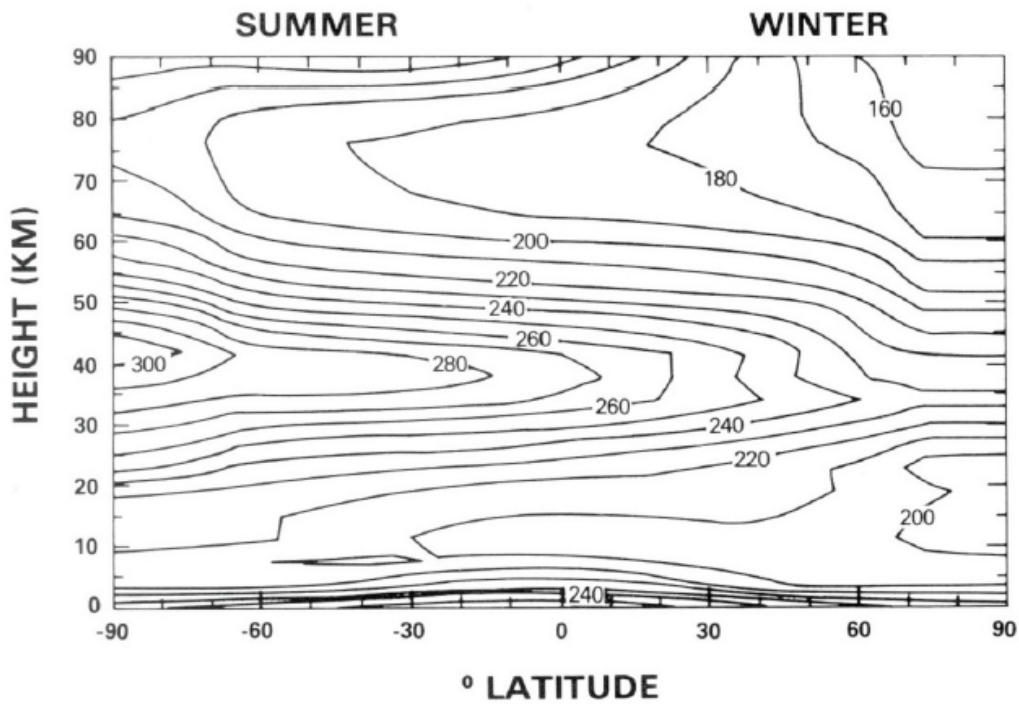


Figure 2a: Radiative equilibrium temperatures (After Geller [1983])

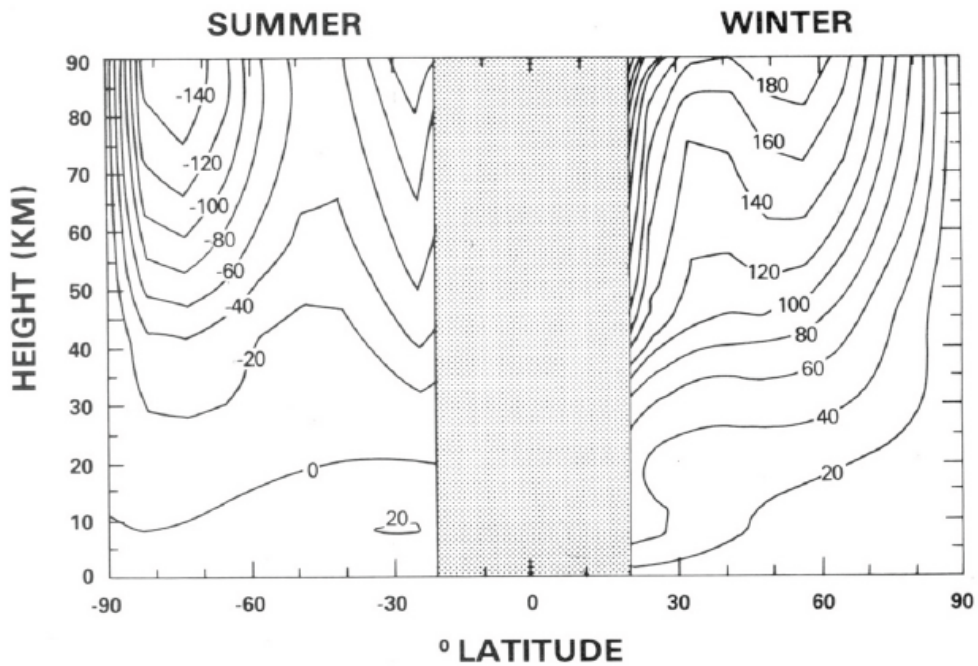


Figure 2b: Radiative equilibrium geostrophic mean zonal winds (After Geller [1983])

The corresponding modeled zonal mean temperature and wind distributions of the atmosphere in which heating due to eddy or wave motions have been included are shown in Figures 3a and 3b respectively. As can be observed in Figure 3a and Figure 3b, the temperature and wind distributions of the semi-empirical COSPAR International Reference Atmosphere, CIRA 86 (Fleming et al., 1988) cannot be reproduced using radiative equilibrium

alone. Substantial deviations are observed in the summer mesosphere due to circulation driven by wave motions. Here both ground and satellite measurements have observed that the polar summer mesopause is the coldest place in the earth with temperatures falling to below 130K during the summer months at polar latitudes [e.g. Lübken, 1999].

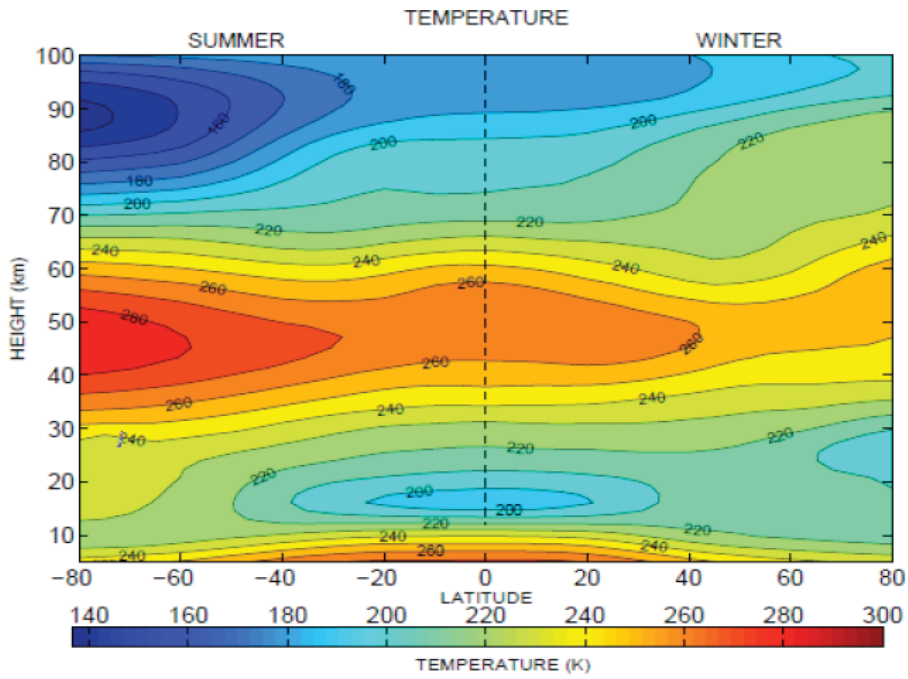


Figure 3a: Zonally averaged temperature predicted by CIRA-86 model during solstice, adapted from Tunbridge (2011)

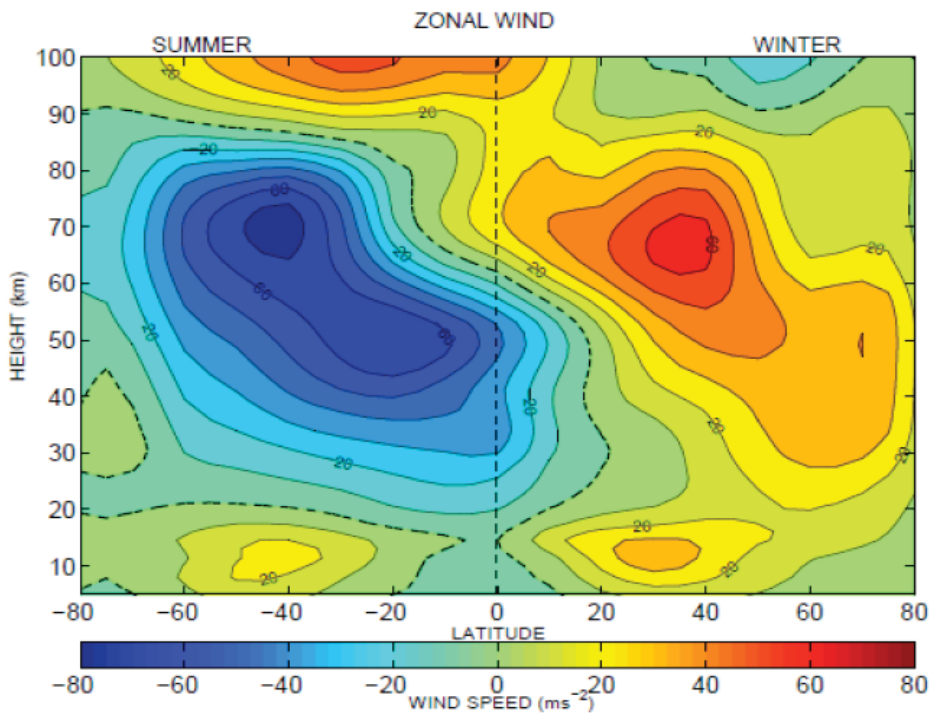


Figure 3b: Zonal mean winds from CIRA-86 model during solstice, adapted from Tunbridge (2011)

A mean vertical upwelling over the summer pole that induces an adiabatic cooling has been a cause for this large deviation of temperature from radiative equilibrium (e.g. Garcia and Solomon, 1985). On the other hand, warming of the winter mesopause is caused by the down-welling over the winter pole. The overturning of atmospheric waves (e.g. gravity waves) and the subsequent deposition of momentum and energy is the key driver for this ageostrophic flow in the mesosphere. Similarly, the wintertime high latitude zonal wind jet, the polar vortex, is substantially weaker than would be expected from radiative equilibrium alone. Here it is the breaking of westward travelling planetary waves that leads to a weakening of the polar vortex. During periods of high planetary wave activity, this can cause the complete breakdown of the vortex known as a stratospheric warming event. It is therefore very important to study waves and their interaction with the mean flow.

## 2.2. Atmospheric waves

Atmospheric waves can be classified into three major oscillations mainly based on their wavelength and periodicity: planetary waves with periods of 2-30 days, gravity waves with periods of about 5 minute to several hours and atmospheric thermal tides with periods of 12 and 24 h (Andrew et al., 1987). These wave motions can be described by the amplitude ( $\theta_o$ ), the frequency ( $\nu$ ), and the phase ( $\phi = \nu t - \alpha$ ) of the motion as shown below:

$$\theta(x, y, z, t) = \theta_o \cos(kx + ly + mz - \nu t - \alpha) \quad (1)$$

Here  $\theta$  represents a perturbation with amplitude  $\theta_o$  of temperature ( $T'$ ), ozone ( $O_3'$ ), zonal ( $u'$ ) or meridional ( $v'$ ) winds in space and time. The wavenumbers  $k$ ,  $l$  and  $m$ , which are related to the wavelength (e.g.  $k = 2\pi/\lambda_x$ ), represent the spatial perturbations in the  $x$  (positive eastward),  $y$  (positive northward),  $z$  (positive upward) directions, respectively (Figure 4 shows the schematic diagram). The temporal perturbation occurs at frequency,  $\nu$ , while  $\alpha$  is phase constant. The spatial orientation of the wave fronts can be represented by the total phase,  $\phi = (kx + ly + mz - \nu t - \alpha)$ . The phase speed ( $c$ ), which is the rate at which the phase of the wave propagates in each of the three dimensions (Lynch and Cassano, 2006) is given by:

$$c_x = \frac{\nu}{k}, c_y = \frac{\nu}{l}, c_z = \frac{\nu}{m} \quad (2)$$

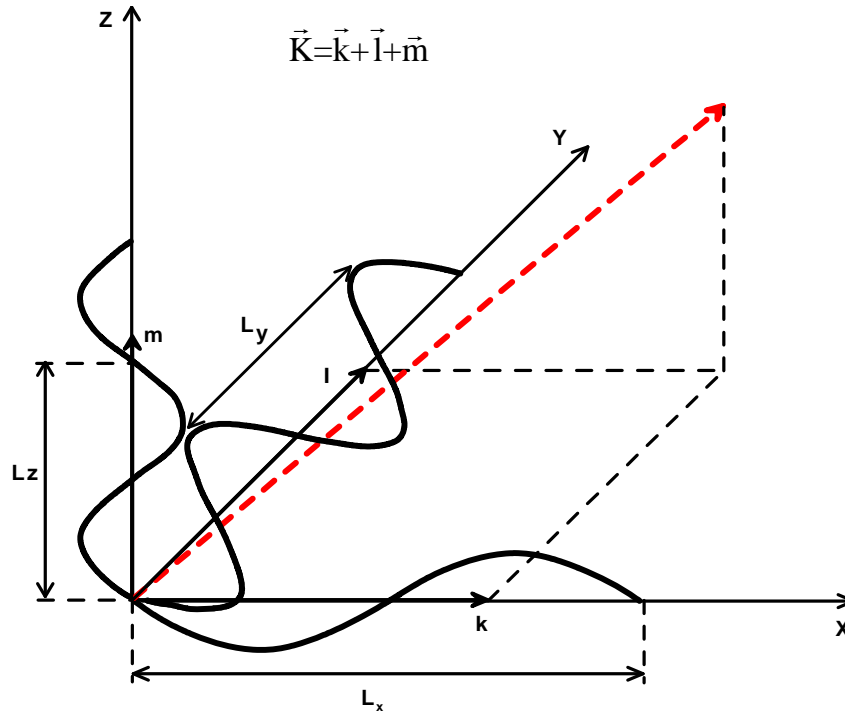


Figure 4: Illustration of a spatially propagating wave, adapted from Serafimovich (2006)

### 2.3. Planetary waves

Planetary waves, also called Rossby waves, are global scale oscillations in the atmosphere, which have horizontal scales of thousands of kilometers, vertical size of several kilometers, and periods from 2 to 30 days (e.g. Salby, 1981; Forbes, 1995). They propagate westward relative to the zonal flow and can be characterized by a zonal wavenumber that represents the number of integral wavelengths around the planet. The waves are generated in the troposphere by large-scale diabatic heating associated with land-sea temperature differences and by orographic disturbances, and they can propagate upward into the middle atmosphere. They redistribute energy, momentum and the atmospheric constituent concentrations across long distances because of their long wavelength. As with any wave, these large-scale oscillations require a positive restoring force, and here it is the variation of the Coriolis force with latitude. The restoring force comes from the meridional gradient of the Coriolis parameter, which can be explained by conservation of the absolute vorticity in a barotropic, non-divergent fluid.

The conservation of absolute vorticity is expressed as:

$$\frac{d\eta}{dt} = \frac{d(\xi + f)}{dt} = 0 \quad (3)$$

Where  $\eta$  is the absolute vorticity,  $\xi$  is the relative vorticity and  $f$  is the planetary vorticity.

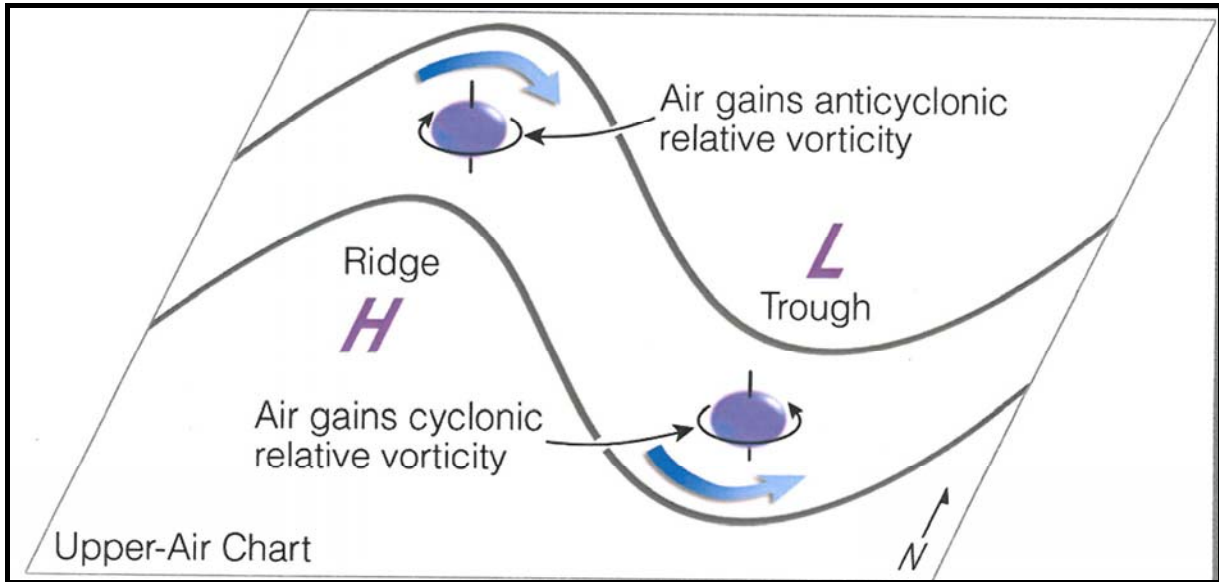


Figure 5: Illustrating the circulation around ridge and trough in terms of conservation of potential vorticity (Courtesy to Steve LaDochy, California state University).

From the conservation of absolute vorticity, horizontal motion of an individual air parcel can be traced. An individual air parcel moving from north to south in the northern hemisphere must rotate in anticlockwise direction in order to compensate for decreasing  $f$ . Similarly, an air parcel which moves from south to north must rotate in the clockwise direction to compensate for increasing  $f$ . Figure 5 demonstrates the conservation of vorticity in the curved areas of the contour lines (troughs and ridges). Air moving through a ridge spins clockwise and gains anti-cyclonic relative vorticity. In the trough area, the air spins anticlockwise and gains cyclonic relative vorticity.

Assuming that the Coriolis parameter varies linearly with latitude, which is known as the beta plane approximation,  $f$  can be written as  $f=f_0 + \beta y$ , where  $f_0 = 2\Omega \sin\phi$  is the Coriolis parameter, and  $\phi$  is the latitude and  $y$  is the northward distance.

In general, the meridional gradient of the Coriolis parameter, also called the Rossby parameter ( $\beta$ ) is expressed as

$$\beta = \frac{2\Omega \cos \phi}{a} \quad (4),$$

Where  $\Omega$  is the angular speed of the Earth's rotation and  $a$  is the mean radius of the earth. Since the zonal phase speeds of planetary waves are often comparable to the mean zonal wind speed, the vertical propagation of planetary waves is very much dependent on the interaction with the mean zonal flow.

The phase speed of planetary motion, for the barotropically stratified uniform non-divergent motion, can be expressed by considering the dispersion relation:

$$c = -\frac{\omega}{k} = U - \frac{\beta}{k^2 + l^2}, \quad (5),$$

Where  $c$  is the zonal wave phase speed,  $U$  is the zonal mean flow,  $\beta$  is the Rossby parameter,  $\omega$  is wave frequency, and  $k$  and  $l$  are the zonal and meridional wavenumbers respectively.

Since the Coriolis parameter is always positive,  $\beta > 0$ , it can be inferred from equation (5) that the velocity of the wave relative to the flow must be negative. As a result,  $U - c > 0$  is always true. Thus the phase speed of the planetary waves must be westward relative to the background mean flow. Planetary waves with lower speed can be swept eastward by the zonal flow while waves with a phase speed greater than eastward mean zonal flow propagate westward during the winter season (Salby, 1996).

The phase speed, as shown in the equation above, is inversely proportional to the square of the horizontal wavenumbers ( $l$  and  $k$ ) such that it increases rapidly with increasing wavelength. Waves of this type, where the phase speed varies with wavelength (known as dispersive waves), become susceptible to the effects of the mean winds as the wave period increases or when the phase speed decreases. For stationary waves, vertical propagation is possible in eastward winds when the wind speed is below an upper limit. The same is true for propagating planetary waves as long as the wind is eastward relative to the wave, meaning  $U - c > 0$ . Strong eastward winds hinder traveling planetary. As a result, planetary waves can only travel in a certain range of mean flows:

$$0 < U - c < U_c \quad (6)$$

Where  $U_c$  is the critical velocity, which is expressed by the Charney-Drazin criterion:

$$U_c = \frac{\beta}{\left[ (k^2 + l^2) + \frac{f_o^2}{4H^2N^2} \right]} \quad (7),$$

Where  $N$  is the buoyancy or Brunt-Vaisälä frequency and  $H$  is the scale height. This criteria by Charney and Drazin (1961), who first investigated the vertical propagation planetary waves, showed that the planetary scale waves propagate only when the zonal winds are eastward ( $U > 0$ ) and not too strong ( $U < U_c$ ) in the winter stratosphere. For a planetary-scale wave, the critical velocity grows as the horizontal wavelength increases, allowing the vertical propagation of the waves in a wider range of eastward flows as compared with the small-scale waves. On the other hand, during summer when the zonal stratospheric mean winds are easterlies, vertical propagation of waves is slowed or absorbed since the waves reach critical levels at points where  $c = U$ . Although the strong easterly zonal wind in the summer stratosphere should block most of the PWs originating in the lower atmosphere, some numerical modeling studies (Geisler and Dickinson, 1976) show that there is a possibility of upward wave propagation. A number of other mechanisms could also be responsible for the existence of PW in the summer mesosphere: They can arise due to ducting mechanisms from the winter mesosphere across the equator (Forbes et al., 1995; Espy et al., 1997, Riggins et al., 2006, Hibbins 2009), baroclinic instability of the mesospheric jet and through gravity wave modulation (Holton, 1984; Smith, 2003).

#### **2.4. Temperature-ozone relationship in the mesosphere**

The relationship between ozone and temperature in the Earth's atmosphere depends on the interaction between radiative, dynamical and photochemical processes. Below 30 km, the chemical lifetime of ozone (and its odd oxygen family) is on the order of a month. Since this is longer than typical dynamical transport times, transport effects will control the ozone concentrations at a given location. This leads to a positive correlation of ozone with temperature (Brasseur and Solomon, 1986). On the other hand, the ozone molecule has a very short chemical lifetime ( $< 1$  day) in the upper stratosphere and mesosphere, and photochemical effects therefore control ozone concentrations at these heights. As a result, ozone and temperature are anti-correlated at these heights since an increase in temperature leads to a non-linear chemical decrease of ozone. A wave can lead to a periodic variation of density as well as temperature, and thus to a change in the ozone mixing ratio. In this thesis,

the variation of ozone mixing ratio and temperature due to the passing of planetary waves and other dynamical and chemical processes will be used to investigate the vertical structure of planetary waves.

Using the Chapman chemistry (Andrews, 2000), the equilibrium mixing ratio of ozone can be modeled and the dependence of ozone on temperature can be expressed as:

$$\mu = \frac{[O_2]}{\sqrt{[M]}} \sqrt{\frac{6.0 \times 10^{-34} j_2 \left(\frac{T}{300}\right)^{-2.4}}{8.0 \times 10^{-12} j_3 \exp\left(\frac{-2060}{T}\right)}} \quad (8),$$

Where [M] is the total number density of air, [O<sub>2</sub>] is the number density of molecular oxygen and  $j_2$  and  $j_3$  are the photo-dissociation rates for O<sub>2</sub> and O<sub>3</sub>, respectively.

An example illustrating the relationship between temperature and ozone variation is shown in Figure 6. The variation of ozone for altitudes 45 km and 70 km (from Kleinknecht 2010) shows that ozone and temperature are anti-correlated.

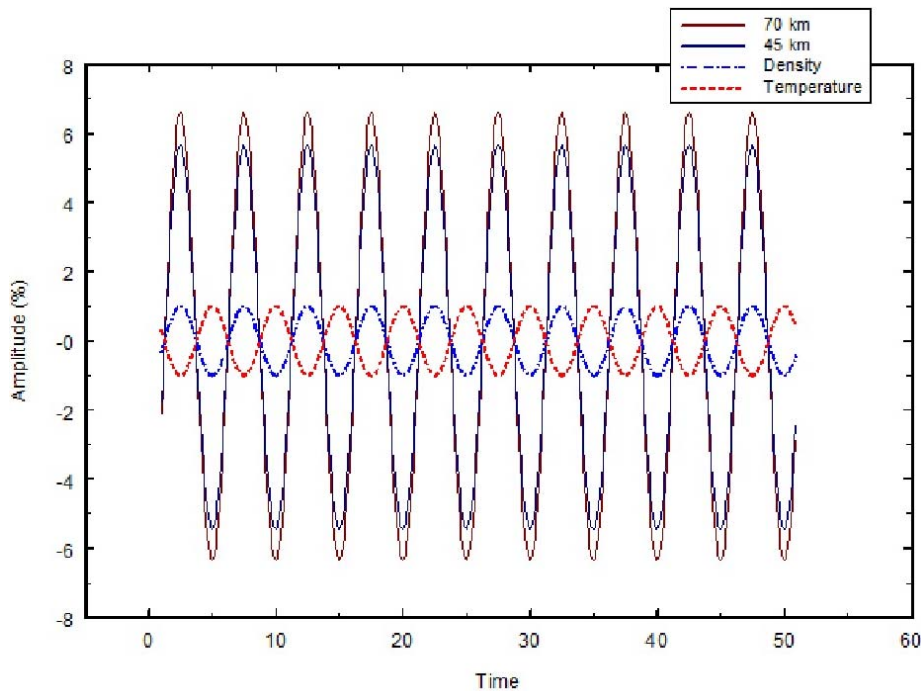


Figure 6: Modeled ozone mixing ratio variation at 45km and 70km due to a 1% temperature variation (Kleinknecht 2010).

The temperature oscillation due to the passing of PW is amplified by O<sub>3</sub> while preserving the phase. Thus, variations in the O<sub>3</sub> as a function of altitude can be used to trace the phase fronts of the PW oscillation.

## 2.5. Gravity waves

Gravity waves are periodic oscillations of air parcels with buoyancy and gravity as the restoring forces in a stably stratified atmosphere (e.g., Andrews et al., 1987). They have horizontal wavelengths that vary from a few to hundreds kilometers (e.g. Manson, 1990) and observed periods ranging from the Brunt Vaisälä period (typically ~5 minutes) to the inertial period (1 day) as detailed in Fritts and Alexander (2003). The major sources of gravity waves are, for example, orographic forcing from airflow over the mountains (e.g. Ralph et al. 1997), thunderstorms (e.g. Alexander and Pfister 1995), and storm fronts (e.g. Fritts and Alexander, 2003). In addition, *in situ* excitation due to gravity- or planetary-wave breaking (Fritts et al. 2003) can occur throughout the middle atmosphere.

Gravity waves generated in the lower atmosphere propagate upwards and their amplitude increases due to the exponential decrease of atmospheric density. As they interact with the background winds, they can encounter regions of dynamical instability, or critical levels, when the wind speed equals the wave speed. Even in a low-wind environment they can grow to become convectively unstable when the amplitude of the temperature perturbation exceeds the adiabatic lapse rate. This leads to the shedding of wave energy to the background atmosphere so as to limit the amplitude growth, and in many cases causes the wave to overturn where it dissipates all its energy or deposits its momentum in the region (Figure 7).

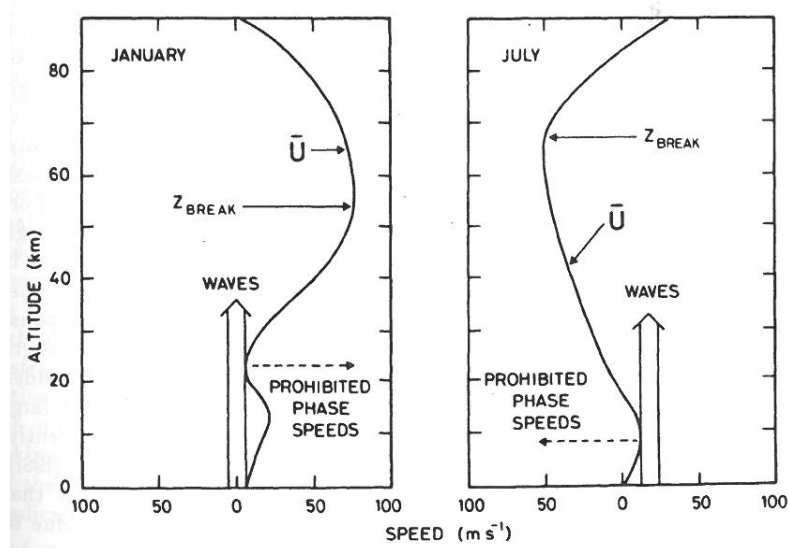


Figure 7: Effect of the wind fields on the propagation of gravity waves (Brasseur and Salomon, 1986).

The vertical propagation of gravity waves is largely controlled by the filtering effect of the thermally driven wind field below  $\sim 60$  km. Figure 6b shows the propagation of gravity waves as they interact with the background wind field. The reflection and absorption of gravity waves at critical levels in the stratosphere and lowermost mesosphere determines the gravity wave spectrum and net momentum transferred to the mesosphere and mesopause region (Lindzen, 1981; McLandress, 1998). As a result, the observed gravity wave characteristics in the mesopause region provide information about their sources as well as about the wind field in the lower atmosphere.

Different approaches and techniques have been employed to observe and study these gravity waves in the middle and upper atmosphere. Noctilucent clouds, which are formed as the result of the extreme cold temperature due to the breaking of gravity waves, can themselves be used to study gravity waves. The structures seen in NLC are a manifestation of the gravity waves (Hines, 1960), and can be analyzed to study the characteristics and origin of gravity waves of different sizes in the high-latitude summer mesopause region (Haurwitz, 1961).

Although there are a number of gravity-wave studies at high latitudes, most of these rely upon analyzing the wave structures induced by the waves in the night airglow (e.g., Taylor et al., 1989; Pautet et al., 2005; Nielsen et al., 2006, 2009; Espy et al 2004; 2006 ). However, these observations are not possible during the high latitude polar summer when the mesosphere remains sunlit. Recently, Pautet et al. (2011) constructed a summertime gravity-wave climatology using the structures present in the NLC (Hines, 1960; Thomas, 1991; Fritts et al, 1993; Chandran et al., 2009, 2010). In paper 3 of this PhD thesis, we used NLC images from a digital camera located in Trondheim, Norway to extend the Pautet et al. (2011) climatology of summertime GWs to higher latitudes. In addition, the present study utilizes the fact that these structures in the NLC are primarily due to the changing density of mesospheric aerosol particles rather than a change in the particle radii. It is therefore possible to quantify the relative wave amplitude in the NLC region, and utilize a ray-tracing model (Eckermann and Marks, 1995; 1997) to identify the source regions of high latitude gravity waves present during the polar summer.

### **3. Data sources and measurement**

The studies in this PhD thesis used data from four primary sources. The ozone mixing ratio profiles used for the two planetary-wave studies in this PhD thesis came from the ground-based microwave radiometer of the British Antarctic Survey (BAS) that was located at the Norwegian Polar Institute Troll station (72°S, 2°N) from February 2008 through January 2010 (Espy et al., 2006; Straub et al., 2013). For the wintertime study of the quasi-16 period oscillations in Antarctica, the ozone mixing ratio was extended into the mesopause region using nighttime averaged temperatures derived from the hydroxyl airglow observations at Rothera, Antarctica (Espy et al., 2003). For the 5- and 6.5-day wave studies in Antarctica during summer of 2009, the Polar Mesospheric Summer Echoes (PMSE) at 85 km, which were extracted from the SuperDARN radar at Sanae that overlooks the field of view of the Troll radiometer (Hosokawa et al., 2005; 2005), were combined with the radiometer ozone mixing ratios. For the study of the characteristics and sources of gravity waves, NLC images from an automated digital camera developed at the Leibniz Institute for Atmospheric Physics (IAP) in Germany (Baumgarten et al., 2009) and mounted at the roof of the Physics department at NTNU are used. Details of the data types, the instrumentation as well as the data analysis are presented in the following sections.

#### **3.1. Ozone measurement and analysis**

The BAS ground-based microwave radiometer (shown in Figure 8a) measures spectra of rotational line of O<sub>3</sub> centered at 249.96 GHz as shown in Figure 8b. Optimal estimation methods, as described by Rodgers [1976], have been used to invert the spectra of the ozone line at 249.96 GHz to obtain ozone profiles. The a priori pressure, temperature, water vapor and ozone values used for the inversion below 45 km are derived from monthly mean ERA-40 profiles. Between 45 and 85 km, monthly mean temperature and pressure values were taken from the MSIS-00 model (Picone et al., 2002), and ozone and water vapor were taken from the US Standard Atmosphere Supplements (1966) for winter and summer conditions.

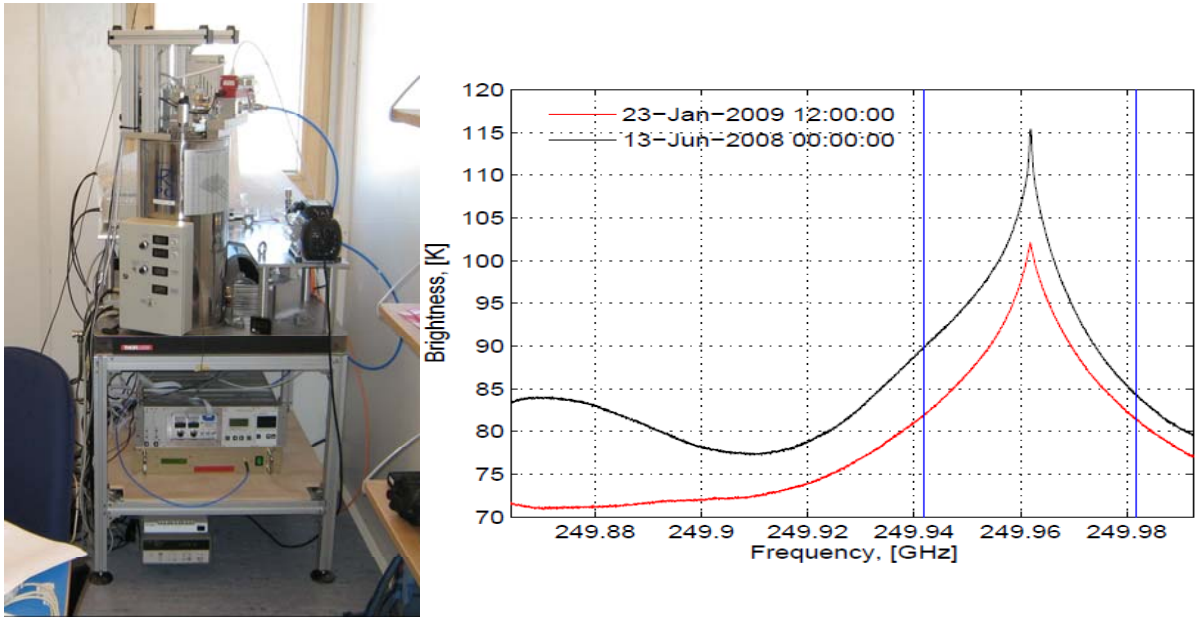


Figure 8: Left-panel: Picture of the microwave radiometer courtesy to D. J. Maxfield at BAS, and Right-panel: Absorption line of ozone (adapted from Daae et al, 2013)

For the wave studies here, the ozone values above 85 km were held at a constant value so as to ensure that the a priori values did not induce oscillations. The retrieved hourly ozone profiles as a function of altitude and time are shown in Figure 9 below. The a priori information dominates the profile at altitudes below 30 km and above 80 km. As can be seen in Figure 9, the first ozone maximum is observed around 35 km and the middle mesospheric maximum is observed around 70 km during the winter. The traditional secondary maximum (at much higher altitude) is not observed due to lack of measurement response in the region above 90 km.

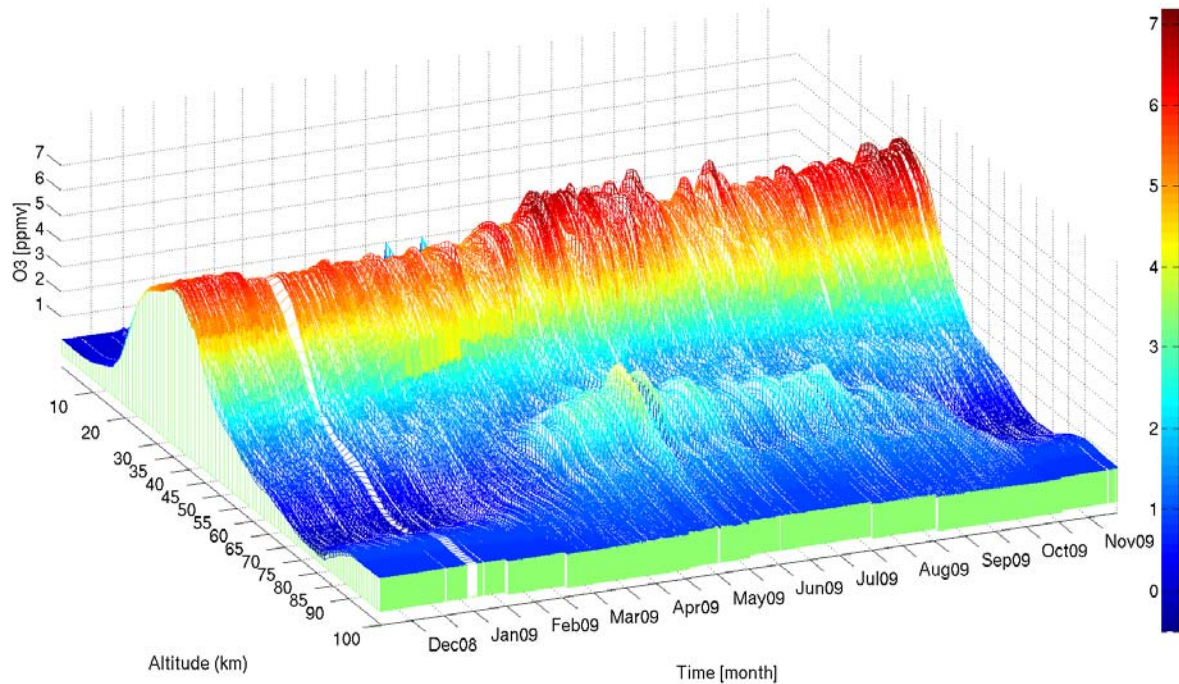


Figure 9: Ozone mixing ratio profile from December 2008 to November 2009 at the Troll station (from Kleinknecht, N. (2010))

### 3.2. Michelson interferometer

A Michelson interferometer placed at the British Antarctic Survey station at Rothera was used to obtain the temperature data near the mesopause. Hydroxyl (OH) is produced at night through the reaction of atomic hydrogen with ozone in a  $\sim 8$  km thick layer centered near 87 km (Baker and Stair, 1988). Because this reaction is highly exothermic, the resulting OH molecule is produced in highly excited vibrational levels (levels 7, 8 and 9). The molecule radiatively relaxes in by making vibrational-rotational transitions, emitting near infrared photons and preferentially lowering its vibrational energy by 2 quanta each time. Because the molecule makes on the order of  $10^3$  collisions as it progresses down the vibrational ladder to the third vibrational level, the closely spaced rotational levels are in thermal equilibrium with the surrounding atmosphere by the time it makes the  $3 \rightarrow 1$  transition (Pendleton et al., 1993), radiating near 1600 nm. Thus, by measuring the relative intensity of the lowest rotational levels ( $< 6$ ), the Boltzmann population, and hence the local temperature from the emitting region near 87 km, can be inferred.

The method of fitting the rotational temperature to the measured spectra is discussed in Espy and Stegman (2002). In this study, a night-time average of the temperature extracted

from the OH Meinel (3, 1) band was used. The weighted mean temperature for each night was calculated for nights which had at least 2 hours of measurements. Nights with missing temperature data due to cloudy weather and instrument downtime were filled by interpolation in order to create an evenly sampled series of data for comparison with the ozone mixing ratio.

### **3.3. SuperDARN radar and extraction of PMSE**

Polar Mesosphere Summer Echoes (PMSE) are strong radar backscatter echoes that have been observed using radars operating above 10 MHz in the layer between 80-90 km occurring during the polar summer (Cho et al, 1993). The Super Dual Auroral Radar Network (SuperDARN) is a network of high frequency (HF) radars, whose combined field of view nearly covers the northern and southern hemisphere polar ionospheres. The radars are typically used to study large-scale dynamical processes in the earth's ionosphere, magnetosphere and neutral atmosphere (Greenwald et al., 1995). There are several SuperDARN radars currently working in both hemispheres, and PMSE have been detected in the near range measurements of the high latitude SuperDARN radars (Ogawa et al., 2002). However, the PMSE must be separated from other backscatter echoes coming from meteors and E region echoes (Hosokawa et al., 2004).

In this study, the algorithm developed by Hosokawa et al., (2005) was applied to the SuperDARN data at Sanae station (70°S, 2°W) to extract PMSE from near-range gate, whose centroid latitude and longitude lie within the field of view of the Troll radiometer. All echoes from the first range-gate measurements were initially identified, including PMSE, E-region backscatter echoes and meteor-trails. Then, the criteria adopted by Hosokawa et al., (2005) were applied to differentiate PMSE from the other two scattering mechanisms. First, the back scattered power was required to be greater than 6 db. Secondly, only Doppler velocities between  $\pm 50 \text{ m s}^{-1}$  were accepted. Finally, the spectral width was required to be less than  $50 \text{ m s}^{-1}$ . Hosokawa et al., 2005 have shown that echoes passing these three criterions have a high probability of being PMSE. Figure 1 in paper II shows the occurrence rate of echoes that passed the selection criteria as a function of local time and day of the year for the first three SuperDARN range gates. In this study, only the first range gate (Gate 0), which covers 80 to 100 km, was used, and the occurrence rate was computed for each

local-time bin during a given day by dividing the number of echoes passing the selection criteria by the total number of observations present there.

### 3.4. NLC camera

An automated high-resolution digital camera, from the Leibniz Institute of Atmospheric Physics of Kühlungsborn, Germany, mounted at the roof of the physics department at NTNU, Trondheim has been collecting NLC images since 2007 (Baumgarten et al, 2009). The observation geometry of the NLC is shown in Figure 10. The clouds become visible when the sun is below the horizon but still illuminating the clouds. The exposure settings and the frame rate are automatically calculated by the camera system depending on the solar elevation angle. The camera takes pictures throughout the twilight period with exposure times of 0.5s and 0.6s with a cadence ranging between 3 to 5 frames per minute depending on the solar elevation angle. The camera views towards the north with a field of view (FOV) of  $54.5 \times 41.5^\circ$ . Figure 11 is an example of the NLC image taken on the night of 16–17 July, 2008, at 22:30 UT.

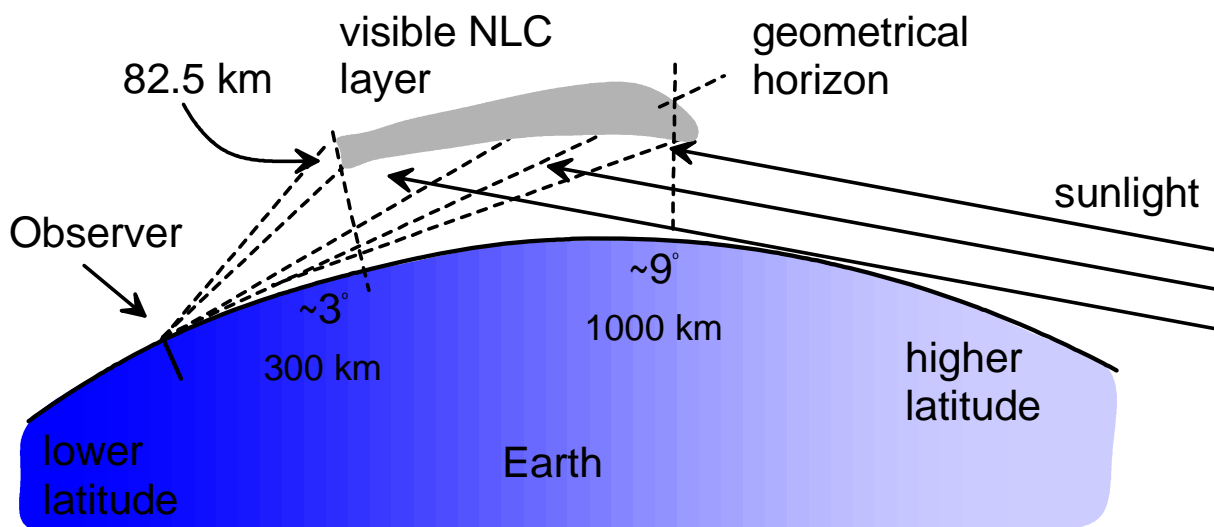


Figure 10: Noctilucent cloud (NLC) observation geometry, adapted from G. Baumgarten (2009)



Figure 11: NLC observed by camera from Trondheim on 30 July 2008 at 23:00 UT

#### 4. Analysis and results

For planetary wave analysis, seasonal and longer time scale variations that are not part of short periodic oscillations were subsequently removed from ozone mixing ratio, temperature and PMSE data to isolate the short periodic motions with periods less than 20 days. One way of doing this is by a harmonic de-trending of the datasets. However, a more robust method is to use a high-pass filter to remove waves with periods larger than 20 days. A high-pass filter was applied to all the datasets to filter out long period oscillations while retaining periodic motions with shorter periods of less than 20 days. A Butterworth IIR high-pass filter was specifically used to remove these long period variations since it has a maximum flat frequency response in the selected pass band (e.g. Stearns, 1975).

A fast Fourier transform (FFT) was then performed on the high-pass filtered datasets to determine the amplitude and phase of periodic fluctuations observed in the ozone, temperature and PMSE fields with periods of less than 20 days. The high-pass filtered data was windowed using a Hamming function (Nuttall, 1981) before the FFT was performed in order to reduce spectral leakage and side-lobe effects in the FFT.

A cross-spectral analysis was performed between two datasets (e.g. ozone and temperature or ozone and PMSE) to examine whether or not the oscillations observed in the two datasets are phase coherent. The cross-spectral analysis provides a frequency-dependent measure of the correlation between the observed peak signals between the two datasets, which may

indicate a physical connection between the two. Having identified frequency regions in the cross-spectrum where the data sets were highly phase coherent, the data were band-pass filtered to isolate these regions so that the correlation between oscillations of a specific frequency could be quantified.

A time-lagged cross correlation analysis was then performed on these filtered data sets, and regions of maximum and minimum correlation traced out the vertical structure of the phase fronts and quantified the coherence of the two datasets at altitudes from 30 to 80 km. Regions where the phase progresses with altitude indicate propagation of energy, whereas regions with little phase shift are indicative of normal mode oscillations. It was also noted that regions where both propagating and normal modes interact with the background wind can be identified by localized sudden shifts in the phase progression with altitude, indicating regions where PW energy and momentum are deposited into the background flow.

For the gravity wave analysis, a number of procedures were followed and they are explained in detail in paper 3. The analysis includes projection of the original NLC pictures; extracting the horizontal wavelength, phase speed and the direction of propagation using FFT and least-square fitting techniques; removing the Rayleigh scattered background to extract the relative Mie scattering amplitude and corresponding relative density fluctuation; and, finally, the Gravity Wave Regional or Global Ray Tracer (GROGRAT), developed by Eckermann and Marks (1997), was used to trace waves upward from different geographic regions to identify the source regions for the gravity waves observed in the NLC.

#### **4.1. Quasi-16 day period oscillations observed in middle atmospheric ozone and temperature in Antarctica**

The purpose of this study was to use temporal variations in the mesopause airglow temperatures and the O<sub>3</sub> vmr profiles in the mesosphere and stratosphere to trace and characterize the vertical behavior of planetary waves reaching the mesopause during the winter. The largest amplitudes in the power spectrum of both the O<sub>3</sub> vmr above Troll station, Antarctica and in the hydroxyl night-glow temperatures above Rothera, Antarctica (Figure 2 in paper 1) during the winter are found to be due to the quasi-16-day oscillations. In the O<sub>3</sub> data, waves with periods <12 days were also strong below the stratopause, but only the 16-day wave persisted into the mesosphere. In addition, the period of the 16-day wave

increased below 42 km due to Doppler shifting (Forbes, 1995) by the increasing eastward zonal winds there (Hibbins et al., 2005). The amplitude of the quasi-16 day wave was also found to vary with height, with minimum amplitudes found near the stratopause. This could be due either to wave absorption by the large negative wind gradients (McDonald et al. 2011) or to the minimum O<sub>3</sub> concentrations found there. Despite the presence of low wave amplitudes, the 16-day oscillations in the mesopause temperature are phase coherent with the corresponding oscillations observed in O<sub>3</sub> vmr at all levels (Figure 3, in paper 1). The 16-day wave is found to have vertical phase fronts consistent with a normal mode structure, and extends from the mesopause down into the upper stratosphere (Figure 4 in paper 1). Thus, utilizing a ground-based radiometer, with its high temporal resolution we were able to observe the phase structure of the 16-day oscillation throughout the middle atmosphere; identify its normal-mode structure; and show where it interacts with the background wind, becomes transiently propagating, and depositing energy and momentum.

#### **4.2. Planetary wave oscillations observed in ozone and PMSE data from Antarctica**

The PMSE occurrence frequency extracted from the SuperDARN radar at Sanae station in Antarctica during the 2009 summer season was combined with spatially and temporally coincident midnight measurements of ozone mixing ratio obtained from the BAS microwave radiometer located at Troll station. These were used to measure the period and vertical structure of planetary waves in stratosphere and mesosphere. The amplitude spectra show that there are a number of oscillations in the ~2-12-day period range, with the 4-5 day and 6-8 day oscillations being the largest in both the PMSE occurrence frequency as well as in the ozone vmr profiles from 30 to 80 km (Figure 4 in paper 2). These waves have been taken to be the 5-day and 6.5-day zonal wave-number one planetary waves.

The study demonstrates that the PMSE oscillations appear to be driven by two planetary waves with similar periods, 5- and 6.5-days, that are known to have similar zonal wavenumber-1 structure. Despite the climatologically westward zonal winds in the middle atmosphere, these waves have been traced downward into the stratosphere using the ozone vmr variations, and they are observed to have distinctly different vertical phase structures (Figure 6a and Figure 6b in Paper 2). The 5-day wave has nearly vertical phase fronts consistent with a normal mode structure, and is seen to extend from the PMSE region near

85 km down to the upper stratosphere. However, the phase structure of the 6.5-day wave indicates that it is propagating upward from the stratosphere into the PMSE region. The amplitude changes of ozone vmr with altitude cannot unambiguously be used to infer the interaction between the waves and the mean flow. However, the rapid phase changes observed in the 6.5 day wave near the zonal wind maximum may be indicative of such interactions.

#### **4.3. Characteristics and sources of gravity waves observed in NLC over Norway**

Beginning in the summer of 2007, four years of NLC pictures from the digital camera in Trondheim are combined with results from a ray tracing model to characterize and identify sources of gravity waves observed in the summer mesosphere. To summarize the characteristics of the summertime gravity wave events, histogram plots of the horizontal wavelength, phase speed and the resulting period are shown in Figures 5, 6, and 7 in paper III. The relative amplitudes derived from the NLC image analysis (Figure 5d in paper III) were compared with the relative amplitudes at NLC heights derived from ray tracing (Figure 6d and 7d in paper III). Waves were launched from two different altitudes (5 and 60 km) to determine the most probable source altitude of the waves. The result shows that waves appearing in the NLC are coming from near the tropopause rather than secondary generation in the stratosphere or mesosphere. The geographic distributions of the number of waves that reached 80 km from the grid points of the source regions at 5km and 60 km (Figure 9a and 9b in paper III) depict that the coastal region of Norway along the latitude of 70N are the primary source regions of gravity waves. Comparison of the direction of propagation of the NLC waves (Figure 8a in paper III) and the ray-traced waves at NLC height (Figure 8b and 8c in paper III) show a large percentage of the NLC waves are moving in a SW direction that the ray tracing has indicated are blocked. These waves appear to be a separate population of short period waves most likely associated with local instabilities accompanying wave breaking (e.g. Fritts et al. 2003). This the unique population of the NLC waves observed moving in SW direction with faster phase speed and shorter period waves stand out differently from other previous studies (Pautet et al., 2011) in this region.

## 5. Conclusions

The vertical phase structure and source regions of mesospheric waves are investigated using a combination of measurements in the middle and upper atmosphere.

The 16-day wave in the winter is found to have a vertical phase fronts consistent with a normal mode structure. It is observed from the mesopause near 87 km to the upper stratosphere, but undergoes a large phase shift and diminished amplitude around 55km, a region of high negative wind shear or negative refractive index has been observed by McDonald et al. [2011]. Thus, it is likely that this normal mode oscillation interacted with mean winds in this region, becoming transiently propagating and dissipating some of its energy. Since it is observed near the mesopause, the wave does not lose all of its energy in this region of negative index of refraction.

The planetary waves present in the PMSE during summer consisted of two  $S_1$  waves closely spaced in frequency (5- and 6.5-days) that were only separable due to the differences in the vertical structure. The 5-day wave has vertical phase fronts consistent with a normal mode structure. However, the phase structure of the 6.5-day wave indicates that it is propagating from the upper stratosphere into the PMSE region.

The climatology of summertime gravity-wave wavelengths, phase speed, period and propagation direction is inferred from the structures present in the NLC between 64° and 74°N. The climatology of gravity-waves observed in NLC between 64° and 74°N is similar to that observed between 60° and 64°N by Pautet et al. (2011). However, a large and unique population of fast, short wavelength waves propagating towards the SW is observed in the NLC, which is consistent with transverse instabilities generated in-situ by breaking gravity waves (Fritts et al. 2003). Comparisons of the relative amplitude of the waves present in the NLC Mie-scatter with ray-tracing results show that gravity waves appearing in the NLC heights in the northern Norway are found to have tropospheric origin, rather than secondary generation in the stratosphere or mesosphere. The coastal region of Norway along the latitude of 70°N is identified as the primary source region of the waves, and the interaction of frontal systems with the coastal mountain terrains or landfall of polar lows can be the mechanisms for the generation of these waves. In general, this study provided a complimentary method to extend gravity wave climatology in high-latitudes during summer

when night time airglow measurements are not possible and identified sources that may be required for parameterization of gravity-wave effects.

## References

- Andrews, D. G., 2000: *An Introduction to Atmospheric Physics*, Cambridge University Press.
- Andrews, D. G., Holton, J. R., Leovy, C. B., 1987: *Middle Atmosphere Dynamics*, International Geophysics Series, Volume 40, Academic Press.
- Brasseur, G., Solomon, S., 1986: *Aeronomy of the Middle Atmosphere - Chemistry and Physics of the Stratosphere and Mesosphere*, 3rd edition, Springer.
- Baker, D. J. and Stair, J. T., 1988: Rocket measurements of the altitude distributions of the hydroxyl airglow, *Physica Scripta.*, 37, 611-622.
- Baumgarten, G., Fiedler, J., Fricke, K. H., Gerding, M., Hervig, M., Hoffmann, P., Müller, N., Pautet, P.-D., Rapp, M., Robert, C., Rusch, D., von Savigny, C., and Singer, W., 2009: The noctilucent cloud (NLC) display during the ECOMA/MASS sounding rocket flights on 3 August 2007: morphology on global to local scales, *Ann. Geophys.*, 27, 953–965.
- Baumgarten, G., Gerding, M., Kaifler, B., and Müller, N., 2009: A trans-European network of cameras for observation of noctilucent clouds from 37°N to 69°N, *Proceedings 19<sup>th</sup> ESA Symposium on European Rocket and Ballon Programmes and Related Research*, Bad Reichenhall, Germany, 7-11 June 2009
- Chandran, A., Rusch, D. W., Palo, S. E., Thomas, G. E., Taylor, M. J., 2009: Gravity wave observations in the summertime polar mesosphere from the cloud imaging and particle size (CIPS) experiment on the AIM spacecraft. *J. Atmos. Sol. Terr. Phys.* 71 (3–4), 285–288.
- Chandran, A., Rusch, D. W., Merkel, A. W., Palo, S. E., Thomas, G. E., Taylor, M. J., Bailey, S. M., Russell III, J. M., 2010: Polar Mesospheric Cloud structures observed from the CIPS experiment on the AIM spacecraft: atmospheric gravity waves as drivers for longitudinal variability in PMC occurrence. *J. Geophys. Res.* doi: 10.1029/2009JD013185.
- Charney, J. G. and Drazin, P. G., 1961: Propagation of planetary-scale disturbances from lower into the upper atmosphere, *J. Geophys. Res.*, 66, 83-109.
- Cho, J. Y., Kelley, M. C., 1993: Polar mesosphere summer radar echoes, *Rev. Geo. phys.*, 31, 243–265.
- Daae, M., Straub, C., Espy, P. J., and Newnham, D. A., 2013: Atmospheric ozone above Troll station, Antarctica observed by a ground based microwave radiometer, in press, *Earth Syst. Sci. Data*
- Eckermann, S. D., and Marks, C. J., 1997: GROGRAT: A new model of the global propagation and dissipation of G.E., 1993. *Wave atmospheric gravity waves*, *Adv. Space Res.*, 20(6), 1253-1256.
- Espy, P. J., Stegman, J., and Witt, G., 1997: Interannual variations of the quasi-16-day oscillation in the polar summer mesospheric temperature. *J. Geophys. Res.*, 102, 1983-1990.

- Espy, P. J. and Stegman, J., 2002: Trends and variability of mesospheric temperature at high-latitudes, *Phys. Chem. Earth*, 27, 543–553.
- Espy, P. J., Hibbins, R. E., Jones, G. O. L., Riggan, D. M., and Fritts, D. C., 2003: Rapid, large-scale temperature changes in the polar mesosphere and their relationship to meridional flows, *Geophys. Res. Lett.*, 30 (5), 1240, doi: 10.1029/2002GL016452.
- Espy, P. J., Jones, G. O. L., Swenson, G. R., Tang, J., and Taylor, M. J., 2004: Seasonal variations of the gravity wave momentum flux in the Antarctic mesosphere and lower thermosphere, *J. Geophys. Res.*, 109, D23109, doi: 10.1029/2003JD004446.
- Espy P. J., Hartogh, P., and Holmén, K., 2006: A microwave radiometer for the remote sensing of nitric oxide and ozone in the middle atmosphere, *Remote Sensing of Clouds and the Atmosphere XI*, Proc. of SPIE, Vol. 6362.
- Fleming, E. L., Chandra, S., Shoeberl, M. R., and Barnett, J. J., 1988: Monthly mean global climatology of temperature, wind, geopotential height and pressure for 0-120 km, NASA Technical Memorandum 100697.
- Forbes, J. M., 1995: Tidal and planetary waves, in *The Upper Mesosphere and Lower Thermosphere: A Review of Experiment and Theory*, *Geophys. Monogr. Ser.*, vol. 87, pp. 67–87, AGU, Washington, D. C., doi: 10.1029/GM087p006.
- Forbes, J. M., Hagan, M. E., Miyahara, S., Vial, F., Manson, A. H., Meek, C. E., and Portnyagin, Y. I., 1995: Quasi-16-day oscillation in the mesosphere and lower thermosphere, *J. Geophys. Res.*, 100, 9149-9163.
- Fritts, D. C., Isler, J. R., Thomas, G. E., Andreassen, Ø, 1993: Wave breaking signatures in noctilucent clouds, *Geophys. Res. Lett.* 20, 2039
- Fritts, D. C., and Alexander M. J., 2003: Gravity wave dynamics and effects in the middle atmosphere, *Rev. Geophys.*, 41, doi: 10.1029/2001RG000106.
- Garcia, R. G., Solomon, S., 1985: The effect of breaking gravity waves on the dynamics and chemical composition of the mesosphere and lower thermosphere. *J. Geophys. Res.*, 90, 3850–3868.
- Geisler, J. E., and Dickinson, R. E., 1976: The five-day wave on a sphere with realistic zonal winds, *J. Atmos. Sci.*, 33, 632–641.
- Geller, M. A., 1983: Dynamics of the middle atmosphere, *Space Sci. Rev.*, 34, 359-375.
- Greenwald, R. A. et al., 1995: DARN/SuperDARN: A global view of the dynamics of high-latitude convection. *Space Sci. Rev.*, 71, 761–796.
- Haurwitz, B., 1961: Wave formations in noctilucent clouds. *Planet. Space Sci.* 5, 92–98.
- Hibbins, R. E., Jarvis, M. J., and Ford, E. A. K., 2009: Quasi-biennial oscillation influence on long-period planetary waves in the Antarctic upper mesosphere. *J. Geophys. Res.*, 114, D09109, doi: 10.1029/2008JD011174.
- Hibbins, R. E., Shanklin, J. D., Espy, P. J., Jarvis, M. J., Riggan, D. M., Fritts, D. C., and Lübken, F. -J., 2005: Seasonal variations in the horizontal wind structure from 0-100 km above Rothera station, Antarctica (67°S, 68°W), *Atmos. Chem. Phys.*, 5 (11), 2973-2980.

- Hines, C. O., 1960: Internal atmospheric gravity waves. *Can. J. Phys.* 38, 1441.
- Holton, J. R., 1984: The Generation of Mesospheric Planetary Waves by Zonally Asymmetric Gravity Wave Breaking. *J. Atmos. Sci.*, 41, 3427–3430.
- Hosokawa, K., Ogawa, T., Sato, N., Yukimatu, A.S., Lyemori, T., 2004: Statistics of Antarctic mesospheric echoes observed with the Super-DARN Syowa radar. *Geophys. Res. Lett.*, 31, L02106, doi: 10.1029/2003GL018776
- Hosokawa, K., Ogawa, T., Arnold, N. F., Lester, M., Sato, N., Yukimatu, A. S., 2005: Extraction of polar mesosphere summer echoes from SuperDARN data, *Geophys. Res. Lett.*, 32, L12801, doi: 10.1029/2005GL022788
- Kleinknecht, N. (2010), Planetary Wave Oscillations Observed in Ozone from Troll Station Antarctica Master Thesis, Norwegian University of Science and Technology (NTNU), Trondheim, Norway.
- Lindzen, R. S., 1981: Turbulence and stress owing to gravity wave and tidal breakdown, *J. Geophys. Res.*, 86, 9707–9714
- London, J., 1980: Radiative energy sources and sinks in the stratosphere and mesosphere. *Proceedings of the NATA Advanced Study Institute on Atmospheric Ozone: Its Variation and Human Influences*. Rep. FAA-EE-80-20, A Aiken, Ed., 703–721.
- Lübken, F. -J., 1999: Thermal structure of the Arctic summer mesosphere, *J. Geophys. Res.*, 104, 9135–9149
- Lynch, A. H., and Cassano, J. J., 2006: *Applied Atmospheric Dynamics*, Chapter 8, John Wiley & Sons
- McLandress, C., 1998: On the importance of gravity waves in the middle atmosphere and their parameterization in general circulation models, *J. Atmos. Solar Terr. Phys.*, 60, 1357–1383.
- Manson, A. H., 1990: Gravity wave horizontal and vertical wavelengths: An update of measurements in the mesopause region (~80-100 km), *J. Atmos. Sci.*, 47, 2765–2773.
- Marks, C. J., and Eckermann, S. D., 1995: A three-dimensional non-hydrostatic ray-tracing model for gravity waves: Formulation and preliminary results for the middle atmosphere. *J. Atmos. Sci.*, 52, 1959–1984.
- McDonald, A. J., Hibbins, R. E., and Jarvis, M. J., 2011: Properties of the quasi-16 day wave derived from EOS MLS observations, *J. Geophys. Res.*, 116, D06112, doi: 10.1029/2010JD014719, 2011
- Nielsen, K., Taylor, M. J., Pautet, P-D., Fritts, D. C., Mitchell, N., Beldon, C., Williams, B. P., Singer, W., Schmidlin, F. J., Goldberg, R. A., 2006: Propagation of short-period gravity waves at high-latitudes during the MaCWAVE winter campaign. *Annales Geophys.*, 24:1227–1243, SRef\_ID:1432-0576/ag/2006- 24-1227.
- Nielsen, K., Taylor, M. J., Hibbins, R. E., Jarvis, M. J., 2009: Climatology of short-period mesospheric gravity waves over Halley, Antarctica (76°S, 27°W). *J. Atmos. Solar-Terr. Phys.*, 71: 991–1000.

- Nuttall, A.H., 1981: Some windows with very good sidelobe behavior. *IEEE Transactions on Acoustics, Speech, Signal Processing*, 29, 84-91.
- Ogawa, T., Nishitani, N., Sato, N., Yamagishi, H., Yukimatu, A. S., 2002: Upper mesosphere summer echoes detected with the Antarctic Syowa HF radar. *J. Geophys. Res. Lett.*, 29 (7), 1157, doi: 10.1029/2001GL014094.
- Pautet P-D, Taylor M. J., Liu A. Z., and Swenson G. R., 2005: Climatology of short-period gravity waves observed over northern Australia during the Darwin area wave experiment (DAWEX) and their dominant source regions. *J Geophys Res* 110:D03S90.
- Pautet P-D, Stegman J, Wrasse C. M., Takahashi H., Taylor M. J., 2011: Analysis of gravity waves structures visible in noctilucent cloud images, global perspectives on the aeronomy of the summer mesopause region, 8th international workshop on layered phenomena in the mesopause region. *J. Atmos. Solar-Terr Phys.*, 73, 2082-2090, doi:10.1016/j.jastp.2010.06.001.
- Pendleton, W.R., Jr., P.J. Espy and M.R. Hammond, Evidence for non-local-thermodynamic-equilibrium in the OH nightglow, *J. Geophys. Res.*, 98, 11567-11579, 1993.
- Picone, J. M., Hedin, A. E., Drob, D. P., and Aikin, A. C.: NRLMSISE-00 empirical model of the atmosphere: Statistical comparisons and scientific issues, *J. Geophys. Res.*, 107, 1468, doi: 10.1029/2002JA009430, 2002
- Plumb, R. A.: Stratospheric transport, *J. Meteorol. Soc. Jpn.*, 80, 793–809, 2002
- Ralph, F. M., 1997: Observation, simulations, and analysis of nonstationary trapped lee waves, *J. Atmos. Sci.*, 54, 1308-1333
- Riggin, D. M., Liu, H. –L., Lieberman, R. S., Roble, R. G., Russell III, J. M., Mertens, C. J., Mlynczak, M. G., Pancheva, D., Franke, S. J., Murayama, Y., Manson, A. H., Meek, C. E., and Vincent, R. A., 2006: Observations of the 5-day wave in the mesosphere and lower thermosphere. *J. Atmos. Sol-Terr. Phys.*, 68, 323–329.
- Rodgers, C.: Retrieval of atmospheric temperature and composition from measurements of thermal radiation, *Rev. Geophys. Space Phys.*, 14 (4), 609-624, 1976.
- Salby, M. L., 1981: Rossby normal modes in nonuniform background configuration. Part II: Equinox and solstice conditions, *J. Atmos. Sci.*, 38(9), 1827-1840.
- Salby, M. L., 1996: *Fundamentals of Atmospheric Physics*, 61, first edition, Academic Press, New York.
- Serafimovich, A., 2006: Investigation of gravity waves with vhf radar measurements, Ph.D. thesis, Universität Rostock, Rostock, Germany.
- Stearns, S. D.: *Digital signal analysis*, Hayden book, Rochelle Park, New Jersey, 1975.
- Straub, C., Espy, P. J., Hibbins, R. E., and Newnham, D. A., 2013: Mesospheric CO above Troll station, Antarctica observed by a ground based microwave radiometer, *Earth Syst. Sci. Data Discuss.*, 6, 1-26, doi: 10.5194/essdd-6-1-2013.
- Shepherd, T. G.: Transport in the middle atmosphere, *J. Meteorol., Soc. Jpn.*, 85B, 165–191, 2007

Smith, A. K.: The origin of stationary planetary waves in the upper mesosphere. *J. Atmos. Sci.*, 60, 3033–3041, 2003.

Taylor, M. J., Henriksen, K., 1989: Gravity wave studies at polar latitudes. In: Sandholt, P.E., Egeland, A. (Eds.), *Electromagnetic Coupling in the Polar Clefts and Caps*. Kluwer Academic Publications, Dordrecht, the Netherlands, pp. 421–434.

Thomas, G. E., 1991: Mesospheric clouds and the physics of the mesopause region. *Reviews of Geophysics* 29, 553–575.

Tunbridge, V. M., 2011: 2-day planetary waves in the stratosphere, mesosphere and lower thermosphere. Thesis (Doctor of Philosophy (PhD)), University of Bath.

U.S. Standard Atmosphere Supplements: U.S. Government Printing Office, Washington, D.C., 1966.

**Paper I**

**Quasi-16 day period oscillations observed in middle atmospheric ozone and temperature in Antarctica**

**T. D. Demissie<sup>1,2</sup>, N. H. Kleinknecht<sup>1</sup>, R. E. Hibbins<sup>1,2</sup>, P. J. Espy<sup>1,2</sup>, C. Straub<sup>1</sup>**

<sup>1</sup>Norwegian University of Science and Technology (NTNU), Trondheim, Norway

<sup>2</sup>Birkeland Centre for Space Science, Bergen, Norway

Ann. Geophys., 31, 1279-1284, doi: 10.5194/angeo-31-1279-2013, 2013





# Quasi-16-day period oscillations observed in middle atmospheric ozone and temperature in Antarctica

T. D. Demissie<sup>1,2</sup>, N. H. Kleinknecht<sup>1</sup>, R. E. Hibbins<sup>1,2</sup>, P. J. Espy<sup>1,2</sup>, and C. Straub<sup>1</sup>

<sup>1</sup>Norwegian University of Science and Technology (NTNU), Trondheim, Norway

<sup>2</sup>Birkeland Centre for Space Science, Bergen, Norway

Correspondence to: T. D. Demissie (teferi.demissie@ntnu.no)

Received: 6 February 2013 – Revised: 20 June 2013 – Accepted: 27 June 2013 – Published: 30 July 2013

**Abstract.** Nightly averaged mesospheric temperature derived from the hydroxyl nightglow at Rothera station (67°34' S, 68°08' W) and nightly midnight measurements of ozone mixing ratio obtained from Troll station (72°01' S, 2°32' E) in Antarctica have been used to investigate the presence and vertical profile of the quasi-16-day planetary wave in the stratosphere and mesosphere during the Antarctic winter of 2009. The variations caused by planetary waves on the ozone mixing ratio and temperature are discussed, and spectral and cross-correlation analyses are performed to extract the wave amplitudes and to examine the vertical structure of the wave from 34 to 80 km. The results show that while planetary-wave signatures with periods 3–12 days are strong below the stratopause, the oscillations associated with the 16-day wave are the strongest and present in both the mesosphere and stratosphere. The period of the wave is found to increase below 42 km due to the Doppler shifting by the strong eastward zonal wind. The 16-day oscillation in the temperature is found to be correlated and phase coherent with the corresponding oscillation observed in O<sub>3</sub> volume mixing ratio at all levels, and the wave is found to have vertical phase fronts consistent with a normal mode structure.

**Keywords.** Meteorology and Atmospheric Dynamics (Middle atmosphere dynamics; Waves and tides)

## 1 Introduction

In the past few decades, a number of studies using ground-based and satellite-borne systems as well as modelling studies have reported quasi-16-day period planetary waves (PWs) in the mesosphere (Manson et al., 1978; Vincent, 1990; Fritts et al., 1999; Miyoshi, 1999). A majority of the studies

suggest that the PWs appearing in the mesosphere are due to the vertical propagation from the troposphere and stratosphere when the stratospheric zonal winds are weak and westerly (Charney and Drazin, 1961; Salby, 1981; Forbes et al., 1995; Lawrence and Jarvis, 2001). Other studies suggest that PWs can be generated in situ in the mesosphere by gravity wave breaking (Smith, 2003), or transported from the winter mesosphere across the equator (Forbes et al., 1995; Espy et al., 1997; Smith, 2003; Riggan et al., 2006; Hibbins et al., 2009). Espy et al. (1997) have further suggested that the QBO modulation of the appearance of the 16-day wave in the summer supports the inter-hemisphere transport hypothesis of Forbes et al. (1995). All the aforementioned studies indicate that the propagation and interaction of PWs with the atmosphere is not yet fully understood, and hence there is a need for further study supported by observations with uninterrupted vertical and temporal coverage.

The observational evidence for 16-day PWs in the mesosphere was first reported using meteor radar winds by Kingsley et al. (1978). Subsequent studies using wind measurements (e.g. Williams and Avery, 1992; Forbes et al., 1995; Mitchell et al., 1999; Luo et al., 2000; Jiang et al., 2005; Das et al., 2010) and temperature measurements (e.g. Espy and Witt, 1996; Espy et al., 1997) confirmed the existence of a quasi-16-day PW in the mesosphere. More recently, satellite data have been used to study the wave throughout the stratosphere and mesosphere (e.g. McDonald et al., 2011; Day et al., 2011).

In this study, we use continuous ground-based measurements of ozone mixing ratio profiles recorded with a microwave radiometer located at Troll station, Antarctica (72°01' S, 2°32' E). Middle atmospheric O<sub>3</sub> has been shown to vary out of phase with temperature (Finger et al., 1995;

Belova et al., 2009) and hence can be used to trace and characterize the vertical phase structure of temperature perturbations caused by PWs. These observations are compared with concurrent ground-based mesopause airglow temperature data recorded at Rothera station Antarctica ( $67^{\circ}34' \text{ S}$ ,  $68^{\circ}08' \text{ W}$ ) in order to determine the PW source regions and their evolution in time and altitude throughout the Antarctic winter. The temperature and  $\text{O}_3$  measurements used in this study span from 1 July 2009 to 21 September 2009. The PW signatures at different altitudes in Antarctica during winter of 2009 are identified and compared using spectral techniques.

## 2 Measurement, analysis and results

This study uses data acquired by the ground-based microwave radiometer of the British Antarctic Survey (BAS radiometer). The instrument was operated from the Norwegian Polar Institute's Troll research station in Antarctica between February 2008 and January 2010. Spectra in the region of the rotational transitions centred at 250.796 GHz (nitric oxide, NO), 249.79 GHz and 249.96 GHz (ozone,  $\text{O}_3$ ) and 230.538 GHz (carbon monoxide, CO) have been observed. A detailed description of the instrument is given in Espy et al. (2006) and Straub et al. (2013). Here we use  $\text{O}_3$  volume mixing ratio (vmr) profiles retrieved from one-hour averaged  $\text{O}_3$  spectra centred around midnight local time recorded between July and September 2009. These profiles cover an altitude range of approximately 34 to 80 km with an altitude resolution of the order of 10 km below 70 km and only column information above that level. A complete description of the optimal estimation retrieval technique (Rodgers, 1976) as applied to these data may be found in Kleinknecht (2010). Briefly, the a priori pressure, temperature, water vapour and ozone values used for the inversion below 45 km were derived from monthly mean ERA-40 profiles (Uppala et al., 2005). Between 45 and 85 km, monthly mean temperature and pressure values were taken from the MSIS-00 model (Picone et al., 2002), and ozone and water vapour were taken from the US Standard Atmosphere Supplements (1966) for winter and summer conditions. For the wave studies here, the  $\text{O}_3$  a priori above 85 km were held at a constant value so as to ensure that the a priori did not induce oscillations. However, the strong dominance of the a priori at high and low altitudes could artificially reduce the amplitude of any oscillations present in the data there.

In addition to  $\text{O}_3$  measurements, this study uses temperature data obtained from a Michelson interferometer at the British Antarctic survey station at Rothera. Hydroxyl night-glow spectra measured by the interferometer were used to derive the rotational temperature from an emitting height centred around 87 km with a thickness of 8 km (Baker and Stair, 1988). The method of fitting the rotational temperature to the measured spectra is discussed in Espy and Hammond (1995). Here we used a night-time average of the

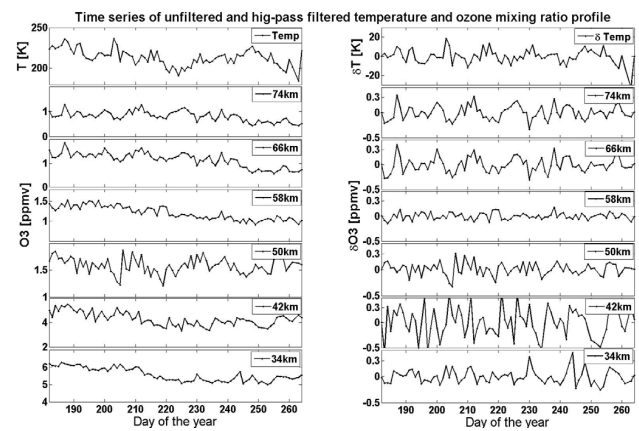


**Fig. 1.** Time series of temperature at 87 km (top panel) and the ozone mixing ratio at selected altitude levels (lower 6 panels). Left: raw (unfiltered) data; right: filtered data.

temperature extracted from the OH Meinel (3,1) band. The weighted mean temperature was calculated for nights which have at least 2 h of data. There are no gaps in the data series used in the analysis period presented in this study.

Nightly averages of temperature and one hour average around midnight values of  $\text{O}_3$  vmr were used to reduce the contribution to the measurements from periodic oscillations less than a day such as photolysis effects and other high frequency signals. Although the hourly averaged  $\text{O}_3$  vmr around midnight was used, the analysis using the average of all values at solar zenith angles greater than 100 degrees gave similar results. A high-pass filter was applied to both datasets to filter out seasonal and long-period oscillations while retaining periodic motions with periods less than 20 days. A Butterworth IIR high-pass filter was specifically used to remove these long-period variations since it has a maximum flat frequency response in the selected pass band (e.g. Stearns, 1975). Figure 1 depicts the time series of unfiltered (left panel) and high-pass filtered (right panel) data of the temperature at 87 km and the  $\text{O}_3$  vmr at six selected altitudes (34 km, 42 km, 50 km, 58 km, 66 km and 74 km). Note that the high-pass filtered datasets have similar features and peaks as that of the raw data. Wave patterns can easily be identified by eye in the vertical profile of the  $\text{O}_3$  data and the temperature at 87 km, and spectral techniques can be used to identify the significant periods in the time series.

A fast Fourier transform (FFT) was performed on the high-pass filtered datasets to determine the amplitude and phase of periodic fluctuations observed in the  $\text{O}_3$  and temperature with periods of less than 20 days. A Hamming window (Nuttall, 1981) was applied to the data before the FFT was performed in order to reduce spectral leakage and side-lobe effects on the FFT. Figure 2 presents the spectra of the oscillations in the high-pass filtered temperature (top panel) and  $\text{O}_3$  vmr (bottom panel) in the altitude range from 34 to 80 km that resulted from the FFT. The amplitude spectra

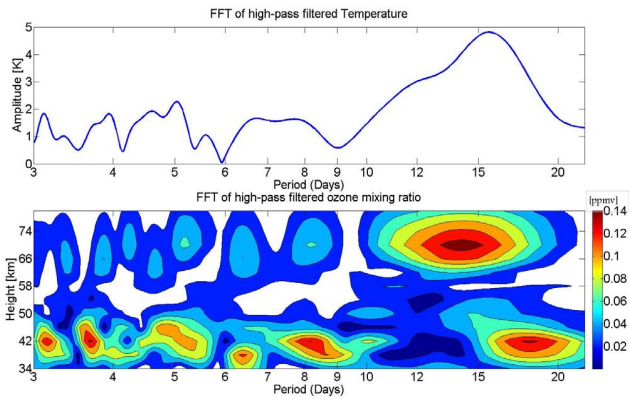


**Fig. 2.** FFT of the high-pass filtered temperature at 87 km (top panel) and O<sub>3</sub> vmr profile (bottom panel) in Antarctica during winter 2009.

(the absolute value of the power spectra) of the temperature and the O<sub>3</sub> vmr profiles show a number of oscillations with periods in the 3–20-day range. The power-spectral analysis shows that the amplitude of oscillations in the range between 12 and 20 days is the strongest and present throughout the stratosphere and mesosphere in the ozone, and also in the OH temperature around the mesopause (87 km). A closer look at the wave period of the dominant oscillation in this range shows that the central period of the peak power varies with altitude between 14 and 18 days in the O<sub>3</sub> vmr and appears around 16 days with an amplitude of 5 K in the OH airglow temperature. This oscillation is most likely associated with the quasi-16-day PW with zonal wave number 1, which has often been observed in mesospheric wind measurements (e.g. Das et al., 2010) and temperature measurements (e.g. Day et al., 2011). It is evident in Fig. 2 that there are also strong wave features below the stratopause at a range of shorter periods. All the wave activity diminishes around the stratopause. The strongest wave activity that reappears above the stratopause is in the range between 12 and 20 days. The other shorter period waves that are seen in the stratosphere are clearly much weaker in the mesosphere.

To examine whether or not the 16-day oscillations observed in the mesopause temperature and O<sub>3</sub> vmr profiles are correlated and phase coherent, a cross-spectral analysis was performed between the two datasets. Figure 3 shows the cross spectrum between the temperature at 87 km and each level of the O<sub>3</sub> vmr as a function of period in days. The cross spectra show that despite the low amplitudes in the FFT, there are oscillations at each altitude at a nominal period of 16 days that are coherent in phase with the same period oscillation in the temperature near 87 km, and this indicates a physical connection between the two. On the other hand, there is little or no coherency between the oscillations of the shorter periods in the ozone and the temperature oscillation at 87 km.

Having documented the presence of the quasi-16-day wave in the data through both the power and cross-spectral

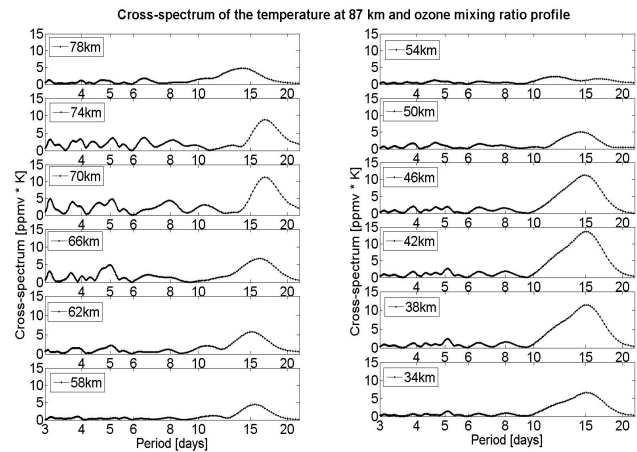


**Fig. 3.** Cross spectrum of the temperature at 87 km and O<sub>3</sub> vmr profile for winter 2009 in Antarctica for different levels in the stratosphere and mesosphere.

analysis, the periodic range of the wave is isolated using a band-pass filter in order to examine the vertical structure of the phase fronts and to quantify the coherence of the quasi-16-day wave. The temperature and O<sub>3</sub> vmr data were band-pass filtered between 12–20 day periods, and a time-lagged cross-correlation analysis was performed on the two datasets. The choice of this range for the band-pass filter was to isolate the wave activity observed in the spectra shown in Fig. 2, and is consistent with the band-pass range used in previous 16-day PW studies (e.g. Luo et al., 2002; Day et al., 2011). The left panel of Fig. 4 shows the time-lagged cross correlation between the temperature at 87 km and each level of O<sub>3</sub> vmr as a function of height and time lag in days. The colour scale in the figure represents the intensity of the correlation, which indicates how much of the O<sub>3</sub> variance at each altitude can be explained by the temperature fluctuations. At zero lag, there are regions with significant anti-correlation between the temperature at 87 km and the O<sub>3</sub> vmr within the altitude range from 34 to 80 km. At altitudes above 65 km and below 55 km, this zero-lag reaches a maximum anti-correlation of approximately  $-0.8$ , and these values are statistically significant at the 95 % confidence level. Near the stratopause, in the region where the FFT and cross-spectral amplitudes were low, the cross correlation is nearly zero and not statistically significant. The right panel of Fig. 4 shows the phase change between the temperature and O<sub>3</sub> vmr at different altitudes along the line of maximum anti-correlation nearest to zero lag. Only the anti-correlation values whose significance is above 95 % are plotted. The phase change between the temperature and O<sub>3</sub> vmr show that there is little vertical tilt of the phase fronts with altitude above 38 km indicating a normal mode structure. However, it should be noted that phase fronts above 70 km are nearly vertical largely because of the poorer altitude resolution of the O<sub>3</sub> vmr above that altitude.

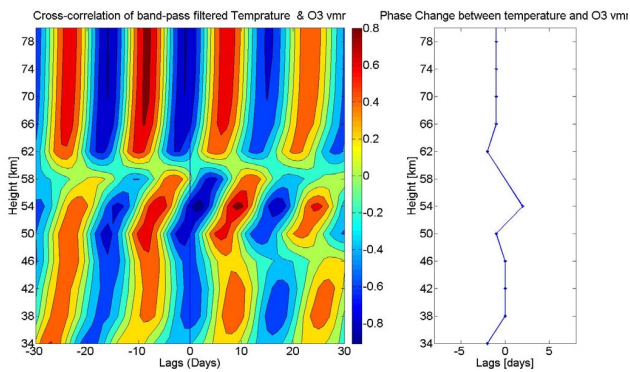


**Fig. 4.** Left panel: the time-lagged cross correlation between winter mesospheric temperature and ozone at different levels. Red colour represents correlation and blue denotes anti-correlation. Right panel: vertical profile of phase change between temperature and O<sub>3</sub> vmr. These phases are all  $\pm 0.5$  days.

### 3 Discussion and conclusion

The purpose of this study was to use temporal variations in the mesopause airglow temperatures and the O<sub>3</sub> vmr profiles in the mesosphere and stratosphere to trace and characterize the vertical behaviour of planetary waves reaching the mesopause during the winter. The results from the power-spectral analysis in Sect. 2 show the largest amplitudes for the quasi-16-day oscillation in both the temperature and O<sub>3</sub> fields in the wintertime over Antarctica. We find that the period of the wave ranges from 14–18 days in the mesosphere and stratosphere, consistent with previous observations (e.g. Luo et al., 2002; Williams and Avery, 1992). The wave period is observed to shift systematically to longer periods below the stratopause, reaching  $\sim 18$  days below 42 km. This suggests that the wave is interacting with the rapidly increasing eastward winds at these altitudes (Hibbins et al., 2005) and Doppler shifting to longer periods as reported by Forbes (1995).

Unlike the oscillations with periods 3–12 days, which the power-spectral analysis shows are mostly confined below the stratopause, the quasi-16-day wave shows large amplitudes above and below the stratopause. The amplitude of the wave decreases markedly close to the stratopause. This may be due to the high negative wind shears above 45 km altering the index of refraction of the planetary wave as has been suggested by McDonald et al. (2011) based on EOS MLS temperature data. However, we cannot rule out that this decrease of amplitude is merely due to low O<sub>3</sub> vmr values that minimise near this altitude. Similarly, the sharp fall off of wave amplitudes at the upper and lower altitudes seen in Fig. 2 is likely due to the large a priori contribution to the retrieved O<sub>3</sub> at these altitudes. The nearly constant a priori values will tend to minimise the wave-induced departures from this profile, reducing the extracted wave amplitudes.

The cross-spectral analysis shows that the 16-day wave observed in the temperature fluctuations around 87 km at Rothera is related and phase coherent with the 16-day wave observed in the O<sub>3</sub> vmr data at all levels from 34–80 km at Troll station. The vertical variation of the cross-spectral amplitude is a reflection of the variation in the power spectral amplitudes. However, the observed phase-coherency indicates that the 16-day wave observed in both the temperature and the O<sub>3</sub> vmr data have a physical connection and could be driven by the same source.

Once the phase-coherent oscillations with periods corresponding to the 16-day wave were identified in the temperature and O<sub>3</sub> vmr at each altitude, the wave was isolated using a band-pass filter and the lagged cross correlation between the two datasets was performed. This was done to quantify the coherence and examine the relative phase between the 16-day oscillations in temperature at 87 km and those in the O<sub>3</sub> vmr at each altitude below. The cross-correlation analysis displayed in the left panel of Fig. 4 shows that at zero lag, the temperature fluctuations close to 87 km are anti-correlated with the O<sub>3</sub> vmr at levels between 34 km to 80 km. This anti-correlation is expected due to the temperature dependency of the O<sub>3</sub> reaction in the upper stratosphere and mesosphere. There, the chemical lifetime of O<sub>3</sub> is much shorter than the transport timescales. As a result, variations in temperature caused by PWs drive the reactions nonlinearly and cause corresponding changes in the O<sub>3</sub> concentration. The inverse temperature dependence of the O<sub>3</sub> production reactions lead to a negative correlation (or an anti-correlation) between the O<sub>3</sub> and temperature fluctuations (Finger et al., 1995; Huang et al., 2008; Belova et al., 2009). The magnitudes of the correlation coefficient minimise near the stratopause, where the power spectral amplitudes are also a minimum. As a result, the correlation values are not statistically significant at 58 km. However, at all other altitudes the anti-correlations are statistically significant above the 95 % confidence level, ranging from  $-0.5$  to  $-0.8$ , showing that the phase-coherent, 16-day variations in mesopause temperature and middle atmospheric O<sub>3</sub> are statistically significant.

The phase change between the temperature and O<sub>3</sub> vmr at different altitudes was determined by extracting the minimum correlation value (maximum anti-correlation) nearest to zero lag. These phase fronts, displayed in the right panel of Fig. 4, show little vertical tilt with altitude above 38 km, indicating a normal mode structure. Although the magnitude of the correlation coefficient is observed to be small and insignificant near the stratopause, whether by instrumental or index of refraction effects (McDonald et al., 2011), we see here that the wave is not completely absorbed and is able to continue above this region. The nearly vertical phase fronts above 70 km are likely a consequence of the coarse altitude resolution of the O<sub>3</sub> vmr data there smoothing any vertical structure. However, we note that there are several observations of the high-latitude southern hemisphere winter 16-day wave in radar wind data that show that the wave continues

above 80 km as a normal mode until it reaches the critical level caused by the wind reversal from east to west near 95 km (e.g. Espy et al., 2005).

In conclusion, we have presented measurements of wintertime 16-day oscillations in both the O<sub>3</sub> vmr above Troll station, Antarctica, from a ground-based microwave radiometer and in the temperature from hydroxyl night glow above Rothera, Antarctica. Power-spectral analysis found that periods around 16 days had the largest amplitudes in both datasets. In the O<sub>3</sub> data, waves with periods 3–12 days were also strong below the stratopause, but only the 16 day wave persisted into the mesosphere. In addition, the period of the 16-day wave increased below 42 km due to Doppler shifting by the increasing eastward zonal winds. The amplitude of the quasi-16-day wave was also found to vary with height, diminishing at the highest and lowest altitudes due to instrumental effects. However, the minimum amplitudes found near the stratopause could be due either to wave absorption by the large negative wind gradients or to the minimum O<sub>3</sub> concentrations found there. Despite the presence of low wave amplitudes, the 16-day oscillations in the temperature are correlated and phase-coherent with the corresponding oscillations observed in O<sub>3</sub> vmr at all levels. The 16-day wave is found to have vertical phase fronts consistent with a normal mode structure, and extends from the mesopause down into the upper stratosphere. Thus, utilizing a ground-based radiometer, with its high temporal resolution allows one to extend radar measurements of PWs from their lower measurements limits, ~ 80 km, down to ~ 34 km. In this way, the vertical phase structure and interaction with the background wind can be quantified throughout the mesosphere and upper stratosphere.

*Acknowledgements.* We thank David Newnham at BAS, Kim Holmén at the Norwegian Polar Institute (NPI) and Paul Hartogh at Max Planck Institute (MPI) for their support of the microwave radiometer. We also thank Asbjørn Djupdal (NPI), David Maxfield and Paul Breen (BAS) for their help. The work has been funded by the Norwegian Research council (NFR) project “Gravity-wave sources and scales in the Polar Regions and their effect on Polar Mesospheric Clouds”. In addition, we acknowledge the Norwegian Polar Institute Antarctic Program which provided funding for Corinne Straub under the project “Observations of carbon monoxide and ozone in the Antarctic and Arctic: Implications for the Inter-hemispheric coupling of vertical motions”.

Topical Editor C. Jacobi thanks C. Meek and one anonymous referee for their help in evaluating this paper.

## References

- Baker, D. J. and Stair, J. T.: Rocket measurements of the altitude distributions of the hydroxyl airglow, *Phys. Scripta.*, 37, 611–622, 1988.
- Belova, A., Kirkwood, S., and Murtagh, D.: Planetary waves in ozone and temperature in the Northern Hemisphere winters of 2002/2003 and early 2005, *Ann. Geophys.*, 27, 1189–1206, doi:10.5194/angeo-27-1189-2009, 2009.
- Charney, J. G. and Drazin, P. G.: Propagation of planetary-scale disturbances from lower into the upper atmosphere, *J. Geophys. Res.*, 66, 83–109, 1961.
- Das, S. S., Kumar, K. K., Veena, S. B., and Ramkumar, G.: Simultaneous observation of quasi 16 day Wave in the mesospheric winds and temperature over low latitudes with the SKiYMET radar, *Radio Sci.*, 45, RS6014, doi:10.1029/2009RS004300, 2010.
- Day, K. A., Hibbins, R. E., and Mitchell, N. J.: Aura MLS observations of the westward-propagating  $s = 1$ , 16-day planetary wave in the stratosphere, mesosphere and lower thermosphere, *Atmos. Chem. Phys.*, 11, 4149–4161, doi:10.5194/acp-11-4149-2011, 2011.
- Espy, P. J. and Hammond, M. R.: Atmospheric transmission coefficients for hydroxyl rotational lines used in rotational temperature determinations, *J. Quant. Spectrosc. Ra.*, 54, 879–889, 1995.
- Espy, P. J. and Witt, G.: Observation of a quasi 16-day oscillation in the polar summer mesospheric temperature, *Geophys. Res. Lett.*, 23, 1071–1074, 1996.
- Espy, P. J., Stegman, J., and Witt, G.: Interannual variations of the quasi-16-day oscillation in the polar summer mesospheric temperature, *J. Geophys. Res.*, 102, 1983–1990, 1997.
- Espy, P. J., Hibbins, R. E., Riggan, D. M., and Fritts, D. C.: Mesospheric planetary waves over Antarctica during 2002, *Geophys. Res. Lett.*, 32, L21804, doi:10.1029/2005GL023886, 2005.
- Espy, P. J., Hartogh, P., and Holmén, K.: A microwave radiometer for the remote sensing of nitric oxide and ozone in the middle atmosphere, *Remote Sensing of Clouds and the Atmosphere XI*, Proc. of SPIE, Vol. 6362, 63620P1–63620P9, doi:10.1117/12.688953, 2006.
- Finger, F. G., Nagatani, R. M., Gelman, M. E., Long, C. S., and Miller, A. J.: Consistency between variations of ozone and temperature in the stratosphere, *Geophys. Res. Lett.*, 22, 3477–3480, 1995.
- Forbes, J. M.: Tidal and planetary waves, in *The Upper Mesosphere and Lower Thermosphere: A Review of Experiment and Theory*, *Geophys. Monogr. Ser.*, Vol. 87, 67–87, AGU, Washington, DC, doi:10.1029/GM087p0067, 1995.
- Forbes, J. M., Hagan, M. E., Miyahara, S., Vial, F., Manson, A. H., Meek, C. E., and Portnyagin, Y. I.: Quasi-16-day oscillation in the mesosphere and lower thermosphere, *J. Geophys. Res.*, 100, 9149–9163, 1995.
- Fritts, D. C., Isler, J. R., Lieberman, R. S., Burrage, M. D., Marsh, D. R., Nakamura, T., Tsuda, T., Vincent, R. A., and Reid, I. M.: Two-day wave structure and mean flow interactions observed by radar and High Resolution Doppler Imager, *J. Geophys. Res.*, 104, 3953–3970, 1999.
- Hibbins, R. E., Shanklin, J. D., Espy, P. J., Jarvis, M. J., Riggan, D. M., Fritts, D. C., and Lübken, F.-J.: Seasonal variations in the horizontal wind structure from 0–100 km above Rothera station, Antarctica (67° S, 68° W), *Atmos. Chem. Phys.*, 5, 2973–2980,

- doi:10.5194/acp-5-2973-2005, 2005.
- Hibbins, R. E., Jarvis, M. J., and Ford, E. A. K.: Quasi-biennial oscillation influence on long-period planetary waves in the Antarctic upper mesosphere, *J. Geophys. Res.*, 114, D09109, doi:10.1029/2008JD011174, 2009.
- Huang, F. T., Mayr, H. G., Reber, C. A., Russell III, J. M., Mlynczak, M. G., and Mengel, J. G.: Ozone quasi-biennial oscillations (QBO), semiannual oscillations (SAO), and correlations with temperature in the mesosphere, lower thermosphere, and stratosphere, based on measurements from SABER on TIMED and MLS on UARS, *J. Geophys. Res.*, 113, A01316, doi:10.1029/2007JA012634, 2008.
- Jiang, G.-Y., Xiong, J.-G., Wan, W.-X., Ning, B.-Q., Liu, L.-B., Vincent, R. A., and Reid, I. M.: The 16-day waves in the mesosphere and lower thermosphere over Wuhan (30.6° N, 114.5° E) and Adelaide (35° S, 138° E), *Adv. Space Res.*, 35, 2005–2010, 2005.
- Kingsley, S. P., Muller, H. G., Nelson, L., and Scholefield, A.: Meteor winds over Sheffield, *J. Atmos. Terr. Phys.*, 40, 917–922, 1978.
- Kleinknecht, N. H.: Planetary Wave Oscillations Observed in Ozone from Troll Station Antarctica, M.Sc. thesis, Norwegian University of Science and Technology (NTNU), Trondheim, Norway, 2010.
- Lawrence, A. R. and Jarvis, M. J.: Initial comparisons of planetary waves in the stratosphere, mesosphere and ionosphere over Antarctica, *Geophys. Res. Lett.*, 28, 203–206, 2001.
- Luo, Y., Manson, A. H., Meek, C. E., Meyer, C. K., and Forbes, J. M.: Quasi 16-day oscillations in the mesosphere and lower thermosphere at Saskatoon (52° N, 107° W), 1980–1996, *J. Geophys. Res.*, 105, 2125–2138, 2000.
- Luo, Y., Manson, A. H., Meek, C. E., Thayaparan, T., MacDougall, J., and Hocking, W. K.: The 16-day wave in the mesosphere and the lower thermosphere: simultaneous observations at Saskatoon (52° N, 107° W), London (43° N, 81° W), Canada, *J. Atmos. Sol.-Terr. Phys.*, 64, 1287–1307, 2002.
- McDonald, A. J., Hibbins, R. E., and Jarvis, M. J.: Properties of the quasi-16 day wave derived from EOS MLS observations, *J. Geophys. Res.*, 116, D06112, doi:10.1029/2010JD014719, 2011.
- Manson, A. H., Gregory, J. B., Meek, C. E., and Stephenson, D.: Wind and wave motions to 110 km at midlatitudes, *J. Atmos. Sci.*, 32, 831–836, 1978.
- Mitchell, N. J., Middleton, H. R., Beard, A. G., Williams, P. J. S., and Muller, H. G.: The 16-day planetary wave in the mesosphere and lower thermosphere, *Ann. Geophys.*, 17, 1447–1456, doi:10.1007/s00585-999-1447-9, 1999.
- Miyoshi, Y.: Numerical simulation of the 5-day and 16-day waves in the mesopause region, *Earth Planets Space*, 51, 763–772, 1999.
- Nuttall, A. H.: Some windows with very good sidelobe behavior, *IEEE T. Acoust. Speech*, 29, 84–91, 1981.
- Picone, J. M., Hedin, A. E., Drob, D. P., and Aikin, A. C.: NRLMSISE-00 empirical model of the atmosphere: Statistical comparisons and scientific issues, *J. Geophys. Res.*, 107, 1468, doi:10.1029/2002JA009430, 2002.
- Riggin, D. M., Liu, H.-L., Lieberman, R. S., Roble, R. G., Russell III, J. M., Mertens, C. J., Mlynczak, M. G., Pancheva, D., Franke, S. J., Murayama, Y., Manson, A. H., Meek, C. E., and Vincent, R. A.: Observations of the 5-day wave in the mesosphere and lower thermosphere, *J. Atmos. Sol-Terr. Phys.*, 68, 323–329, 2006.
- Rodgers, C.: Retrieval of atmospheric temperature and composition from measurements of thermal radiation, *Rev. Geophys. Space Phys.*, 14, 609–624, 1976.
- Salby, M. L.: Rossby normal modes in nonuniform background configuration. Part II: Equinox and solstice conditions, *J. Atmos. Sci.*, 38, 1827–1840, 1981.
- Smith, A. K.: The origin of stationary planetary waves in the upper mesosphere, *J. Atmos. Sci.*, 60, 3033–3041, 2003.
- Stearns, S. D.: Digital signal analysis, Hayden book, Rochelle Park, New Jersey, 1975.
- Straub, C., Espy, P. J., Hibbins, R. E., and Newnham, D. A.: Mesospheric CO above Troll station, Antarctica observed by a ground based microwave radiometer, *Earth Syst. Sci. Data*, 5, 199–208, doi:10.5194/essd-5-199-2013, 2013.
- Uppala, S. M., Källberg, P. W., Simmons, A. J., Andrae, U., Da Costa Bechtold, V., Fiorino, M., Gibson J. K., Haseler, J., Hernandez, A., Kelly, G. A., Li, X., Onogi, K., Saarinen, S., Sokka, N., Allan, R. P., Andersson, E., Arpe, K., Balmaseda, M. A., Beljaars, A. C. M., Van De Berg, L., Bidlot, J., Bormann, N., Caires, S., Chevallier, F., Dethof, A., Dragosavac, M., Fisher, M., Fuentes, M., Hagemann, S., Hólm, E., Hoskins, B. J., Isaksen, I., Janssen, P. A. E. M., Jenne, R., McNally, A. P., Mahfouf, J.-F., Morcrette, J.-J., Rayner, N. A., Saunders, R. W., Simon, P., Sterl, A., Trenberth, K. E., Untch, A., Vasiljevic, D., Viterbo, P., and Woollen, J.: The ERA-40 re-analysis, *Q. J. Roy. Meteorol. Soc.*, 131, 2961–3012, doi:10.1256/qj.04.176, 2005.
- US Standard Atmosphere Supplements: U.S. Government Printing Office, Washington, DC, 1966.
- Vincent, R. A.: Planetary and gravity waves in the mesosphere and lower thermosphere, *Adv. Space Res.*, 10, 93–101, 1990.
- Williams, C. R. and Avery, S. K.: Analysis of long-period waves using the mesosphere-stratosphere-troposphere radar at poker flats, Alaska, *J. Geophys. Res.*, 97, 20855–20861, 1992.

## **Paper II**

# **Planetary wave oscillations observed in ozone and PMSE data from Antarctica**

**T. D. Demissie<sup>1</sup>, K. Hosokawa<sup>2</sup>, N. H. Kleinknecht<sup>1</sup>, P. J. Espy<sup>1,3</sup>, R. E. Hibbins<sup>1,3</sup>**

<sup>1</sup>Norwegian University of Science and Technology (NTNU), Trondheim, Norway

<sup>2</sup>Department of Communication Engineering and Informatics, University of Electro-Communications, Tokyo, Japan

<sup>3</sup>Birkeland Centre for Space Science, Bergen, Norway

Corresponding author: Teferi D Demissie, Department of Physics, Norwegian University of Science and Technology (NTNU), Hoegskoleringen 5, NO-7491 Trondheim, Norway. Phone: +4745069493. Fax: +47 73 59 77 10. E-mail: teferi.demissie@ntnu.no.

*In review at journal of Atmospheric and Solar-Terrestrial Physics (JASTP)*



# Planetary wave oscillations observed in ozone and PMSE data from Antarctica

T. D. Demissie<sup>1</sup>, K. Hosokawa<sup>2</sup>, N. H. Kleinknecht<sup>1</sup>, P. J. Espy<sup>1,3</sup>, R. E. Hibbins<sup>1,3</sup>

<sup>1</sup>Norwegian University of Science and Technology (NTNU), Trondheim, Norway

<sup>2</sup>Department of Communication Engineering and Informatics, University of Electro-Communications, Tokyo, Japan

<sup>3</sup>Birkeland Centre for Space Science, Bergen, Norway

Corresponding author: Teferi D Demissie, Department of Physics, Norwegian University of Science and Technology (NTNU), Hoegskoleringen 5, NO-7491 Trondheim, Norway. Phone: +4745069493. Fax: +47 73 59 77 10. E-mail: teferi.demissie@ntnu.no.

## Abstract

The effect of temperature variations caused by planetary waves on the occurrence of Polar Mesospheric Summer Echoes (PMSE) has been a subject of recent research. These same temperature fluctuations have also been shown to modulate the ozone volume mixing ratio above 30 km. In this study, ground-based radiometer measurements of ozone mixing ratio profiles at Troll station (72°S, 2°E), Antarctica are compared with PMSE extracted from the near-range measurements of the Sanae (72°S, 2°W) Super Dual Auroral Radar (SuperDARN) over the radiometer field of view. We show here that the resulting quasi-periodic fluctuations in PMSE correlate with the variations seen in the ozone, and that these ozone mixing-ratio variations can be used to trace the phase variation of planetary waves with height to demonstrate that they extend from the stratosphere up to the mesopause. The results indicate that the modulation of PMSE occurrence frequency during the summer of 2009/10 is the result of two planetary waves with similar zonal structure and period, but with different vertical phase structures.

## 1 Introduction

Travelling planetary waves (PW) are large-scale density and temperature oscillations in the stratosphere and mesosphere, which have horizontal scales of thousands of kilometers, vertical sizes of 10's of kilometers, and periods from 2 to 30 days (e.g. Randel, 1987; Salby, 1981; Smith, 1997). A number of ground and satellite-based studies have shown that temperature

fluctuations associated with planetary waves can modulate Polar Mesospheric Clouds (PMC) and Polar Mesosphere Summer Echoes (PMSE) in the mesosphere (Kirkwood and Réchou, 1998; Kirkwood et al., 2002; Kirkwood and Stebel, 2003; Merkel et al., 2003, 2008; von Savigny et al., 2007). Kirkwood and Réchou (1998) and Kirkwood et al. (2002) found that the temperature fluctuations associated with the 5-day PW in the stratosphere are negatively correlated with PMSE variations at a height of 80-90 km. In another study, Kirkwood and Stebel (2003) used ground-based observations of PMC over northwest Europe to investigate the effect of planetary waves on PMC. The results of their study showed a correlation between the 16-day and 5-day PW observed in stratospheric assimilation temperatures, extrapolated to the mesopause, and the probability of occurrence of PMC between 80 and 85 km. Merkel et al., (2003, 2008) identified a 5-day periodicity in the variation of PMC brightness, which they associated with the 5-day PW in the polar summer mesosphere. Merkel et al., (2008) further compared this 5-day periodicity in PMC brightness with mesospheric temperature variations measured by the SABER instrument on board the TIMED satellite, and found that the two were highly anti-correlated.

Belova et al. (2009) used satellite radiometric measurements to demonstrate that the ozone mixing ratio above 30 km in the upper stratosphere is controlled by temperature, with temperature and ozone variations 180° out of phase. Belova et al. (2008) also used satellite radiometric measurements to isolate the geographical structure of the 5-day wave in O<sub>3</sub> at several altitudes for comparison with mesospheric temperature variations. However, to our knowledge, none of these studies have used coincident and simultaneous observations of PMSE and ozone to trace and quantify the vertical propagation of the PWs modulating the mesospheric aerosols throughout the middle and upper atmosphere so as to identify their phase structure and source regions.

In this study, ground-based radiometer measurements of the ozone mixing ratio profile at Troll station in Antarctica, together with PMSE extracted from near range measurements of the Sanae SuperDARN radar over the radiometer field of view are used as proxies for planetary wave temperature variations. The temperature oscillations modulating the PMSE at a single location may be the superposition of many PWs (Palo et al., 1999), so here we use ozone mixing

ratio profiles to quantify the vertical phase structure of these waves in order to ascertain their source regions and their evolution in time and altitude throughout the Antarctic summer. Section 2, below, describes the data analysis techniques, and this is followed in section 3 by a description of the planetary wave signatures in the O<sub>3</sub> mixing ratio and PMSE rate of occurrence.

## 2 Data analysis

### 2.1 Extraction of PMSE from SuperDARN radar data

Polar Mesosphere Summer Echoes (PMSE) are strong radar backscatter echoes occurring between 80-90 km during the polar summer that have been observed using radars operating above 10 MHz (Cho et al, 1993). The Super Dual Auroral Radar Network (SuperDARN) is a network of high frequency (HF) radars, whose combined field of view covers a large part of the northern and southern hemisphere polar ionospheres. The radars are typically used to study large-scale dynamical processes in the earth's ionosphere, magnetosphere and neutral atmosphere (Greenwald et al., 1995). There are a number of high-latitude SuperDARN radars currently working in both hemispheres, and PMSE have been detected in the near range measurements of these radars (Ogawa et al., 2002). However, the PMSE must be separated from other backscatter echoes coming from meteors and E region echoes (Hosokawa et al., 2004), as described below.

In this study, the algorithm developed by Hosokawa et al., (2005) was applied to the SuperDARN data at Sanae station (72°S, 2°W). The centroid latitude and longitude of the Sanae beam pattern lie within the field of view of the Troll radiometer, and PMSE were extracted from the first range gate (Gate 0), which includes the PMSE altitude range from 80 to 100 km. All echoes from the first range gate measurements were initially identified, including PMSE, E-region backscatter and meteor-trail echoes. Then, the criteria adopted by Hosokawa et al., (2005) were applied to differentiate PMSE from the other two scattering mechanisms. First, the back-scattered power was required to be greater than 6 dB. Secondly, only Doppler velocities between  $\pm 50 \text{ m s}^{-1}$  were accepted. Finally, the spectral width was required to be less than  $50 \text{ m s}^{-1}$ . Hosokawa et al., (2005) have shown that echoes passing these three criteria have a high

probability of being PMSE. The occurrence rate for the first range gate was computed for each 10 minute local-time (LT) bin during a given day by dividing the number of echoes passing the selection criteria by the total number of observations present there. Figure 1 shows the occurrence rate of echoes that passed the selection criteria as a function of local time and day of the year.

## 2.2 Ozone measurement and analysis

Ozone measurements were obtained from the British Antarctic Survey's Antarctic Radiometer for Ozone and Nitric oxide (ARON) mm-wave radiometer. The instrument was operated at the Norwegian Polar Institute Troll station (72°S, 2°E) from December 2008 to January 2010, observing carbon monoxide (CO), nitric oxide (NO) and ozone (O<sub>3</sub>) in different spectral lines ranging from 230–250 GHz. A detailed description of the Troll microwave radiometer and measurements may be found in Espy et al. (2006). Optimal estimation methods, as described by Rodgers (1976), have been used to invert the spectra of the ozone line at 249.96 GHz to obtain ozone volume mixing ratio (vmr) profiles (Kleinknecht, 2010). The a priori pressure, temperature, water vapour and ozone values used for the inversion below 45 km are derived from monthly mean ERA-40 profiles. Between 45 and 85 km, monthly mean temperature and pressure values were taken from the MSIS-00 model (Picone et al., 2002), and the ozone vmr was taken from the US Standard Atmosphere (1976) for winter and summer conditions. For the wave studies here, the a priori ozone values above 85 km were held at a constant value so as to ensure that the a priori values did not induce oscillations. The retrieved hourly ozone profiles as a function of altitude and time are shown in Figure 2. As can be seen in Figure 2a, the first ozone maximum is observed around 35 km, but the secondary maximum is not clearly identified due to lack of measurement response in the region above 80 km as shown in Figure 2b. The vertical resolution, which is interpreted from the full width of half maximum (FWHM) of the averaging kernels, is ~10 km below 65 km, increasing to ~17 km by 75 km (Figure 2c). The large altitude resolution above 70 km results in highly correlated data above this altitude.

### 3 Analysis and results

To extract wave periods in the PMSE and ozone mixing ratio profile as function of altitude, spectral analysis was performed on each of the two datasets. In order to prepare the data for analysis, the ten-minute PMSE data were averaged into hourly bins over the period from November 1, 2009 – January 12, 2010. PMSE have been observed to maximize around 12:00 LT (Morris et al., 2009; Palmer et al., 1996) whilst meteor echoes maximize around 07:00 LT and decrease through to late afternoon (Beldon and Mitchell, 2010; Singer et al., 2004). In addition, E-region echoes occur mostly at night (Milan and Lester, 2001). Thus, the hourly average between 11:00 to 12:00 LT was chosen to maximize the discrimination of PMSE from meteors and E-region echoes. Only four days of data were missing and linear interpolation was used to fill these data gaps. In the case of ozone, the ozone mixing ratio was averaged for one hour about midnight, where mesospheric ozone maximizes. This daily averaged profile at 4 km intervals between 30 and 80 km was used for comparison with the PMSE.

Longer time-scale variations of PMSE and ozone mixing ratio were removed since our interest was on waves with periods between 2 and 12 days. Temperature fluctuations, which cause changes in both ozone and PMSE, have been observed to have strong annual and semi-annual oscillations (Niciejewski and Killeen, 1995), and significant oscillations with periods from months to as long as a solar cycle (Espy and Stegman, 2002). A high-pass filter was applied to both datasets to remove long-period background fluctuations while retaining the variations with shorter periods (higher frequency). A Butterworth IIR high-pass filter was used to remove periods greater than 12 days since it has a flat frequency response in the selected pass band. Figure 3 shows the time series of the unfiltered and high-pass filtered PMSE occurrence around 87 km as well as the high-pass filtered ozone vmr profiles from 30 km to 80 km. Due to the change of ozone mixing ratio as a function of height, the lower panel in figure 3 is further subdivided into two parts, with the upper section, covering from 56 to 80 km, expanded by a factor of 10. Figure 3 shows a large amount of variability in wave activity in the period ranging from 2 to 10 days at all heights.

A fast Fourier transform (FFT) was performed on the filtered datasets to confirm the removal of the long-period backgrounds and to identify periodic fluctuations observed in the ozone and PMSE fields at higher frequencies. The high-pass filtered data were apodized using a Hamming window (Nuttall, 1981) before the FFT was performed in order to minimize spectral leakage and side-lobe effects in the FFT. Figure 4 shows the amplitude of the PMSE and ozone vmr at each height. Three distinct high-amplitude regions are found with periods around 2-3 days, 4-5 days and 6-8 days. Due to the daily sampling, periods between 2-3 days are too close to the Nyquist limit to yield quantitative results, and will therefore not be discussed here. The oscillation with a 4-5 day period is most likely associated with the nominal 5-day wave, which has often been observed in PMSE and PMC (e.g. Kirkwood et al., 2002; Merkel et al., 2003). The longest oscillation, which has the largest amplitude in the PMSE, has a period of 6-8 days and is taken to be the ~6.5 day zonal wave number 1 planetary wave (Talaat et al., 2001; 2002; Jiang et al., 2008). Though present at all altitudes, the amplitude of both waves increases below 55 km. Unfortunately this technique cannot determine whether this amplitude change tracks the downward increase in ozone vmr, or if it decreases at high altitudes as the waves approach the zonal wind maximum near 68 km (Forbes, 1995; Hibbins et al., 2005; Day and Mitchell, 2010; MacDonald et al. 2011). Below 40 km, the fall in wave amplitude is likely due to the large a priori contribution to the retrieved  $O_3$ , as the nearly constant a priori value tends to minimize the wave-induced departures from the a priori and reduce the extracted wave amplitudes.

To determine whether or not the 4-5 day or 6-8 day peaks in the Ozone and PMSE are related and phase coherent, a Fourier-based cross-spectral analysis was performed between the two datasets. Figure 5 shows the cross-spectra between the PMSE and the ozone vmr at each level as a function of period in days. The cross-spectra show that despite the low amplitudes in the FFT, the amplitude associated with both waves in the  $O_3$  vmr is coherent and phase-locked with the oscillation in the PMSE occurrence frequency. The amplitudes of the cross-spectra in Figure 5 are reflections of the amplitudes in Figure 4, which are influenced by a combination of factors. These include changes in the  $O_3$  vmr or interaction with background wind, as well as a priori effects.

Having documented the presence of coherent and phase-locked 5-day and 6.5-day waves in both the PMSE and ozone vmr through the amplitude- and cross-spectral analysis, the data were band-pass filtered to isolate the two periods. In this way the vertical phase structure of each individual component could be examined. Again, identical Butterworth IIR filters were used on the two data sets, with half-power points of 4 and 5 days for the 4-5 day wave, and 6 and 8 days for the 6-8 day oscillation, consistent with their periods in the cross-spectra. A time-lagged cross-correlation was performed between the PMSE and ozone vmr for each of these filtered data sets. The cross-correlation coefficients between the PMSE and the ozone vmr at each altitude for the 4-5 day and 6-8 day oscillations are shown in the left-panel of Figure 6a and Figure 6b. Both oscillations show a high degree of coherence between the PMSE and ozone oscillations with correlation coefficient magnitudes exceeding 0.7, indicating that the underlying temperature fluctuations are highly correlated and locked in phase over altitude. In addition, the strong periodic modulation with lag indicates that both oscillations persist and are coherent over the entire data period.

#### 4 Discussion and conclusions

The PMSE occurrence frequency has been extracted from the SuperDARN radar at Sanae station in Antarctica during the 2009 summer season using the algorithm developed by Hosokawa et al (2005). These were combined with spatially and temporally coincident midnight measurements of ozone mixing ratio obtained from the BAS microwave radiometer located at Troll station (72°S, 2°E) to measure the period and vertical structure of planetary waves in stratosphere and mesosphere. This is possible due to the short chemical lifetime of ozone relative to transport times above ~30 km. This means that the planetary wave induced temperature fluctuations that modulate PMSE occurrence will also modulate the ozone mixing ratio, with minima in temperatures associated with maxima in ozone (Finger et al., 1995; Huang et al., 2008; Belova et al., 2009). As a result these planetary wave variations in the PMSE have been traced downward to the upper stratosphere using variations in the ozone vmr.

The amplitude spectra show that there are a number of oscillations in the ~2-12-day period range, with the 4-5 day and 6-8 day oscillations being the most dominant and frequent in both

the PMSE occurrence frequency as well as in the ozone vmr profiles from 30 to 80 km. These waves have been taken to be the 5-day and 6.5-day zonal wave-number one planetary waves. The 5-day wave is known to be a strong feature in the stratosphere and mesosphere during the polar summer (Salby, 1981; Williams and Avery, 1992; Meyer and Forbes, 1997; Kirkwood et al., 2002; Riggin et al., 2006; Belova et al., 2008; Day and Mitchell, 2010). However, the 6.5-day wave, while often observed in the lower stratosphere during the polar summer (Talaat et al., 2001), has only been observed sporadically in the westward zonal winds characteristic of that season (Jiang et al., 2008). In the present study, the amplitude of the waves in the ozone is observed to decrease above 55 km. This may be due to the interactions of the waves with the increasing westward zonal winds at these altitudes (Wu et al., 1994; Forbes, 1995; Day and Mitchell, 2010; MacDonald et al. 2011). However, we cannot rule out that this decrease of amplitude is merely due to the decreasing  $O_3$  vmr values above 55 km. Indeed, the strong wave amplitudes observed in the PMSE near 85 km would favour the latter explanation. Similarly, the decrease in wave amplitude below 40 km is likely due to the large a priori contribution to the retrieved  $O_3$  at these altitudes minimizing the wave-induced departures and reducing the extracted wave amplitudes

Despite the instrumental effects, the cross-spectral analysis demonstrates that the amplitude corresponding to the 5-day and 6.5-day PW oscillations in the  $O_3$  is coherent and phase locked with the corresponding oscillation in the PMSE occurrence frequency. This indicates a common cause, and the temperature fluctuations associated with the planetary waves, known to affect both the  $O_3$  and the PMSE, are likely responsible (e.g. Belova et al., 2009; Kirkwood and Stebel, 2003). The presence of peaks in the cross spectra demonstrates that despite the low amplitudes, this coherence is maintained at all altitudes from 30-70 km. The variation in amplitude of the cross spectrum reflects the variation in the amplitude spectra, with low amplitudes between 55 and 80 km.

The oscillations in the  $O_3$  vmr have the same frequency and are phase locked to those in the PMSE. Therefore, a band-pass filter was used to isolate the individual 5-day and 6.5-day components, and a lagged cross-correlation was performed for each. For the 5-day wave, the

peak magnitudes of the correlation coefficient are between 0.63 and 0.21, with the majority significantly different from zero at the 95% confidence level. This indicates a significant correlation between the temperature fluctuations in the middle atmosphere and the PMSE variations near the mesopause. The continuity of high correlation magnitudes with lag demonstrates the persistence of the wave over the data period, while the stability of the correlation pattern with altitude illustrates the vertical phase structure of the wave. Tracing either a single minimum or maximum in the correlation downward yields the altitude variation of the wave's phase. For the 5-day wave, the lag of the minimum correlation nearest to 0 lag is shown in the middle panel of Figure 6a. As shown in the right panel of the same figure, only points significant at the 95% level have been used. The lag is seen to vary between 1 and -4 days, or less than one cycle of phase shift between 38 and 70 km. This very nearly vertical phase structure is consistent with the 5-day wave having a normal mode oscillation (Miyoshi, 1999).

The magnitude of the correlation coefficient of the 6.5-day wave is similar to the 5-day wave, exceeding 0.8 at the upper altitudes. However, here the phase lag, shown in the middle panel of Figure 6b, is seen to change by 9 days, or almost 1.4 cycles, from 34 to 66 km. Once again, only points significant at the 95% level have been used in the phase analysis. This large phase shift with altitude would indicate that the wave is propagating upward through the upper stratosphere and mesosphere into the PMSE region with a vertical wavelength on the order of 23 km, consistent with the findings of Talaat et al. (2001; 2002) and Jiang et al. (2008). There is an abrupt change in phase of the wave between 65 and 70 km, near the peak in the summertime zonal wind jets around these latitudes (Hibbins et al., 2005). This may indicate that this slower wave may be more strongly Doppler shifted by the winds (e.g. Wu et al., 1994 and references therein). However, we cannot rule out instrumental effects as the cause of this phase change as it does occur at the altitude above which the degraded altitude resolution of the measurements creates a constant phase.

In conclusion, this study demonstrates that the PMSE oscillations appear to be driven by two planetary waves with similar periods, 5- and 6.5-days, that are known to have similar zonal

wavenumber-1 structure. Despite the climatologically westward zonal winds in the middle atmosphere, these waves have been traced downward into the stratosphere using the ozone vmr variations, and they are observed to have distinctly different vertical structures. The 5-day wave has nearly vertical phase fronts consistent with a normal mode structure, and is seen to extend from the PMSE region near 85 km down to the upper stratosphere. However, the phase structure of the 6.5-day wave indicates that it is propagating upward from the stratosphere into the PMSE region. The amplitude changes of ozone vmr with altitude cannot unambiguously be used to infer the interaction between the waves and the mean flow. However, the rapid phase changes observed in the 6.5 day wave near the zonal wind maximum may be indicative of such interactions.

### Acknowledgments

We thank David Newnham at BAS, Kim Holmén at the Norwegian Polar Institute (NPI) and Paul Hartogh at Max Planck Institute (MPI) for their support of the microwave radiometer. We also thank Asbjørn Djupdal (NPI), David Maxfield and Paul Breen (BAS) for their help. The work has been funded by the Norwegian Research council (NFR) project "Gravity wave sources and scales in the Polar Regions and their effect on Polar Mesospheric Clouds". In addition, we acknowledge the Norwegian Polar Institute Antarctic Program which provided funding under the project "Observations of carbon monoxide and ozone in the Antarctic and Arctic: Implications for the Inter-hemispheric coupling of vertical motions".

### References

- Beldon, C.L., Mitchell, N.J., 2010. Gravity wave tidal interactions in the mesosphere and lower thermosphere over Rothera, Antarctica (68°S, 68°W). *J. Geophys. Res.*, 115, D18101, doi: 10.1029/2009JD013617.
- Belova, A., Kirkwood, S., Murtagh, D., 2009. Planetary waves in ozone and temperature in the Northern hemisphere winter of 2002-2003 by Odin satellite data. *Ann. Geophys.*, 27, 1189-1206.
- Belova, A., Kirkwood, S., Murtagh, D., Mitchell, N., Singer, W., Hocking, W., 2008. Five-day planetary waves in the middle atmosphere from Odin satellite data and ground-based Instruments in Northern Hemisphere summer 2003, 2004, 2005 and 2007. *Ann. Geophys.*, 26(11), 3557 – 3570.
- Cho, J.Y., Kelley, M.C., 1993. Polar mesosphere summer radar echoes. *Rev. Geo. phys.*, 31, 243–265.
- Day, K.A., Mitchell, N.J., 2010. The 5-day wave in the Arctic and Antarctic mesosphere and lower thermosphere. *J. Geophys. Res.*, 115, D01109, doi: 10.1029/2009JD012545.
- Espy, P.J., Stegman, J., 2002. Trends and variability of mesospheric temperature at highlatitudes. *J. Phys. Chem. Earth*, 27, 543-553, 2002.

Espy P.J., Hartogh, P., Holmén, K., 2006. A microwave radiometer for the remote sensing of nitric oxide and ozone in the middle atmosphere, *Remote Sensing of Clouds and the Atmosphere XI. Proc. of SPIE Vol. 6362*.

Finger, F.G., Nagatani, R.M., Gelman, M.E., Long, C.S., Miller, A.J., 1995. Consistency between variations of ozone and temperature in the stratosphere. *Geophys. Res. Lett.*, 22, 3477.

Forbes, J.M., Hagan, M.E., Miyahara, S., Vial, F., Manson, A.H., Meek, C.E., Portnyagin, Y.I., 1995. Quasi-16-day oscillation in the mesosphere and lower thermosphere. *J. Geophys. Res.*, 100, 9149–9163

Greenwald, R. A. et al., 1995. DARN/SuperDARN: A global view of the dynamics of high-latitude convection. *Space Sci. Rev.*, 71, 761–796.

Hibbins, R.E., Shanklin, J.D., Espy, P.J., Jarvis, M.J., Riggan, D.M., Fritts, D.C., Lübken, F.-J., 2005. Seasonal variations in the horizontal wind structure from 0-100 km above Rothera station, Antarctica (67S, 68W), *Atmo. Chem. and Phys.*, 5 (11), 2973-2980

Hosokawa, K., Ogawa, T., Sato, N., Yukimatu, A.S., Lyemori, T., 2004. Statistics of Antarctic mesospheric echoes observed with the Super-DARN Syowa radar. *Geophys. Res. Lett.*, 31, L02106, doi: 10.1029/2003GL018776

Hosokawa, K., Ogawa, T., Arnold, N.F., Lester, M., Sato, N., Yukimatu, A.S., 2005. Extraction of polar mesosphere summer echoes from SuperDARN data, *Geophys. Res. Lett.*, 32, L12801, doi: 10.1029/2005GL022788

Huang, F.T., Mayr, H.G., Reber, C.A., Russell III, J.M., Mlynczak, M.G., Mengel, J.G., 2008. Ozone quasi-biennial oscillations (QBO), semiannual oscillations (SAO), and correlations with temperature in the mesosphere, lower thermosphere, and stratosphere, based on measurements from SABER on TIMED and MLS on UARS. *J. Geophys. Res.*, 113, A01316, doi: 10.1029/2007JA012634.

Jiang, G., Xiong, J., et al., 2008. Observation of 6.5-day waves in the MLT region over Wuhan. *J. Atmos. Sol. Terr. Phys.*, 70(1): 41-48.

Kirkwood, S., Rechou, A., 1998. Planetary-wave modulation of PMSE. *Geophys. Res. Lett.*, 25 (24), 4509-4512.

Kirkwood, S., Barabash, V., Brändström, B.U.E., Moström, A., Stebel, K., Mitchell, N.J., Hocking, W., 2002. Noctilucent clouds, PMSE and 5-day planetary waves: A case study. *Geophys. Res. Lett.*, 29(10), 1411, doi: 10.1029/2001GL014022.

Kirkwood, S., Stebel, K., 2003. Influence of planetary waves on noctilucent cloud occurrence over NW Europe. *J. Geophys. Res.*, 208, D8, 10.1029/2002JD002356.

McDonald, A.J., Hibbins, R.E., Jarvis, M.J., 2011. Properties of the quasi-16 day wave derived from EOS MLS observations. *J. Geophys. Res.*, 116(479), D06112, doi: 10.1029/2010JD014719.

Merkel, A.W., Thomas, G.E., Palo, S.E., Bailey, S.M., 2003. Observations of the 5-day planetary wave in PMC measurements from the Student Nitric Oxide Explorer satellite. *Geophys. Res. Lett.*, 30(4), 1196, doi: 10.1029/2002GL016524.

- Merkel, A.W., Garcia, R.R., Bailey, S.M., Russell III, J.M., 2008. Observational studies of planetary waves in PMCs and mesospheric temperature measured by SNOE and SABER. *J. Geophys. Res.*, 113, D14202, doi: 10.1029/2007JD009396
- Meyer, C.K., Forbes, J. M., 1997. A 6.5-day westward propagating planetary wave: Origin and characteristics, *J. Geophys. Res.*, 102(D22), 26,173– 26,178
- Milan, S.E., Lester, M., 2001. A classification of spectral populations observed in HF radar backscatter from the E region auroral electrojets, *Ann. Geophys.*, 19, 189– 204.
- Miyoshi, Y., 1999. Numerical simulation of the 5-day and 16-day waves in the mesopause region. *Earth Planets Space*, 51, 763-772.
- Morris, R.J., Holdsworth, D.A., Klekociuk, A.R., Latteck, R., Murphy, D.J., Singer, W., 2009. Inter-hemispheric asymmetry in polar mesosphere summer echoes and temperature at 69° latitude. *J. Atmos. Solar Terr. Phys.* 71 (3–4), 464–469.
- Niciejewski, R.J., Killeen, T.L., 1995. Annual and semi-annual temperature oscillations in the upper mesosphere. *Geophys. Res. Lett.*, 22, 3243-3246.
- Nuttall, A.H., 1981. Some windows with very good sidelobe behavior. *IEEE Transactions on Acoustics, Speech, Signal Processing*, 29, 84-91.
- Ogawa, T., Nishitani, N., Sato, N., Yamagishi, H., Yukimatu, A.S., 2002. Upper mesosphere summer echoes detected with the Antarctic Syowa HF radar. *J. Geophys. Res. Lett.*, 29 (7), 1157, doi: 10.1029/2001GL014094.
- Palmer, J.R., Rishbeth, H., Jones, G.O.L., Williams, P.J.S., 1996. A statistical study of polar mesosphere summer echoes observed by EISCAT. *J. Atmos. Terr. Phys.*, 58, 307–315.
- Palo, S.E., Roble, R.G., Hagan, M.E., 1999. Simulation of the quasi-two-day wave using the TIME-GCM: Dynamical effects in the middle atmosphere. *Earth Planets Space*, 51, 629– 647.
- Picone, J.M., Hedin, A.E., Drob, D.P., Aikin, A.C., 2002. NRLMSISE-00 empirical model of the atmosphere: Statistical comparisons and scientific issues. *J. Geophys. Res.*, 107, 1468, doi: 10.1029/2002JA009430.
- Randel, W.J., 1987b. A study of planetary-waves in the southern winter troposphere and stratosphere: 1. Wave structure and vertical propagation. *J. Atmos. Sci.*, 44(6), 917– 935.
- Rodgers, C., 1976. Retrieval of atmospheric temperature and composition from measurements of thermal radiation. *Rev. Geophys. Space Phys.*, 14 (4), 609-624.
- Riggin, D.M., et. al., 2006. Observations of the 5-day wave in the mesosphere and lower thermosphere. *J. Atmos. Sol. Terr. Phys.*, 68, 323–339
- Salby, M.L., 1981. Rossby normal modes in nonuniform background configurations. Part II: Equinox and solstice conditions, *J. Atmos. Sci.*, 38(9), 1827–1840.
- Singer, W., Von Zahn, U., Weiss, J., 2004. Diurnal and annual variations of meteor rates at the Arctic circle. *J. Atmos. Chem. Phys.*, 4, 1355.

Smith, A.K., 1997. Stationary planetary waves in upper mesospheric winds. *J. Atmos. Sci.*, 54, 2129–2145.

Talaat, E.R., Yee, J.-H., Zhu, X., 2001. Observations of the 6.5-day wave in the mesosphere and lower thermosphere. *J. Geophys. Res.*, 106(D18), 20715–20723, doi: 10.1029/2001JD900227.

Talaat, E.R., Yee, J.-H., Zhu, X., 2002. The 6.5-day wave in the tropical stratosphere and mesosphere. *J. Geophys. Res.*, 107(D12), 4133, doi: 10.1029/2001JD000822.

U.S. Standard Atmosphere, 1976, U.S. Government Printing Office, Washington, D.C., 1976.

Von Savigny, C., Roberts, C., Bovensmann, H., Burrows, J.P., Schwartz, M., 2007. Satellite observations of the quasi 5 day wave in noctilucent clouds and mesopause temperatures, *Geophys. Res. Lett.*, 34, L24808, doi: 10.1029/2007GL030987.

Williams, C.R., Avery, S.K., 1992. Analysis of long-period waves using the mesosphere-stratosphere-troposphere radar at Poker Flat, Alaska. *J. Geophys. Res.*, 97, 20 855–20 861.

Wu, D.L., Hays, P.B., Skinner, W.R., 1994. Observations of the 5-day wave in the mesosphere and lower thermosphere, *Geophys. Res. Lett.*, 21, 2733– 2736.

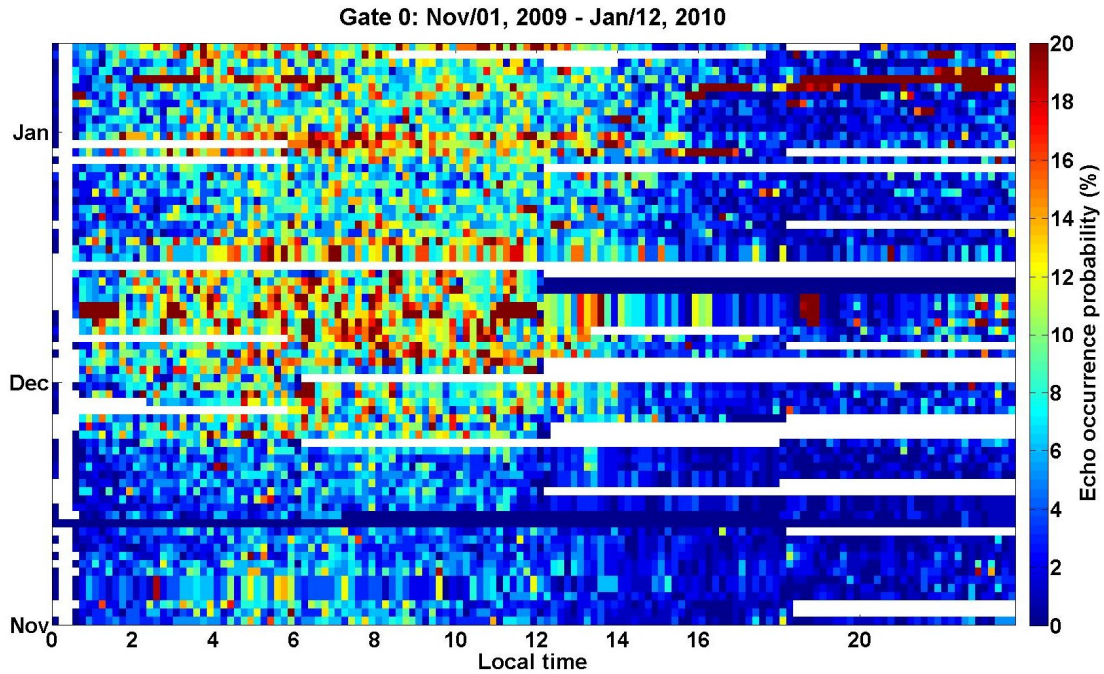


Figure 1: Occurrence rates of PMSE (in percent of total measurements) from the SuperDARN radar at Sanae from November 1, 2009 to January 12, 2010 as a function of local time. White areas indicate periods of unavailable data.

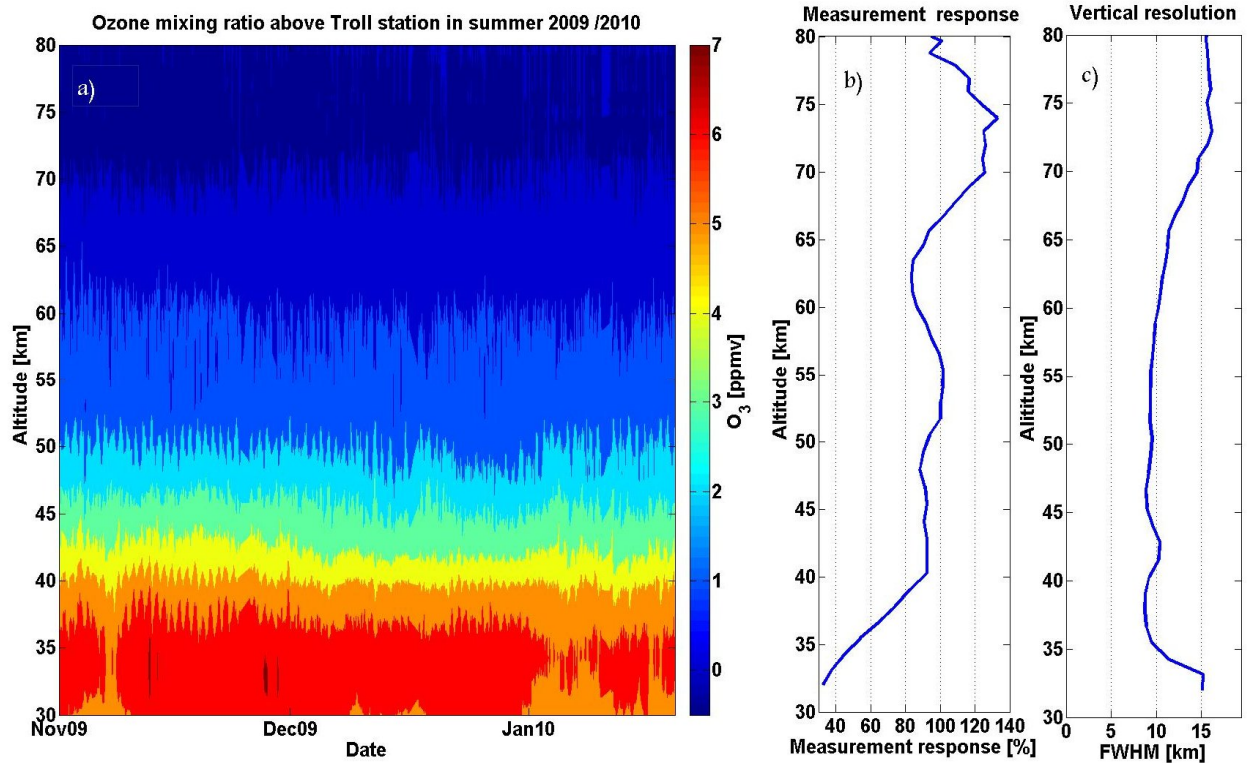


Figure 2: a) Retrieved ozone mixing ratio profile from November 1, 2009 to January 12, 2010 at the Troll station. b) Measurement response of a sample inversion. The lower the response, the greater the contribution the a priori value has to the retrieved profile. c) Vertical resolution of a sample inversion given as the FWHM of the averaging kernel in km.

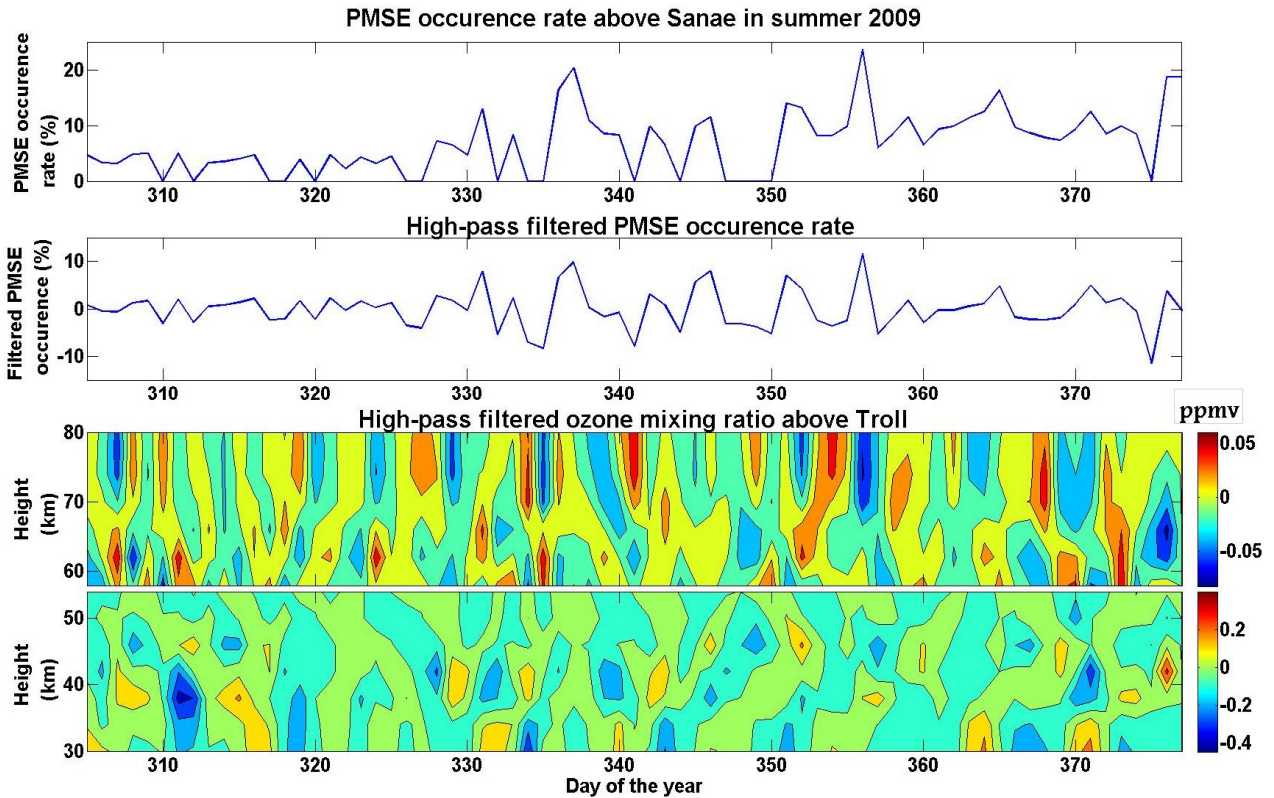


Figure 3. Upper-panel: Unfiltered PMSE occurrence rate data averaged around 12:00 LT from November 1, 2009 to January 12, 2010. Middle-panel: High-pass filtered PMSE occurrence rate. Lower two panels: Ozone mixing ratio profile data from November 1, 2009 to January 12, 2010 for the altitude range of 30 to 80 km.

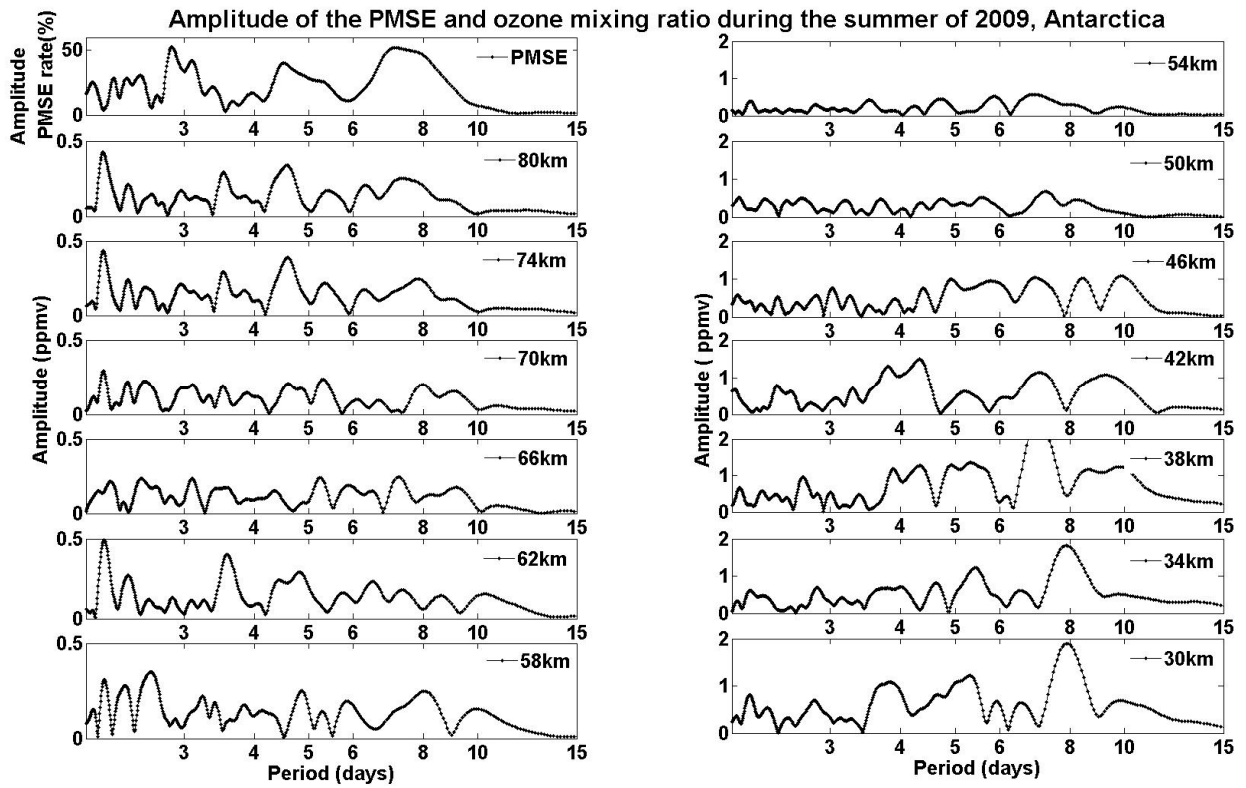


Figure 4: Amplitude of the PMSE occurrence around the mesopause (upper left-panel) and ozone mixing ratio from heights 30 to 80 km with an interval of ~4 km

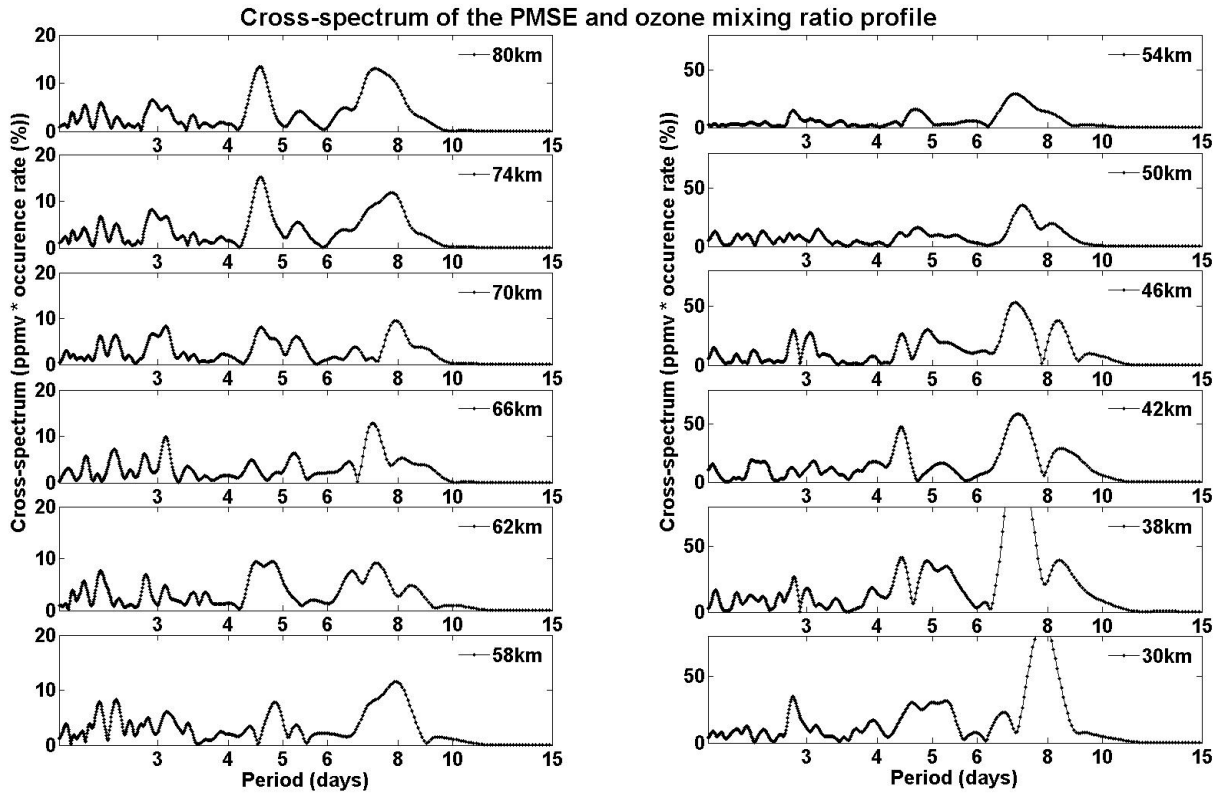
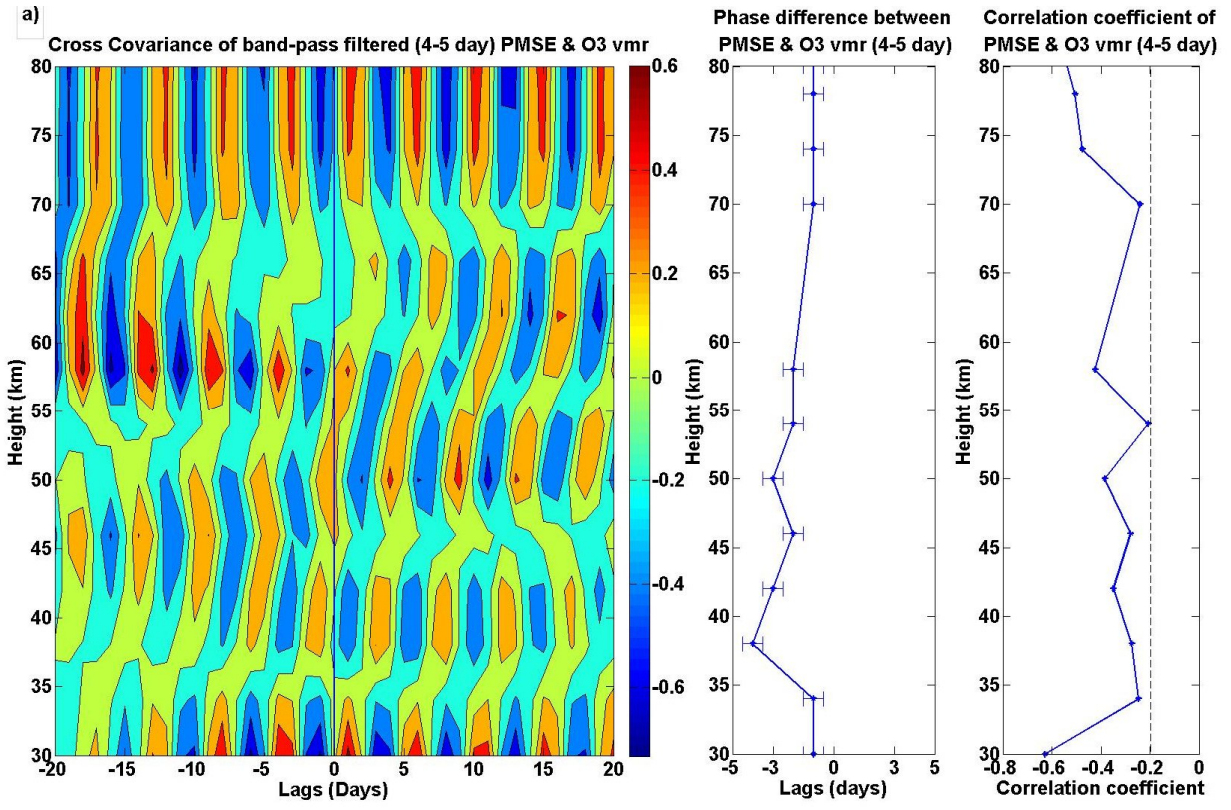
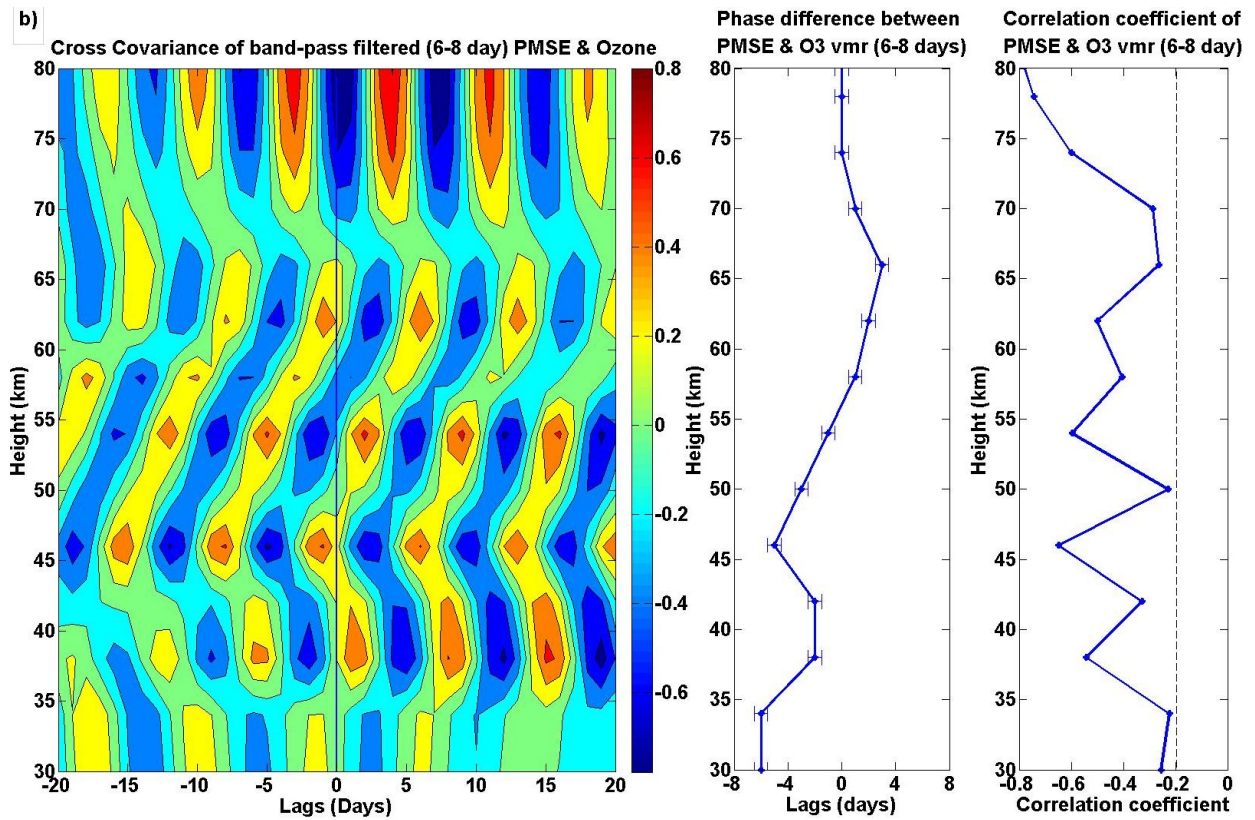


Figure 5: Cross-spectrum of the PMSE occurrence and ozone vmr for different levels in the stratosphere and mesosphere during the summer of 2009 in Antarctica.





Paper III

## Characteristics and sources of gravity waves observed in NLC over Norway

T. D. Demissie<sup>1,2</sup>, N. H. Kleinknecht<sup>1</sup>, P. J. Espy<sup>1,2</sup>, N. Kaifler<sup>3</sup>, Gerd Baumgarten<sup>3</sup>

<sup>1</sup>Norwegian University of Science and Technology (NTNU), Trondheim, Norway

<sup>2</sup>Birkeland Centre for Space Science, Bergen, Norway

<sup>3</sup>Leibniz-Institut für Atmosphärenphysik e. V., 18225 Kühlungsborn, Germany

Corresponding author: Teferi D Demissie, Department of Physics, Norwegian University of Science and Technology (NTNU), Hoegskoleringen 5, NO-7491 Trondheim, Norway. Phone: +4745069493. Fax: +47 73 59 77 10. E-mail: teferi.demissie@ntnu.no.

Submitted to journal of Atmospheric Chemistry and Physics Discussion (ACPD)



# Characteristics and sources of gravity waves observed in NLC over Norway

T. D. Demissie<sup>1,2</sup>, P. J. Espy<sup>1,2</sup>, N. H. Kleinknecht<sup>1</sup>, N. Kaifler<sup>3</sup>, G. Baumgarten<sup>3</sup>

<sup>1</sup>Norwegian University of Science and Technology (NTNU), Trondheim, Norway

<sup>2</sup>Birkeland Centre for Space Science, Bergen, Norway

<sup>3</sup>Leibniz-Institut für Atmosphärenphysik e. V., 18225 Kühlungsborn, Germany

## Abstract

Four years of noctilucent cloud (NLC) images from an automated digital camera in Trondheim and results from a ray tracing model are used to extend the climatology of gravity waves to higher latitudes and to identify their sources at high latitudes during summertime. The climatology of the summertime gravity-waves detected in NLC between 64° and 74°N is similar to that observed between 60° and 64°N by Pautet et al. (2011). The direction of propagation of gravity waves observed in the NLC north of 64°N is a continuation of the north and northeast propagation as observed in south of 64°N. However, a unique population of fast, short wavelength waves propagating towards the SW is observed in the NLC, which is consistent with transverse instabilities generated *in-situ* by breaking gravity waves (Fritts et al. 2003). The relative amplitude of the waves observed in the NLC Mie-scatter have been combined with ray-tracing results to show that waves propagating from near the tropopause, rather than those resulting from secondary generation in the stratosphere or mesosphere, are more likely to be the sources of the prominent wave structures observed in the NLC. The coastal region of Norway along the latitude of 70°N is identified as the primary source region of the waves generated near the tropopause.

## 1. Introduction

Gravity waves play a major role in the global dynamics, circulation and thermal balance of the mesosphere and lower thermosphere. These waves are typically generated in the lower atmosphere through the action of weather systems or orographic lifting of air masses (Fritts and Alexander, 2003, and references therein). The waves grow in amplitude as they propagate upward into the rarefied mesosphere, where they become unstable and locally dissipate their energy and deposit their

momentum (Lindzen, 1981; Holton, 1983; Garcia and Solomon, 1985). The filtering action of the winds below causes this input of momentum to create a drag force on the zonal wind that establishes the global, pole-to-pole circulation in the mesosphere (Lindzen, 1981; Holton, 1982, 1983; Garcia and Solomon, 1985). The resulting wintertime convergent and downward flow, and the corresponding summertime divergent and upward flow, adiabatically drive the polar mesospheric temperatures far from radiative equilibrium and create a warm winter and cold summer mesopause in the polar regions (Haurwitz, 1961; Garcia and Solomon, 1985; Lübken et al., 1990; Fritts and Luo, 1995; Luo et al., 1995; Espy and Stegman, 2002; Fritts and Alexander, 2003). This adiabatic cooling drives the summer polar mesopause temperatures below 150 K, and the small amounts of water vapour present can condense into the ice clouds known as Noctilucent Clouds (NLC) when viewed from the ground, or Polar Mesospheric Clouds (PMC) when viewed from space.

The strength of this inter-hemispheric circulation, and thus the degree of heating or cooling at the polar mesopause, depends upon the amount of gravity-wave momentum deposited in the mesosphere that is in the opposite direction to the zonal flow. Thus, the major role gravity waves play in the determination of the global circulation and thermal balance makes them an essential element of global circulation models (GCMs). Current GCMs, while explicitly resolving longer scale gravity waves, must parameterize the shorter-scale waves (Hamilton, 1996) that carry the bulk of the energy and momentum to the mesosphere (Vincent, 1984). Most parameterizations require temporal and spatial variations to reproduce the wave-driven circulation effects adequately (e.g. Rind et al., 1988; Hamilton, 1995). Hence, knowledge of the seasonal and latitudinal behaviour of gravity waves, as well as their source regions, is essential to both guide and constrain these parameterizations, particularly in the Polar Regions (Garcia and Boville, 1994; Hamilton, 1996).

Although there are a number of gravity-wave studies at high latitudes, most of these rely upon analysing the wave structures induced by the waves in the night airglow (e.g., Taylor and Henriksen, 1989; Pautet et al., 2005; Nielsen et al., 2006, 2009; Espy et al 2004; 2006 ). However, these observations are not possible during the high latitude polar summer when the mesosphere remains sunlit. Recently, Pautet et al. (2011) recognized that even though it is not possible to use the airglow during this period, the structures present in the NLC, known to be caused by gravity waves and their

instabilities (Hines, 1960; Thomas, 1991; Fritts et al., 1993; Chandran et al., 2009, 2010), could themselves be used to infer the gravity waves present. Analysing NLC images from Stockholm, Sweden (59.5°N, 18.2°E), they were able to provide the first climatology of gravity-wave wavelengths, phase speeds and propagation directions from 60 to 64 °N during the polar summer. Similarly, using observations from the Aeronomy of Ice in the Mesosphere (AIM) satellite, Taylor et al. (2011, and references therein) have compiled an impressive climatology of gravity wave wavelengths and wave-front orientation from 75 to 85° N and S for waves with wavelengths >20 km.

We present here an extension of the Pautet et al. (2011) climatology to higher latitudes (64 to 74°N) using NLC images taken from Trondheim, Norway (63.4°N, 10.5°E). In doing so, this study also fills the gap between the ground-based and satellite studies. In addition, we seek to expand those studies by characterizing the relative amplitude of the waves in the NLC and utilizing a ray-tracing model to identify the source regions of high latitude gravity waves present during the polar summer. Together, these observations provide a critical extension of the summertime gravity-wave climatology and information as to the efficiency of different sources required for parameterization of gravity-wave effects.

## **2. Observation and processing techniques of the NLC images**

Four years of NLC pictures, since the summer of 2007, have been collected using an automatic digital camera (Canon EOS 450D) from Trondheim, Norway by the Leibniz Institute of Atmospheric Physics of Kühlungsborn, Germany (Baumgarten et al., 2009). The camera takes pictures throughout the twilight period with exposure times of 0.5s and 0.6s with a cadence ranging between two to three frames per minute depending on the solar elevation angle. The camera views towards the north with a field of view (FOV) of 54.5 x 41.5°.

Figure 1 is an example of the NLC image taken on the night of 16–17 July, 2008, at 22:30 UT, which is 23:12 Local Solar Time (LST). At this time, the Sun is in the north-northwest, towards the bottom and left of the image. The NLC are clearly visible in the image when the solar Mie scattering from the clouds is brighter than the column-integrated Rayleigh scattered sunlight from the atmosphere. However, in the lower part of the image, towards the Sun, the clouds are not visible due to the loss

of contrast against the atmospheric Rayleigh scatter. Similarly, they are not visible in the upper part of the image as the Sun no longer illuminates the clouds. In those areas where the clouds are visible, different types of structures with various forms and sizes are clearly seen in the sunlit NLC. This is the result of short-period gravity waves modulating the ice-particle density, and the resulting intensity fluctuations trace out the waves in the centre and centre right of the image. In addition, very small scale structures are visible that may be the result of instabilities that develop as the gravity waves begin to break (Fritts et al., 1993).

As a first step in the image analysis, the NLC images are mapped to a horizontal plane through the NLC layer “the satellite view” (Witt, 1962; Pautet and Moreels, 2002). In order to accurately project the NLC images, the viewing geometry of the camera, including the FOV, azimuth and elevation angles as well as rotation of the optical axis, were first calibrated using the visible stars that are manually identified in the images (Garcia et al., 1997). After the images were projected on a linear-scale grid using an optical ray tracer where the refractive index was calculated from air densities taken from MSISE-00. Each pixel of the camera was traced from the camera to the NLC altitude (Baumgarten et al. 2009). Figure 2 shows image of the NLC picture shown in Figure 1 projected onto a latitude and longitude grid assuming an NLC average height of 83 km (e.g. Witt, 1962; Fiedler et al., 2009). These images were used to identify gravity-wave events and measure the wavelength, horizontal phase velocity, direction of propagation and relative intensity fluctuation of each event.

### **3. The estimation of wave parameters**

#### **3.1. Estimation of wavelength and phase**

The next step was the wave analysis where individual wave events in the NLC images were visually identified. Within a sequence of images, organized structures propagating in a uniform direction for at least 20 minutes were identified as gravity-wave events. Due to the short observational periods and challenging scattering conditions, a total of 34 such events were identified in this manner from the four summer observing seasons.

In order to infer the wave parameters, we have developed a robust method using a combination of FFT and a least-squares fitting of a sinusoidal function of the intensity data in order to quantify the

horizontal wavelength, phase speed and direction of propagation of the waves in the NLC images. This method is different from the 2-D FFT method used by Pautet et al. (2011), originally developed by Garcia et al. (1997), to analyse the gravity waves from the Stockholm NLC images. Although this fitting method is more labour intensive and more subjective than the Pautet et al. (2011) method, given the low contrast of these high latitude observations it was necessary to manually identify the wave parameters.

Since the images are mapped to an equally spaced latitude and longitude grid, the raw pixel values in the projected image are first converted into kilometre space. Once a wave structure has been visually identified in the NLC image, a line was drawn normal to the wave front. To ensure that the chosen line of sight was truly normal to the wave front, a series of profiles were extracted by slightly changing the angle of the line. The frequency (wavelength) of the wave pattern along each of these lines was determined using a Fourier transform technique. The line with the smallest wavelength is taken to be normal to the wave front (shown in figure 2 as an arrow) and is along the propagation direction of the wave. This line was then used for the analysis of the wave structure. In cases where there was more than one wavelength present, the largest wavelength was selected for analysis. In some cases, where the images are blurred or contaminated, the FFT of the difference image, i.e. the image formed by subtracting two adjacent images, provided the wavelength.

To determine the phase velocity of the wave, several consecutive images, i.e. time steps, of the same wave structure were analysed. First a bias, linear slope and a sinusoid at the fixed, minimum wavelength determined above were fit to the intensity variations along the propagation direction. The bias and linear slope were then removed from the wave structure, and an FFT was applied to the de-trended intensity variations to determine the wavelength and phase of the wave structure along the propagation direction. The same procedure was carried out for all consecutive images to observe the change of the phase of the largest wavelength. It should be noted that the wavelength was determined only from the first image and held constant in all consecutive pictures. This is because other waves can propagate into the analysis regions and become the largest component of the wave structure. However, for the correct calculation of the phase values for each time step and hence the phase speeds of the wave it is important that the same wave is observed in all consecutive pictures.

Figure 3 and 4 shows an example of the Hovmöller diagrams of the raw data and the extracted wave structure along the propagation direction for consecutive time steps.

### **3.2 Extracting the amplitudes**

In order to compare with gravity wave ray-tracing results, it is necessary to have an estimate of the relative amplitude of the waves present in the NLC. Particles can take hours to grow to visible sizes, but evaporation times approach seconds when temperatures are raised (Gadsden and Schröder, 1989). Thus, while the long term effect of short-period waves on NLC will be to reduce their visibility (Rapp et al, 2002), the bright and dark periodic structures in the NLC, with time scales of minutes, are primarily due to the density perturbations caused by the gravity wave rather than changes in the particle radius due to temperature effects. Thus, the relative amplitude of the waves was determined by the amplitude of the NLC intensity variations, determined above, divided by the average Mie scatter of the structured cloud.

Here the background that was fitted to the raw image above has two components, the Rayleigh scatter from the background atmosphere plus the Mie scatter from the clouds. Due to the limited spatial scales of the NLC, the images were filtered to remove high spatial frequencies in order to determine the Rayleigh scatter component. Tests were done on nights with no apparent NLC to ensure that the pure Rayleigh scatter in these images was not affected by the filtering process. Nights with NLC present were filtered, and the Rayleigh-scattered component was compared to background nights at similar solar angles to ensure that the Mie scattering from the clouds was removed. Dividing the raw NLC image by the filtered “Rayleigh” image resulted in a flat background modulated only by the NLC wave perturbations. Along the direction of propagation, the background fitted to this ratio image represents the ratio of the average Mie plus Rayleigh scatter to Rayleigh scatter. This may be combined with the background from the raw image to obtain the average Mie scatter in the display being analysed. In this way, the relative amplitude of the NLC Mie scatter could be obtained. Since the wave structures are the result of density enhancements associated with the gravity waves, the relative amplitude of the Mie scatter was taken to be directly proportional to the relative density fluctuation caused by the wave.

#### 4. Ray-tracing analysis

In order to examine the possible source regions for the gravity waves observed in our field of view, we used the Gravity Wave Regional or Global Ray Tracer (GROGRAT) model developed by Eckermann and Marks (1997). GROGRAT is a four-dimensional ray tracing algorithm that traces the evolution of a gravity wave's propagation and amplitude under the effect of background temperature and wind variations in the lower and middle atmosphere (Eckermann and Marks, 1995; 1997). Here, we launch a spectrum of gravity waves from an array of latitude and longitude points, and utilize GROGRAT to determine those waves that enter the FOV of the camera at Trondheim.

In this study, the spectrum of waves suggested by Eckermann (1992), which was obtained from their experimental studies, is used. This spectrum consists of waves with uniform amplitudes of  $0.3 \text{ m}\cdot\text{s}^{-1}$  and discrete wavelengths of 12.5, 25, 50, 100, 200 and 400 km. Each wavelength is launched with phase speeds of 10, 20, 30, and  $40 \text{ m}\cdot\text{s}^{-1}$  at each  $45^\circ$  of azimuth starting from the north. These waves are launched every  $5^\circ$  of latitude between  $60^\circ$  and  $80^\circ\text{N}$ , and every  $10^\circ$  of longitude between  $0^\circ$  and  $50^\circ\text{E}$ . The specific parameters entered into GROGRAT for each ray include an initial latitude, longitude, altitude, horizontal wave numbers and initial frequency. The background temperature and pressure fields used in GROGRAT were generated at 2 km altitude intervals from 0 to 80 km using the Mass Spectrometer-Incoherent Scatter Extended empirical model (MSISE-00) (Hedin, 1991) for the time of the display. Similarly, the wind fields were generated using the empirical Horizontal Wind Model HWM-93 (Hedin et al., 1996), for the time of the display. As the waves propagate upward to 80 km, the trajectories and spatial distributions of waves as a function of time is derived due to the interaction with these fields.

Source regions for gravity waves may lie near the tropopause (Fritts and Alexander, 2003) as in the case of convective activity or orographic lifting. However, they may be the result of secondary generation at higher altitudes by either wave breaking (Holton and Alexander, 1999; Vadas and Fritts, 2003) or as a result of the strong zonal wind shears in the mesosphere (Fritts, 2003). To test this, waves were launched from both tropopause heights, 5 km, as well as from 60 km at the same geographic grid points, and the relative amplitudes at NLC heights could be compared with those derived from the NLC image analysis to determine the most probable source altitude.

## 5. Results

The characteristic horizontal wave parameters such as wavelength, phase velocity, period, propagation direction and amplitude of the gravity waves were inferred from the NLC images, and a histogram of these wave parameters and the direction of propagation of the waves are shown in Figure 5 and 8, respectively. For comparison, histograms of the wave parameters from the ray-traced waves that reached the NLC altitude from the source region of 5 km and 60 km are shown in Figure 6 and Figure 7, respectively.

The histogram of wave structures derived from the NLC images (Figure 5a) shows that there is a strong preference for structures with scales less than 35 km, with an average wavelength of 24 km. However, the characteristic horizontal wavelengths for the ray-traced waves launched from both the 5 km and 60 km altitudes show that while these short wavelength waves do propagate to NLC heights, both distributions are similar and increase with wavelength. Thus the ray tracing shows that most of the waves reaching the mesosphere from either tropospheric or stratospheric sources have wavelengths greater than 40 km. This discrepancy is likely due to the spatial constraints of the camera. Due to the size of the field of view ( $53^\circ \times 41^\circ$ ) of the NLC camera, the maximum observable horizontal wavelength is less than 100 km (Pautet et al., 2011). Thus, very long waves will not be observable as a modulation of the intensity within a single image and will not be identified as waves. Similarly, the high levels of Rayleigh scattering present in our high-latitude images further restrict our usable field of view and will bias us towards shorter period waves.

The observed phase speeds of the waves observed in the NLC (Figure 5b) and those resulting from the wave tracing (Figures 6b and 7b) all average around 31 m/s. However, whereas the ray-traced waves from 5 km and 60 km both show a peak in the distribution near the average value, the waves observed in the NLC have a broader range of phase speeds, with most waves having a phase speed of between 10 and 20 m/s. Conversely, most of the waves detected in the NLC and those traced upward from both 5 km and 60 km (figures 5c, 6c and 7c) have observed periods below 20 minutes. However, the NLC waves have nearly and equal percentage of waves with observed periods near 30-40 minutes, resulting in an average observed period of 24 minutes. In contrast, the waves traced upward from 5 km and 60 km predominantly occur with observed periods less than 5 minutes, with a steadily

decreasing number of waves at longer observed periods, and few waves occurring with periods longer than 20 minutes.

Perhaps the most prominent difference between the waves propagating up from the tropopause and those originating in the stratosphere are their relative amplitudes at NLC altitudes, shown in Figures 6d and 7d, respectively. We see in Figure 6d that the waves originating near the tropopause attain relative amplitudes ranging between  $\sim 1$  and 8%, whereas those initiated near 60 km, shown in Figure 7d, only grow to between  $\sim 0.1$  and 0.3%. The relative wave amplitudes observed in the NLC, shown in figure 5d, range from  $\sim 1$  to 10%. Thus, the amplitude of the majority of waves observed in the NLC Mie scatter would be more consistent with sources near the tropopause. However, this is not to say that waves generated in the stratosphere do not perturb NLC. Rather, there is likely an observational bias to the large amplitude waves from lower altitudes that present the largest contrast and are easiest to detect.

The propagation directions of the ray-traced waves, shown in Figure 8b and 8c, indicate that the waves originating from near the tropopause or from 60 km both have similar eastward directions when they reach NLC altitudes. While the waves observed in the NLC also show a tendency for eastward propagation, Figure 8a shows that they tend to be directed more towards the north. Additionally a large percentage of the NLC waves are observed moving in a WSW direction (240-270° azimuth) and towards the ENE (60-90° azimuth) that the ray tracing has indicated are blocked. A null hypothesis t-test was applied on the characteristics of these waves propagating in in these two “blocked” directions to determine whether their wave characteristics differ from the rest of the population. The results, shown in Table 2, indicate that the ENE waves are not significantly different from the general population, but that the WSW waves represent a unique population of waves with shorter wavelengths ( $\lambda_{\text{avg}} = 14.4$  km compared to 24 km) and higher phase speeds ( $c_{\text{avg}} = 42.4$  m/s compared to 31 m/s). Fritts et al. (2002) have shown that these fast, short period waves are associated with local instabilities generated during wave breaking. These instabilities tend to move along the wave front and transverse to the general wave propagation direction, similar to what is observed here.

In order to examine possible source regions for the gravity waves observed in the NLC, the grid points from which the waves were launched at 5 km and 60 km are shown on a map in figures 9a and 9b, respectively. The size of the symbol indicates the percentage of waves originating from a particular grid point that enter the field of view of the NLC imager at Trondheim. The geographical distribution of the wave sources at the two altitudes depict that the coastal regions of Norway at the latitude of 70°N are the primary source regions of gravity waves propagating upward from 5 km. The waves propagating upward from 60 km represent a broader source region that extends eastward and southward of the camera field of view, but, as indicated above, these would cause smaller perturbations in the NLC.

## 6. Discussion

We can compare these climatological results over Norway with the previous work of Pautet et al 2011, which used imager data from Sweden from 2004 to 2007 that extended to the southern limit of our observations. The comparison of the average horizontal wavelength of the waves shows reasonable agreement, with a mean value of 24 km and 25 km over ~69°N and ~62°N, respectively. Thus, the wave-like perturbations derived from the NLC images in the summer mesosphere are similar in scale from 60° to 74°N. In addition, they are similar to mesospheric short-period GWs observed in the air-glow emissions at middle (Taylor et al, 1998), polar (Nielsen et al., 2006) and equatorial (Nakamura et al., 2003) latitudes, where peak horizontal wavelengths around 25-30 km are found.

The average observed phase speed for the Trondheim data was found to be 31 m/s, which also compares favourably with the average value of 27 m/s found by Pautet et al. (2011) for the summertime data taken from Stockholm. Similarly, there is no significant difference in the average observed periods of the two data sets: 24 min at ~69°N and 22 min at ~62°N. However, these observed phase speeds measured using NLC data during the high latitude summer are smaller than other previous long-term studies of gravity waves observed at slightly higher altitude in the airglow emission. For example, Taylor et al., (1997) and Nakamura et al. (2003) found an average value of approximately 48 m/s at low latitudes (2°S), and Hecht et al., (2001) found a mean value of 50 m/s at middle latitudes (40°N). Similarly, the high latitude measurements in the southern hemisphere at

Halley (76°S) found a mean value of 48 m/s (Nielsen et al., 2009) during winter. Correspondingly, the observed periods found in these studies are typically on the order of 8-10 minutes. However, Ejiri et al. (2003) found an average value of 35 m/s at mid latitude (40°N), similar to this work. This wide range of values could be due to different GW sources, for example orographic versus frontal generation, where the observed phase speeds would be Doppler shifted due to speed of the source relative to the observer.

The directions of propagation of the waves observed in the NLC show that the majority of the waves in Norway are propagating towards the north and northeast at azimuths between 0° and 30°, but there is a separate population of small-scale fast waves propagating towards the southwest between 240° and 270° of azimuth. Similarly, Pautet et al. (2011) found that 60% of the waves in Sweden propagate towards the north or the northeast directions, but did not observe the waves moving towards the southwest. This matches the propagation directions found for the waves launched from 5 km and 60 km, where the SW direction is blocked by the wind field. Given this blocking, and the fact that the waves we observe moving towards the SW have significantly shorter wavelengths and higher phase speeds than those propagating northward or north-eastward, indicate that these are formed as a result of local, transverse instabilities accompanying wave breaking (Fritts et al. 2002). The shorter observing times available each night at Trondheim as compared to Stockholm, as well as the more restricted field of view resulting from the higher levels of Rayleigh scatter means that these fast moving, short scale instabilities were more likely to have been picked for analysis.

## **7. Conclusions**

The climatology of summertime gravity-waves detected in NLC between 64° and 74°N is similar to that observed between 60° and 64°N by Pautet et al. (2011). While the average horizontal wavelengths observed in these two studies agree with previous results from airglow imaging, the observed phase speeds are much slower, and the observed periods correspondingly longer, than those observed in the airglow at lower latitudes and during high-latitude winter. This could be due to differences in the gravity-wave sources, or an observational bias brought on by the more restrictive fields of view available to the NLC cameras when compared to the nearly all-sky airglow observations. The gravity-waves observed in the NLC north of 64°N continue to propagate towards the north or

northeast as they have been observed to do south of 64°N. However, the unique population of fast, short wavelength waves propagating towards the SW is consistent with transverse instabilities generated *in-situ* by breaking gravity waves. Finally, comparison of the relative amplitude of the waves observed in the NLC Mie-scatter with ray-tracing results show that waves propagating from the tropopause, rather than those resulting from secondary generation in the stratosphere or mesosphere, are more likely to be the sources of the prominent wave structures observed in the NLC. The geographic distribution of the waves generated near the tropopause that can be ray traced into the observational field of view identify the coastal region of Norway along the latitude of 70°N as the primary source region. As this is the region where many of the polar low pressure systems make landfall, interaction of the frontal systems with the coastal mountainous terrain is a likely generation mechanism for the prominent wave structures observed in the NLC near the mesopause.

*Acknowledgements.* We would like to thank Professor F. -J. Lübken, director of IAP, for the opportunity of carrying part of the present work at IAP. This study is supported by Research Council of Norway projects “Gravity-wave sources and scales in the Polar Regions and their effect on Polar Mesospheric Clouds”, and the “Birkeland Centre of Excellence for Space Science”.

## **REFERENCES**

Baumgarten,G., Fiedler, J., Fricke, K. H., Gerding, M., Hervig, M., Hoffmann, P., Müller, N., Pautet, P.-D., Rapp, M., Robert, C., Rusch, D., von Savigny, C., and Singer, W., 2009: The noctilucent cloud (NLC) display during the ECOMA/MASS sounding rocket flights on 3 August 2007: morphology on global to local scales, *Ann. Geophys.*, 27, 953–965.

Baumgarten, G., Gerding, M., Kaifler, B., and Müller, N., 2009: A trans-European network of cameras for observation of noctilucent clouds from 37°N to 69°N, *Proceedings 19<sup>th</sup> ESA Symposium on European Rocket and Ballon Programmes and Related Research*, Bad Reichenhall, Germany, 7-11 June 2009

Chandran, A., Rusch, D.W., Palo, S.E., Thomas, G.E., Taylor, M.J., 2009: Gravity wave observations in the summertime polar mesosphere from the cloud imaging and particle size (CIPS) experiment on the AIM spacecraft. *J. Atmos. Sol. Terr. Phys.* 71 (3–4), 285–288.

Chandran, A., Rusch, D.W., Merkel, A.W., Palo, S.E., Thomas, G.E., Taylor, M.J., Bailey, S.M., Russell III, J.M., 2010. Polar Mesospheric Cloud structures observed from the CIPS experiment on the AIM

spacecraft: atmospheric gravity waves as drivers for longitudinal variability in PMC occurrence. *J. Geophys. Res.* doi:10.1029/2009JD013185.

Eckermann, S. D., and Marks, C. J., 1997: GROGRAT: A new model of the global propagation and dissipation of G.E., 1993. Wave atmospheric gravity waves, *Adv. Space Res.*, 20(6), 1253-1256.

Ejiri, M. K., Shiokawa, K., Ogawa, T., Igarashi, K., Nakamura, T., Tsuda, T., 2003: Statistical study of short-period gravity waves in OH and OI nightglow images at two separated sites. *J. Geophys. Res.*, 108 (D21), 4679.

Espy, P. J. and Stegman, J., 2002: Trends and variability of mesospheric temperature at high-latitudes, *Phys. Chem. Earth*, 27, 543–553, 2002

Espy, P. J., Jones, G. O. L., Swenson, G. R., Tang, J., and Taylor, M. J., 2004: Seasonal variations of the gravity-wave momentum flux in the Antarctic mesosphere and lower thermosphere, *J. Geophys. Res.*, 109, D23109, doi: 10.1029/2003JD004446, 2004.

Espy, P. J., Hibbins, R. E., Swenson, G. R., Tang, J., Taylor, M. J., Riggin, D. M., and Fritts, D. C., 2006: Regional variations of mesospheric gravity-wave momentum flux over Antarctica, *Annales Geophys.*, 24, 81-88.

Fiedler, J., Baumgarten, G., and Lübken, F. -J., 2009: NLC observations during one solar cycle above ALOMAR, *J. Atmos. Solar-Terr. Phys.*, 71, 424

Fritts, D. C., Isler, J. R., Thomas, G. E., Andreassen, Ø, 1993: Wave breaking signatures in noctilucent clouds. *Geophys. Res. Lett.* 20, 2039

Fritts, D. C. and Luo, Z. G., 1995: Dynamical and radiative forcing of the summer mesopause circulation and thermal structure. 1. Mean solstice conditions, *J. Geophys. Res.*, 100, 3119–3128.

Fritts, D.C., and Alexander, M. J., 2003: Gravity wave dynamics and effects in the middle atmosphere, *Rev. Geophys.*, 41, 1, doi: 10.1029/2001RG000106.

Gadsden, M., and Schröder, M., 1989: *Noctilucent Clouds*, Springer-Verlag, pp165.

Garcia, R.G., Solomon, S., 1985: The effect of breaking gravity waves on the dynamics and chemical composition of the mesosphere and lower thermo- sphere. *J. Geophys. Res.*, 90, 3850–3868.

Garcia, R. R., and Boville, B. A., 1994: “Downward control” of the mean meridional circulation and temperature distribution of the polar winter stratosphere, *J. Atmos. Sci.*, 51, 2238– 2245.

Garcia, F. J., Taylor, M. J., Kelley, M. C., 1997: Two-dimensional spectral analysis of mesospheric airglow image data. *Appl. Opt.* 36 (29), 7374–7385.

- Geller, M. A., Dynamics of the middle atmosphere, *Space Sci. Rev.*, 34, 359-375, 1983
- Hamilton, K., 1995: Comprehensive modeling of the middle atmosphere climate: Some recent results, *Clim. Dyn.*, 11, 223–241.
- Hamilton, K., 1996: Comprehensive meteorological modeling of the middle atmosphere: A tutorial review, *J. Atmos. Solar-Terr. Phys.*, 58, 1591–1627
- Haurwitz, B., 1961: Wave formations in noctilucent clouds. *Planet. Space Sci.* 5, 92–98.
- Hecht, J. H., Walterscheid, R. L., Hickey, M. P., Franke, S. J., 2001: Climatology and modeling of quasi-monochromatic atmospheric gravity waves observed over Urbana Illinois. *J. Geophys. Res.*, 106 (D6), 5181–5195.
- Hedin, A. E., 1991: Extension of the MSIS thermospheric model into the middle and lower atmosphere. *Journal of Geophysical Research* 96 (A2), 1159–1172.
- Hedin, A. E., Fleming, E. L., Manson, A. H., Schmidlin, F. J., Avery, S. K., Clark, R. R., Franke, S. J., Fraser, G. J., Tsuda, T., Vial, F., Vincent, R. A., 1996: Empirical wind model for the upper, middle and lower atmosphere, *J. Atmos. Solar-Terr. Phys.*, 58 (13), 1421–1447.
- Hines, C.O., 1960: Internal atmospheric gravity waves. *Can. J. Phys.* 38, 1441.
- Holton, J. R., 1982: The role of gravity wave induced drag and diffusion in the momentum budget of the mesosphere, *J. Atmos. Sci.*, 39, 791-799.
- Holton, J. R., 1983: The influence of gravity wave breaking on the general circulation of the middle atmosphere. *J. Atmos. Sci.*, 40, 2497–2507.
- Holton, J. R., and M. J. Alexander (1999), Gravity waves in the mesosphere generated by tropospheric convection, *Tellus, Ser. B*, 51, 45–58.
- Horinouchi, T., T. Nakamura, and J. Kosaka, 2002: Convectively generated mesoscale gravity waves simulated throughout the middle atmosphere, *Geophys. Res. Lett.*, 29(21), 2007, doi: 10.1029/2002GL016069.
- Lindzen, R. S., 1981: Turbulence and stress owing to gravity wave and tidal breakdown, *J. Geophys. Res.*, 86, 9707-9714.
- Lübken, F.-J., Jarvis, M. J., and Jones, G. O. L., 1999: First in situ temperature measurements at the Antarctic summer mesopause. *Geophys. Res. Lett.*, 26, 3581–3584.

- Luo, Z. G., Fritts, D. C., Portmann, R. W., and Thomas, G. E., 1995: Dynamical and radiative forcing of the summer mesopause circulation and thermal structure. 2. Seasonal-variations, *J. Geophys. Res.*, 100, 3129–3137.
- Marks, C. J., and Eckermann, S. D., 1995: A three-dimensional non-hydrostatic ray-tracing model for gravity waves: Formulation and preliminary results for the middle atmosphere. *J. Atmos. Sci.*, 52, 1959–1984.
- Nakamura, T. A., Tsuda, T., Admiranto, T., Achmad, A. G., Suranto, E., 2003: Mesospheric gravity waves over a tropical convective region observed by OH airglow imaging in Indonesia. *Geophys. Res. Lett.*, 30(17), 1882.
- Nielsen, K., Taylor, M. J., Pautet, P-D., Fritts, D. C., Mitchell, N., Beldon, C., Williams, B. P., Singer, W., Schmidlin, F. J., Goldberg, R. A., 2006: Propagation of short-period gravity waves at high-latitudes during the MaCWAVE winter campaign. *Annales Geophys.*, 24:1227–1243, SRef\_ID:1432-0576/ag/2006- 24-1227.
- Nielsen, K., Taylor, M. J., Hibbins, R. E., Jarvis, M. J., 2009: Climatology of short-period mesospheric gravity waves over Halley, Antarctica (76°S, 27°W). *J. Atmos. Solar-Terr. Phys.*, 71: 991–1000.
- Pautet, D. and Moreels, G., 2002: Ground-based satellite-type images of the upper-atmosphere emissive layer, *Appl. Optics*, 41, 823–831, doi:10.1364/AO.41.000823.
- Pautet P-D, Taylor M. J., Liu A. Z., and Swenson G. R., 2005: Climatology of short-period gravity waves observed over northern Australia during the Darwin area wave experiment (DAWEX) and their dominant source regions. *J Geophys Res* 110:D03S90.
- Pautet P-D, Stegman J, Wrasse C. M., Takahashi H., Taylor M. J., 2011: Analysis of gravity waves structures visible in noctilucent cloud images, global perspectives on the aeronomy of the summer mesopause region, 8th international workshop on layered phenomena in the mesopause region. *J. Atmos. Solar-Terr Phys.*, 73, 2082-2090, doi:10.1016/j.jastp.2010.06.001.
- Rapp, M., Lübken, F.-J., Müllemann, A., Thomas, G., Jensen, E., 2002: Smallscale temperature variations in the vicinity of NLC: experimental and model results. *J. Geophys. Res.*107 (D19), 4392.doi:10.1029/2001JD001241
- Rapp, M., F. –J Lübken, 2003: On the nature of PMSE: Electron diffusion in the vicinity of charged particles revisited, *J. Geophys. Res.* 108, (10.1029/2002JD002857, eid: 8437).
- Rapp, M. and Thomas, G. E., 2006: Modeling the microphysics of mesospheric ice particles – Assessment of current capabilities and basic sensitivities, *J. Atmos. Solar-Terr. Phys.*, 68, 715–744.

Rind, D., Suozzo, R., Balachandran, N. K., Lacis, A., and Russell, G., 1988: The GISS global climate-middle atmosphere model: Part I: Model structure and climatology, *J. Atmos. Sci.*, 45, 329– 370.

Schmidlin, F. J., 1992: First observation of mesopause temperatures lower than 100 K, *Geophys. Res. Lett.*, 19, 1643

Stroud, W. G., W. Nordberg, W. R. Bandeen, F. L. Bartman, and P. Titus, 1959: Rocket-grenade observation of atmospheric heating in the Arctic, *J. Geophys. Res.*, 64, 1342

Taylor, M. J., Henriksen, K., 1989: Gravity wave studies at polar latitudes. In: Sandholt, P.E., Egeland, A. (Eds.), *Electromagnetic Coupling in the Polar Clefts and Caps*. Kluwer Academic Publications, Dordrecht, the Netherlands, pp. 421–434.

Taylor, M. J., Pendleton Jr., W. R., Clark, S., Takahashi, H., Gobbi, D., Goldberg, R. A., 1997: Image measurements of short-period gravity waves at equatorial latitudes. *J. Geophys. Res.* 102 (D22), 26283–26299.

Taylor, M. J., Seo, S. H., Nakamura, T., Tsuda, T., Fukunishi, H., Takahashi, Y., 1998: Long base-line measurements of short-period mesospheric gravity waves during the SEEK campaign. *Geophys. Res. Lett.*, 25 (11), 1797–1800.

Taylor, M. J., Pautet, P. -D., Zhao, Y., Randall, C. E., Lumpe, J., Bailey, S. M., Carstens, J., Nielsen, K., Russell III, James M., and Stegman, J., 2011: High-Latitude GravityWaveMeasurements in Noctilucent Clouds and Polar Mesospheric Clouds, in *Aeronomy of the Earth's Atmosphere and Ionosphere*, in IAGA Special Sopron Book Series Volume 2, pp 93-105 , Abdu, Mangalathayil Ali; Pancheva, Dora; Bhattacharyya, Archana (Eds.) 2011, XXI, 480p, Springer.

Thomas, G. E., 1991: Mesospheric clouds and the physics of the mesopause region. *Reviews of Geophysics* 29, 553–575.

Thomas, G. E., Olivero, J. J., Jensen, E. J., Schroder, W., Toon, O. B., 1989b: Relation between increasing methane and the presence of ice at the mesopause. *Nature* 338, 490–492

Vadas, S. L., D. C. Fritts, and M. J. Alexander (2003), Mechanisms for the generation of secondary waves in wave breaking regions, *J. Atmos. Sci.*, 60, 194– 214.

Vincent, R. A., 1984: Gravity-wave motions in the mesosphere, *J. Atmos. Terr. Phys.*, 46, 119– 128.

Witt G (1962): Height, structure and displacements of noctilucent clouds. *Tellus* 14:1–18

Table 2: Result of the t-test

T-test between the waves that propagate East (60-90) and the rest of the waves excluding SW wave							
	Average values for East wave	Std for East wave	Avg. for the other	Std for the other	tstat	df	p
Wavelength	23.72	4.99	28.73	19.35	-1.0265	22.75	68.45%
Phase speed	23.04	13.66	28.29	18.51	-0.7489	11.42	53.09%
Period	21.68	11.83	25.03	23.08	-0.4670	17.3	17.3%
T-test between the waves that propagate SW and the rest of the waves							
	Average values for SW wave	Std for SW wave	Avg for the other	Std for the other	tstat	df	p
Wavelength	14.42	5.64	27.53	17.05	-3.3667	31.95	99.8%
Phase speed	42.4	27.67	27.03	17.35	1.5599	10.357	85.12%
Period	23.94	51.94	24.23	20.76	-0.0159	8.9363	1.24%
T-test between the waves that propagate SW and Eastward (60-90)							
	Average values for SW wave	Std for SW wave	Avg for the East	Std for the East	tstat	df	p
Wavelength	14.42	5.64	23.72	4.99	-3.3516	11.779	99.41%
Phase speed	42.4	27.67	23.04	13.66	1.7964	12.289	90.03
Period	23.94	51.94	21.68	11.83	0.126	9.204	9.73



Figure 1: Noctilucent cloud observed by camera from Trondheim on 30 July 2008 at 23:00 UT

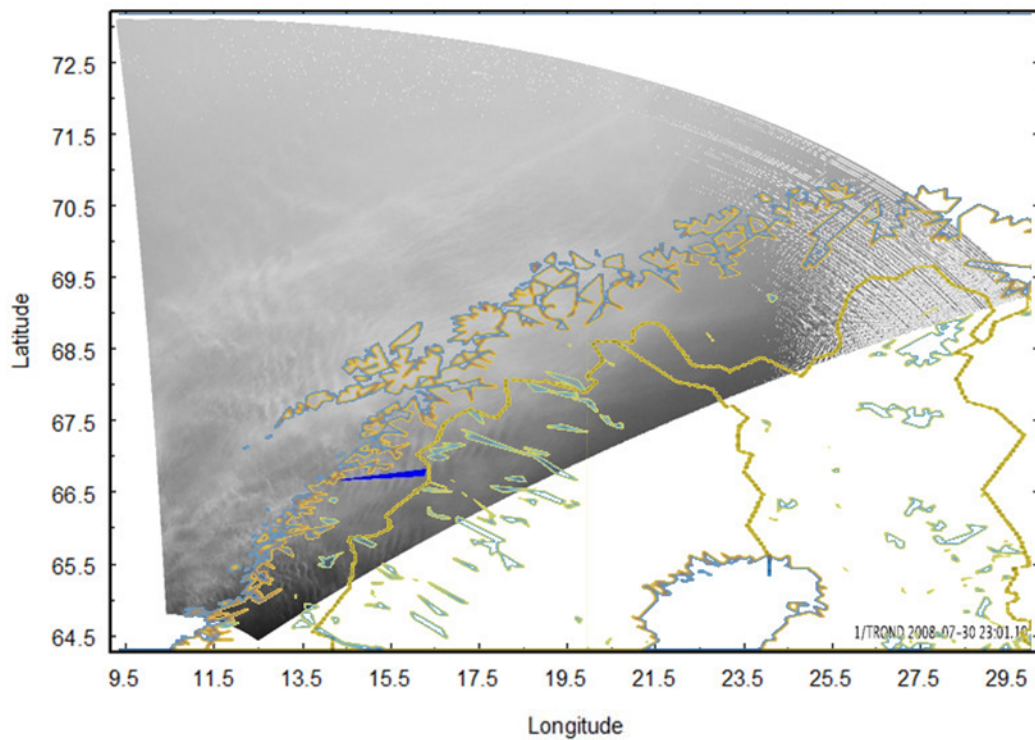


Figure 2: Image of the noctilucent cloud observed by camera from Trondheim on 30 July 2008 at 23:01 UT projected onto latitude and longitude (given in degrees).

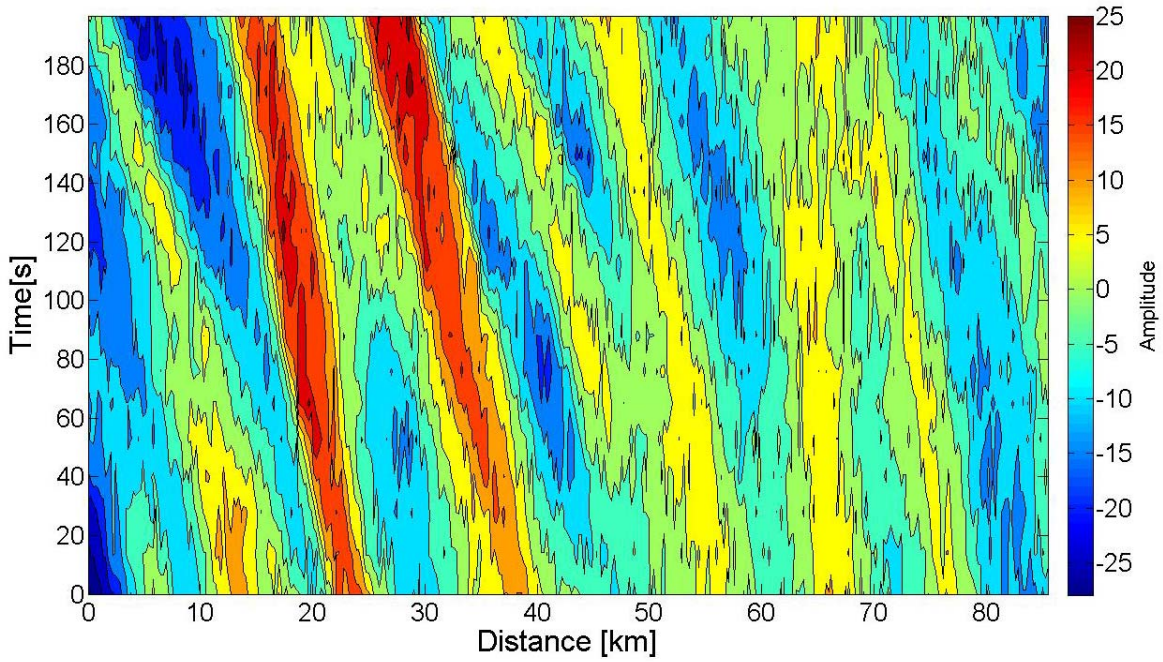


Figure 3: Hovmöller diagrams of the raw data along the propagation direction for consecutive time steps

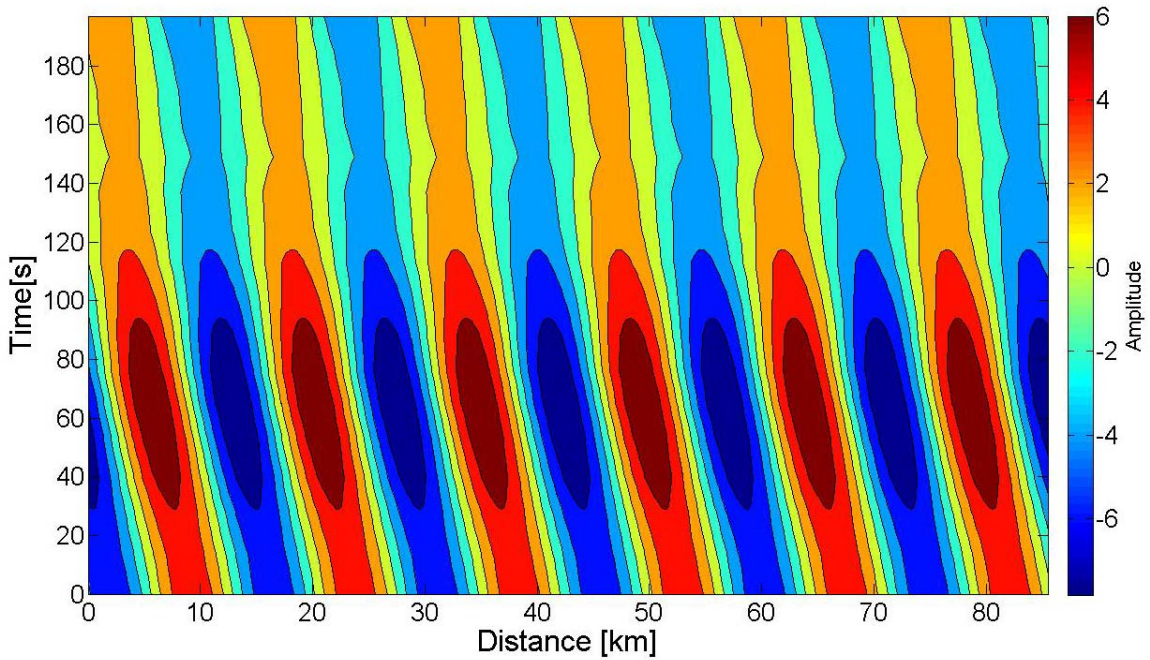


Figure 4: Hovmöller diagrams of the reconstructed wave structure along the propagation direction for consecutive time steps

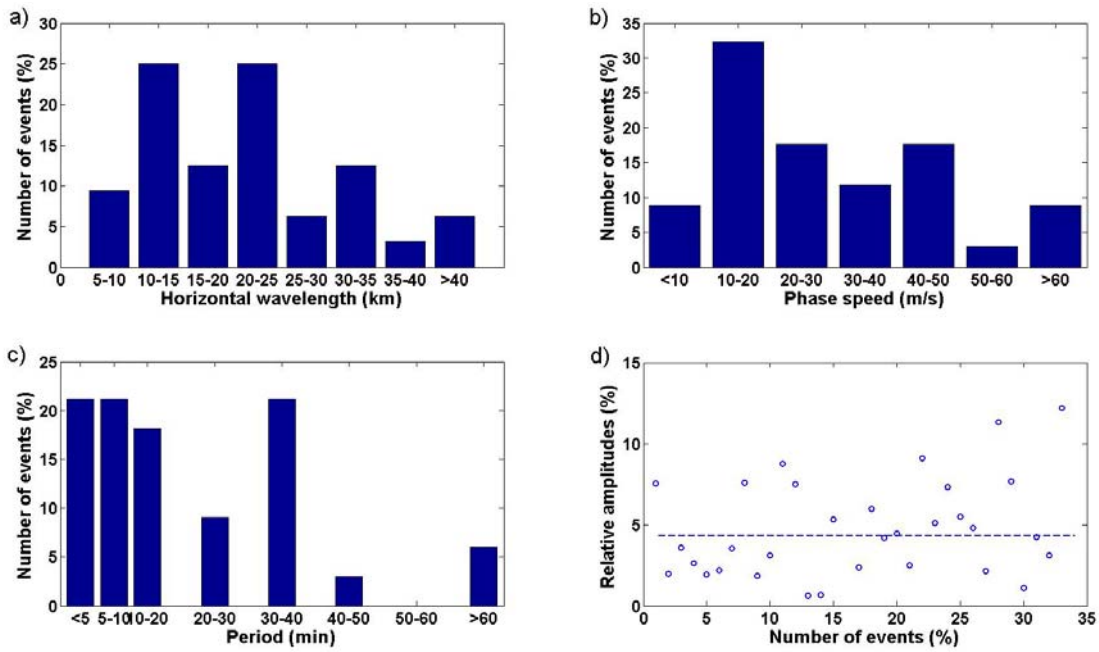


Figure 5: Histogram of the a) Horizontal wavelength, b) Phase speed, c) Period, and d) Relative amplitudes for the 34 waves observed in NLC using the camera in TRD

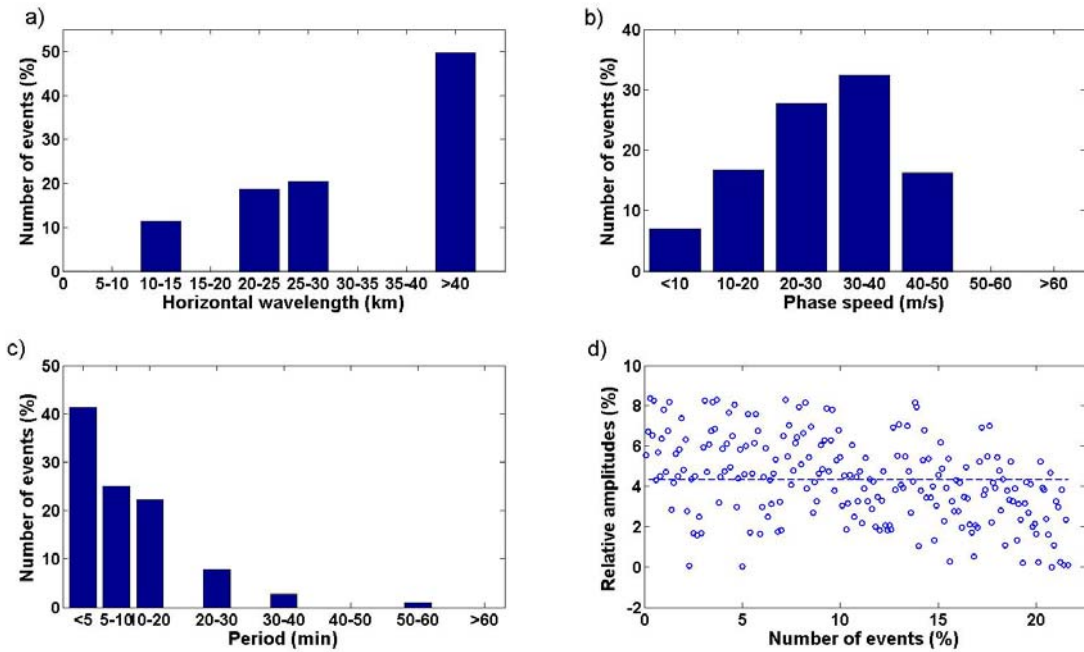


Figure 6: Histograms of the a) Horizontal wavelength, b) Phase speed, c) Period, and d) Relative amplitude for the gravity waves traced from 5 km to 80 km

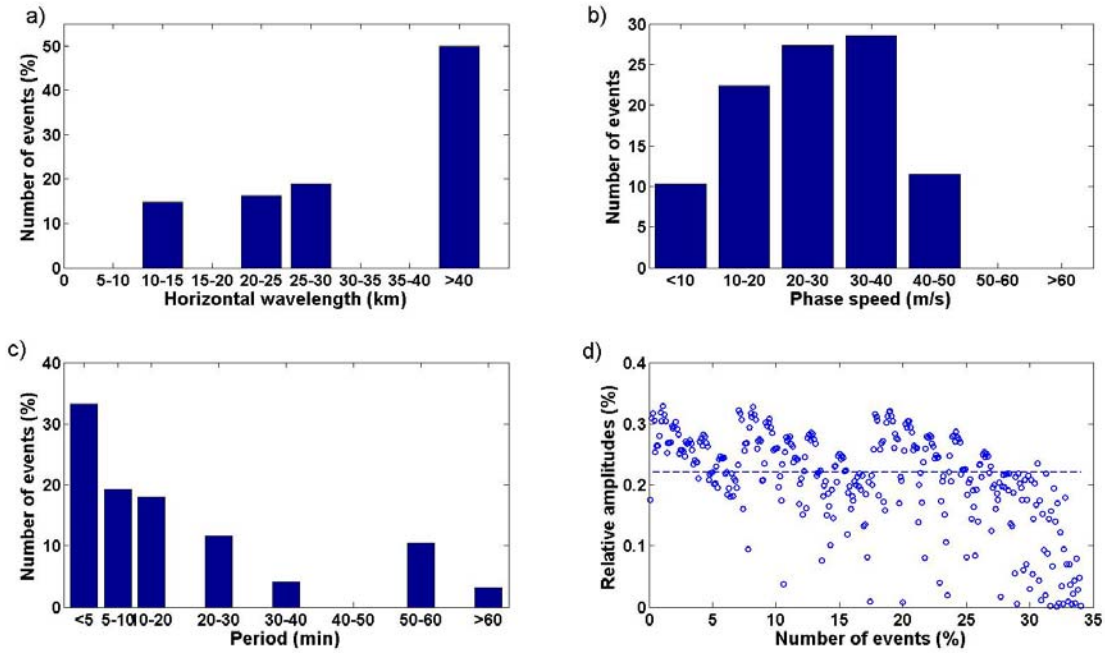


Figure 7: Histograms of the a) Horizontal wavelength, b) Phase speed, c) Period, and d) Relative amplitude for the gravity waves traced from 60 km to 80 km

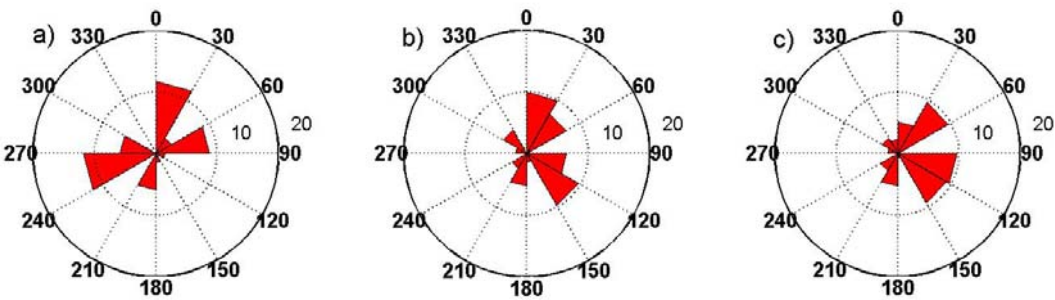


Figure 8: Direction of propagation of gravity waves, a) for the 34 waves observed in NLC using the camera in TRD, b) traced from 5km to 80 km, and c) traced from 60 km to 80 km.

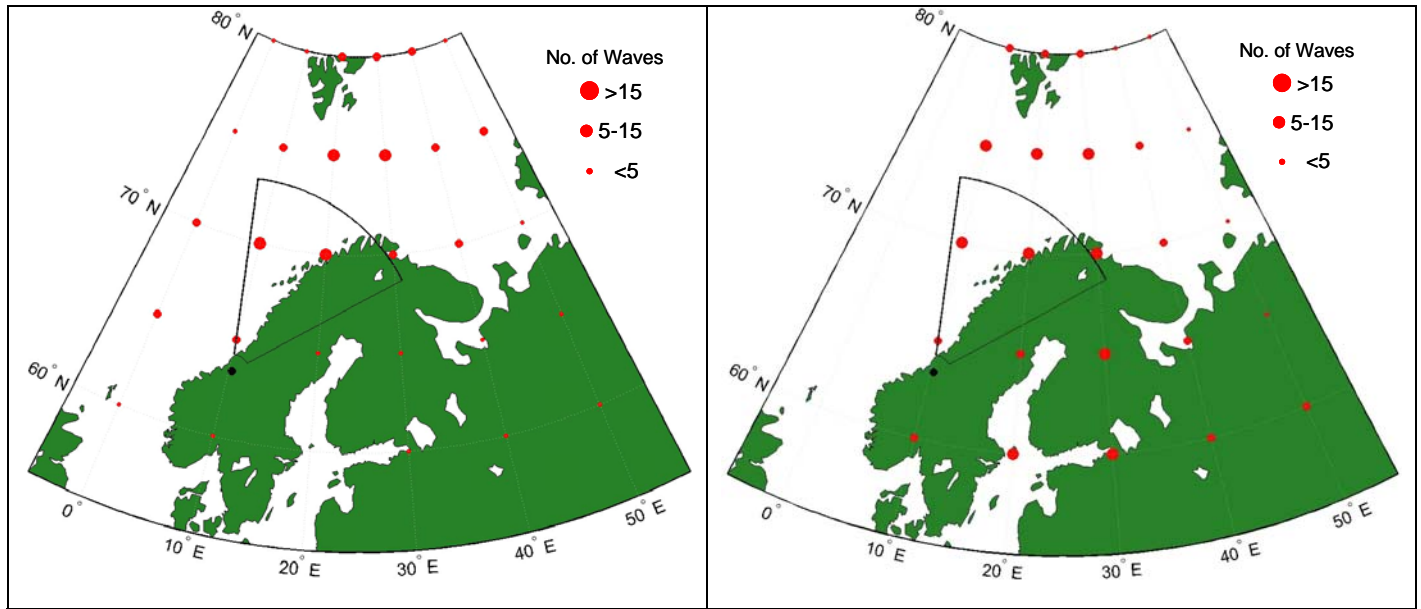


Figure 9: Geographic source regions for waves appearing in the FOV of the camera at NLC altitudes. The left panel shows the starting location of waves that have propagated upward from 5 km and entered the FOV. The right-panel shows the location of waves originating at 60 km that enter the FOV. For the grid points left blank there are no waves that enter the FOV of camera at NLC altitudes.

## **Appendix 1**

B. U. E. Brändström, C. -F. Enell, O. Widell, T. Hansson, D. Whiter, S. Mäkinen, D. Mikhaylova, K. Axelsson, F. Sigernes, N. Gulbrandsen, N. M. Schlatter, A. G. Gjendem, L. Cai, J. P. Reistad, M. Daae, **T. Dejene Demissie**, Y. L. Andalsvik, O. Roberts, S. Poluyanov, and S. Chernouss, 2012: **Results from the intercalibration of optical low-light calibration sources 2011.**

Geosci. Instrum. Method. Data Syst., 1, 91-107, 2011





## Results from the intercalibration of optical low light calibration sources 2011

B. U. E. Brändström<sup>1</sup>, C.-F. Enell<sup>2</sup>, O. Widell<sup>3</sup>, T. Hansson<sup>3</sup>, D. Whiter<sup>4</sup>, S. Mäkinen<sup>4</sup>, D. Mikhaylova<sup>1</sup>, K. Axelsson<sup>1</sup>, F. Sigernes<sup>5</sup>, N. Gulbrandsen<sup>6</sup>, N. M. Schlatter<sup>7</sup>, A. G. Gjendem<sup>8</sup>, L. Cai<sup>9</sup>, J. P. Reistad<sup>10</sup>, M. Daae<sup>8</sup>, T. D. Demissie<sup>8</sup>, Y. L. Andalsvik<sup>11</sup>, O. Roberts<sup>12</sup>, S. Poluyanov<sup>13</sup>, and S. Chernouss<sup>14</sup>

<sup>1</sup>Swedish Institute of Space Physics, Kiruna, Sweden

<sup>2</sup>Sodankylä Geophysical Observatory, University of Oulu, Sodankylä, Finland

<sup>3</sup>SSC, ESRANGE, Kiruna, Sweden

<sup>4</sup>Finnish Meteorological Institute, Helsinki, Finland

<sup>5</sup>The Kjell Henriksen Observatory, UNIS, Longyearbyen, Norway

<sup>6</sup>University of Tromsø, Tromsø, Norway

<sup>7</sup>School of Electrical Engineering, Royal Institute of Technology, Stockholm, Sweden

<sup>8</sup>Norwegian University of Science and Technology, Trondheim, Norway

<sup>9</sup>Department of Physics, University of Oulu, Oulu, Finland

<sup>10</sup>University of Bergen, Bergen, Norway

<sup>11</sup>Department of Physics, University of Oslo, Oslo, Norway

<sup>12</sup>Aberystwyth University, Aberystwyth, UK

<sup>13</sup>Polar Geophysical Institute, Murmansk, Russia

<sup>14</sup>Polar Geophysical Institute, Apatity, Russia

Correspondence to: B. U. E. Brändström (urban.brandstrom@irf.se)

Received: 5 December 2011 – Published in Geosci. Instrum. Method. Data Syst. Discuss.: 21 December 2011

Revised: 30 March 2012 – Accepted: 11 April 2012 – Published: 3 May 2012

**Abstract.** Following the 38th Annual European Meeting on Atmospheric Studies by Optical Methods in Siuntio in Finland, an intercalibration workshop for optical low light calibration sources was held in Sodankylä, Finland. The main purpose of this workshop was to provide a comparable scale for absolute measurements of aurora and airglow. All sources brought to the intercalibration workshop were compared to the Fritz Peak reference source using the Lindau Calibration Photometer built by Wilhelm Barke and Hans Lauche in 1984. The results were compared to several earlier intercalibration workshops. It was found that most sources were fairly stable over time, with errors in the range of 5–25%. To further validate the results, two sources were also intercalibrated at UNIS, Longyearbyen, Svalbard. Preliminary analysis indicates agreement with the intercalibration in Sodankylä within about 15–25%.

### 1 Introduction

Following the first absolute measurement of night airglow by Rayleigh (1930), accurate absolute measurements of airglow and aurora have become increasingly important (see, for example, Trondsen, 1998; Syrjäsoo, 2001; Brändström, 2003; Gustavsson et al., 2006; Dahlgren et al., 2011 and references therein). Such absolute measurements are traditionally expressed in rayleighs, as proposed by Hunten et al. (1956). Further discussions about the definition of the rayleigh unit appear in Chamberlain (1995, App. II) and Baker (1974). In SI units the rayleigh is defined as follows (Baker and Romick, 1976):

$$1 \text{ rayleigh} \equiv 1 \text{ R} \triangleq 10^{10} \frac{\text{photons}}{\text{s m}^2 \text{ column}} \quad (1)$$

The word column is often inserted in the units above and denotes the concept of an emission rate from a column of unspecified length along the line of sight (Hunten et al., 1956).

The apparent spectral radiant sterance (spectral radiance),  $L_\gamma(\lambda)$ , can be obtained from the spectral column emission rate,  $I(\lambda)$ , (in  $\text{R}/\text{\AA}$ ) according to Baker and Romick (1976):

$$L_\gamma(\lambda) = \frac{10^{10} I(\lambda)}{4\pi} \frac{\text{photons}}{\text{s m}^2 \text{ sr } \text{\AA}}. \quad (2)$$

Integrating the spectral quantities  $L_\gamma(\lambda)$  and  $I(\lambda)$  over wavelength yields the, maybe more familiar, quantities radiance and column emission rate. In this work the rayleigh and the ångström ( $1 \text{\AA} = 10^{-10} \text{ m}$ ) will be used to preserve continuity with earlier intercalibration results, which expressed spectral column emission rate in  $\text{R}/\text{\AA}$ .

After removing the instrument signature (bias, dark current, flat field, bad pixels, etc.), optical instruments are usually absolute calibrated by exposing the instrument to a calibration light source with a known spectral radiant sterance corresponding to a certain column emission rate (see, for example, Trondsen, 1998; Mäkinen, 2001; Brändström, 2003, and references therein). Instead of using calibration light sources, some instruments are calibrated by using known spectra of stars (for example Dahlgren et al., 2011).

This work reports the results of comparisons of calibration light sources during 2011. This is part of a long-term international effort to place aurora and airglow measurements taken at various locations around the world on a common calibration (and hence intensity) standard (Torr and Espy, 1981). In addition, a brief description of the intercalibration method in effect since 1985 is provided.

Following initial efforts in the 1960s by Michael Gadsden (Torr, 1983) and by Torr et al. (1976, 1977), regular intercalibration workshops have been organised (see Table 1 and references therein). After the intercalibration workshop in Katlenburg-Lindau in 1983, Lauche and Barke (1986) constructed the Lindau Calibration Photometer for comparison of low brightness sources (Fig. 1). This was done in order to support the work by M. Torr in the European sector. Yet, calibration sources from other countries have participated in some workshops over the years. As seen in Table 1, some intercalibration workshops have also taken place in non-European countries.

When Hans Lauche retired, Widell and Henricson (2003) took over the responsibility for the Lindau Calibration Photometer, and following Ola Widell's retirement in 2011, this responsibility was handed over to the corresponding author of this paper. Table 1 is an attempt to list all known official intercalibration workshops to date.

## 2 Calibration sources

In this calibration effort nine calibration sources were compared to the Fritz Peak (FP) reference source (this source is labelled "Fritz Peak international standard source"). This radioactive  $^{14}\text{C}$ -activated phosphor source is only used at intercalibration workshops. Apart from the FP reference source,

**Table 1.** Known official intercalibration workshops. The 1967–1972 intercalibrations are mentioned by Torr (1983). Regarding later calibration workshops lacking a literature reference, the results and raw data are archived by the corresponding author of this paper. Copies are available upon request. The column # refers to the number of participating calibration sources.

Year	#	Location	Reference/responsible
1967		Fritz Peak	Gadsden and Marovich
1968		Paris	Weill
1969		Tokyo	Huruhata
1970		Kitt Peak	Broadfoot
1970		Harvard	Noxon
1970		Johns Hopkins	Schaeffer and Fastie
1972		Lindau	Leinert and Klüppelberg
1979	9	Seattle	Torr (1981)
1981	30	Aberdeen	Torr and Espy (1981)
1983	21	Lindau	Lauche
1985	16	Lysebu	Lauche and Barke (1986)
1987	14	Saskatoon	Lauche
1989	1	Lindau	Lauche
1991	6	Wien	Lauche (IAGA)
1995	4	Boulder	Lauche
1999	18	Lindau	Lauche and Widell (2000b)
2000	9	Stockholm	Lauche and Widell (2000a)
2001	10	Oulu	Widell and Henricson (2003)
2003	8	Longyearbyen	Widell and Mämmi (2003)
2006	7	Kiruna	Widell and Henricson (2008)
2007	6	Andøya	Henricson (2008)
2011a	10	Kiruna	This work
2011b	10	Sodankylä	This work
2011c	3	Longyearbyen	This work (prel. results)

the IRF UJO 920B, L1614, Y275 and the MPI-2 sources are also radioactive  $^{14}\text{C}$  activated phosphor sources. The spectral output is continuous and depends on the phosphor. The IRF UJO sources are "light standards", probably manufactured by U.S. Radium Corp. in the 1960s and labelled with phosphor type and luminance values, "920B  $< 20 \mu\text{L}$ ", "L1614  $7 \mu\text{L} \pm 10 \%$ " and "Y275  $15 \mu\text{L} \pm 10 \%$ ", respectively. The lambert L is a non-SI unit of luminance; 1L corresponds to  $10^4/\pi \text{ cd m}^{-2}$ . It is furthermore a photometric unit, involving the spectral sensitivity of the human eye. These luminance values have probably never been used for calibration purposes, at least not in recent years.

Several of these sources have participated in intercalibrations dating back to the late 1960s (see Torr, 1983, Fig. 1). Although stable and easy to handle, these sources are nowadays rather difficult to transport due to flight safety regulations.

The ESRANGE tungsten lamp and the IRF Lauche lamp are tungsten lamps that operated at a predefined lamp current. Both were designed by Hans Lauche. The ESRANGE tungsten lamp was powered by an external power supply, while the IRF Lauche lamp has its own constant current supply.

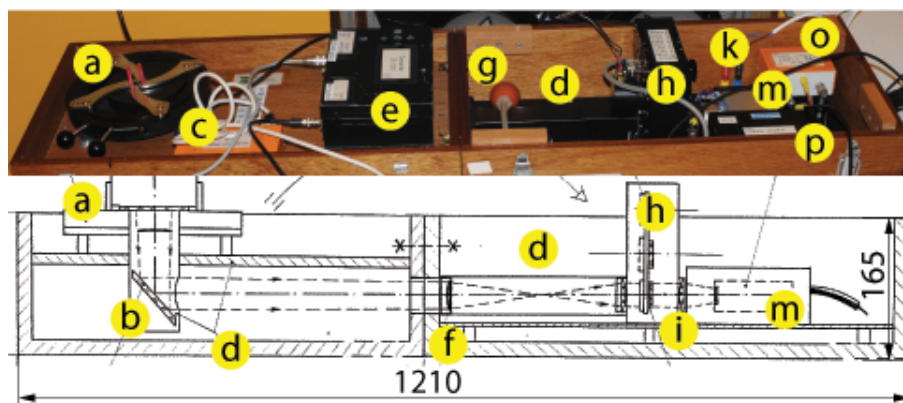


**Fig. 1.** The Lindau Calibration Photometer built by W. Barke and Hans Lauche at Max Planck Institute for Aeronomy, Katlenburg-Lindau (1984). (a) centering device for source under measurement (b) deflecting mirror, (c) power supply for pulse amplifier, (d) collimators, (e) HV supply. (f) objective lens, (g) dehumidifier, (h) filter wheel, (i) field stop, (k) Peltier cooler connector, (m) PMT Hamamatsu R-632, (o) connection box and (p) pulse amplifier.

These sources are not considered as stable as the radioactive sources, but on the other hand, they are much easier to transport.

The stability of the radioactive sources and the IRF Lauche lamp is discussed in Sect. 6.

Two sources are based on light-emitting diodes (LEDs): the ESRANGE MSP1 and the PGI Chernouss-38AM. The ESRANGE MSP1 has internal current regulators and is powered by a 28 V supply, while the PGI Chernouss-38AM is battery powered. Both participating LED sources consist of several LEDs and none of them has participated in earlier intercalibration workshops.

The FMI sphere (Mäkinen, 2001) consists of an integrating sphere, three identical 30 W internal tungsten lamps, a 75 W external tungsten lamp with a mechanical attenuator and several neutral density (ND) filters. The ND filters are required to decrease the output of the sphere to acceptable levels for low light instrumentation. The output of the sphere is calibrated by the manufacturer in foot-lamberts (an American customary unit for luminance; 1 ft-L corresponds to  $3.426 \text{ cd m}^{-2}$ ). Note that this is a photometric unit involving the spectral sensitivity of the human eye, and that this calibrated luminance value is valid at the exit aperture of the integrating sphere, i.e. before the ND filters. Thus, for the intercalibrating effort described here, the luminance value should only be regarded as a source setting. However, knowing the spectral response of the ND filters, it is possible to compare the calibrated output of the sphere to the results presented in this report. It is hoped that this will be done in the future.

It should be noted that the ESRANGE sources were intercalibrated on 16 September 2011 at the Swedish Institute of Space Physics in Kiruna (referred to as 2011a), while all other sources except the FMI sphere were intercalibrated on 19 October 2011, at Sodankylä Geophysical Observatory in Sodankylä, Finland. The FMI sphere was intercalibrated on

the same date at the calibration laboratory at Finnish Meteorological Institute's Arctic Research Centre (FMI-ARC), also in Sodankylä. Both Sodankylä intercalibrations above are referred to as 2011b. The IRF sources as well as the MPI-2 source were intercalibrated at both locations.

During the course "Optical methods in auroral physics research" held in November 2011 at the University Centre in Svalbard (UNIS), the IRF Lauche lamp and the PGI Chernouss-38AM sources were intercalibrated with an SN-1633 NIST-traceable tungsten lamp in the calibration laboratory at UNIS (Sigernes et al., 2007). This intercalibration is referred to as 2011c.

During earlier intercalibration workshops the source naming conventions have been somewhat different for some sources. To remedy this in the future, a unique source identification number (SID) was introduced in 2011 to simplify future comparisons. Radioactive calibration sources have been assigned SID in the range 1–99; other sources are numbered from 101 (see Table 2).

This report only concerns sources intercalibrated in 2011. A full list of all sources that participated in this long-term calibration series is under preparation. Some of the participating calibration sources are shown in Fig. 2.

### 3 The Lindau Calibration Photometer

The Lindau Calibration Photometer is described by Lauche and Barke (1986). Furthermore, all technical documentation and design drawings, raw data and results from the calibration photometer as well as previous intercalibration workshops are archived by the corresponding author of this paper and are available upon request. As soon as time permits, this information will be scanned and made available on the Internet.

**Table 2.** Results of the intercalibration workshop. All values are spectral column emission rates in R/Å. The absolute calibration values at 3914 Å should be considered less reliable (see Sect. 6). Filter transmittance plots are available upon request. SID is source identification number.

Filter position	1	2	3	4	5	6	7			
Filter CW	3914	4280	4866	5573	5882	6299	6562	[Å]		
Filter bandwidth (FWHM)	41	27	25	16	13	12	15	[Å]		
Source name	SID								Settings	Note
FP reference source	1	0.34	5.7	3.2	2.6	5.1	9.2	15	Torr and Espy (1981)	
MPI-2	2			2	173	263	187	93	<sup>14</sup> C	
IRF UJO 920B	3	4	101	62	22	13	8	4	<sup>14</sup> C Phosphor 920B	
IRF UJO L1614	4	5	1	38	34	9			<sup>14</sup> C Phosphor L1614	
IRF UJO Y275	5			4	261	362	201	107	<sup>14</sup> C Phosphor Y275	
IRF Lauche lamp	101		1	8	54	96	207	352	1.62 V, 198.50 mA	1
IRF Lycksele lamp	102		1	9	72	150	360	489	6.21 V, 22.7 mA	2
ESRANGE tungsten lamp	103	3	10	61	359	544	728	635	10.9 V, 217.5 mA	2, 3
ESRANGE tungsten lamp	103			1	6	12	20	32	5.10 V 141.00 mA	2, 3
ESRANGE MSP1	104	226	335	150	280	308	523	299	LED 28 V supply	1, 3
PGI Chernouss-38AM	105	12	164	382	710	639	1520	1782	LED, setting 3 (max)	4
FMI sphere	106		5	26	72	78	180	353	L:C, A:150, ND:7, 1473.3 ft-L	5
FMI sphere	106		9	49	139	150	348	696	L:C, A:255, ND:7, 3092.0 ft-L	5
FMI sphere	106	1	13	67	170	189	422	809	L:BC, A:100, ND:7, 3388.0 ft-L	5
FMI sphere	106	1	20	100	294	304	682	1311	L:BC, A:255, ND:7, 5947.0 ft-L	5

Notes: 1. Constant current supply, 2. adjustable power supply, 3. 2011a intercalibration (Kiruna 16 September), 4. battery powered, 5. settings refer to lamp(s) in use (L), attenuator setting (A), neutral density filter (ND) and luminance in foot-lamberts (before the neutral density filters).



**Fig. 2.** Some of the low light sources intercalibrated at this workshop: (a) IRF Lauche lamp (SID 101) with power supply, (b) PGI Chernouss-38AM (SID 105), (c) IRF UJO Y275 (SID 5), (d) IRF UJO L1614 (SID 4), (e) IRF UJO 920B (SID 3), (f) FP reference source (SID 1), (g) MPI-2 source (SID 2) and (h) IRF Lycksele lamp (SID 102).

Figure 1 shows the general layout of the instrument. The source is attached to the centering device (a) and light passes a mirror (b), collimating tubes (d), an objective lens (f), filter wheel (h), with telecentric optics and field stop (i) and finally reaches the Peltier-cooled photomultiplier tube (PMT, Hamamatsu R632 GA37). Datasheets with plots of spectral response and quantum efficiency for this

PMT are available on the Internet ([www.datasheetcatalog.org/datasheet/hamamatsu/R632.pdf](http://www.datasheetcatalog.org/datasheet/hamamatsu/R632.pdf)). The length of the instrument is 1210 mm, and the height is 165 mm. The two parts are folded together during transportation.

#### 4 Intercalibration procedure

The Lindau Calibration Photometer was installed in a darkroom and the Peltier cooler was switched on several hours before measurements, so that the photomultiplier tube (PMT) would be sufficiently cooled and thermally stable. One person operated the calibration photometer and sources in the darkroom, while another person recorded the filter position and PMT counts using a filter position display and a precision frequency counter (HP 5328A and HP 53181A for 2011a and 2011b, respectively) located outside the darkroom. The frequency counter was set for a long gate time (3–5 s). In addition, an intercom was available between the darkroom and the outside. Filter position 0 is blocked and corresponds to dark current; the remaining positions correspond to seven filters from 3914 to 6562 Å (listed in Table 2). The filter bandwidths in the table correspond to the full width at half maximum (FWHM). Position 8 corresponds to a filter with centre wavelength 6707 Å. This filter is included in the intercalibration procedure, but the results are traditionally discarded since the FP reference source lacks calibration data for this wavelength. Transmittance curves for each filter exist in the calibration photometer documentation and are available upon request. Each source was then compared to the FP reference source. This was done according to the following procedure:

1. The FP reference source was attached to the centering device of the calibration photometer (Fig. 1a).
2. Three measurements were recorded from the frequency counter for each of the nine filter wheel positions (including dark current). As the filter wheel was rotated manually, the filter changes were announced and verified over the intercom and by using the filter position display.
3. The FP reference source was then replaced with the calibration source and step 2 above was repeated for that source. Metadata was recorded (filter temperature, start and stop times, etc.).
4. Steps 1–3 above were repeated for each of the nine calibration sources.

The spectral column emission rate ( $I_{Sp}$ ) at filter position  $p$  (1...8) was then calculated from the following equation (by using a spreadsheet):

$$I_{Sp} = \frac{I_{Rp}(\bar{S}_p - \bar{S}_0)}{\bar{R}_p - \bar{R}_0} \frac{R}{\text{Å}} \quad (3)$$

where  $\bar{S}_p$  and  $\bar{R}_p$  are the average measured count rates for the calibration source and the FP reference source, respectively;  $\bar{S}_0$  and  $\bar{R}_0$  are averaged dark current measurements (filter position 0).  $I_{Rp}$  is the FP reference spectral column emission rate for filter  $p$  (refer to Table 2). To preserve continuity this procedure has been changed as little as possible since 1985.

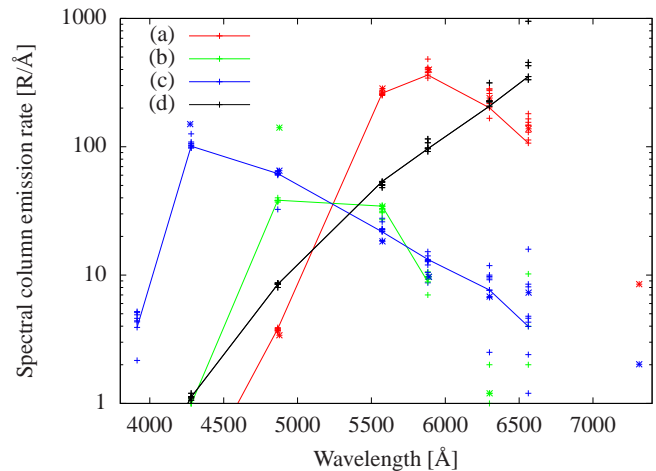


**Fig. 3.** Intercalibration results for three sources since 1981: (a) IRF UJO Y275 (SID 5), (b) IRF UJO L1614 (SID 4), (c) IRF UJO 920B (SID 3), (d) IRF Lauche lamp (SID 101, since 2000). The 2011b intercalibration results are connected with lines, giving a rough idea of the spectra of these sources. The 1981 intercalibration used different filters indicated by a “\*”.

#### 5 Results

The results from this intercalibration effort are given in Table 2. Note that spectral column emission rates less than 1 R/Å have been removed in Table 2 due to poor signal-to-noise ratio. All raw data and preliminary results before post-processing are available at <http://alis.irf.se/ewoc/2011>.

Figure 3 plots all intercalibration results from 1981 until the present time for three radioactive and one tungsten lamp source. Table 3 lists the ratios of this intercalibration to earlier intercalibration workshops, as well as to the mean value of all listed workshops. Sources not appearing in Table 3 have only been intercalibrated once, or earlier intercalibration data have not been located yet. Figure 4 plots selected ratios from Table 3 as a time series. The ratios and wavelengths are selected based on the normal usage of the source for calibration of optical instrumentation.

The intercalibration was done under two assumptions: (1) the spectral radiant sterance of the FP reference source is stable and sufficiently well known, and (2) the calibration photometer is linear and stable during the calibration.

#### 6 Discussion

The FP reference source is traceable to intercalibrations in the late 1960s (Torr, 1983) and the present absolute calibration values, obtained with a national standard source (Q47 tungsten filament lamp, calibrated by the National Bureau of Standards in 1977) from an intercalibration done by Torr and Espy (1981). Since 1981 the FP reference source has been used as reference source for intercalibration workshops in the

**Table 3.** Ratios of the 2011b intercalibration (Sodankylä) to earlier intercalibrations and to the mean value of all listed measurements. Sources not appearing in this table lack information of earlier calibration workshops. SID is source identification number.

Source name	SID	Year	Filter [Å]						
			3914	4280	4866	5573	5882	6299	6562
IRF UJO 920B	3	1981		0.67	0.95	1.19	1.36	1.12	0.55
		1985	0.77	0.80	1.01	1.17	1.26	1.14	0.49
		1999	0.89	0.99	1.03	0.99	1.10	1.01	1.66
		2000	0.85	0.93	0.97	0.95	1.04	0.77	0.47
		2001	0.75	0.96	0.95	0.99	1.02	0.83	3.32
		2006	0.80	0.95	1.00	0.95	0.94	0.81	0.25
		2007	0.91	1.03	1.01	0.96	0.87	0.65	0.86
		2011a	1.81	1.03	0.99	0.84	1.03	0.78	0.83
		Mean	1.02	0.91	0.99	0.99	1.05	0.87	0.63
IRF UJO L1614	4	1981		1.24	0.27	1.00	0.91		2.20
		1985	1.14	1.36	1.18	1.24	1.02		0.23
		1999	0.13	0.99	1.04	1.04	0.95		0.49
		2000	1.14	0.99	0.96	0.98	0.92		1.74
		2001	0.80	0.90	1.01	1.28	1.26		0.10
		2006	0.57	0.93	1.00	1.10	0.83		0.25
		2007	1.33	0.99	1.01	1.07	0.91		
		2011a	0.80	1.03	1.01	1.13	0.93		
		Mean	0.59	1.03	0.78	1.09	0.96		0.52
IRF UJO Y275	5	1981		6.00	1.12	0.92	0.91	0.84	0.77
		1985	0.33	0.70	1.01	1.04	0.96	0.93	0.94
		1999	1.00	1.05	1.01	0.99	0.94	0.71	0.65
		2000	1.00	0.95	0.98	0.95	0.89	0.71	0.59
		2001	5.00	1.17	1.06	1.01	0.75	0.73	0.69
		2006		0.91	1.03	1.03	0.91	0.89	0.72
		2007	1.00	1.11	1.04	1.02	0.87	0.77	0.82
		2011a	0.33	1.00	1.03	0.98	1.06	1.21	0.73
		Mean	0.88	1.06	1.03	0.99	0.91	0.84	0.75
IRF Lauche lamp	101	2000	0.95	1.02	1.00	1.07	0.98	0.93	0.78
		2001	1.06	0.93	1.06	1.12	0.84	0.91	0.82
		2007	1.20	1.06	0.98	1.06	0.90	0.92	1.06
		2011a	1.06	0.99	0.98	1.02	1.05	0.66	0.37
		Mean	1.05	1.00	1.00	1.05	0.95	0.86	0.70

aurora/airglow optical community. Note that the 1981 calibration did not include 3914 Å and 6707 Å. The origin of the absolute calibration value at 3914 Å (0.34 R/Å) is currently unknown. This is under investigation, and until further notice it should be treated as less reliable (extrapolated). As 1981 is a rather long time ago, doubts can clearly be cast on the stability of the FP reference source. It is thus of great importance to compare the FP reference source to a source traceable to a National Bureau of Standards as soon as possible. Although strongly desired, this has not been possible yet. Some steps have therefore been taken to indirectly assess the stability of the FP reference source.

Preliminary results from the independent 2011c intercalibration (Longyearbyen) of two sources are given in Table 4.

In addition, the spectra of these two sources were measured with a spectrograph. For the IRF Lauche source (SID 101), deviations appear to be less than  $\pm 15\%$  for wavelengths from 5573 Å. For shorter wavelengths this source has a very low output, as should be expected from a tungsten lamp. The ratios for the PGI Chernouss-38AM (SID 105) source are a bit more puzzling and, in particular, the large difference for 4866 Å is still under investigation. The spectrum of the PGI Chernouss-38AM LED source was found to be continuous but with two sharp peaks. One possible preliminary explanation for the discrepancy is that while the former calibrations were done by a filtered photometer, the 2011c calibration was done with a spectrograph. The spectrograph had a bandpass of approximately 100 Å, while the photometer filters have

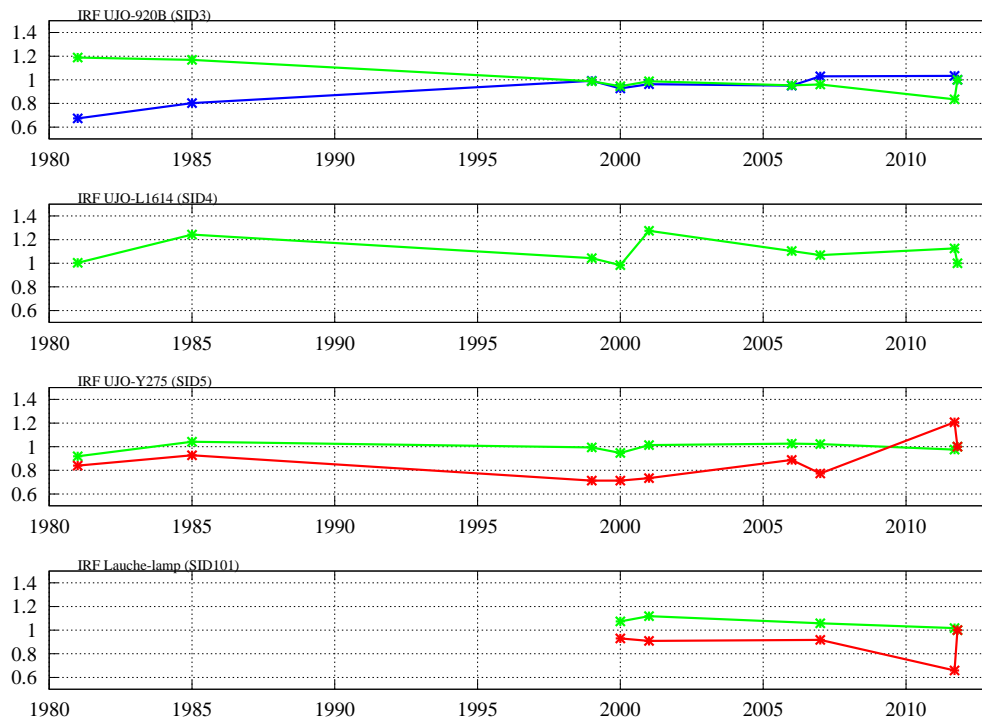


**Fig. 4.** Ratios of 2011b intercalibration in Sodankylä to earlier intercalibrations for IRF UJO 920B (SID3, top panel), IRF UJO L1614 (SID 4), IRF UJO Y275 (SID5) and IRF Lauche lamp (SID101) (bottom panel): (blue) 4280 Å, (green) 5573 Å and (red) 6299 Å. Note that none of these sources were intercalibrated 1987–1995.

a bandpass around 20 Å. As this source has no earlier intercalibration history, additional measurements are required. A preliminary conclusion from the 2011c intercalibration is that the intercalibration error for the FP reference source is probably less than  $\pm 25\%$  for wavelengths from 5573 Å. This preliminary, but promising, conclusion is to be confirmed by the final results from the 2011c intercalibration session.

The FMI MIRACLE EMCCD imager normally operated at Kilpisjärvi was recently calibrated by the manufacturer, Keo Scientific in Canada (T. S. Trondsen, personal communication, 2011). For further validation, this imager was then calibrated by the FMI integrating sphere and two of the IRF radioactive sources (920B and Y275). Data from this effort are not analysed yet and will appear in a later publication. Then, it will be possible to compare the 2011b intercalibration both to the calibration by Keo Scientific in Canada as well as to the FMI integrating sphere.

Furthermore, if the FP reference source should become unstable over time, it is highly likely that other  $^{14}\text{C}$ -activated phosphor sources also would become unstable. This would be noticed as increasing deviations between the intercalibration workshops.

It has been found that Torr and Espy (1981) and Lauche and Barke (1986) did not use exactly the same filter sets. This is under investigation and might explain the difference in ratios for 1981 and 1985 (Fig. 4).

The 2011a intercalibration was mainly a practice run by a new calibration team before the official 2011b intercalibration in Sodankylä. This might explain the larger deviations seen for the 2011a intercalibration (Table 3 and Fig. 4). The 2011a intercalibration should therefore be excluded from the long-term series, if results from later workshops confirm it to be an outlier.

Aging effects of various components (sources, filters, PMT, etc.) will also contribute to the errors. Looking at Fig. 3 it is seen that the intercalibration errors tend to increase towards the red part of the spectra. This is under investigation and is probably related either to aging effects (PMT and/or filters), stray light, or to design compromises of the calibration photometer.

On the other hand, the IRF UJO Y275 (SID 5) source appears very stable over time at 5573 Å (Fig. 4). In fact, recovered fragments of old documentation (1960s) concerning “light calibration by C14 activated light standards from U.S. Radium Corp.” appear to indicate 262.65 R/Å for the IRF UJO Y275 (SID 5) at 5600 Å (by conversion of the luminance values stamped onto the source; see Sect. 2). This is to be compared to the 2011b intercalibration that gave 261 R/Å at 5573 Å. To confirm this, the spectra of these sources must be measured. It is hoped that this will be possible in the autumn of 2012.

The mean ratios in Table 3 indicate a typical deviation, ranging from a few percent to around  $\pm 10\%$  for wavelengths

**Table 4.** Preliminary ratios of this intercalibration to measurements in November 2011 at the calibration laboratory at UNIS, Longyearbyen, Svalbard (2011c). The large differences for wavelengths below 5573 Å are expected since the IRF Lauche lamp is a tungsten lamp. For the PGI Chernouss-38AM source, the large difference at 4866 Å is more puzzling and remains to be explained.

Source name	SID	Filter [Å]						
		3914	4280	4866	5573	5882	6299	6562
IRF Lauche lamp	101	0.02	0.10	0.32	0.85	0.89	0.96	1.11
PGI Chernouss-38AM	105	0.53	0.86	0.30	0.69	0.75	0.95	1.09

4280, 4866, 5573 and 5882 Å. For 6299 Å this value is around  $\pm 15\%$ .

While none of what is said above provides hard evidence concerning the validity of the 30-year-old absolute calibration of the FP reference source, it is probably safe to assume that absolute calibration errors are probably less than 15–25 %, with a few exceptions and not including filters at 3914 and 6707 Å. This is also in agreement with Torr and Espy (1981), who report an accuracy of  $\pm 10\%$  over a 12-year-period. This should be compared to differences up to a factor of six during the early phases of this long-term intercalibration effort (Torr et al., 1977). Finally, even in the case that the absolute calibration values are completely wrong, the relative intercalibration is not affected by this, and thus it would be possible to correct these errors in the future.

## 7 Conclusions

This work presents the official results from the intercalibration workshop following the 38th Annual European Meeting on Atmospheric Studies by Optical Methods (in Table 2). Ratios of this intercalibration to earlier work are presented in Table 3 and Fig. 4. Preliminary results of the independent 2011c intercalibration (Longyearbyen) of two sources are given in Table 4.

A brief description of the intercalibration method, in effect since 1985, is provided. Furthermore, a large set of documentation and publications regarding this long-term intercalibration effort has been collected. As much as possible of this information will be made available on the Internet (<http://alis.irf.se/ewoc/>).

It is concluded that well-justified doubts exist about the validity of the absolute calibration of the FP reference source after 30 years. On the other hand, preliminary results from the 2011c intercalibration (Table 4) suggest errors of around  $\pm 15\%$  for wavelengths from 5573 Å and possibly also at 4280 Å. This is to be confirmed by the final results of the 2011c intercalibration as well as to be compared to the calibrations of the FMI MIRACLE EMCCD, performed in Canada by Keo Scientific and to the certified luminance values of the FMI sphere. Until this is done the absolute calibration error is estimated at 15–25 % and the relative intercalibration error at 5–25 %.

## Future work

Following the intercalibration efforts in 2011, several radioactive calibration light sources have been found in Norway (Y. L. Andalsvik, personal communication, 2012). Many of these sources appear in earlier intercalibration workshops, in particular at the Lysebu 1985 workshop (Lauche and Barke, 1986). In addition, at least two calibration sources have been found at University of Oulu, Finland. Therefore, it would be desirable to include these sources in the intercalibration workshop planned for the autumn of 2012 in Sodankylä.

For the next workshop it will hopefully also be possible to measure the spectra of all participating sources. This is of general importance for improving the quality of this long-term intercalibration effort, but, in particular, it might help resolve problems related to LED-based sources, such as the PGI Chernouss-38AM source (SID 105).

This intercalibration effort should also be compared to absolute calibration methods involving the known spectra of stars.

The intercalibration procedure from 1985 is a rather tedious and manual nature. To automate the filter wheel operation and data acquisition would probably both improve the accuracy and speed up the intercalibration procedure.

Last but not least, it is of the utmost importance to perform an intercalibration of the FP reference source to a source traceable to a National Bureau of Standards source as soon as possible.

*Acknowledgements.* This work is presented in memory of Ingrid Sandahl who passed away in 2011. This work was funded by a University of Oulu grant for short-term international research visits. The comparison at UNIS was financed by a grant from the Nordic Council of Ministers. The authors also wish to thank two anonymous referees for their unusually helpful and thorough review of this work.

Edited by: A. Benedetto

## References

- Baker, D. J.: Rayleigh, the Unit for Light Radiance, *Appl. Optics*, 13, 2160–2163, 1974.
- Baker, D. J. and Romick, G. J.: The Rayleigh: interpretation of the unit in terms of column emission rate or apparent radiance expressed in SI units, *Appl. Optics*, 15, 1966–1968, 1976.
- Brändström, U.: The Auroral Large Imaging System – Design, operation and scientific results, Ph.D. thesis, Swedish Institute of Space Physics, Kiruna, Sweden, (IRF Scientific Report 279), ISBN: 91-7305-405-4, 2003.
- Chamberlain, J. W.: Physics of the aurora and airglow, *Classics in geophysics*, AGU (American Geophysical Union), (A reprint of the original work from 1961), 1995.
- Dahlgren, H., Gustavsson, B., Lanchester, B. S., Ivchenko, N., Brändström, U., Whiter, D. K., Sergienko, T., Sandahl, I., and Marklund, G.: Energy and flux variations across thin auroral arcs, *Ann. Geophys.*, 29, 1699–1712, doi:10.5194/angeo-29-1699-2011, 2011.
- Gustavsson, B., Leyser, T. B., Kosch, M., Rietveld, M. T., Åke Steen, Brändström, B. U. E., and Aso, T.: Electron Gyroharmonic Effects in Ionization and Electron Acceleration during High-Frequency Pumping in the Ionosphere, *Phys. Rev. Lett.*, 97, 195002, doi:10.1103/PhysRevLett.97.195002, 2006.
- Henricson, H.: Results from the intercalibration of low light level sources at Andøya 2007, in: *Proceedings of the 33rd Annual European Meeting on Atmospheric Studies by Optical Methods*, edited by: Sandahl, I. and Arvelius, J., no. 292 in IRF Scientific report, p. 131, Swedish Institute of Space Physics, Kiruna, <http://www.irf.se/publications/proc33AM>, 2008.
- Hunten, D. M., Roach, F. E., and Chamberlain, J. W.: A photometric unit for the aurora and airglow, *J. Atmos. Terr. Phys.*, 8, 345–346, 1956.
- Lauche, H. and Barke, W.: A calibration photometer for low brightness sources, in: *Proceedings of the 13th annual Meeting on Upper Atmosphere Studies by Optical Methods*, edited by: Måseide, K., University of Oslo, Department of Physics, 86–28, 364–370, 1986.
- Lauche, H. and Widell, O.: Intercalibration of low light level sources, in: *Proc. of 27th Annual European Meeting on Atmospheric Studies by Optical Methods*, Stockholm, Sweden, Meteorological institution, Stockholm university, Sweden, 2000a.
- Lauche, H. and Widell, O.: Intercalibration of low light level sources, *Phys. Chem. Earth*, B25, 483–483, 2000b.
- Mäkinen, S.: All-sky camera calibration, Master's thesis, Helsinki University of Technology (now Aalto University), 2001.
- Rayleigh, L.: Absolute Intensity of the Aurora Line in the Night Sky, and the number of Atomic Transitions Required to Maintain it, *P. R. Soc. London*, A129, 458–467, 1930.
- Sigernes, F., Holmes, J. M., Dyrland, M., Lorentzen, D. A., Chernous, S. A., Svenøe, T., Moen, J., and Deehr, C. S.: Absolute calibration of optical devices with a small field of view, *J. Opt. Technol.*, 74, 669–674, 2007.
- Syrjäsuu, M. T.: Auroral monitoring network: From all-sky camera system to automated image analysis (D.Sc.(Tech.)-thesis), Finnish Meteorological Institute, Helsinki, Finland, Contribution series 32, ISBN: 951-697-551-8, 2001.
- Torr, M. R.: Intercalibration of instrumentation used in the observation of atmospheric emissions: A progress report 1976–1979, Tech. Rep. 100, Utah State University, Center for atmospheric and space sciences, Logan Utah, 1981.
- Torr, M. R.: Report on a project to intercalibrate instrumentation used in the observation of visible atmospheric emissions, Tech. rep., Utah State University, Center for atmospheric and space sciences, Logan Utah, 1983.
- Torr, M. R. and Espy, P.: Intercalibration of instrumentation used in the observation of atmospheric emissions: Second progress report, Tech. Rep. 101, Utah State University, Center for atmospheric and space sciences, Logan Utah, 1981.
- Torr, M. R., Hays, P. B., Kennedy, B. C., and Torr, D. G.: Photometer calibration error using extended standard sources, *Appl. Optics*, 15, 600–602, doi:10.1364/AO.15.000600, 1976.
- Torr, M. R., Hays, P. B., Kennedy, B. C., and Walker, J. C. G.: Intercalibration of airglow observatories with the Atmosphere Explorer satellite, *Planet Space Sci.*, 25, 173–184, 1977.
- Trondsen, T. S.: High spatial and temporal resolution auroral imaging, Ph.D. thesis, University of Tromsø, 1998.
- Widell, O. and Henricson, H.: Intercalibration of low light level sources, in: *Proc. of 28th Annual European Meeting on Atmospheric Studies by Optical Methods*, 19–24.8.2001, Oulu, Finland, edited by: Kaila, K. U., Jussila, J. R. T., and Holma, H., Sodankylä Geophysical Observatory, 92, 125–125, 2003.
- Widell, O. and Henricson, H.: Results from the intercalibration of low light level sources at IRF 2006, in: *Proceedings of the 33rd Annual European Meeting on Atmospheric Studies by Optical Methods*, edited by: Sandahl, I. and Arvelius, J., no. 292 in IRF Scientific report, Swedish Institute of Space Physics, Kiruna, p. 130, <http://www.irf.se/publications/proc33AM>, 2008.
- Widell, O. and Mämmi, S.: Results from the intercalibration of low light level sources at Svalbard 2003, in: *Proceedings of the 30th Annual European Meeting on Atmospheric Studies by Optical Methods*, edited by: Sigernes, F. and Lorentzen, D., The University Centre on Svalbard, Longyearbyen, p. 121, 2003.

## **Appendix 2**

Geerts, B., and T. Dejene, 2005: **Regional and diurnal variability of the vertical structure of precipitation systems in Africa based on space-borne radar data.** *J. Climate*, 18, 893-916



## Regional and Diurnal Variability of the Vertical Structure of Precipitation Systems in Africa Based on Spaceborne Radar Data

BART GEERTS AND TEFERI DEJENE

*Department of Atmospheric Science, University of Wyoming, Laramie, Wyoming*

(Manuscript received 13 April 2004, in final form 2 September 2004)

### ABSTRACT

The Tropical Rainfall Measuring Mission (TRMM) 2A25 radar reflectivity profiles and derived surface rain rates are used to describe the vertical structure of precipitation systems in Africa. Five years of data are used in both the boreal and austral summer rainy seasons. A number of climate regions are isolated and compared. To place the composite reflectivity profiles in context, they are contrasted against TRMM 2A25 observations over the Amazon.

In all of tropical Africa, precipitation systems tend to be deeper and more intense than in the Amazon, and shallow warm-rain events are less common. In all African regions, but especially in the Sahel and northern Savanna, storms are characterized by high echo tops, high hydrometeor loading aloft, little indication of a radar brightband maximum at the freezing level, and evidence for low-level evaporation.

Storms in Africa are generally most common, and deepest, in the late afternoon, and weaker shallow systems are relatively more common around noon. The diurnal modulation is regionally variable. The amplitude of the diurnal cycle of the mean echo top height decreases from the arid margins of the zenithal rain region toward the equatorial region, and is smallest in the Amazon. A secondary predawn (0000–0600 LT) maximum occurs in the Congo, in terms of rainfall frequency, rainfall intensity, and echo tops. The storm intensity indicators generally peak a few hours later in the Sahel and northern Savanna than in other regions in Africa.

The difference between all African regions and the Amazon, and the relatively smaller differences between regions in Africa, can be understood in terms of the climatological humidity, CAPE, and low-level shear values.

### 1. Introduction

Spaceborne rainfall estimation has evolved dramatically over the last two decades (e.g., Huffman et al. 1997). Spaceborne techniques, usually guided by rain gauge data, have been developed based on IR brightness temperatures (e.g., Vicente et al. 1996), multifrequency passive microwave radiances (e.g., Kummerow and Giglio 1994), or a combination of these two. Obviously IR-based techniques have weaknesses, in particular because the anvil of large convective systems is much larger than the precipitation shafts underneath, and the anvil topography is more uniform. Upwelling microwave radiation, emitted or scattered by hydrometeors at all levels in the precipitation column, is more sensitive to these underlying precipitation shafts.

A new era of spaceborne precipitation research started in late November 1997 with the launch of the

Tropical Rainfall Measuring Mission (TRMM) satellite (Kummerow et al. 2000). The TRMM satellite instrument package includes a 13.8-GHz (2.2-cm) radar, the Precipitation Radar (PR; Kummerow et al. 1998). Radar reflectivity data, especially its vertical structure, can be used to improve surface rainfall estimation (e.g., Ferreira et al. 2001). Large differences exist between passive microwave and radar-based rain-rate estimates, mainly on an instantaneous basis, but also cumulatively (Kummerow et al. 2000).

Spaceborne radar data can be used also to characterize the horizontal and vertical structure of precipitation systems. Precipitation Radar reflectivity maps document the horizontal structure of storms and yield information about mesoscale organization, which links to storm longevity (e.g., Heymsfield et al. 2000). Especially intriguing is the PR's ability to describe the vertical structure of storms in detail, on account of the PR's near-vertical incidence. The vertical profile of reflectivity can be used to estimate the profiles of radiative and latent heating (Jensen and Del Genio 2003): as storms develop and decay, they leave behind footprints of condensational heating and evaporative cooling at various levels in the troposphere, and these are an im-

---

*Corresponding author address:* Dr. Bart Geerts, Department of Atmospheric Science, University of Wyoming, Laramie, WY 82071.  
E-mail: geerts@uwyo.edu

portant component in the tropical general circulation (e.g., Mapes and Houze 1993).

This paper focuses on the vertical structure of precipitation systems. Most tropical precipitation systems are deep, but a significant portion of tropical rainfall results from shallow systems with tops near the freezing level (Petty 1999; Johnson et al. 1999; Berg et al. 2002). The fraction of the rainfall from shallow systems, either cumuli congesti or shallow nimbostratus, is poorly understood, and it probably varies significantly regionally and seasonally.

A fundamental distinction exists between convective and stratiform precipitation regions within deep precipitation systems (Houze 1997). In stratiform regions, hydrometeors fall from the upper-cloud layers while they grow, and they produce a distinct reflectivity maximum at the freezing level (FL), known as the bright band (Houze 1993). In essence this bright band is due to the wet coating of melting snowflakes (Battán 1973). In regions of deep convection, a bright band is absent, because the melting of heavily rimed hydrometeors occurs over a deeper layer, and the changes in fall speed are smaller. Also, reflectivity decays more slowly with height above the FL, when compared with that in stratiform regions. The rain type distinction is important because different rain types have different  $Z-R$  (reflectivity–rain-rate) relationships (e.g., Steiner and Houze 1997), and different profiles of latent heating. The above-mentioned discrepancy between passive microwave and radar-based rain-rate estimates appears to be related to differences in vertical structure of precipitation systems, specifically their depth and convective/stratiform nature (Masunaga et al. 2002).

The TRMM PR data, in conjunction with passive microwave and lightning data collected aboard the TRMM satellite, have revealed remarkable differences between continental and maritime precipitation systems in the Tropics (e.g., Toracinta et al. 2002; Cecil and Zipser 2002; Nesbitt and Zipser 2003). Maritime systems tend to have less lightning, less ice aloft, more stratiform characteristics, and they are less diurnally modulated, as compared to continental systems. A comparison between two equatorial wet regions, the Congo and the Amazon basins, revealed that the Congo has deeper storms, a higher reflectivity above the FL in storms (for example, at 7 km), a stronger 85-GHz ice scattering signature, and also more lightning activity, as compared to the Amazon (Boccippio et al. 2000; Petersen and Rutledge 2001; Toracinta et al. 2002). Essentially precipitation systems over the Amazon are more maritime in nature than those over the Congo.

This study describes the vertical structure of precipitation systems in Africa in more detail. The focus is on regional differences in Africa, but a comparison with the Amazon Basin is included, in order to provide a context. Storm systems in the Amazon have been studied in some depth (e.g., Stith et al. 2002; Petersen et al. 2002; Sorooshian et al. 2002), in part thanks to the

TRMM Large-Scale Biosphere–Atmosphere (LBA) field campaign in the Amazon. To our knowledge none of the TRMM-based precipitation studies has focused on regional variations in Africa, except two. These two (Adeyewa and Nakamura 2003; Nicholson et al. 2003) compare TRMM-based rainfall estimates to those based on other satellite data and rain gauges. Clearly much research has been conducted into rainfall variability in Africa using other data sources (e.g., Lebel and Amani 1999; Nicholson et al. 2000), but this is beyond the scope of the current study, which focuses on the vertical structure of precipitation systems. That structure has been described for some isolated cases, all large convective systems in West Africa, mainly based on ground-based radar data (e.g., Roux et al. 1984; Chalon et al. 1988; Roux and Sun 1990), but these studies do not represent a climatology of precipitation systems. In short, the typical vertical structure of precipitation systems in various climate regions of Africa remains undocumented. This is the motivation for the present study, which aims to describe the regional, diurnal, and seasonal variations of the vertical structure of precipitation systems in Africa, and to interpret these variations in terms of typical stability and shear profiles. Specifically, *we aim to answer whether the vertical structure of precipitation systems, and its diurnal variation, is different in the distinct climatic zones of Africa, and different from that in the Amazon Basin.*

The broader impact of this study is obvious: the economy of most African countries primarily depends on agriculture, and agriculture in Africa is highly dependent on the performance of precipitation. To better understand rainfall variability, the vertical structure and evolution of precipitation-generating systems needs to be documented, and this information has been unavailable in Africa, in part because of the lack of scanning radar networks. Thus TRMM has come to fill one data void over Africa. This study will also provide a climatological and regional context for the detailed observations of precipitation systems in West Africa, to be collected during the African Monsoon Multidisciplinary Analysis (AMMA, whose field phase is to be conducted in 2006; see online at <http://www.joss.ucar.edu/amma>).

Following a description of the data sources and analysis method (section 2), the vertical structure of African precipitating systems is presented (section 3). An analysis of the diurnal variation of TRMM PR surface precipitation and storm structure follows in section 4, and the findings of this study are interpreted in the context of regional variations of climatological values of humidity, wind shear, and stability in section 5.

## 2. Analysis method

### a. Data source

The TRMM satellite follows a 35°-inclination non-sun-synchronous low-earth orbit (Kummerow et al.

1998). Its orbit altitude was about 350 km above the earth before August 2001, and 403 km afterwards. Its instruments include a four-frequency microwave radiometer and a 13.8-GHz radar (the PR). The TRMM radar and passive microwave radiometers have been building a superbly calibrated dataset of rainfall rate and vertical structure of precipitating systems over land and ocean since December 1997. The nonsynchronicity with the sun is rather unique compared to other earth observing satellites, and it is important, because over time it enables the deduction of the diurnal variability.

Spaceborne radar observations are superior to ground-based radar data for the description of the storm vertical structure, because of the near-nadir vantage point (Heymsfield et al. 2000; Hirose and Nakamura 2002). They are superior also to a network of ground radars for regional precipitation climatology studies, because there are no range-related problems such as variable resolution, variable minimum echo height, and variable sensitivity, nor are there regional variations in radar calibration (Anagnostou et al. 2001). The drawback of the spaceborne radar observations is the data scarcity: the TRMM PR swath, 220 km wide, visits the same location only once or twice a day (Negri et al. 2002).

The PR's minimum detectable signal is about 17 dBZ (Iguchi et al. 2000). Assuming uniform beam filling, this implies a rain rate of about  $0.3 \text{ mm h}^{-1}$  (Fisher 2004). The horizontal resolution of the PR is about 4.3 km at nadir, before the orbit boost (5.7 km after the boost). This allows the TRMM PR to observe precipitation systems larger than about  $10 \text{ km}^2$  (Wilcox and Ramanathan 2001). Sauvageot et al. (1999) use a ground-based radar to show that less than a quarter of all rain cells in Niger, Africa, have diameters larger than 5 km. If this finding applies generally in Africa, then clearly the storms analyzed in this study are mainly the larger ones: the effects of limited horizontal resolution and low sensitivity combine to exclude isolated, small storm cells from the PR's view (Heymsfield et al. 2000). An attempt has been made to correct for this nonuniform beam-filling effect on PR-based surface rain estimation (Durden et al. 1998), but reflectivity profiles are not "corrected." All this suggests that the present study is biased toward the larger precipitation systems, but then, they carry the bulk of the rain [e.g., Fig. 9.1 in Houze (1993)].

The PR's range resolution is 250 m. Therefore its vertical resolution is 250 m at nadir, decreasing to about 1.6 km (Gaussian weighted) at the outer incidence angle ( $17^\circ$ ). Because this study focuses on the vertical structure, only the profiles with an incidence angle less than  $5^\circ$  on either side of nadir are included.

The primary dataset for this study is the TRMM-PR 2A25 volumetric radar reflectivity and surface rainfall rate (Kummerow et al. 1998). The 2A25 equivalent reflectivity profiles are corrected for attenuation by heavy rain, mainly using the surface reference technique (Igu-

chi and Meneghini 1994), and the rain rates are corrected for nonuniform beam filling (Iguchi et al. 2000). The 2A25 surface rain rate is estimated from the near-surface reflectivity, assuming a  $Z$ - $R$  relationship specific to the rain type:  $Z = 148R^{1.55}$  for convective and  $Z = 276R^{1.49}$  for stratiform precipitation. The rain type is defined based on both horizontal and vertical storm structure information, in the 2A23 algorithm. The 2A23 rain type classification itself is not used in this work. This study focuses on the vertical structure of precipitation profiles, irrespective of their classification. Certainly the shape of the reflectivity profiles will reveal stratiform or convective characteristics (Houze 1997; Geerts and Dawei 2004b), but the profiles are not a priori classified.

This study only considers those reflectivity profiles with path-integrated attenuation, that is, with detectable scatterers above the ground. A threshold of 17 dBZ is imposed, even though the 2A25 dataset includes reflectivity values down to 15 dBZ. These are referred to as the precipitation profiles. Most but not all of the precipitation profiles are also surface rain profiles. There is a number "virga" profiles, with echoes stronger than 17 dBZ at some level, but no detectable rain reaching the surface (2A25 surface rain rate equals zero). The fraction of virga profiles is generally less than 20%. The 2A25 reflectivity data are composited as a function of height. This is the height above the standard geoid, which is very close to mean sea level. Especially for the African continent it is important to note that the height shown is not above ground level.

The TRMM 3B42 daily  $1^\circ \times 1^\circ$  data are also used in this study to describe the basic seasonal swing of precipitation over Africa. The 3B42 dataset is based on a combination of infrared (IR), passive microwave, and radar data from TRMM and IR data from the geostationary satellites. Finally, for the interpretation of the TRMM data, we use the National Centers for Environmental Prediction (NCEP)-National Center for Atmospheric Research (NCAR) global reanalysis dataset, which is based on upper-air and satellite data (Kalnay et al. 1996). We use monthly mean values of atmospheric variables for the period 1968-96. We obtained these data through the Web site of the U.S. Climate Diagnostics Center (available online at <http://www.cdc.noaa.gov>).

#### *b. Regional classification*

The seasonal march of precipitation in Africa is well established (Fig. 1). Regions between  $10^\circ$  and  $25^\circ$  latitude experience a single wet season peaking shortly after the summer solstice. Precipitation is rare outside of this 3-5-month-long wet season. Regions near the equator tend to have two peaks, at or shortly after the equinoxes, with otherwise little seasonal variation in rainfall.

To make regional comparisons, Africa is categorized into nine broad climatic regions (Table 1). Those re-

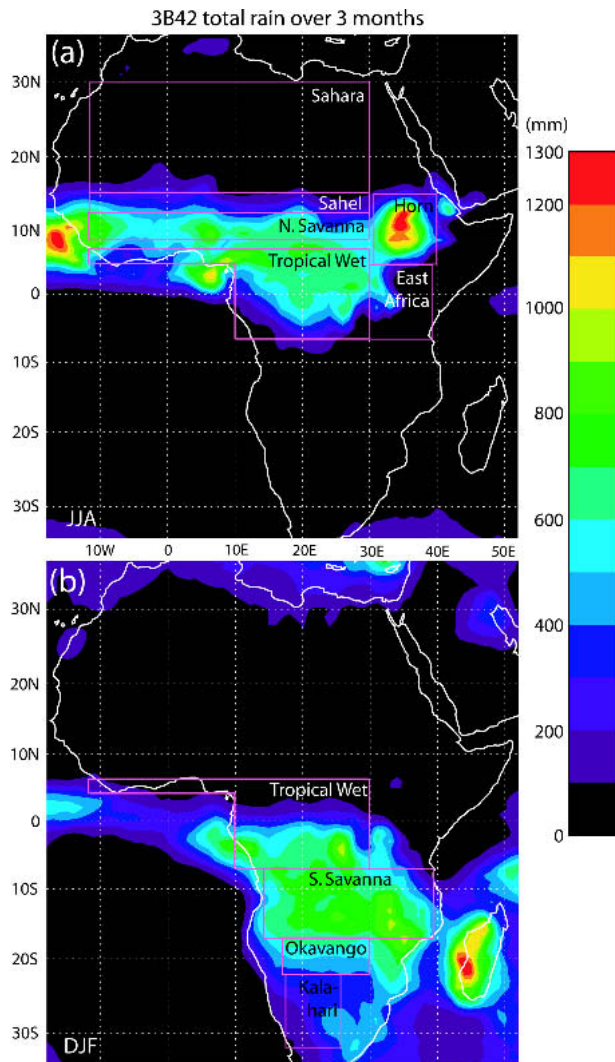


FIG. 1. Mean rainfall over Africa for 1998–2002 based on TRMM 3B42 data. The units are mm in 3 months. Also shown are the geographical regions studied here. (a) JJA and (b) DJF.

ceiving the bulk of the precipitation in the boreal summer are the Sahara ( $15^{\circ}$ – $30^{\circ}$ N,  $11.5^{\circ}$ W– $30^{\circ}$ E), the northern semiarid region (Sahel,  $12^{\circ}$ – $15^{\circ}$ N,  $11.5^{\circ}$ W– $30^{\circ}$ E), the northern Savanna belt ( $8^{\circ}$ – $12^{\circ}$ N,  $11.5^{\circ}$ W– $30^{\circ}$ E), the Horn of Africa ( $4^{\circ}$ – $14.5^{\circ}$ N,  $31^{\circ}$ – $40^{\circ}$ E), the plateau region of Eastern Africa ( $6.5^{\circ}$ S– $4^{\circ}$ N,  $30^{\circ}$ – $39^{\circ}$ E), and the Tropical Wet region. The latter includes the Congo Basin ( $6.5^{\circ}$ S– $6.5^{\circ}$ N,  $10^{\circ}$ – $30^{\circ}$ E) plus the south coast region of West Africa ( $4.5^{\circ}$ – $6.5^{\circ}$ N,  $11.5^{\circ}$ W– $10^{\circ}$ E); both parts largely have an Am climate in the Köppen classification. At first, the south coast region of West Africa was treated separately from the Congo Basin, but the reflectivity profiles are very similar, so the two regions are combined. In any event, the Tropical Wet region is dominated by the Congo Basin, which occupies 86% of that region. Fifteen months of 2A25 data are used for the six regions shown in Fig. 1a: June, July,

TABLE 1. Summary statistics of the climatic regions in Africa. The Amazon Basin is included for comparison. The number of rain events per unit area is the total over 15 months (3 months in each of 5 yr). The average surface rain rate is conditional (i.e., when it rains at the surface).

	Area ( $10^6$ km $^2$ )	Season	No. of rain profiles per $10^3$ km $^2$	Avg rain rate (mm h $^{-1}$ )
Sahara	7.09	JJA	9	4.43
Sahel	1.49	JJA	88	5.06
Savanna North	2.01	JJA	112	4.33
Horn	1.15	JJA	82	4.6
East Africa	1.16	JJA	24	4.59
		MAM	71	4.20
Tropical Wet	3.73	JJA	62	4.45
		DJF	45	5.25
Savanna South	3.16	DJF	113	3.36
Okavango	0.75	DJF	107	3.46
Kalahari	0.93	DJF	73	4.29
Amazon	1.23	JFM	153	2.94

and August (JJA) 1998–2002. In some regions the wet season is centered on August rather than July, but the JJA period includes the majority of the precipitation systems in most regions, including the early monsoon convection.

The three remaining regions receive most of their precipitation in the austral summer: the southern Savanna belt ( $17^{\circ}$ – $6.5^{\circ}$ S,  $14^{\circ}$ – $39^{\circ}$ E), the southern semiarid region (Okavango,  $22^{\circ}$ – $17^{\circ}$ S,  $17^{\circ}$ – $30^{\circ}$ E), and the Kalahari ( $22^{\circ}$ – $32^{\circ}$ S,  $17.5^{\circ}$ – $26^{\circ}$ E). Again fifteen months of 2A25 data are used for these regions: December, January, and February (DJF) 1998–2002 (including December 1997 but excluding December 2002). The Tropical Wet and East Africa have year-round precipitation somewhere within their respective regions, and neither the JJA nor the DJF periods capture the wettest periods. For the Tropical Wet region, we include both JJA and DJF periods. For East Africa we include both the JJA period, which is relatively dry except in the northwestern part (Fig. 1a), as well as the MAM (March–April–May) period, because it is the wettest 3-month period for the entire region. The winter-wet season in the Mediterranean climates of northern Africa and the southwestern corner of Africa is ignored in this study, because the precipitation systems are extratropical. Finally, we included the central Amazon Basin well inland from the coast ( $1^{\circ}$ – $11^{\circ}$ S,  $65^{\circ}$ – $55^{\circ}$ W), because the Amazon is relatively well-studied (see section 1), thus its PR data provide a context for the African data. The wettest period in the central Amazon is the JFM period.

This regional classification is mainly based on the distinct rainfall climatology of each region (Fig. 1). It is rather standard (e.g., Leroux 2001) and similar to that by Adeyewa and Nakamura (2003). The latter study ignores the Horn, East Africa, and the Kalahari. The regional boundaries are a simplification of the regionalization by Nicholson and colleagues (e.g., Nicholson

et al. 2000). Clearly the regions defined in this study do not have the same incidence of precipitation systems (Table 1): the Sahara for instance encounters some 12 times fewer rain events per unit area than does the northern Savanna. Yet when it rains, the average surface rain rate is about the same in these two regions, and indeed in all regions in Africa.

### c. Analysis of diurnal variability

Determining the diurnal variability of precipitation matters, not only because it places fixed-time rainfall estimates from other polar-orbiting satellites, on a sun-synchronous orbit, in a diurnal context (Bell and Reid 1993), but also because it helps to understand the dynamics of precipitating systems in response to diurnally varying surface energy fluxes and lower-tropospheric wind profiles (e.g., Dai et al. 1999). The diurnal variability of precipitation is not captured well by operational numerical weather prediction models (e.g., Davis et al. 2003) or general circulation models (e.g., Lin et al. 2000), in part because convection is parameterized. The diurnal variation of precipitation, as observed by satellite or rain gauges, has received much attention [see Dai (2001) for a review], but the focus here is on the diurnal variation of vertical storm structure.

To study the diurnal variation, reflectivity profiles and surface rain rates are binned at a 3-h temporal resolution. The TRMM orbit is such that the chances of an overpass are about equal for each 3-h bin, over the course of a month or longer. Comparison with a dense network of rain gauge data in Oklahoma has shown that the TRMM PR captures the diurnal variation of the surface rain well (Fisher 2004; B. Fisher 2004, personal communication). A 3-h bin size is rather coarse, but it allows maximization of the sample size. A temporal resolution of 1 h, even using three years of PR data, is inadequate to describe the local (single pixel) diurnal cycle of precipitation due to spatially inconsistent sampling (Negri et al. 2002). Spatial averaging over rather large regions of course allows a finer time resolution. Considering the large size of the climatic regions selected for this study (Table 1) and the 5-yr data period, temporal sampling was done every 3 h, which is a trade-off between statistical significance and the ability to capture the true diurnal variability. The number of samples (TRMM PR profiles with path-integrated attenuation) per 3-h time bin averages  $18 \times 10^3$  (this can be inferred from columns 2 and 4 in Table 1) and ranges between 1339 (East Africa, 0600–0900 LT<sup>1</sup>) and 55 038 (Savanna South, 1500–1800 LT). Thus the sample size appears sufficient to study diurnal variability.

<sup>1</sup> For each reflectivity profile, the local solar time (LT) is used instead of universal time (UTC) because it is the relevant time in the description of the diurnal variation. The local solar time is such that the sun is highest in the sky at local solar noon.

## 3. Regional variability of the vertical structure of precipitation systems in Africa

### a. Composite vertical structure

The probability density function of radar reflectivity as a function of height is shown in Fig. 2 for regions with mainly JJA rainfall and in Fig. 3 for regions with rain mainly in DJF. Shown in these frequency-by-altitude diagrams (FADs) is the probability  $N(Z, h)$  for a given reflectivity  $Z$  (in dBZ units) at a certain height  $h$ , normalized such that the sum of all frequencies plotted equals 100—that is,  $\sum_Z \sum_h N(Z, h) = 100$ . The FADs include all attenuated profiles. The FADs are truncated on the left due to the PR's limited sensitivity, so the entire reflectivity distribution, as shown for instance in Geerts and Dawei (2004b), is not known. The FADs are further partitioned between light surface rain ( $<8 \text{ mm h}^{-1}$ ) and heavy surface rain ( $>8 \text{ mm h}^{-1}$ ).

A first observation is that *the regional differences in the vertical structure of precipitation systems in Africa are relatively small*. Precipitation systems appear generally deep; relatively large or numerous hydrometeors are found high above the FL. In most regions echoes between 17 and 25 dBZ are more common at 6 km, above the FL, than at 3 km. Even light surface rainfall events (less than  $8 \text{ mm h}^{-1}$ ) are generally associated with deep precipitation columns. In some regions, especially the Sahara (Fig. 2, upper-left graph), a surface rain rate less than  $8 \text{ mm h}^{-1}$  often seems to be associated with low-level evaporation. In general low-level evaporation is suggested by the more frequent occurrence of higher reflectivities near 4 km, as compared to levels closer to the ground. As a result, frequency isolines just below the FL tilt to the left toward the ground in several regions. More steeply tilting isolines are present in the FADs for systems with a surface rain rate less than  $4 \text{ mm h}^{-1}$  and less than  $2 \text{ mm h}^{-1}$  in the Sahel and Sahara (not shown). Such tilt is absent in more humid regions, such as in the Savanna South (Fig. 3) and in the south coast region of West Africa, part of the Tropical Wet region in JJA. On the other hand, some frequency isolines below the FL slightly tilt to the right in the Amazon region, indicating low-level rain drop growth by collision-coalescence, and a low cloud base (Fig. 3).<sup>2</sup>

A shift to the right (higher reflectivities) can be seen in a thin layer at a height of about 4.5 km (that is, near the FL) in most FADs. This is associated with the occurrence of a bright band, a signature of stratiform precipitation. The brightband spike is better defined for the light rain cases, suggesting that the light rain group

<sup>2</sup> Some caution is warranted in the interpretation of the FAD at low levels. In regions with much elevated terrain—such as East Africa, the Horn, the southern Savanna, the Okavango, and the Kalahari—the rapid decay of frequencies between 1- and 2-km height obviously is related to the terrain.

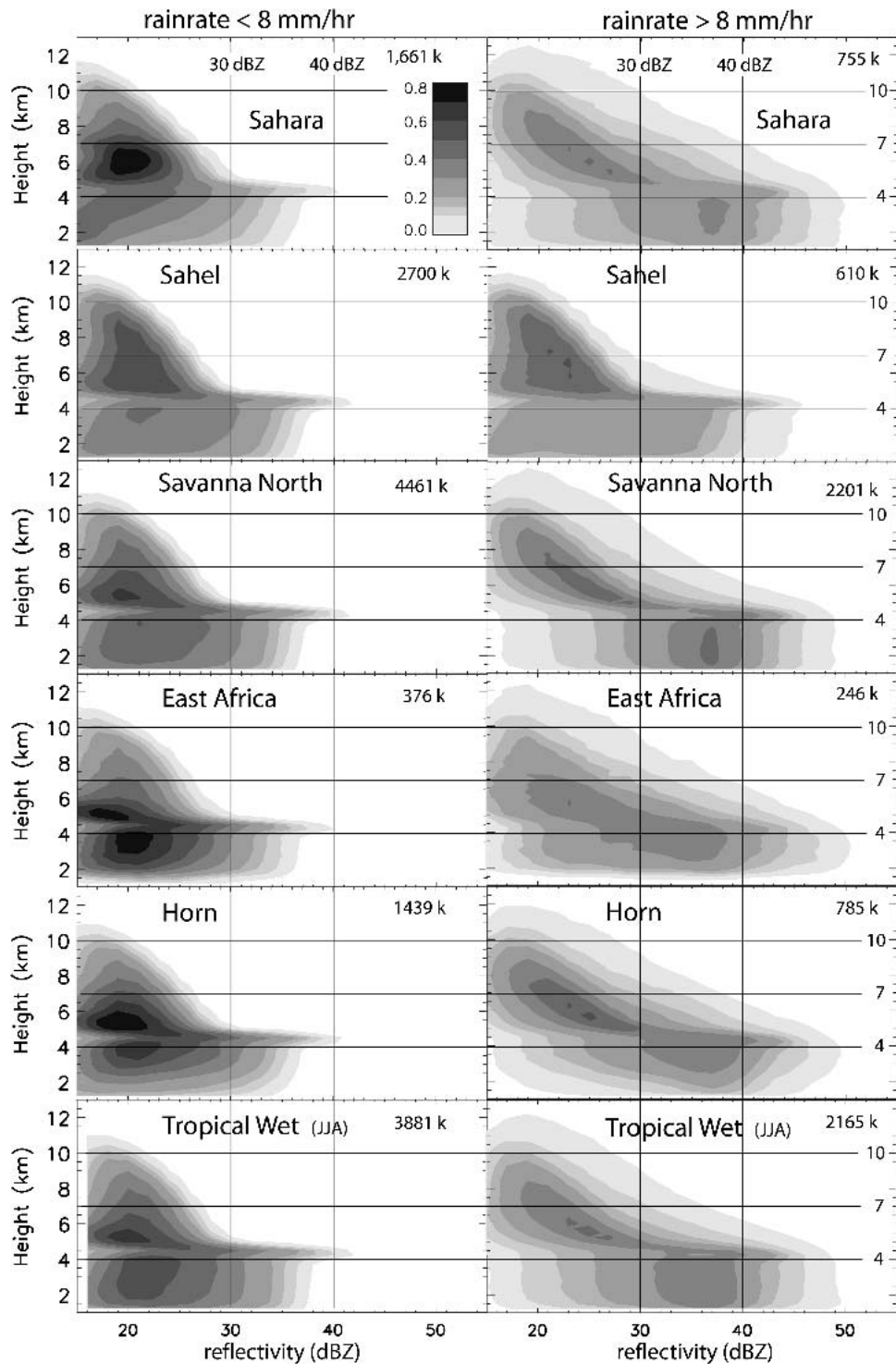


FIG. 2. Probability density functions of reflectivity-by-altitude for all cases with PR-detected surface rain rate ( $R$ ) (left)  $0 < R \leq 8 \text{ mm h}^{-1}$  and (right)  $R > 8 \text{ mm h}^{-1}$  for all regions with a JJA wet season, based on JJA 1998–2002 2A25 data. The probability is normalized, i.e., it is the number of occurrences per 2 dBZ per 250 m, divided by all occurrences in all reflectivity and height bins, and expressed as a percentage. The total number of occurrences is shown in the upper-right corner of each plot, in thousands. Vertical lines are drawn at 30 and 40 dBZ, and horizontal lines at 4-, 7-, and 10-km height.

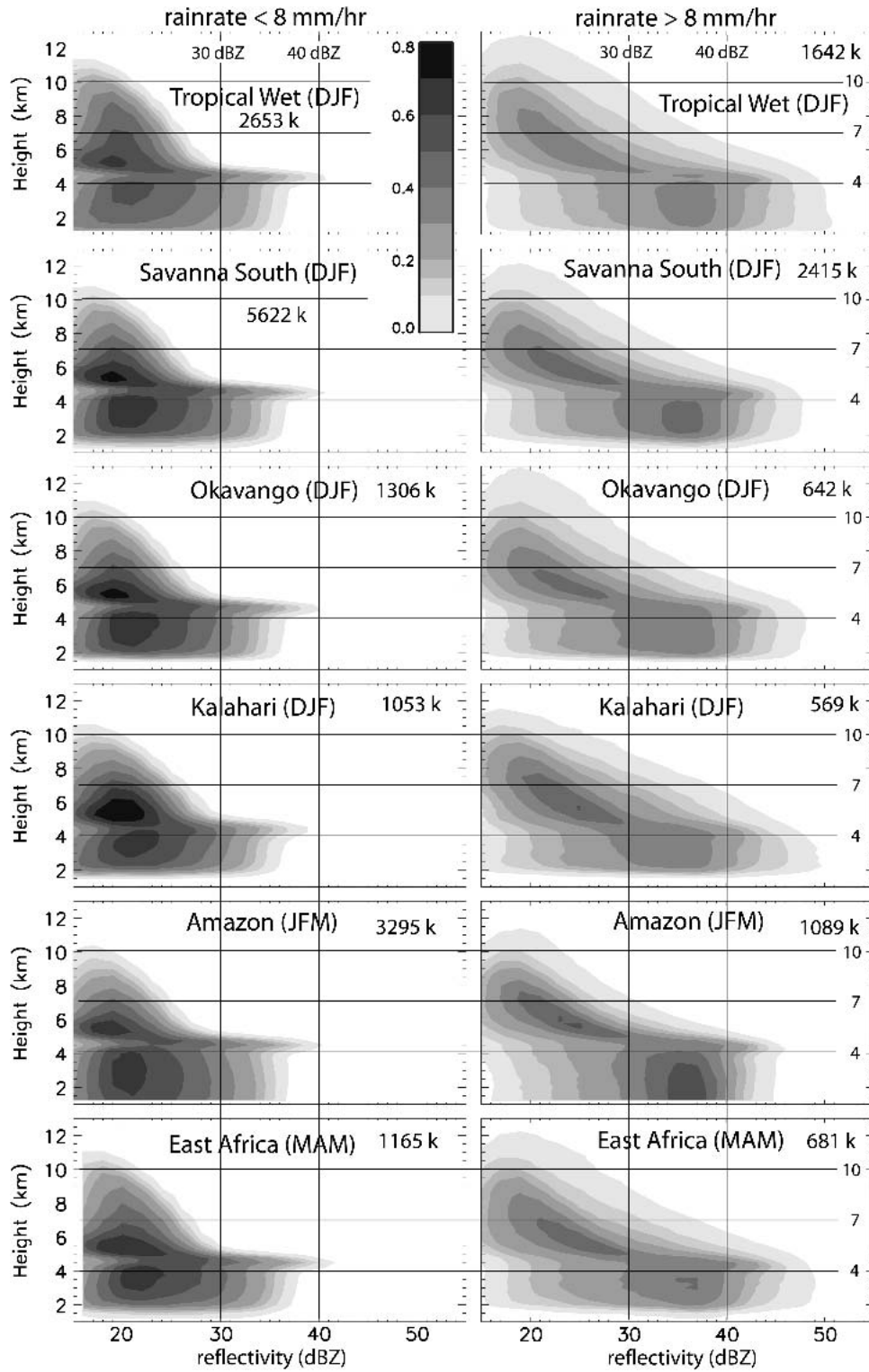


FIG. 3. As in Fig. 2, but for the regions with a DJF wet season. Also included here are East Africa (MAM) and the Amazon Basin (JFM).

TABLE 2. Frequency of virga and of warm rain, expressed as a percentage of all precipitation profiles.

Region—season	Virga	Warm rain
Sahara—JJA	28	2.9
Sahel—JJA	16	3.1
Savanna North—JJA	15	5.7
Tropical Wet—JJA	12	9.7
East Africa—JJA	12	9.0
Horn Africa—JJA	13	3.1
Kalahari—DJF	15	6.4
Okavango—DJF	13	6.7
Savanna South—DJF	12	7.2
Tropical Wet—DJF	15	7.4
East Africa—MAM	10	8.0
Amazon—JFM	10	16.7

has a larger fraction of stratiform precipitation. It is well-defined in the Amazon, although not better than in some African regions, such as the Tropical Wet in JJA. It is absent in case of heavy rain in many regions (e.g., the Horn and East Africa in JJA, or the Tropical Wet in DJF), suggesting that the heavy rain there is largely convective. In the Horn and East Africa these may be mostly orographically controlled precipitation systems that do not develop much mesoscale organization. The brightband spike is least defined in the desert regions (Kalahari and Sahara) and best defined in the Sahel and northern Savanna regions, where it can be seen even in the heavy rain cases. This may be due to the occurrence of large mesoscale convective systems and associated stratiform regions there (e.g., Roux et al. 1984; Chalon et al. 1988). Storms producing heavy rain differ little regionally in terms of vertical structure. Over the northern arid and semiarid regions they tend to be a little deeper, and have higher reflectivities aloft,

than in the Tropical Wet region, but the FADs are quite similar.

The FADs discussed above includes profiles in which rain does not reach the ground. The fraction of virga profiles varies from 10% in the Amazon, 10%–16% in all regions of Africa (except the Sahara), to 28% in the Sahara (Table 2). Virga-producing storms are often quite deep, but their peak reflectivity is generally below 30 dBZ (Fig. 4). In arid regions such as the Sahara, the virga profiles tend to be more top-heavy than in the Tropical Wet, in terms of the vertical distribution of reflectivity, and thus they may have a larger ice hydrometeor concentration and a stronger 85-GHz ice scattering signature than in the Tropical Wet. This, plus the higher virga fraction in the Sahara implies that passive-microwave-based surface rain-rate estimations may be too high in the Sahara.

In all regions the virga FADs show a spike at the FL, more so in the Tropical Wet than the Sahara. This spike is more clearly defined than in the corresponding FADs for light rain events ( $<8 \text{ mm h}^{-1}$ ; Fig. 2), suggesting that virga profiles are often stratiform. Many of the virga profiles may be associated with mesoscale convective systems in their mature to dissipating stages (Smull and Houze 1987; Houze 1997). Mesoscale convective complexes are more common in the Sahara, Sahel, and northern Savanna than in other regions (Laing and Fritsch 1993). This may contribute to the relative prevalence of virga profiles in these regions (Table 2).

#### b. Storm intensity

To further compare and contrast the typical vertical storm structure in various regions in Africa, we examine the frequency distribution of reflectivities as a func-

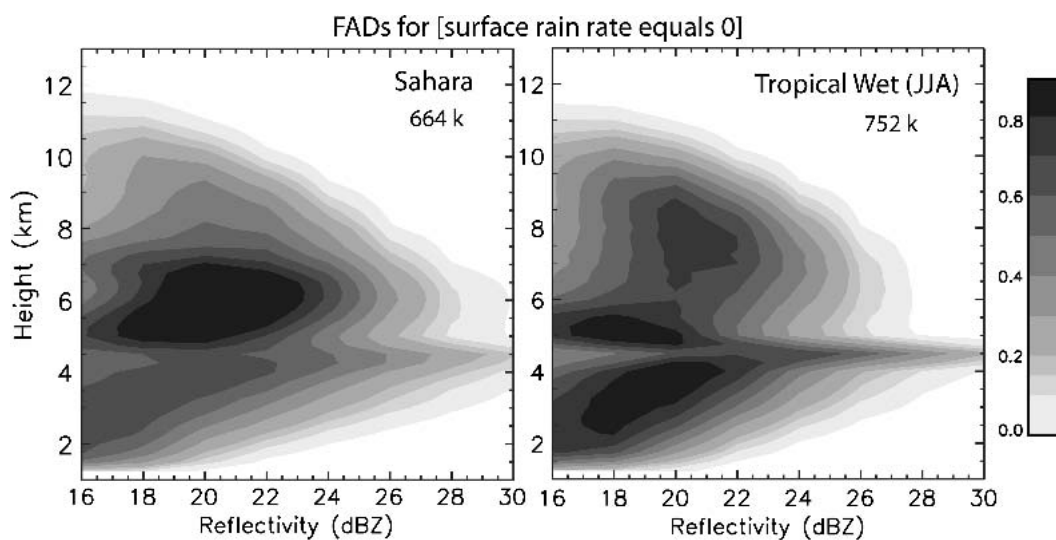


FIG. 4. As in Fig. 2, but for virga profiles only, in the Sahara and the Tropical Wet (JJA) region. Note that the maximum reflectivity plotted is only 30 dBZ. The last contour peaks at 32 dBZ in the Sahara and 33 dBZ in the Tropical Wet region.

tion of height, for various exceedance levels (Fig. 5). The frequencies are divided by the total number of precipitation profiles in each region, so Fig. 5 shows the probability of a reflectivity of at least the threshold value (17, 27, or 37 dBZ) as a function of height. Such PDFs are preferred over mean reflectivity profiles, because the calculated mean reflectivity will be above the true mean if only the measured population ( $>17$  dBZ) is included in the average, and below the true mean if all profiles are included and the unsampled population ( $<17$  dBZ) is given an arbitrary value, for example,  $Z = 0 \text{ mm}^6 \text{ m}^{-3}$ . Also, even if the PR were able to measure the full reflectivity spectrum, the mean reflectivity at any level is based a decreasing sample size in the upper troposphere, thus its profile does not repre-

sent the same population at all levels, and at its highest level it only represents the deepest storm. In short, mean reflectivity profiles are not very meaningful. To assess sensitivity to the normalization method, the frequencies shown in Fig. 5 were normalized also by the total number of reflectivity occurrences at all levels (listed in Figs. 2 and 3), and the results are essentially the same. The maxima remain  $<100\%$  in the left panels of Fig. 5, because there may be precipitation profiles (possibly virga) that do not have a detectable echo at the level of these maxima.

We also examine the mixing ratio  $q_h$  of hydrometeors (Fig. 6). Hydrometeors are defined here as rain or snow large and widespread enough within the PR footprint to produce an echo of at least 17 dBZ. This mixing

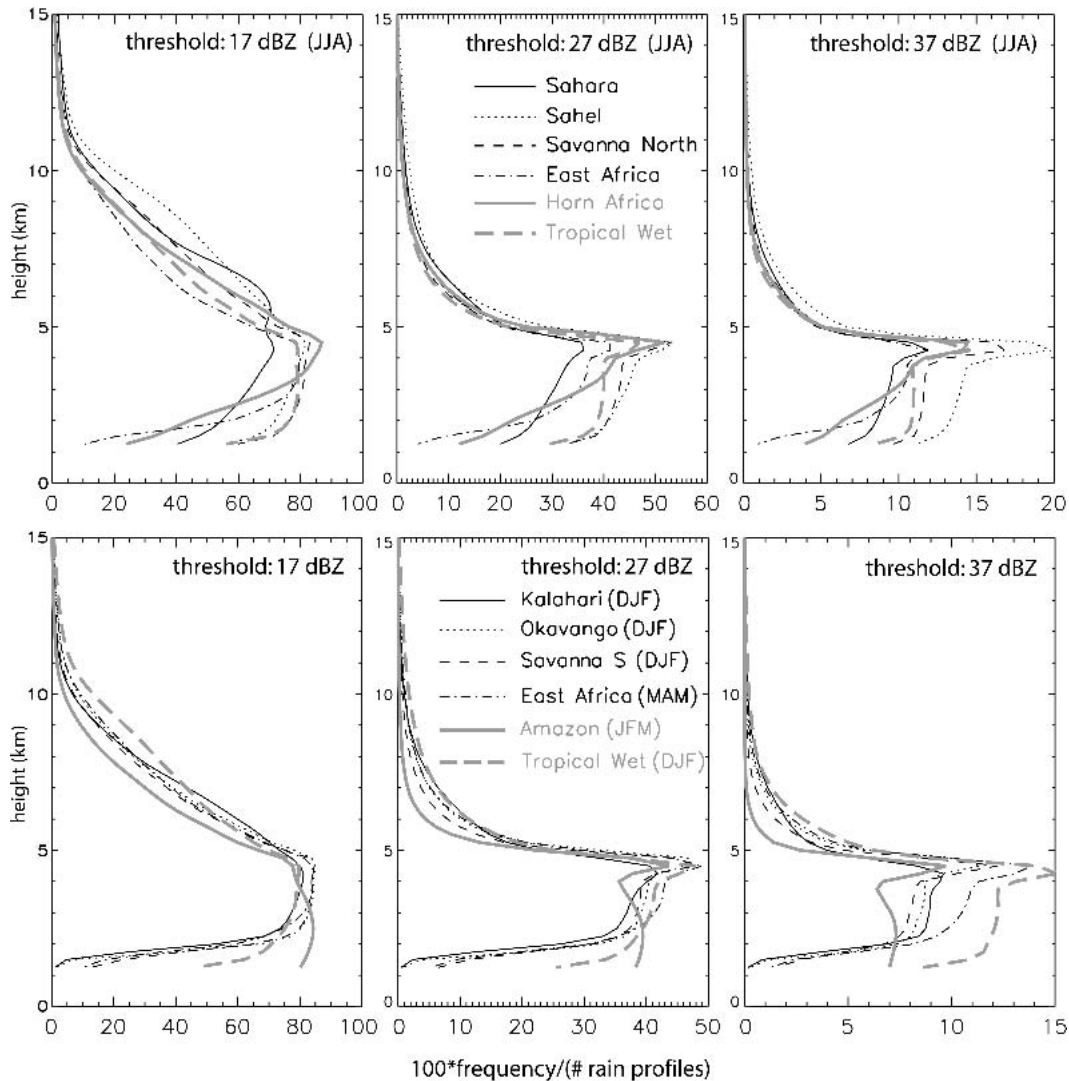


FIG. 5. Frequency distribution of reflectivity values with height. Three thresholds are used: (left) 17, (middle) 27, and (right) 37 dBZ. (top) JJA regions and (bottom) DJF regions. Note that the range displayed along the  $x$  axis varies.

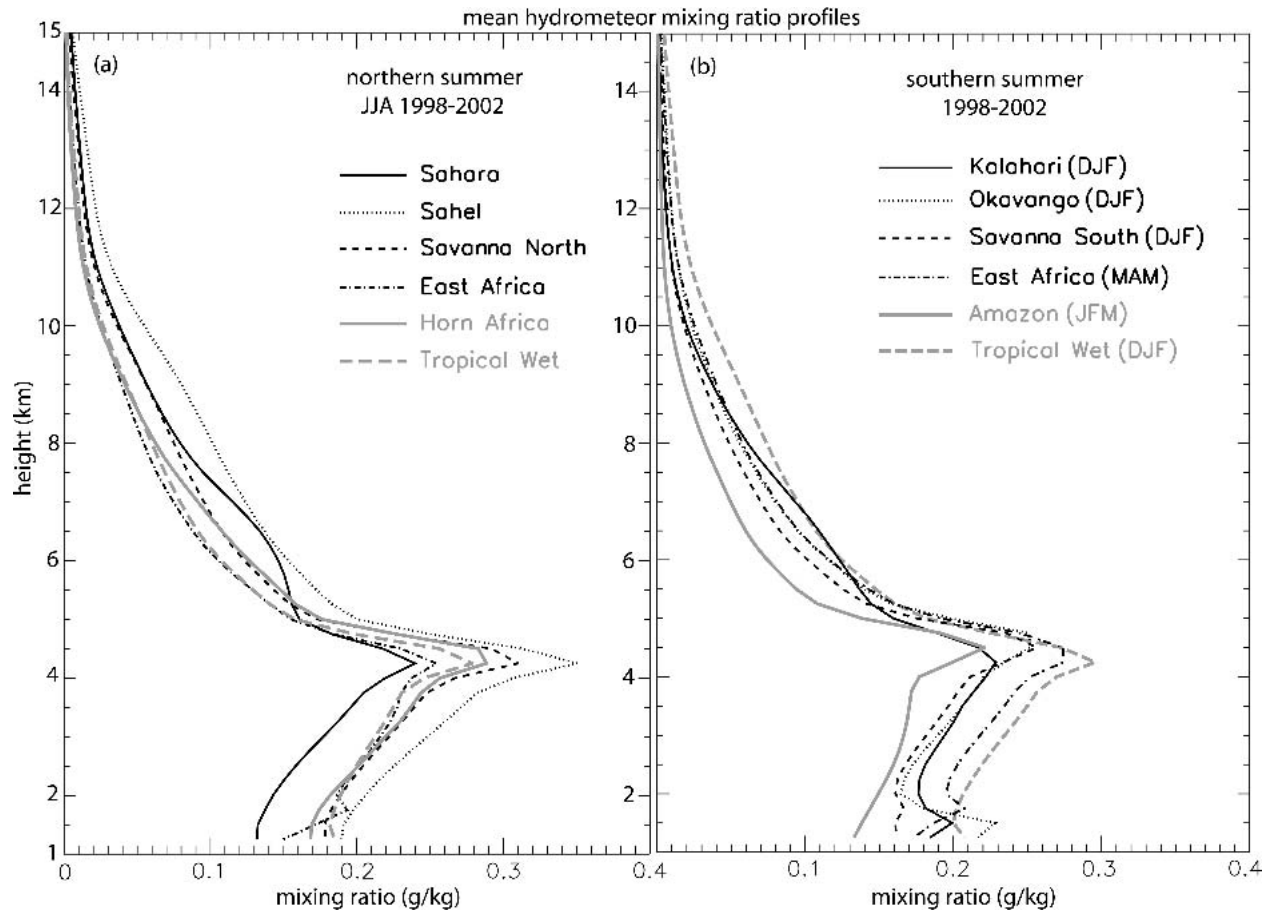


FIG. 6. Profiles of hydrometeor water content for all regions. See text for details. (a) JJA regions and (b) DJF regions.

ratio  $q_h$  ( $\text{g kg}^{-1}$ ) is derived from an empirical  $Z$ - $q_h$  relationship,

$$q_h = 3.2 * 10^{-3} Z^{0.55} e^{h/8} \quad (\text{rain: for } h < 4.5 \text{ km}), \quad (1a)$$

$$q_h = 6.8 * 10^{-3} Z^{0.45} e^{h/8} \quad (\text{snow: for } h \geq 4.5 \text{ km}), \quad (1b)$$

where  $h$  is the height in km,  $Z$  the equivalent reflectivity in  $\text{mm}^6 \text{m}^{-3}$ , and  $e$  the exponent. The constants are based on Eqs. (7.13c) and (7.13d) in Battan (1973) for liquid and frozen hydrometeors in an array of summertime precipitation systems in North America. These relationships are experimental, and no effort was made to validate them. We are merely interested in the regional variation of the profile and the vertically integrated amount, as a proxy for the true hydrometeor water contents in storms in Africa.

Some interesting regional differences appear in the vertical storm structure in Africa. The Sahel region experiences the most intense storms, in terms of the frequency of echo strength above 7 km, the occurrence of strong echoes at low levels (Fig. 5), and the hydrometeor content (Fig. 6). The Sahara storms tend to be nearly as intense aloft (especially near 6 km), but the

low-level reflectivity is lower, and the kink at the FL is less defined, as compared to the Sahel. The Tropical Wet region tends to have deeper, more intense storms in the southern summer than the northern summer; in fact, the deepest, most intense storms in the southern summer tend to be found in the Tropical Wet region, mostly in the southern Congo Basin. The average conditional rain rate at the ground in DJF in the Tropical Wet region is higher than elsewhere, even the Sahel (Table 1).

In general the northern zenithal rain regions (Sahara, Sahel, and Savanna) tend to have deeper storms than their southern counterparts (Kalahari, Okavango, and southern Savanna, respectively) (Figs. 2, 3, 5). Echo frequency generally decreases for all thresholds in Fig. 5 from below the FL to a level still above the terrain in all regions of Africa (say 2 km). This suggests evaporation (or breakup) of raindrops.

A clear difference does exist between storms in any African region and those over the Amazon: Amazon storms tend to be more shallow and their mean profile has a more stratiform appearance than in Africa, with a clear brightband maximum in the 27- and 37-dBZ thresholds (Fig. 5) and a remarkably rapid decay of

reflectivity counts with height above the bright band. Rain events are quite frequent in the Amazon (Table 1), but the average conditional rain rate at the ground, as derived by the PR, is lower than in any African region (Table 1), which is consistent with the low hydrometeor mixing ratio in the Amazon near the ground (Fig. 6b). Also, the reflectivity counts in the Amazon tend to increase from 4 km down to 2 km for all thresholds (Fig. 5). This unusual property suggests that rain drops grow toward the ground, which may imply a low average cloud base in the Amazon region.

*c. Echo tops*

The regional variation of echo tops is shown in Fig. 7. The echo top is defined for each profile as the highest occurrence of the 20-dBZ contour. The value of 20 dBZ is close to the minimum detectable signal and it has been used elsewhere (e.g., Toracinta et al. 2002). In addition to the echo top distributions for the various

regions, Fig. 7 also shows the distribution inferred from Short and Nakamura (2000, their Fig. 2). That study uses the TRMM 3A25 (monthly mean) parameter “storm height,” which is the highest measurable echo at the PR sensitivity, for all storms over land between 30°N and 30°S for JJA and DJF 1998. The Short and Nakamura (2000) curves correspond with the echo top PDFs in Africa (Fig. 7).

The 20-dBZ echo top is clearly most likely to occur near the FL in most regions in Africa. Short and Nakamura (2000) confirm the existence of this maximum over all tropical land regions; however, their maximum is less spiked, because their vertical resolution is worse (500 m). The peak near the FL may represent a population of warm cumulus congesti, which have been shown to be important over tropical oceans (Johnson et al. 1999). Or they may be rather weak stratiform precipitation regions with snow aloft, but too weak to be detected above the bright band. The PR horizontal resolution may also contribute: even intense storms,

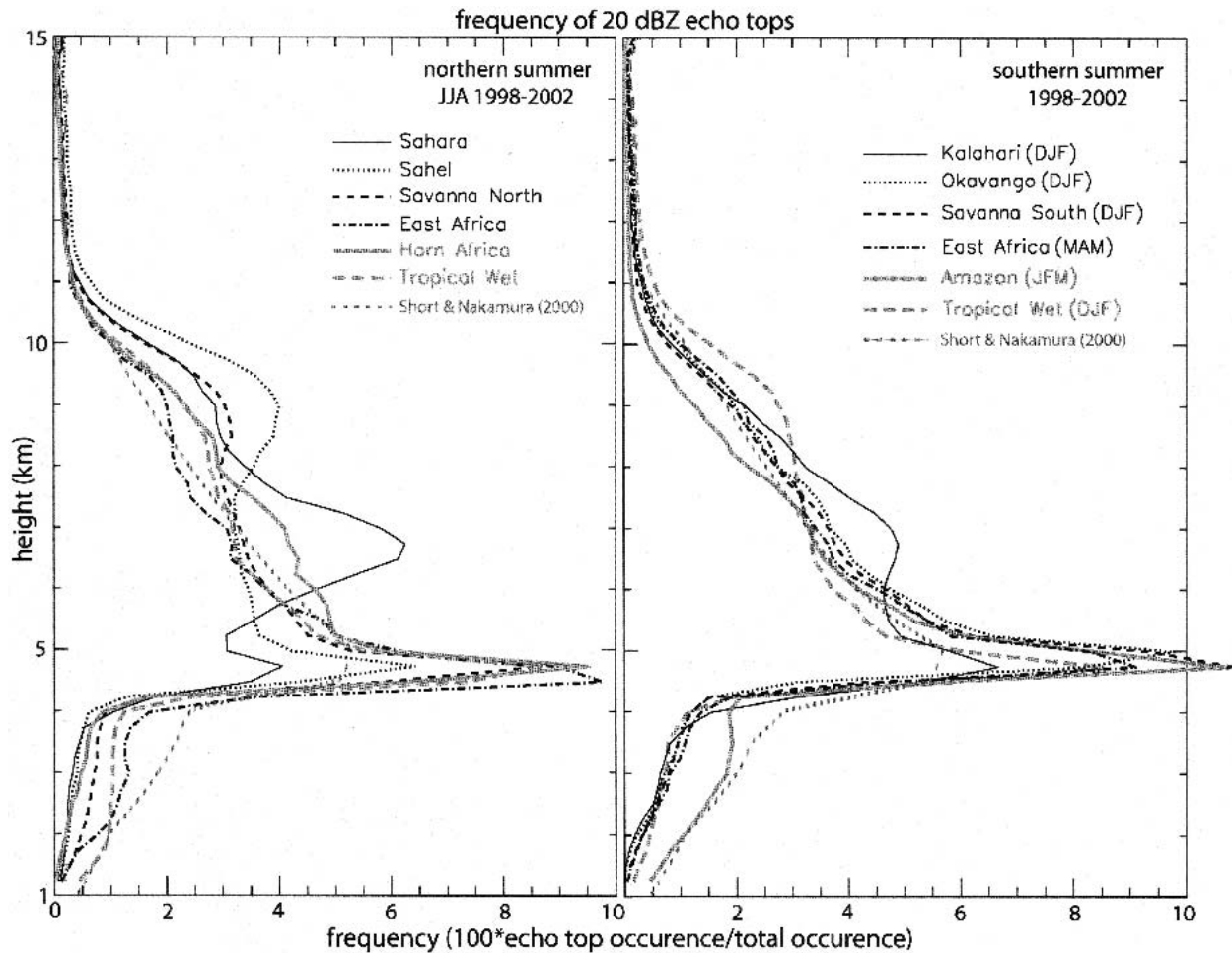


FIG. 7. Probability density functions of 20-dBZ echo tops for all surface rain profiles. The probability is normalized, i.e., it is the number of occurrences per 250 m, divided by all occurrences in all height bins, and expressed as a percentage. PDFs inferred from Short and Nakamura (2000) are shown as well, for both seasons.

smaller than the PR footprint, may only become detectable near the FL (Heymsfield et al. 2000). This clustering of 20-dBZ echo tops near the FL is most pronounced in the Amazon (Fig. 7), where high reflectivity values above the FL are rare, even in heavy rain events ( $>8 \text{ mm h}^{-1}$ ; Fig. 3).

Within Africa, a remarkable difference exists between storm depths in the arid regions and those elsewhere (Fig. 7). The Tropical Wet, Savanna, East Africa, Horn, and Okavango regions all have a single maximum echo top at the FL. The Sahara and Kalahari regions have a peak just below 7 km. The secondary echo top maximum at 9 km in the Sahel is another confirmation that storms there are most intense (Figs. 5, 6). Deep, vigorous storms are also common in the Tropical Wet region in the southern summer (Figs. 5, 7). These observations will be interpreted in terms of climatological thermodynamic profiles in section 5.

Shallow, warm-rain events are relatively rare in Africa. Warm-rain events are defined as those PR profiles with rain at the surface *and* a 17-dBZ echo top below 4.25 km, the lowest level that may be affected by the

brightband maximum (Fig. 7). Warm rain is 2.5 times more likely in the Amazon than in the African regions, on average (Table 2). In fact, the Amazon echo top distribution has a secondary maximum below the FL (Fig. 7), something that is more clearly established over the tropical oceans (Short and Nakamura 2000). This confirms that Amazon precipitation profiles are more maritime in character than those in Africa.

Warm rain is less common in the arid, semiarid, and savanna regions of the north than in the corresponding climatic regions in the south (Table 2). This is especially remarkable since the southern part of the continent is about 1.5-km high, thus warm-rain processes are confined to a more shallow depth. In Africa warm rain is most common in the Tropical Wet region, especially in JJA. An FAD of the warm-rain profiles in this region (Fig. 8) shows that reflectivity increases from the echo tops toward the lowest levels. This reflectivity profile is consistent with a low cloud base and growth by collision/coalescence. A similar composite reflectivity profile has been documented for warm-rain events in the Amazon (Geerts and Dawei 2004b).

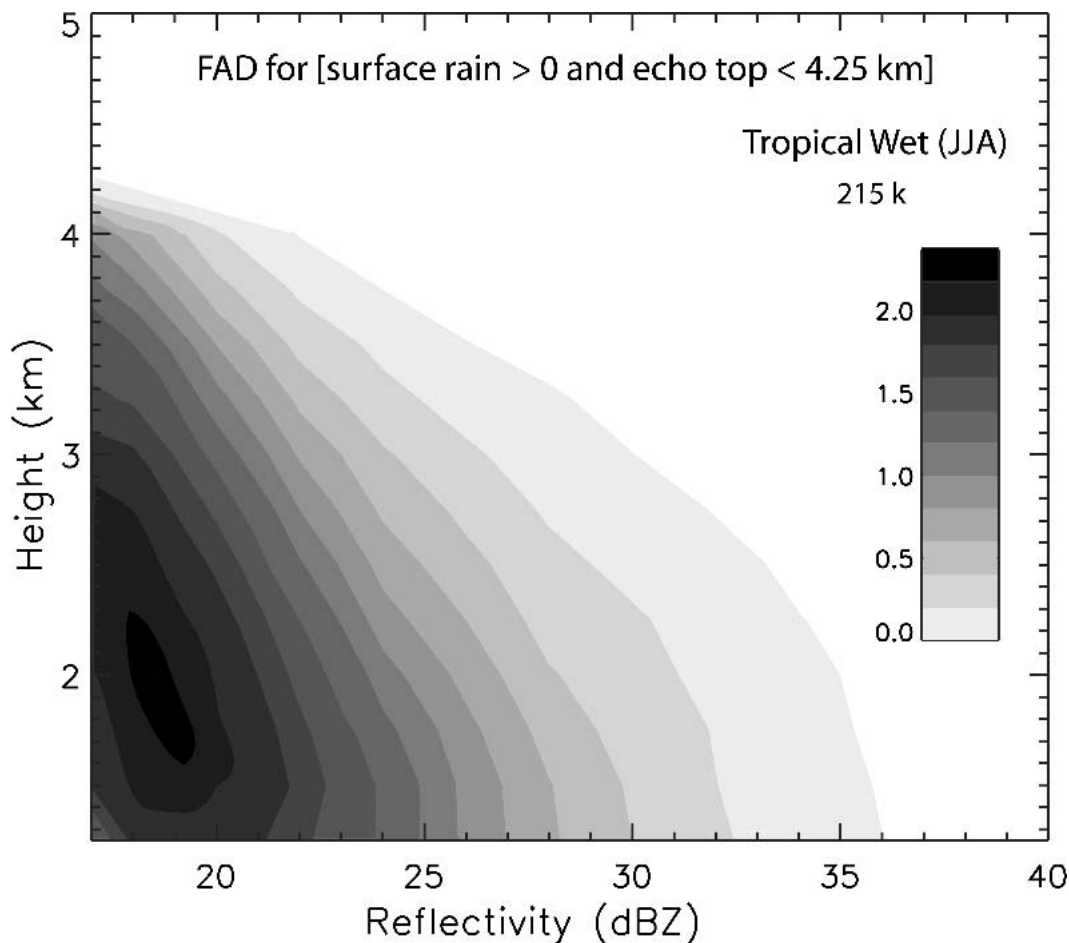


FIG. 8. As in Fig. 2, but for warm-rain profiles only, in the Tropical Wet (JJA) region.

#### d. Indices of vertical storm structure

Some indices are derived to facilitate a comparison of the characteristic vertical storm structure between regions (Table 3). The *evaporative index* (EI) is defined as the reflectivity at 4.0 km minus that at 2.0-km height. The 4.0-km level is the highest one not contaminated by a bright band, and the 2.0 km is the lowest one above the Earth surface in most places of Africa. A rapid decrease in reflectivity from 4 km down to 2 km, at a scale resolved by the PR, is likely to indicate evaporation of raindrops. The EI is computed for each individual profile in dBZ units, and profiles with reflectivity values below the PR's threshold sensitivity at either level are ignored.

The *stratiform index* (SI) is defined as the reflectivity at 7.0 km minus that at 4.5-km height. The average FL during the wet season in tropical Africa is 4.5–4.6 km; therefore, the 4.5-km level is the most likely location of a bright band, as is evident in Fig. 2. This index is called the stratiform index, because it combines two characteristics of stratiform precipitation: the presence of a bright band, and the rapid decay of reflectivity above the bright band (Geerts and Dawei 2004a). Just as the EI, the SI is computed for each profile as a difference in dBZ units. Again profiles with reflectivities below the PR's threshold sensitivity at 7 km or at 4.5 km are ignored.

The *hydrometeor precipitable water* (HPW) is defined as the vertically integrated liquid or frozen hydrometeor content, and is expressed as a depth of water (mm):

$$\text{HPW} = \frac{1}{\rho_l} \int_0^{\text{top}} \rho q_h dz, \quad (2)$$

where  $\rho_l$  is the density of water ( $\rho_l = 10^3 \text{ kg m}^{-3}$ ) and  $\rho$  is the density of air ( $\text{kg m}^{-3}$ ). The mixing ratio  $q_h$  ( $\text{g kg}^{-1}$ ) of rain and snow is estimated from reflectivity using Eq. (1). Finally, the *storm productivity index* (SPI) is defined as the ratio of the surface rain rate  $R$

( $\text{mm h}^{-1}$ ) over the vertically integrated hydrometeor content HPW:

$$\text{SPI} = \frac{\rho_l R}{\int_0^{\text{top}} \rho q_h dz}. \quad (3)$$

The SPI has units of  $\text{h}^{-1}$ . The rain rate  $R$  is a PR-based variable in the 2A25 files. While the HPW is affected by the drop-size distribution (rain type), the SPI is rather insensitive to uncertainties in mean drop size, because it is a ratio [see section 2a and Eq. (1)]. The larger the SPI, the more rain is generated by a storm with a given reflectivity profile. Shallow storms have a higher SPI than deep ones. The SPI of storms over high terrain also tends to be higher because of the reduced depth of the reflectivity profile. In both cases the cloud base tends to be closer to the ground, thus less low-level evaporation occurs. Therefore the SPI is somewhat related to the precipitation efficiency of a storm, which is the ratio of the amount of precipitation at the surface to the amount of liquid or frozen cloud water generated by the storm (Hobbs et al. 1980).

The exact values for both the HPW and the SPI are of little meaning, given the uncertainty of the  $q_h$ - $Z$  relationships [Eq. (1)]. The indices are used merely to highlight regional differences. All indices listed above, including the EI, are based on profiles with surface rain.

The regional variation of these indices is summarized in Table 3. Storms in the Sahara carry much water above the FL, producing a low SI, yet much water evaporates before reaching the ground, yielding the highest EI (Table 3) and virga fraction (Table 2) of all regions, yet the lowest SPI. The Sahel has a low SPI as well, but that is due more to the great depth of the storms (Fig. 5; i.e., the high HPW, than to low-level evaporation; Table 3). From the arid regions in both hemispheres toward the Tropical Wet, the EI and the virga fraction steadily decrease and the SI generally increases. On exception is that the SI is slightly higher in the Savanna regions (north and south) than in the Tropical Wet. This is consistent with the fact that during the respective wet seasons, the savanna regions are wetter than the Tropical Wet (Table 1). The EI and virga fraction are higher in the northern regions (JJA) than in the corresponding regions south of the equator (DJF), which is consistent with differences in warm-rain fraction (Table 2). The SI is roughly the same in corresponding regions across the equator. The SPI tends to be higher in the equatorial regions, especially in the Horn and East Africa, where the terrain is higher. The higher terrain is also consistent with the higher SPI in the southern regions than the corresponding northern regions.

The fractions in Table 2 and indices in Table 3 highlight how distinct the Amazon is compared to any region in Africa: the EI is negative (low-level rain

TABLE 3. Mean values of the EI (between 4 and 2 km), the SI (between 4.5 and 7 km), the HPW, and the SPI for the various regions and seasons. See text for the definition of these indices.

Region—season	EI dBZ	SI dBZ	HPW mm	SPI $\text{h}^{-1}$
Sahara—JJA	1.99	6.8	0.82	3.11
Sahel—JJA	1.52	9.7	1.11	3.12
Savanna North—JJA	0.99	10.4	0.96	3.39
Tropical Wet—JJA	0.76	9.8	0.74	4.12
East Africa—JJA	0.68	8.8	0.71	4.71
Horn Africa—JJA	1.17	10.0	0.79	4.25
Kalahari—DJF	1.2	7.3	0.72	3.89
Okavango—DJF	0.74	9.7	0.74	3.58
Savanna South—DJF	0.64	10.6	0.71	3.64
Tropical Wet—DJF	0.57	10.1	0.87	3.8
East Africa—MAM	0.68	10.5	0.80	4.09
Amazon—JFM	-0.35	11.6	0.65	3.98

growth) and the virga fraction is low. Storms tend to be relatively shallow and weak, with a high warm-rain fraction and a strong stratiform signature, implying a high SI and a low HPW. Only the SPI is similar to that in Africa, because the impacts of the typically low rain rates (Table 1) and the low HPW cancel each other.

#### 4. Diurnal variability

##### a. 2A25 surface rain rate

The diurnal cycle of the average 2A25 surface rain rate ( $R$ ) during rain events is shown in Fig. 9. Heavy rainfall is most likely in the afternoon and evening over most regions in Africa. In most regions the peak rainfall occurs during the 1500–1800 LT period. It is possible that the diurnal variation of the TRMM PR surface rain is partly due to the variation in mean drop diameter ( $D$ ), since the reflectivity factor  $Z \sim D^6$ : afternoon convective rain may have a larger mean drop size than late-night precipitation (A. Tokay 2004, personal communication). The change in mean drop size is accounted for, somewhat, by applying a different  $Z$ – $R$  (rain rate) relationship for different rain types, convective or stratiform (section 2a). Nevertheless, the possibility remains, and the diurnal variation in rain amount (Fig. 10) may be due more to a variation in rainfall frequency than one in rain rate (Dai 2001). No attempt is made to compare PR-based surface rain data to passive microwave rainfall over Africa.

The sunrise-to-noon quartile is the most suppressed in terms of both rain rate and rain amount in all regions. The diurnal modulation of rain rate and rainfall amount is strongest in East Africa (JJA) and the desert regions

(Kalahari, Sahara). Within Africa, it is weakest in the Tropical Wet region. It is even weaker in the Amazon, at least in terms of rain rate. The radar-based study of Rickenbach (2004) describes a similar, slightly higher diurnal rain-rate variation, although the region, Rondonia, is only partially within the Amazon box as defined in this study.

A single 1500–1800 LT peak dominates in the mountainous region of East Africa (JJA), again both in terms of rain rate and rain amount. The semiarid regions in the north (Sahel and northern Savanna) peak later (1800–2100 LT); those in the south (Okavango and southern Savanna) peak earlier (1200–1500 LT). A secondary nocturnal peak in rain rate (Fig. 9) and rain amount (Fig. 10) is observed in the Tropical Wet region, both in the Congo Basin and in the south coast region of West Africa (Fig. 1), in both seasons (DJF and JJA). These secondary peaks occur between midnight and sunrise. It is not clear what causes this secondary maximum in the Congo Basin, but in the West African coastal strip that secondary maximum is due mostly to convection offshore, such as over the Bay of Benin, which is included in the coastal strip. The primary maximum there corresponds with onshore convection, possibly triggered by a sea-breeze circulation (Fig. 11). This see-saw in coastal convective precipitation has been described by means of radar or passive microwave data in this region (Negri et al. 1994) and elsewhere in the Tropics (Houze et al. 1981; Dai 2001; Mapes et al. 2003). The diurnal see-saw in the coastal strip is slightly offset compared to the diurnal peaks in the Tropical Wet region (Fig. 10): the offshore peak is delayed until 0600–0900 LT, that is, after sunrise, and

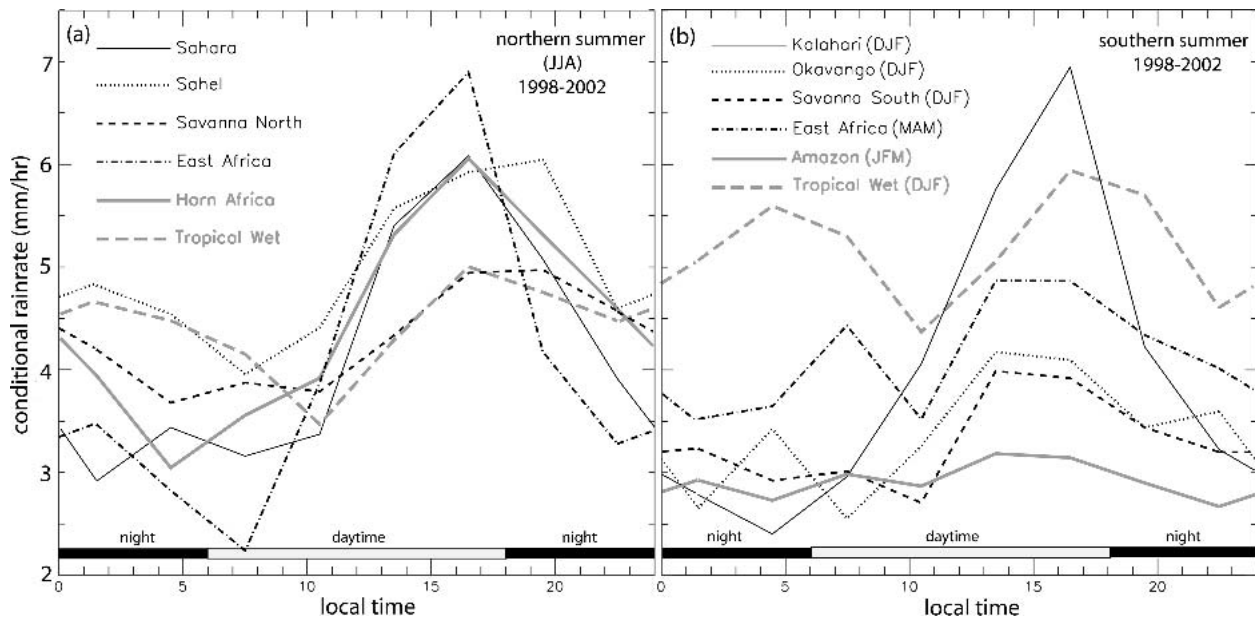


FIG. 9. Diurnal variation of the average surface rain rate, when rainfall is detected, for (a) JJA regions and (b) mostly DJF regions.

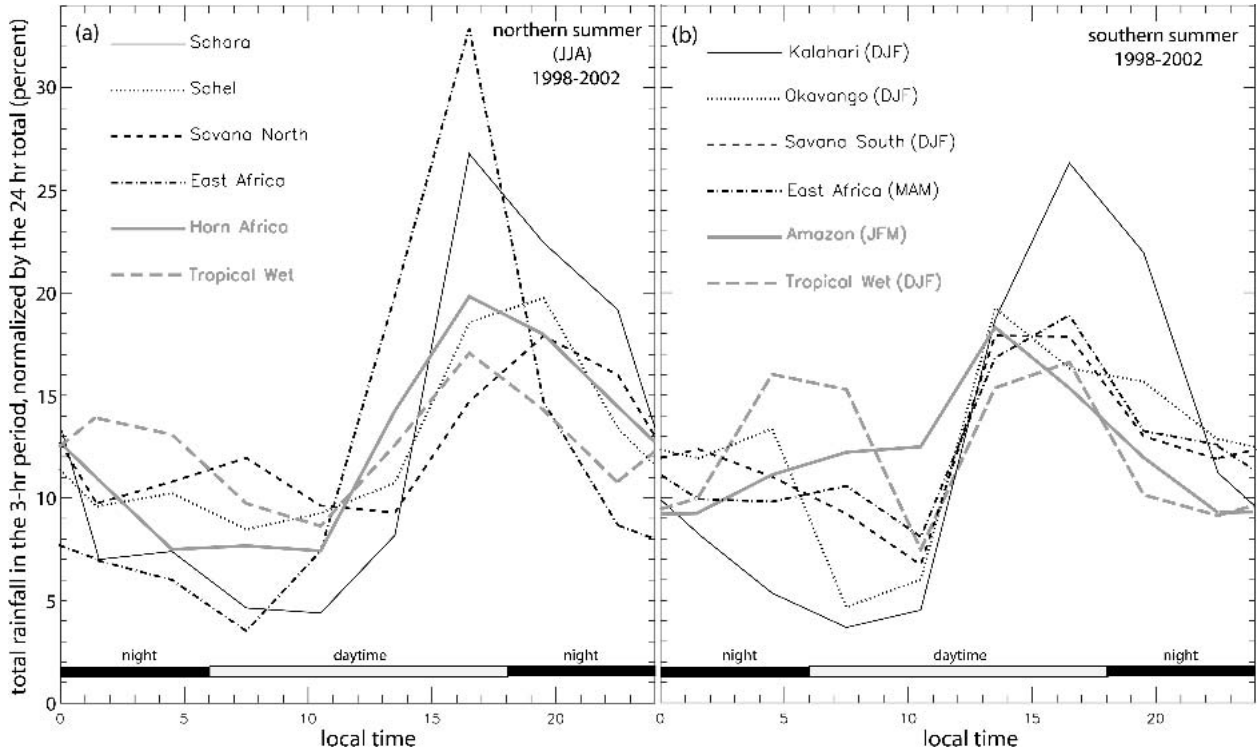


FIG. 10. Diurnal variation of the surface rain total for (a) JJA regions and (b) mostly DJF regions. The total in any 3-h time bin is normalized by the rainfall in all eight time bins, so the average value is 12.5.

the onshore peak seems to occur earlier in the afternoon (1200–1800 LT). As a result, the dawn offshore peak and afternoon onshore peak are separated by only 6 h. Mapes et al. (2003, their Fig. 7) observe a similar asymmetry along the Columbian coastal region, although there some nine hours exist between the dawn offshore and afternoon onshore peaks. The secondary nocturnal peak in the Tropical Wet remains present when the coastal strip is excluded, that is, in the Congo Basin.

#### b. Storm vertical structure

It was shown in section 3c that the 20-dBZ echo top heights vary regionally. They also vary diurnally, as shown in Fig. 12. On average they are 0.5–2.3 km more shallow in the morning quartile (sunrise to noon) than near sunset in Africa. Mean echo tops generally increase rapidly from just before noon to late afternoon, and then they decrease slowly during the night and early morning. Consistent with the rain-rate variation (Fig. 9), the echo tops in the southern Savanna and Okavango tend to peak earlier in the afternoon (1500–1800 LT) than those in the northern Savanna and Sahel. Also, the diurnal variation of echo top height is weakest in the Amazon, and the Tropical Wet has a secondary maximum before sunrise (at least in DJF). Consistent with Fig. 7, the echo tops tend to be highest in the Sahel

and lowest in the Amazon. In East Africa, the diurnal modulations of echo tops, as well as that of rain rate (Fig. 9) and rain amount, are strong in the transition season (JJA), while in the wet season (MAM) they are weaker, and more comparable to that in the Tropical Wet (DJF) region.

We now describe the diurnal variation of the reflectivity FADs as a way to gain an insight into the observed changes in echo top height. Shown in Fig. 13 are the frequencies in any 3-h time bin, normalized as in Fig. 2, and then shown as an anomaly from the 24-h mean, for all echoes observed over five JJA seasons in the Sahel. To clarify, let  $N_t(Z, h)$  be the normalized frequency for a reflectivity value  $Z$  at a height  $h$ , within the time bin  $t$ , such that  $\sum_Z \sum_h N_t(Z, h) = 100$ . Shown in Fig. 13 is the difference  $N_t(Z, h) - \bar{N}(Z, h)$ , where  $\bar{N}(Z, h)$  is the 24-h mean frequency. Clearly the integrated anomaly, at any time bin, will be zero:

$$\sum_Z \sum_h \{N_t(Z, h) - \bar{N}(Z, h)\} = 0$$

$$\sum_Z \sum_h N_t(Z, h) - \sum_Z \sum_h \bar{N}(Z, h) = 100 - 100 = 0. \quad (4)$$

Thus the diurnal anomaly FADs do not reveal the changes in rainfall frequency during the day (shown in

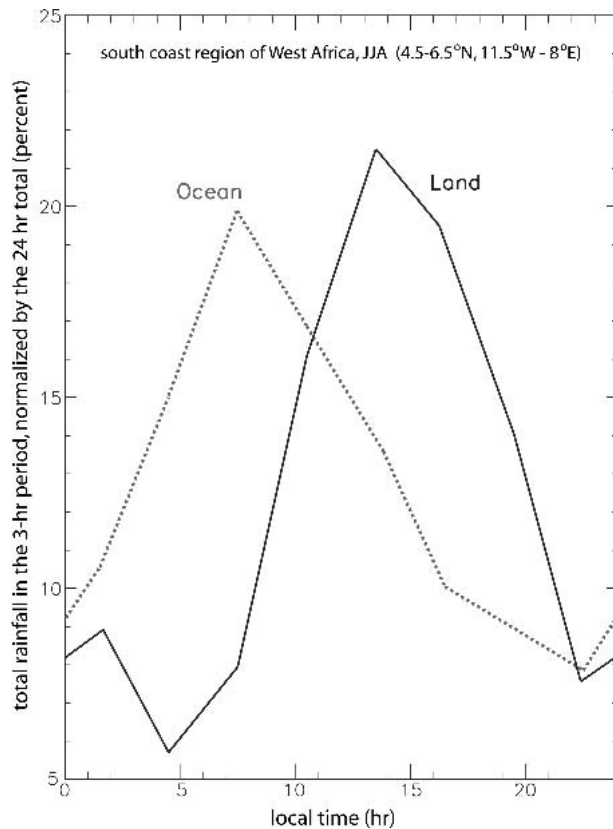


FIG. 11. As in Fig. 10, but for the coastal strip of West Africa in JJA. The land section is contrasted against the coastal Atlantic Ocean.

Fig. 10). They show the anomalous vertical structure of a storm occurring at a certain time, as compared to the normal (daily mean) vertical structure. But for each time bin in Fig. 13, the sample size is shown. The diurnal cycles of the vertical structure of storms in other African regions contain similarities with the patterns shown in Fig. 13 for the Sahel. Diurnal anomaly FADs as the one shown in Fig. 13 were analyzed for the six JJA regions and the six (mainly) DJF regions. The analysis is summarized in Table 4.

Three observations can be drawn from Fig. 13 and Table 4. First, a range of reflectivity values, especially high ones, commonly occur around the FL between 0300–1200 LT. This suggests more frequent stratiform precipitation in that time period. Such “BB max” period does not occur in East Africa (JJA), possibly indicating less storm organization.

Second, echoes below the FL are anomalously common when the sun is high in the sky (0900–1500 LT), suggesting that shallow convection (possibly warm-rain cumuli) are relatively more frequent at that time. This anomaly is more marked in the southern regions than their northern counterparts, and it is especially marked in East Africa, in the JJA transition season. However the latter anomaly occurs remarkably early: it peaks

between near dawn (0600–0900 LT; Table 4) in fact it is present between 0000–1200 LT. Echo tops tend to be most shallow in East Africa (JJA) at dawn (Fig. 12), and precipitation light (Fig. 9). Thus we interpret this 0600–0900 LT shallow anomaly as a result of the virtual absence of deep convection over East Africa (JJA) near dawn. This stands in contrast with the Tropical Wet (DJF) region, which also has a nocturnal maximum of shallow events (Table 4), but these events are associated with heavy rain (Figs. 9, 10).

And third, strong, deep echoes prevail in the evening hours (1500–2400 and mainly 1800–2100 LT). This indicates that deep, vigorous convection dominates at that time. The height of this anomaly decreases from the 1500–1800 LT bin to the 2100–2400 LT bin (Fig. 13). This is especially clear in the Sahel, over a large height range, and stronger in the northern (semi)arid regions than in the southern ones.

We summarize the diurnal variation of storm vertical structure in Fig. 14, a FAD of detectable echoes at various times of the day. This diagram reveals changes both in storm vertical structure and in storm frequency. The diurnal amplitude is small in the Tropical Wet and the Amazon, which is consistent with rainfall data (Figs. 9, 10). In other regions, especially the (semi)arid regions and in the transition season (East Africa JJA), storm echoes become more numerous and deeper from 0900–1500 to 1500–2100 LT. Clearly this pulsating echo structure implies diurnal pulses of latent heat release over the African troposphere. Also note that the echo count decays more rapidly with height above the FL at 0300–0900 than at 1500–2100 LT, particularly in the Sahel and northern Savanna regions. This suggests that vigorous convection is less likely around dawn than around sunset, and that storms are more stratiform and less deep around dawn.

## 5. Discussion

We now aim to interpret the main observations arising from the 2A25 data analysis by means of differences in the large-scale basic-state atmosphere, as documented by the NCEP–NCAR reanalysis dataset. Summarizing the observations, we found that in all regions in Africa, including the Tropical Wet, storms appear more vigorous than over the Amazon. Storms over the Amazon tend to be shallower (Fig. 7; many of them “shallow” or “warm-rain” echoes; Table 2), and they tend to have a lower HPW (Fig. 6), and a better-defined bright-band signature (Fig. 5). Also, reflectivity decays rapidly above the FL in the Amazon region (Fig. 3, Table 3), and the echo strength tends to increase from 4 km toward the ground (Table 3). Within Africa, the Sahel, and to a lesser degree the northern Savanna, stand out for vigorous storms, characterized by high echo tops (Fig. 7) and high hydrometeor loading aloft (Fig. 6). The lack of clear brightband spike (Fig. 2)

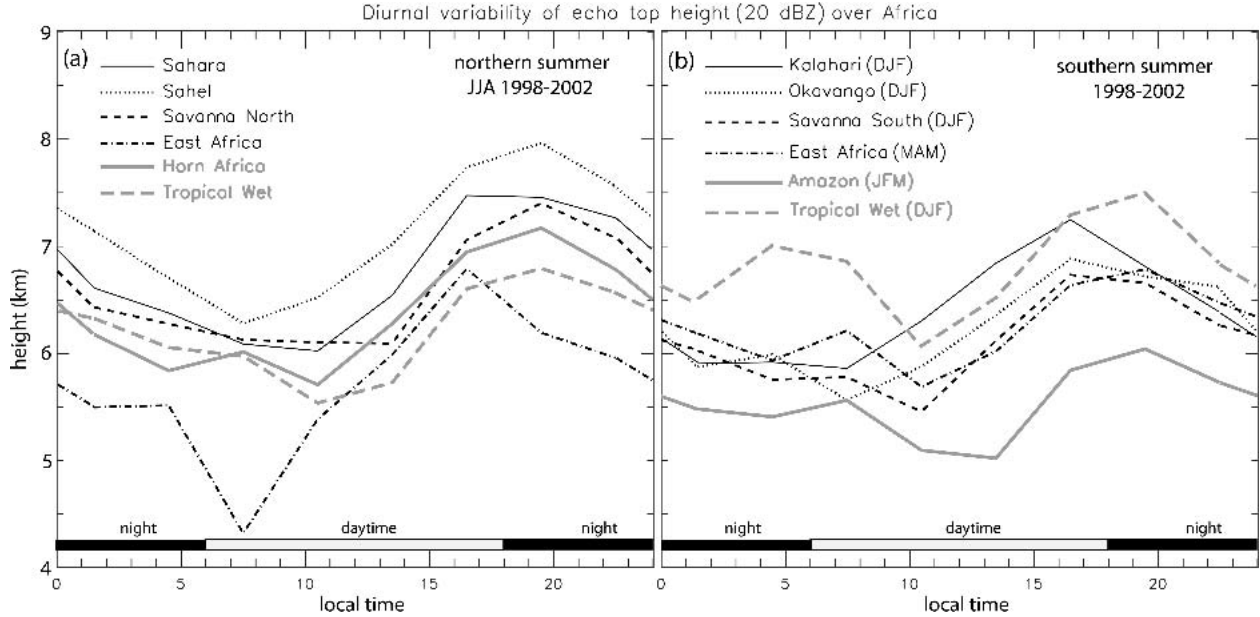


FIG. 12. Diurnal variation of the average 20-dBZ echo top height for (a) JJA regions and (b) mostly DJF regions.

suggests that these storms are mostly convective. In the Sahel and especially the Sahara, there is evidence for low-level evaporation (Table 3). Finally, rainfall (Figs. 9, 10) and vertical storm structure are least diurnally modulated over the Amazon and most strongly in the arid regions of Africa (Fig. 14, Table 4). In many regions the echo tops are highest (Fig. 12) and rainfall most intense (Figs. 9, 10) in afternoon (1500–1800 LT), but the diurnal peak is delayed to 1800–2100 LT in the Sahel and the northern Savanna.

The higher EI and virga fractions in the northern (semi)arid regions (JJA), compared to those south of the equator (DJF; Tables 2, 3), are consistent with the lower climatological relative humidity at the surface in the northern (semi)arid regions (Fig. 15). The average surface relative humidity values are 19%, 51%, and 83% for the Sahara, Sahel, and northern Savanna, respectively (JJA), while they are 37%, 67%, and 83% for the Kalahari, Okavango, and southern Savanna regions, respectively (DJF), according to the NCEP–NCAR reanalysis dataset.

Storm intensity is broadly related to the amount of potential (static) energy harbored in the environment. Shown in Fig. 16 are the profiles of  $\theta_e^*$  (saturated equivalent potential temperature) for select regions, based on the NCEP–NCAR reanalysis dataset for the corresponding seasons. The reanalysis data are averaged over each region, except for the Sahara where only the southern third is used (15°–20°N), because almost all of the storms in the Sahara database (Table 1) occurred there. From the  $\theta_e^*$  profile and the equivalent potential temperature  $\theta_e$  at 1000 mb ( $\theta_{e,sfc}$ ), one can estimate the level of free convection ( $LFC_e$ , mb) as the level where the  $\theta_{e,sfc}$  value intersects the ambient  $\theta_e^*$

curve. This  $LFC_e$  is not the same as the LFC traditionally defined on an aerological diagram, but it is related. The reason is that the  $\theta_e$  of an undiluted parcel rising from the surface is conserved, thus above the  $LFC_e$ , where the parcel is saturated, the parcel  $\theta_e$  (or moist static energy) is larger than the ambient  $\theta_e^*$  and thus also the ambient  $\theta_e$ .

We also compute a measure of convective available potential energy (CAPE;  $J kg^{-1}$ ). The CAPE is the integral of the buoyancy of an undiluted parcel from the LFC to the level of neutral buoyancy (LNB). We define the latter as the level where  $\theta_{e,sfc}$  rejoins the ambient  $\theta_e^*$  curve (Fig. 16), and denote it as  $LNB_e$ . We then define a measure of CAPE ( $CAPE_e$ ) as the excess of  $\theta_{e,sfc}$  over the ambient  $\theta_e^*$ , following Petersen and Rutledge (2001) and others. Thus

$$CAPE_e = R_d \int_{LFC_e}^{LNB_e} (\theta_e^* - \theta_{e,sfc}) d \ln p, \quad (5)$$

where  $R_d$  is the specific gas constant for dry air ( $287 J kg^{-1} K^{-1}$ ). The derivation of  $CAPE_e$ ,  $LFC_e$ , and  $LNB_e$  is shown in Fig. 16, and their values are listed in Table 5. The  $CAPE_e$  values are larger than the true CAPE values in the vicinity of storms, which may be surprising since that CAPE based on climatological values normally is much less than the preconvective CAPE. Clearly CAPE and  $CAPE_e$  are not the same, and the purpose here is merely to compare  $CAPE_e$  values between regions. The highest  $CAPE_e$  value is found in the Sahel, followed by the Tropical Wet (DJF; Table 5). These  $CAPE_e$  values are more than twice that in the Amazon. The difference is due less to differences in the  $\theta_e^*$  profiles, but rather to the higher value of  $\theta_{e,sfc}$

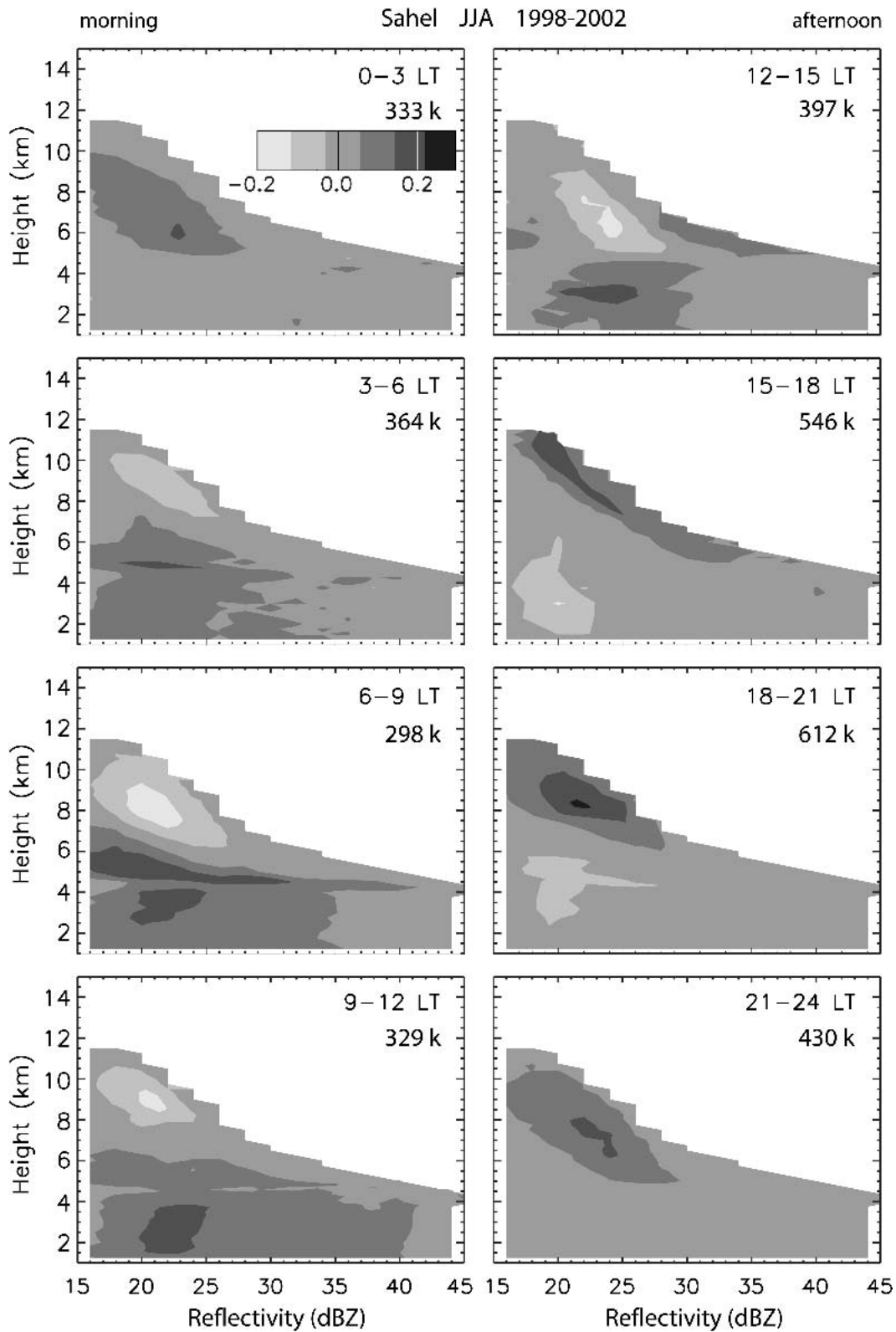


FIG. 13. Diurnal variation of the reflectivity FAD, for the Sahel [units  $(2 \text{ dBZ})^{-1} (250 \text{ m})^{-1}$ ]. The normalized frequencies are expressed as a difference from the normalized 24-h mean values. The total number of occurrences in a time bin is shown for each FAD.

TABLE 4. Summary of the diurnal variations of the reflectivity FAD in various regions. The figures are derived from FADs as the ones in Fig. 13, for each region. The “strength” is the peak strength of the positive anomaly, in normalized units as displayed in Fig. 13. The “period” refers to the local time during which this anomaly occurred (3-h bins). The “height” is the level of the peak strength of the positive anomaly. The “BB max” column lists the time period when echoes of various strengths are anomalously frequent at the freezing level.

Region	Season (units)	Shallow maxima			Deep maxima			BB max Period (h LT)
		Period (h LT)	Height (km)	Strength 1/ (2 dBZ)(250 m)	Period (h LT)	Height (km)	Strength 1/ (2 dBZ)(250 m)	
Sahara	JJA	1200–1500	4.0	0.19	1800–2400	7.75	0.25	0600–1200
Sahel	JJA	0900–1500	3.0	0.21	1500–2400	8.5	0.29	0300–0900
Savanna North	JJA	1200–1500	2.5	0.17	1800–2400	8.5	0.21	0300–1200
Tropical Wet	JJA	0900–1500	2.25	0.27	1800–2400	7.5	0.20	0300–0900
East Africa	JJA	0600–0900	2.25	0.43	1800–2400	8.0	0.19	—
Horn Africa	JJA	0900–1200	3.75	0.30	1800–2400	8.5	0.29	0300–0600
Kalahari	DJF	0000–0900	2.75–3.5	0.28	1500–2100	7.5	0.23	0600–0900
Okavango	DJF	0900–1200	2.75	0.22	1500–2400	7.75	0.20	0300–0900
Savanna South	DJF	0900–1200	3	0.26	1500–2100	8.0	0.29	0000–0900
Tropical Wet	DJF	0000–0300	3.25	0.22	1500–2100	9.0	0.19	0900–1200
		1200–1500	3	0.17				
East Africa	MAM	0900–1200	2.25	0.20	1800–2400	7.75	0.19	0300–0600
Amazon	JFM	0900–1500	2–2.75	0.14	1500–2100	8.25	0.16	0600–0900

in the Sahel (and the Tropical Wet), compared to the Amazon. The higher  $\theta_{e,sfc}$  in the Sahel is mostly due to a higher temperature there (5–7 K), not a higher relative humidity, compared to the Amazon. The Sahel and Tropical Wet (DJF) regions also have a more elevated LNB<sub>e</sub> than does the Amazon (Table 5), which is consistent with the more frequent occurrence of PR-measurable echoes at upper levels in those regions (Fig. 7). In a broader context, our findings are consistent with several TRMM-based studies that indicate that the most intense storms in the Earth’s tropical belt (23.5°N–23.5°S) are found in Africa [see review article by Zipser (2003)]. The relatively weaker, more stratiform storms and higher warm-rain fraction over the Amazon are consistent with the lower CAPE and lower LFC there, compared to wet-season values anywhere in tropical Africa. The fundamental reason for this difference is that trade winds from the Indian Ocean are partially blocked by the high terrain of eastern Africa, while in the Amazon the blocking high terrain is on the downwind west side of the basin.

The Sahara has the lowest CAPE<sub>e</sub> in Table 5, which is due to the low specific humidity there:  $\theta_{e,sfc}^*$  greatly exceeds  $\theta_{e,sfc}$  (Fig. 16). As a consequence the LFC<sub>e</sub> is nearly 1 km higher than in the other regions. The  $\theta_e^*$  continues to be higher in the Sahara than in other regions up to about 500 mb, mainly because of higher temperatures, but in the upper troposphere  $\theta_e^*$  is slightly lower than in most other regions, which is consistent with the rather high echo tops of Sahara storms (Fig. 7). In fact, the secondary echo top maximum around 6–7 km (Fig. 7) may be related to the deeper layer of conditional instability ( $\theta_e^*/p > 0$ ) in the Sahara, compared to that in other regions (Fig. 16).

Finally we interpret the diurnal delay in rainfall and echo top height maxima in the Sahel and the northern Savanna, compared to other regions in Africa. This de-

lay may be related to land cover (Mohr et al. 2003), but it is more likely that deep convection, triggered by daytime heating, becomes more organized during the evening. This is consistent with the larger low-level wind shear there, which is a factor in the longevity of squall lines (Rotunno et al. 1988). In JJA, the climatological wind shear in the lowest 3 km (1000–700 mb) is northeasterly and its magnitude averages (peaks) at  $3.7 \cdot 10^{-3} \text{ s}^{-1}$  ( $5.0 \cdot 10^{-3} \text{ s}^{-1}$ ) in the Sahel and northern Savanna, according to the NCEP–NCAR reanalysis dataset. The climatological DJF wind shear for the Okavango and southern Savanna regions over roughly the same depth (between the level closest to the ground, 850 and 550 mb) is mostly southeasterly and its magnitude averages (peaks) at merely  $1.2 \cdot 10^{-3} \text{ s}^{-1}$  ( $1.7 \cdot 10^{-3} \text{ s}^{-1}$ ). Under weak shear, short-lived airmass thunderstorms prevail, and these are most numerous earlier in the afternoon. According to numerical simulations by Weisman et al. (1988), the optimal shear for long-lived squall lines is 15–25  $\text{m s}^{-1}$  over the lowest 2.5 km. Several long-lived squall lines have been documented in the northern Savanna region (e.g., Roux et al. 1984), and IR satellite imagery suggests that large organized convective systems are far more common in the northern zenithal rain belt than in the southern one (Laing and Fritsch 1993). The weak diurnal cycle of rain rate in the northern Savanna (Fig. 9) and the secondary maximum in rain amount near dawn (Fig. 10: 0600–0900 LT in the northern Savanna; 0300–0600 LT in the Sahel and even the Sahara) is consistent with the eastward progression of nocturnal squall lines across the subSaharan zenithal rain belt in JJA, which has been observed on several occasions in the western Sahel (Chalon et al. 1988; Roux and Sun 1990). This is not unlike the nocturnal westward progression of organized convection across the Plains of the central United States (Carbone et al. 2002).

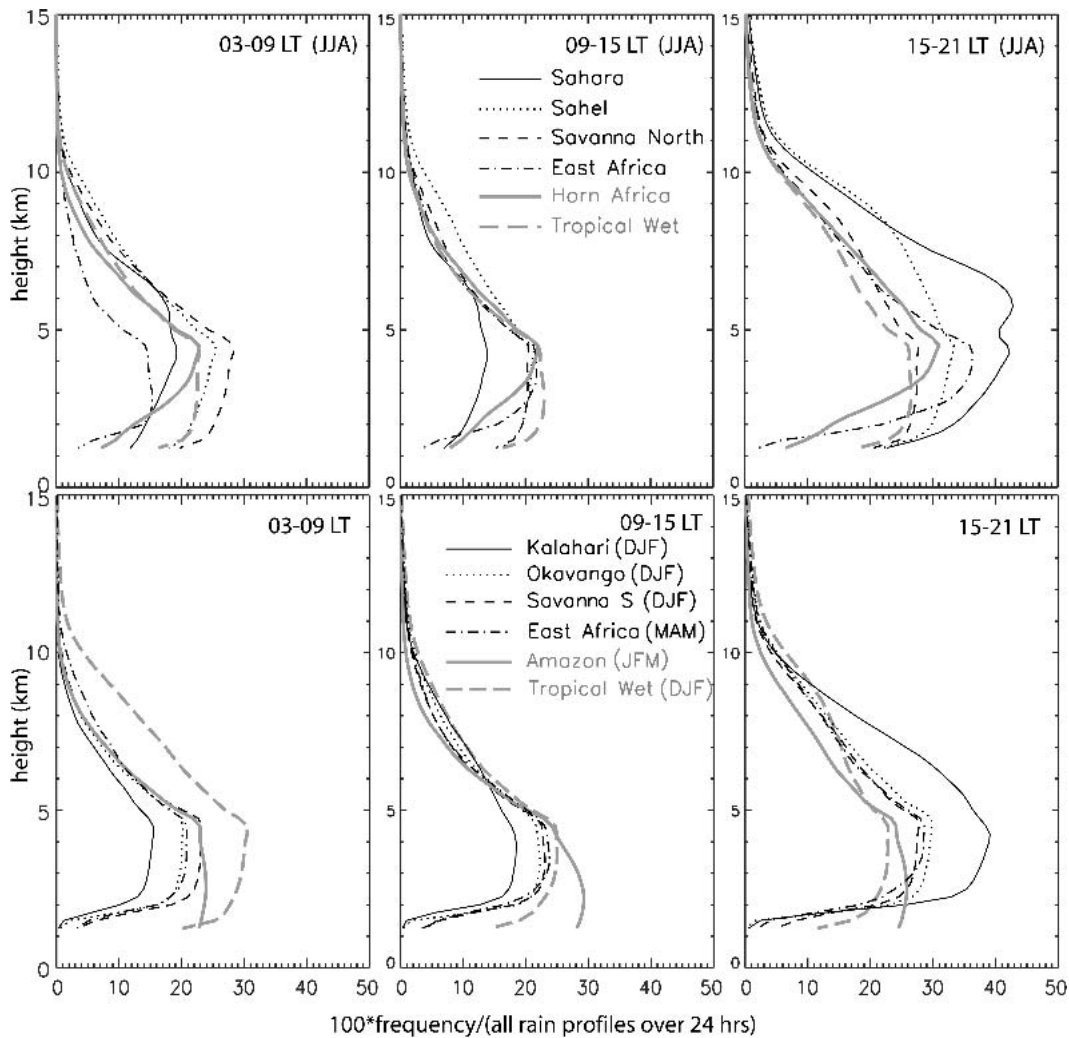


FIG. 14. As Fig. 5, but for one threshold only (17 dBZ). Three 6-h periods are isolated: (left) 0300–0900, (middle) 0900–1500, and (right) 1500–2100 LT. Frequencies are normalized by the total number of rain profiles in each region. (top) JJA regions and (bottom) DJF regions. Note that all  $x$  axes are the same.

## 6. Conclusions

This study aims to describe the regional and diurnal variability of the vertical structure of storms in tropical Africa, by means of 5 yr of extreme-season (DJF and JJA) TRMM Precipitation Radar data. The regional storm characteristics are contrasted against those in the Amazon. The key TRMM product used here is the 2A25 reflectivity profile, which is truncated at about 17 dBZ, and the radar-derived surface rain rate. The main findings of this study are as follows.

- In all of tropical Africa, including the Tropical Wet region (which is mainly the Congo Basin), storms tend to be more vigorous than over the Amazon. Storms over the Amazon tend to be more shallow, and warm-rain events (whose echoes peak below

the freezing level) are more common. Amazon storms are less likely to have high reflectivity values aloft, and they have a better-defined brightband signature.

- Some regional differences in storm vertical structure exists within tropical Africa, although these are small compared to that between the Amazon and Africa. Vigorous storms frequent the Sahel, and to a lesser degree the adjacent northern Savanna and the Tropical Wet region (in the latter especially in DJF). Sahel storms are marked by high echo tops and high hydrometeor loading aloft. The lack of a clear brightband spike suggests that these storms are mostly convective. Comparing the northern (semi)arid regions (the Sahel and the Sahara) to the southern ones (the Okavango and Kalahari, respectively), low-level evaporation is more common/intense in the former

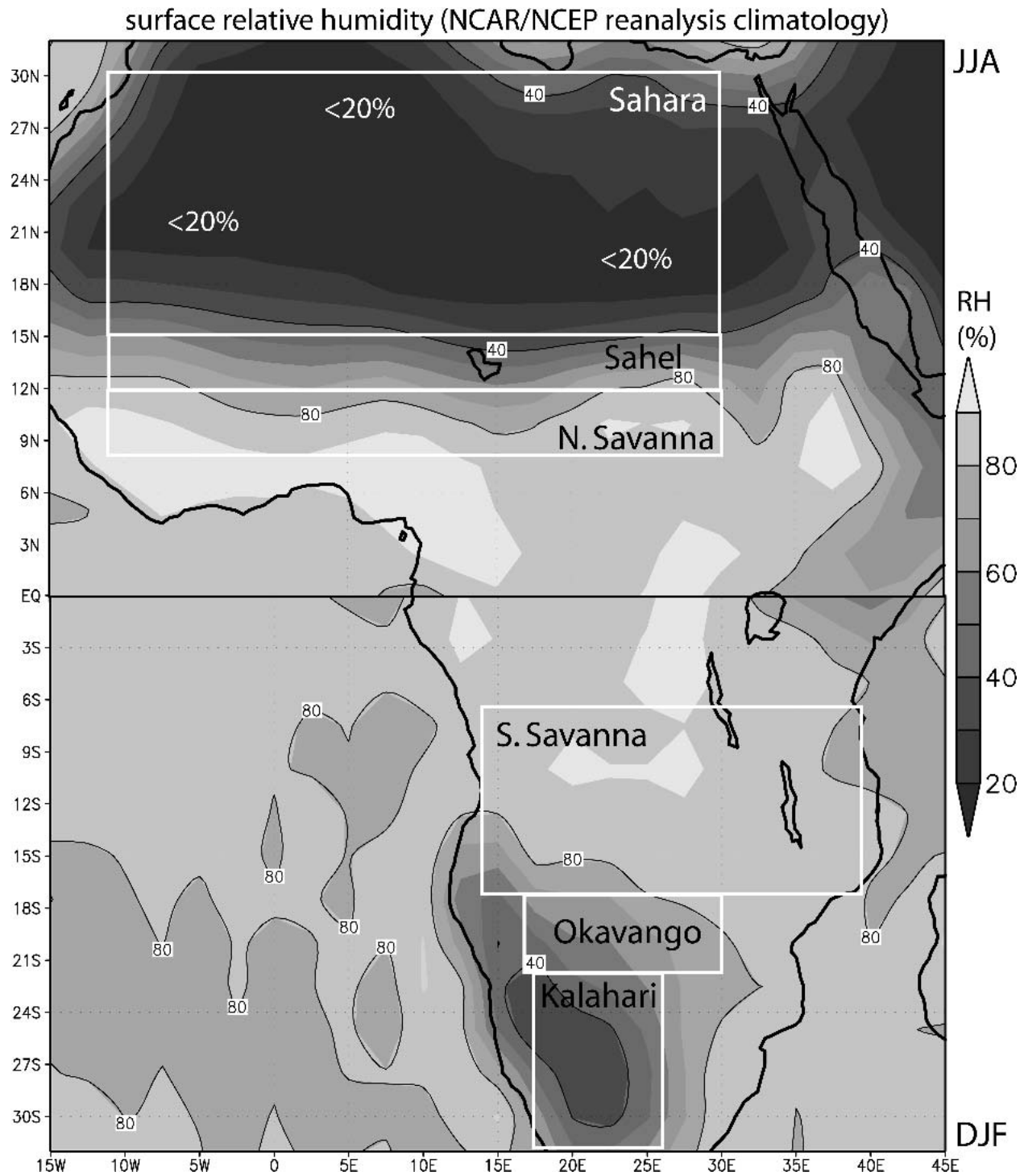


FIG. 15. The climatological surface relative humidity, according to the NCEP–NCAR reanalysis dataset for JJA (north of the equator) and DJF (south of the equator).

regions and warm-rain events are more common in the latter.

- The diurnal modulation of rainfall and vertical storm structure is minimal over the Amazon and largest in

the arid regions of Africa. In many African regions the echo tops are highest and rainfall is most intense in the afternoon (1500–1800 local time), but the diurnal peak is delayed by a few hours in the Sahel and

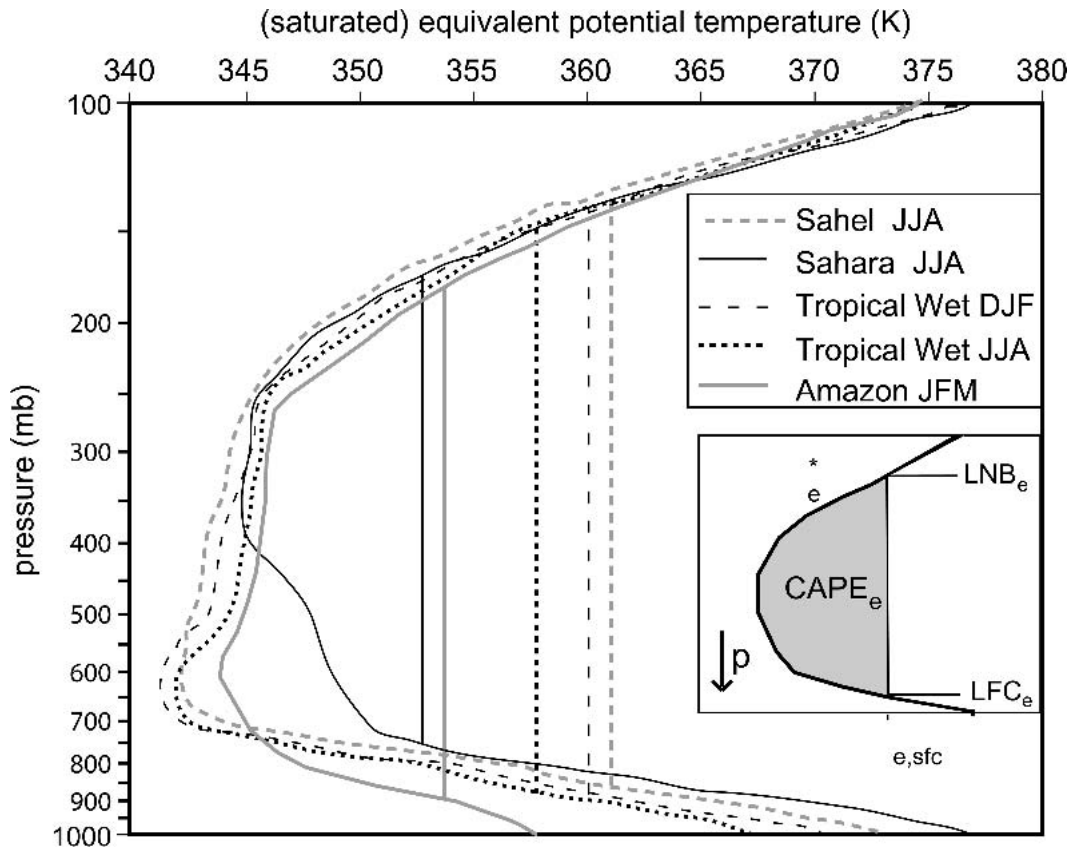


FIG. 16. Vertical profiles of  $\theta_e^*$  (curved lines) plotted as a function of pressure (log coordinates, i.e., height) for various regions. The vertical lines are corresponding values of surface  $\theta_e$ , derived from the temperature and the specific humidity at 1000 mb. Data are based on the NCEP–NCAR reanalysis dataset. These data are averaged over the full area of each region except for the Sahara, where only the southern third ( $15^\circ$ – $20^\circ$ N) is used.

the northern Savanna. The echo top height and rainfall distribution in the Tropical Wet region has a secondary maximum in the second half of the night.

- The regional variation of the vertical structure of storms in Africa, and the contrast between Africa and the Amazon, are consistent with thermodynamic properties of the basic-state environment.

This study has focused on the typical vertical structure of storms in Africa. In a follow-up study, we plan to examine interannual variability of precipitation systems in Africa, in the context of observed departures from the mean flow and thermodynamic conditions.

TABLE 5. Values of  $\text{CAPE}_e$ ,  $\text{LFC}_e$ , and  $\text{LNB}_e$  inferred from the profiles shown in Fig. 16.

Region	Season	$\text{CAPE}_e$ ( $\text{J kg}^{-1}$ )	$\text{LFC}_e$ (mb)	$\text{LNB}_e$ (mb)
Sahel	JJA	7375	864	137
Sahara	JJA	2214	758	176
Tropical Wet	DJF	6776	873	141
Tropical Wet	JJA	5427	876	149
Amazon	JFM	3059	886	185

**Acknowledgments.** This research was supported by the National Aeronautics and Space Administration EPSCoR Grant 5-33395. The second author benefited from the interaction with Mircea Grecu, Erich Stocker, and others at NASA Goddard Code 912 during and after his Earth Science Enterprise summer 2003 graduate fellowship.

#### REFERENCES

- Adeyewa, Z. D., and K. Nakamura, 2003: Validation of TRMM radar rainfall data over major climatic regions in Africa. *J. Appl. Meteor.*, **42**, 331–347.
- Anagnostou, E. N., C. A. Morales, and T. Dinku, 2001: The use of TRMM precipitation radar observations in determining ground radar calibration biases. *J. Atmos. Oceanic Technol.*, **18**, 616–628.
- Battán, L. J., 1973: *Radar Observations of the Atmosphere*. University of Chicago Press, 324 pp.
- Bell, T. L., and N. Reid, 1993: Detecting the diurnal cycle of rainfall using satellite observations. *J. Appl. Meteor.*, **32**, 311–322.
- Berg, W., C. Kummerow, and C. A. Morales, 2002: Differences between east and west Pacific rainfall systems. *J. Climate*, **15**, 3659–3672.
- Boccippio, D. J., S. J. Goodman, and S. Heckman, 2000: Regional

- differences in tropical lightning distributions. *J. Appl. Meteor.*, **39**, 2231–2248.
- Carbone, R. E., J. D. Tuttle, D. A. Ahijevych, and S. B. Trier, 2002: Inferences of predictability associated with warm season precipitation episodes. *J. Atmos. Sci.*, **59**, 2033–2056.
- Cecil, D. J., and E. J. Zipser, 2002: Reflectivity, ice scattering, and lightning characteristics of hurricane eyewalls and rainbands. Part II: Intercomparison of observations. *Mon. Wea. Rev.*, **130**, 785–801.
- Chalon, J. P., G. Jaubert, J. P. Lafore, and F. Roux, 1988: The West African squall line observed on 23 June 1981 during COPT 81: Mesoscale structure and transports. *J. Atmos. Sci.*, **45**, 2744–2763.
- Dai, A., 2001: Global precipitation and thunderstorm frequencies. Part II: Diurnal variations. *J. Climate*, **14**, 1112–1128.
- , F. Giorgi, and K. E. Trenberth, 1999: Observed and model simulated precipitation diurnal cycle over the contiguous United States. *J. Geophys. Res.*, **104**, 6377–6402.
- Davis, C. A., K. W. Manning, R. E. Carbone, S. B. Trier, and J. D. Tuttle, 2003: Coherence of warm-season continental rainfall in numerical weather prediction models. *Mon. Wea. Rev.*, **131**, 2667–2679.
- Durden, S. L., Z. S. Haddad, A. Kitiyakara, and F. K. Li, 1998: Effects of non-uniform beam filling on rainfall retrieval for the TRMM precipitation radar. *J. Atmos. Oceanic Technol.*, **15**, 635–646.
- Ferreira, F., P. Amayenc, S. Oury, and J. Testud, 2001: Study and tests of improved rain estimates from the TRMM precipitation radar. *J. Appl. Meteor.*, **40**, 1878–1899.
- Fisher, B. L., 2004: Climatological validation of TRMM TMI and PR monthly rain products over Oklahoma. *J. Appl. Meteor.*, **43**, 519–535.
- Geerts, B., and Y. Dawei, 2004a: Classification and characterization of tropical precipitation based on high-resolution airborne vertical-incidence radar. Part I: Classification. *J. Appl. Meteor.*, **43**, 1554–1566.
- , and —, 2004b: Classification and characterization of tropical precipitation based on high-resolution airborne vertical incidence radar. Part II: Composite vertical structure of hurricanes versus storms over Florida and the Amazon. *J. Appl. Meteor.*, **43**, 1567–1585.
- Heymsfield, G. M., B. Geerts, and L. Tian, 2000: TRMM precipitation radar reflectivity profiles as compared with high-resolution airborne and ground-based radar measurements. *J. Appl. Meteor.*, **39**, 2080–2102.
- Hirose, M., and K. Nakamura, 2002: Spatial and seasonal variation of rain profiles over Asia observed by space-borne precipitation radar. *J. Climate*, **15**, 3443–3458.
- Hobbs, P. V., T. J. Matejka, P. H. Herzegh, J. D. Locatelli, and R. A. Houze, 1980: The mesoscale and microscale structure and organization of clouds and precipitation in midlatitude cyclones. Part I: A case study of a cold front. *J. Atmos. Sci.*, **37**, 568–596.
- Houze, R. A., Jr., 1993: *Cloud Dynamics*. Academic Press, 573 pp.
- , 1997: Stratiform precipitation in regions of convection: A meteorological paradox? *Bull. Amer. Meteor. Soc.*, **78**, 2179–2196.
- , S. G. Geotis, F. D. Marks Jr., and A. K. West, 1981: Winter monsoon convection in the vicinity of north Borneo. Part I: Structure and time variation of the clouds and precipitation. *Mon. Wea. Rev.*, **109**, 1595–1614.
- Huffman, G. J., and Coauthors, 1997: The Global Precipitation Climatology Project (GPCP) combined precipitation dataset. *Bull. Amer. Meteor. Soc.*, **78**, 5–20.
- Iguchi, T., and R. Meneghini, 1994: Intercomparison of single-frequency methods for retrieving a vertical rain profile from airborne or spaceborne radar data. *J. Atmos. Oceanic Technol.*, **11**, 1507–1516.
- , T. Kozu, R. Meneghini, J. Awaka, and K. Okamoto, 2000: Rain-profiling algorithm for the TRMM precipitation radar. *J. Appl. Meteor.*, **39**, 2038–2052.
- Jensen, M. P., and A. D. Del Genio, 2003: Radiative and microphysical characteristics of deep convective systems in the tropical western Pacific. *J. Appl. Meteor.*, **42**, 1234–1254.
- Johnson, R. H., T. M. Rickenbach, S. A. Rutledge, P. E. Ciesielski, and W. H. Schubert, 1999: Trimodal characteristics of tropical convection. *J. Climate*, **12**, 2397–2418.
- Kalnay, E., and Coauthors, 1996: The NCAR/NCEP 40-Year Reanalysis Project. *Bull. Amer. Meteor. Soc.*, **77**, 437–471.
- Kummerow, C., and L. Giglio, 1994: A passive microwave technique for estimating rainfall and vertical structure information from space. Part I: Algorithm description. *J. Appl. Meteor.*, **33**, 3–18.
- , W. Barnes, T. Kozu, J. Shiue, and J. Simpson, 1998: The Tropical Rainfall Measuring Mission (TRMM) sensor package. *J. Atmos. Oceanic Technol.*, **15**, 809–817.
- , and Coauthors, 2000: The status of the Tropical Rainfall Measuring Mission (TRMM) after two years in orbit. *J. Appl. Meteor.*, **39**, 1965–1982.
- Laing, A. G., and J. M. Fritsch, 1993: Mesoscale convective complexes in Africa. *Mon. Wea. Rev.*, **121**, 2254–2263.
- Lebel, T., and A. Amani, 1999: Rainfall estimation in the Sahel: What is the ground truth? *J. Appl. Meteor.*, **38**, 555–568.
- Leroux, M., 2001: *The Meteorology and Climate of Tropical Africa*. Springer-Verlag, 548 pp.
- Lin, X., D. A. Randall, and L. D. Fowler, 2000: Diurnal variability of the hydrologic cycle and radiative fluxes: Comparisons between observations and a GCM. *J. Climate*, **13**, 4159–4179.
- Mapes, B. E., and R. A. Houze, 1993: Cloud clusters and superclusters over the oceanic warm pool. *Mon. Wea. Rev.*, **121**, 1398–1416.
- , T. T. Warner, M. Xu, and A. J. Negri, 2003: Diurnal patterns of rainfall in northwestern South America. Part I: Observations and context. *Mon. Wea. Rev.*, **131**, 799–812.
- Masunaga, H., T. Iguchi, R. Oki, and M. Kachi, 2002: Comparison of rainfall products derived from TRMM Microwave Imager and Precipitation Radar. *J. Appl. Meteor.*, **41**, 849–862.
- Mohr, K. I., D. R. Baker, W.-K. Tao, and J. S. Famiglietti, 2003: The sensitivity of West African convective line water budgets to land cover. *J. Hydrometeorol.*, **4**, 62–76.
- Negri, A. J., R. F. Adler, E. J. Nelkin, and G. J. Huffman, 1994: Regional rainfall climatologies derived from Special Sensor Microwave Imager (SSM/I) data. *Bull. Amer. Meteor. Soc.*, **75**, 1165–1182.
- , T. L. Bell, and L. Xu, 2002: Sampling of the diurnal cycle of precipitation using TRMM. *J. Atmos. Oceanic Technol.*, **19**, 1333–1344.
- Nesbitt, S. W., and E. J. Zipser, 2003: The diurnal cycle of rainfall and convective intensity according to three years of TRMM measurements. *J. Climate*, **16**, 1456–1475.
- Nicholson, S. E., B. Some, and B. Kone, 2000: An analysis of recent rainfall conditions in West Africa, including the rainy seasons of the 1997 El Niño and the 1998 La Niña years. *J. Climate*, **13**, 2628–2640.
- , and Coauthors, 2003: Validation of TRMM and other rainfall estimates with a high-density gauge dataset for West Africa. Part II: Validation of TRMM rainfall products. *J. Appl. Meteor.*, **42**, 1355–1368.
- Petersen, W. A., and S. A. Rutledge, 2001: Regional variability in tropical convection: Observations from TRMM. *J. Climate*, **14**, 3566–3586.
- , S. W. Nesbitt, R. J. Blakeslee, R. Cifelli, P. Hein, and S. A. Rutledge, 2002: TRMM observations of intraseasonal variability in convective regimes over the Amazon. *J. Climate*, **15**, 1278–1294.
- Petty, G. W., 1999: Prevalence of precipitation from warm-topped clouds over eastern Asia and the western Pacific. *J. Climate*, **12**, 220–229.
- Rickenbach, T. M., 2004: Nocturnal cloud systems and the diurnal

- variation of clouds and rainfall in southwestern Amazonia. *Mon. Wea. Rev.*, **132**, 1201–1219.
- Roux, F., and J. Sun, 1990: Single-Doppler observations of a West African squall line on 27–28 May 1981 during COPT 81: Kinematics, thermodynamics, and water budget. *Mon. Wea. Rev.*, **118**, 1826–1854.
- , J. Testud, M. Payen, and B. Pinty, 1984: West African squall-line thermodynamic structure retrieved from dual-Doppler radar observations. *J. Atmos. Sci.*, **41**, 3104–3121.
- Rotunno, R., J. B. Klemp, and M. L. Weisman, 1988: A theory for strong, long-lived squall lines. *J. Atmos. Sci.*, **45**, 463–485.
- Sauvageot, H., F. Mesnard, and R. S. Tenorio, 1999: The relation between the area-average rain rate and the rain cell size distribution parameters. *J. Atmos. Sci.*, **56**, 57–70.
- Short, D. A., and K. Nakamura, 2000: TRMM radar observations of shallow precipitation over the tropical oceans. *J. Climate*, **13**, 4107–4124.
- Smull, B. F., and R. A. Houze, 1987: Rear inflow in squall lines with trailing stratiform precipitation. *Mon. Wea. Rev.*, **115**, 2869–2889.
- Sorooshian, S., X. Gao, K. Hsu, R. A. Maddox, Y. Hong, H. V. Gupta, and B. Imam, 2002: Diurnal variability of tropical rainfall retrieved from combined GOES and TRMM satellite information. *J. Climate*, **15**, 983–1001.
- Steiner, M., and R. A. Houze Jr., 1997: Sensitivity of the estimated monthly convective rain fraction to the choice of Z–R relation. *J. Appl. Meteor.*, **36**, 452–462.
- Stith, J. L., J. E. Dye, A. Bansemmer, A. J. Heymsfield, C. A. Grainger, W. A. Petersen, and R. Cifelli, 2002: Microphysical observations of tropical clouds. *J. Appl. Meteor.*, **41**, 97–117.
- Toracinta, E. R., D. J. Cecil, E. J. Zipser, and S. W. Nesbitt, 2002: Radar, passive microwave, and lightning characteristics of precipitating systems in the Tropics. *Mon. Wea. Rev.*, **130**, 802–824.
- Vicente, G. A., R. A. Scofield, and W. P. Menzel, 1998: The operational GOES infrared rainfall estimation technique. *Bull. Amer. Meteor. Soc.*, **79**, 1883–1898.
- Weisman, M. L., J. B. Klemp, and R. Rotunno, 1988: Structure and evolution of numerically simulated squall lines. *J. Atmos. Sci.*, **45**, 1990–2013.
- Wilcox, E. M., and V. Ramanathan, 2001: Scale dependence of the thermodynamic forcing of tropical monsoon clouds: Results from TRMM observations. *J. Climate*, **14**, 1511–1524.
- Zipser, E. J., 2003: Some views on “hot towers” after 50 years of tropical field programs and two years of TRMM data. *Cloud Systems, Hurricanes, and the Tropical Rainfall Measuring Mission (TRMM): A Tribute to Dr. Joanne Simpson*, Meteor. Monogr., No. 29, Amer. Meteor. Soc., 49–69.

### **Appendix 3**

Fuentes J. D, B. Geerts, T. Dejene, P. D'Odorico, and E Joseph, 2007: **Vertical attributes of precipitation in West Africa and adjacent ocean. Theoretical and Applied Climatology.**, 000, 1-13 (2007) DOI 10.1007/s00704 – 007-0318-0



<sup>1</sup> Department of Environmental Sciences, University of Virginia, Charlottesville, VA, USA

<sup>2</sup> Department of Atmospheric Science, University of Wyoming, Laramie, WY, USA

<sup>3</sup> Department of Physics, Howard University, Washington, DC, USA

## Vertical attributes of precipitation systems in West Africa and adjacent Atlantic Ocean

J. D. Fuentes<sup>1</sup>, B. Geerts<sup>2</sup>, T. Dejene<sup>1</sup>, P. D'Odorico<sup>1</sup>, and E. Joseph<sup>3</sup>

With 9 Figures

Received October 23, 2006; revised February 22, 2007; accepted March 7, 2007

Published online July 9, 2007 © Springer-Verlag 2007

### Summary

This study reports the findings of TRMM (Tropical Rainfall Measuring Mission) satellite data analyses undertaken to investigate differences in intensity and depth of precipitating systems in the transition region from continental to maritime environments in West Africa during the rainy season of June to September in 1998–2004. The results of this study are interpreted in the context of regional thermodynamic variables such as equivalent potential temperature and equivalent convective available potential energy to discern the processes governing storm development. Over continental West Africa, convective-type precipitating storms exhibit a substantially larger vertical extent compared to the ones over the eastern Atlantic Ocean. In contrast, the stratiform precipitating systems show similar vertical reflectivity patterns, depth and intensity over both land and adjacent ocean in West Africa. The differences in the attributes of storms, as they move from the continent to the ocean, can be partly explained in terms of the surface-atmosphere interactions that provide the necessary transports of energy and water vapor from the surface to the cloud layer.

### 1. Introduction

Much of the rainfall over West Africa and adjacent Atlantic Ocean is the result of organized convection. The characteristics of West Africa mesoscale convective systems (MCSs) have been studied using geostationary satellites (Hodges and

Thorncroft, 1997; Diedhiou et al., 1999) and radars during field campaigns such as the GARP (Global Atmospheric Research Program) Atlantic Tropical Experiment (GATE), (Reed, 1977; Houze and Betts, 1981). Based on these and limited field work (e.g. Roux, 1988), it is now established that most of the rainfall in West Africa is associated with linear or more amorphous MCSs whose spatial extent can reach 500 km (Lebel et al., 2003). Typical MSCs tend to last 12 h (unless they become Cape Verde tropical cyclones) and some squall lines can persist for 2 days (Laing and Fritsch, 1997; Redelsperger et al., 2002). Mesoscale organized convection is often associated with the African Easterly Jet and tends to occur in regions of synoptic-scale low-level convergence (Cook, 1999; Lebel et al., 2003). In general, substantial atmospheric instability due to warm, moisture-rich boundary-layer air, and strong low-level vertical wind shear are the necessary conditions to sustain the propagation of squall lines in West Africa (Rotunno et al., 1988; Rowell and Milford, 1993; Weisman and Rotunno, 2004). Over the West African land area, MSCs move faster due to the stronger African Easterly Jet and have shorter lifetimes compared to the ones over the east Atlantic Ocean (Hodges and Thorncroft, 1997).

Despite the extensive research carried out over West Africa during the last four decades, limited knowledge still exists on the dynamics, thermodynamics, and microphysical characteristics of precipitating storms as they migrate from continental to maritime environments.

The launching of the TRMM (Tropical Rainfall Measuring Mission) satellite during 1997 started a new era of space borne precipitation research (Simpson et al., 1988). With the TRMM data it is now possible to investigate the vertical attributes of precipitation systems using reflectivity profiles derived from the Precipitation Radar (PR) aboard the satellite (Kummerow et al., 2000; Kozu et al., 2001). TRMM-derived vertical profiles of precipitation and hydrometeors indicate in which layers of the atmosphere diabatic heating occurs (Lin et al., 2004; Schumacher et al., 2004). Knowledge of the vertical distribution of diabatic heating is crucial to establish the energy balance of the tropical atmosphere. The TRMM PR products also allow establishing a distinction between convective or stratiform rainfall (Schumacher and Houze, 2003). Such distinction is important because of the resulting different relationships between radar reflectivity,  $Z$ , and rain rates,  $R$  ( $Z$ - $R$  relationships), that can be defined for the estimation of spatial rainfall (Steiner and Houze, 1997). The  $Z$  is expressed in the units of  $\text{mm}^6 \text{m}^{-3}$ . For practical purposes, in this study and elsewhere the decibel (dB) units are used because of the large range in  $Z$  values.  $Z$  can be interpreted as a range-independent measure of radar backscatter intensity. If all scatterers are spherical drops too small to reach the Mie scattering regime (about 3 mm in diameter for the case of the PR) then  $Z$  equals the integral of the 6<sup>th</sup> power of the droplet diameter,  $D$ . In practice,  $Z$  is an equivalent reflectivity.  $R$  is the rain rate at the level of the  $Z$  measurement, although it is often applied at the surface. Because  $Z$  is proportional to the 6<sup>th</sup> power of  $D$  and  $R$  is proportional to the 3-4<sup>th</sup> power of  $D$ , the  $Z$ - $R$  relationships are not necessarily exact. Nevertheless radars are widely used, even in space, with the primary purpose of estimating rain rates.

Utilizing TRMM data, the attributes of convection and precipitation-type designation (Houze, 1997) in remote regions such as the Congo Basin in central Africa and the Amazon region in South America can be studied. For instance, compared to the Amazon region, the Congo Basin experi-

ences deeper storms with higher reflectivity values above the freezing level (e.g. at 7 km), higher fraction of convective-type rainfall, stronger 85-GHz ice scattering signature, and more lightning activity (Boccippio et al., 2000; Petersen and Rutledge, 2001; Toracinta et al., 2002; Sealy et al., 2003; Geerts and Dejene, 2005; Petersen et al., 2006; Schumacher and Houze, 2006). The identified storm attributes indicate that precipitation systems over the Congo Basin exhibit characteristics of tropical continental convection whereas those over the Amazon show similar aspects of maritime convection (Cecil and Zipser, 2002; Toracinta et al., 2002; Nesbitt and Zipser, 2003). In essence, the term maritime refers to the characteristic rain drop size distribution, which in turn is governed by the number of cloud condensation nuclei. Several studies (Stith et al., 2002; Williams et al., 2002) have documented Amazonian cloud droplet spectra similar to those observed over maritime environments, especially during easterly flow regimes (Halverson et al., 2002). The fundamental reason of the difference between Amazonian and Congo storms is that the low-level Easterly Trade winds proceed unimpeded from the Atlantic into the Amazon whereas the access of these winds into the Congo Basin is blocked by the elevated terrain of East Africa.

Several TRMM-PR-based studies have focused on sub-Saharan Africa. For example, Adeyewa and Nakamura (2003) showed that the TRMM-PR climatological rainfall patterns in Africa exhibit a significant difference, compared to rain gauges and other satellite-derived rainfall estimates. This difference is seasonally- and regionally-dependent and it is smallest in the wet season of the northern savanna region. Nicholson et al. (2003) performed a similar comparison, and found that the TRMM PR rainfall tends to exceed rain gauge rainfall in West Africa. Given this uncertainty, Geerts and Dejene (2005) did not examine the TRMM-PR surface rainfall, and instead studied the vertical features of precipitating systems over Africa as inferred from the TRMM PR data. They found that in all African regions, but especially in the Sahel and northern savannas, storms exhibit high echo tops, high hydrometeor loading aloft, and a low-level evaporation signature. Also, their work revealed a strong diurnal modulation of storms in the Sahel and northern savannas where they are most common around sunset.

Schumacher and Houze (2006) recently investigated stratiform-precipitation production over sub-Saharan Africa and the eastern Atlantic Ocean. They showed that the east Atlantic Ocean has more rainfall arising from shallow storms, while sub-Saharan Africa experiences more non-precipitating anvils. In an investigation of the temporal variability of precipitation in sub-Saharan Africa, Mohr (2004) concluded that the diurnal rainfall cycle is strongly influenced by organized convection.

The thermodynamics and microphysical characteristics of storms in West Africa and eastern Atlantic Ocean remain poorly understood. The TRMM data sets provide a unique opportunity to investigate the spatial and temporal characteristics of storms over a region of the world where ground-based rainfall measurements remain sparse. Therefore, the main goal of the present study is to investigate differences in radar reflectivity of precipitating storms in both West Africa and downstream maritime environments. Seven years of TRMM PR data are used for the rainy season (June–September). The results of this study are interpreted in the context of regional thermodynamic variables such as equivalent potential temperature and “equivalent” convective available potential energy ( $CAPE_e$ ) as these variables exert influences on storm development. In previous studies (Geerts and Dejene, 2005), a methodology was developed for binning individual TRMM PR precipitation profiles in terms of time of day, region, and criteria such as season and surface rain rates. The emphasis of earlier studies was to identify the vertical features of storms and associated diurnal precipitation variability in several regions of Africa. The present investigation adopts a similar methodology as that included in Geerts and Dejene (2005) but focuses on different regions in West Africa to consider the climatological attributes of storms in the zonal belt stretching from sub-Sahara Africa to the adjacent Atlantic Ocean.

## 2. Research methodology

### 2.1 Data sources

The data included in this study came from two sources. The TRMM data are one source. Before August 2001 the TRMM satellite orbited at an

altitude of about 350 km above mean sea level. After August 2001 the satellite orbiting altitude became 403 km above mean sea level. The satellite carries a 13.8-GHz precipitation radar (PR), the multi-frequency TRMM imager (TMI), the Visible and Infrared Scanner (VIRS), the lightning imaging sensor (LIS), and the clouds and Earth's radiant energy system (CERES) (Kummerow et al., 1998). Since December 1997, measurements made with the TRMM radar and passive microwave radiometer are providing uninterrupted data sets of rainfall rate and vertical attributes of precipitating systems. The TRMM satellite follows a non-Sun-synchronous orbit, specifically designed such that at any location all times of the day have a roughly equal overpass chance. Thus, a sufficiently long composite of TRMM data will represent the full diurnal cycle and will enable studies of the diurnal variability of precipitation. The PR range resolution is 250 m. Thus, for zenith beams the vertical resolution of the reflectivity profile is 250 m. However, at high ( $>15^\circ$ ) inclination angles the vertical resolution decreases to 1000 m due to the relatively large footprint size (Heymsfield et al., 2000). Because the low inclination angles allow for a higher resolution in the vertical profile, only measurements made at inclinations of  $\pm 12^\circ$  from nadir were included in the analyses presented here. Before the TRMM satellite was boosted to a new orbiting altitude, the horizontal resolution of the PR was about 4.3 km at nadir and about 5 km at the maximum inclination of  $17^\circ$  (Kummerow et al., 1998). After the TRMM satellite was boosted, the horizontal resolution at nadir became 5 km. The above-mentioned uncertainty in surface rainfall applies to both ends of the rain rate spectrum. At the low end, the limited horizontal and low radar sensitivity (17 dBZ) prevent the observation of isolated and small ( $<5$  km in diameter) storm cells (Heymsfield et al., 2000). This limitation can introduce an underestimate of surface rainfall by as much as 25%, mostly in regions outside of deep convection (Sauvageot et al., 1999). However, an improvement of surface rainfall estimates has resulted from the implementation of a correction for the effect of non-uniform beam filling (Durden et al., 1998). The PR-based reflectivity profiles included in the present study were corrected for attenuation by heavy rain using the surface reference technique (Iguchi and

Meneghini, 1994). The TRMM 2A25-volumetric radar reflectivities, surface rain rates (Iguchi et al., 2000), and rain type (Awaka et al., 1997), and the TRMM PR 3B42 monthly-mean surface rain rate are the primary datasets used in this study.

The second source of information was the National Center for Environmental Prediction (NCEP)–National Center for Atmospheric Research (NCAR) global re-analysis data set (Kalnay et al., 1996). Thermodynamic variables were determined from the NCEP reanalysis to aid with the interpretation of TRMM data analyses and the associated results included in the present study.

## 2.2 Data processing

Seven years (from 1998 to 2004) of data were included to derive vertical profiles of reflectivity over West Africa and the eastern Atlantic Ocean (Fig. 1) during the course of the rainy season corresponding to the months of June to September. The full vertical resolution of the 2A25 PR (250 m) data was considered as this study focused on the reflectivity profile of precipitating systems. The 3-hour temporal resolution was chosen to capture the diurnal variation in rainfall, while maintaining statistical significance by using a relatively large sample size. Here the temporal resolution relates to the data bin size. The choice of temporal resolution was based on the results reported by Negri et al. (2002). Based on 3 years of TRMM data they concluded that, because of spatially inconsistent sampling, the 1-hour temporal

resolution is inadequate to describe the diurnal cycle of precipitation. More recently, Hirose et al. (2007) determined that the currently available 8 years of TRMM data allow a depiction of the diurnal cycle of precipitation at 1-hour resolution in areas as small as  $0.2^\circ \times 0.2^\circ$  blocks ( $\sim 20 \times 20 \text{ km}^2$ ). This is more optimistic than Negri et al. (2002), who used only 3 years of data. Given that the blocks used here are larger than  $20 \times 20 \text{ km}^2$ , our results are statistically robust. The relatively large region (Fig. 1) selected for this study permitted the use of a 3-hour temporal sampling to adequately capture important features in the diurnal variability of precipitating systems. The results are reported in local solar time.

To study changes in the characteristics of precipitating storms along a zonal transect from continental West Africa to the Atlantic Ocean, differences in reflectivity profiles were investigated for the following three regions, from east to west (Fig. 1): I) Continental West Africa ( $5^\circ \text{ W}–20^\circ \text{ E}$ ), II) coastal West Africa ( $17.2–5^\circ \text{ W}$ ), and III) eastern Atlantic Ocean ( $25.0–17.2^\circ \text{ W}$ ). These regions share a common meridional extent ( $4.5–17.5^\circ \text{ N}$ ). This study focuses on east-west variations. Most of the rainfall, and thus most of the reflectivity profiles in this study, occur in a narrow belt between  $6$  and  $10^\circ \text{ N}$  (Fig. 1), corresponding to the belt of most frequent wet-season MCSs and highest sea surface temperature offshore, ranging between  $27$  and  $28^\circ \text{ C}$  (Fontaine and Janicot, 1996). This regional classification was mainly based on the expected distinct attributes

TRMM 3B42 June to September mean rainfall, based on the period 1998–2004

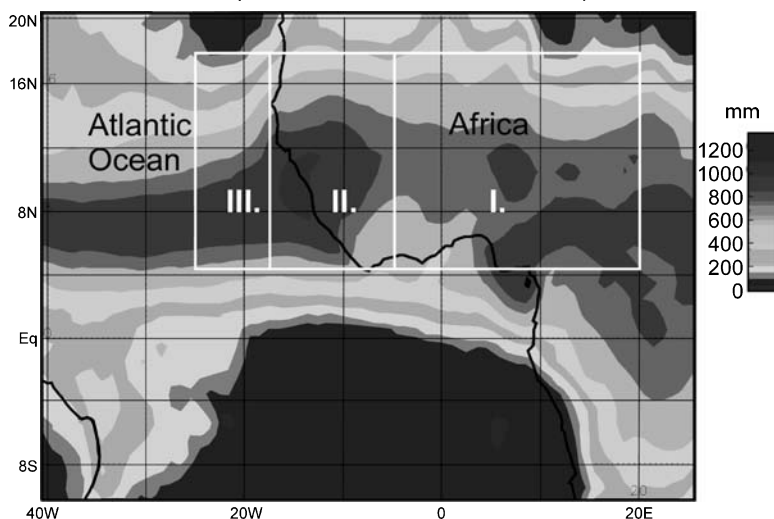


**Fig. 1.** Map of West Africa illustrating the three regions (marked with the boxes) established for the present study. The shaded contours represent the average precipitation patterns (in mm) estimated for the months of June to September during 1998–2004 using TRMM 3B42

of storms associated with easterly waves that move from the continent to the ocean (Reed, 1977). Figure 1 shows the spatially average rainfall patterns estimated for the months of June to September during 1998–2004 using TRMM 3B42 data.

The frequency distribution of the TRMM PR reflectivity as a function of altitude was estimated for the available satellite data in each region. The estimated frequency distribution for a given reflectivity,  $Z$ , at a certain altitude,  $z$ , was normalized in such a manner that the sum of all frequencies amounted to 100% (Yuter and Houze, 1995). In each region, the estimated frequency distribution was grouped into stratiform and convective regimes based on the rain data type designation of the 2A25 TRMM data algorithm (version 6). Here we will contrast characteristic storm intensity and depth for both convective and stratiform regimes.

Following Geerts and Dejene (2005), several indices were defined to identify differences in vertical storm characteristics for the regions considered in the present study. The evaporative index (EI) was defined to evaluate the differences in the potential rates of low-level evaporation of rainfall. The EI was estimated as the difference in reflectivity between the altitudes of 4.0 km, the highest level unambiguously below the radar bright band (Battan, 1973), and 2.0 km. To identify the presence of the bright band and determine the decay of reflectivity above the bright band, the stratiform index (SI) was defined as the difference in reflectivity between the altitudes of 7.0 and 4.5 km. Both EI and SI were estimated for individual reflectivity profiles and were expressed in dBZ units. Reflectivity values below the PR threshold sensitivity (17 dBZ) were not included in the EI and SI calculations. Also, the hydrometeor precipitable water (HPW) was estimated as the integral of water content in the atmospheric column from the surface to the top of the atmosphere (1).

$$\text{HPW} = \frac{1}{\rho_1} \int_0^{\text{Top}} \rho(z)q(z) dz \quad (1)$$

$\rho_1$  and  $\rho(z)$  are water and air density ( $\text{kg m}^{-3}$ ), respectively. The vertical distribution of water vapor mixing ratio ( $\text{g kg}^{-1}$ ),  $q(z)$ , was estimated based on reported algorithms (Battan, 1973) relating reflectivity ( $Z$ ) to  $q(z)$ , applicable to summertime precipitation (in North America). The

units of HPW are depth (m or mm) of the water column. From the surface to 4.5 km, where rain is assumed to occur,  $q(z)$  was estimated using (2a). Relationship (2b) was considered in the  $q(z)$  calculations for altitudes greater than 4.5 km, where snow is assumed to occur.

$$q(z) = 0.0032 Z^{0.55} \exp\left(\frac{z}{8}\right) \quad (2a)$$

$$q(z) = 0.0068 Z^{0.45} \exp\left(\frac{z}{8}\right) \quad (2b)$$

In (2)  $z$  represents altitude (in km) and  $Z$  is the reflectivity (expressed in  $\text{mm}^6 \text{m}^{-3}$ , in dB units, dBZ). Additionally, to discern the precipitation efficiency (Hobbs et al., 1980) of the storms for the identified three regions, the storm productivity index (SPI, units of  $\text{hour}^{-1}$ ) was defined as the ratio of the surface rain rate (in mm per hour) over the HPW generated by a given storm.

To examine thermodynamic differences among the storms in the identified regions, the NCEP–NCAR re-analysis data were used to interpret the main observations deduced from the 2A25 TRMM data. For each region,  $\text{CAPE}_e$  (in  $\text{J kg}^{-1}$ ) was estimated for the months of June to September, based on profiles of monthly-mean temperature and humidity. The  $\text{CAPE}_e$  values were estimated using relationship (3) (Petersen and Rutledge, 2001).

$$\text{CAPE}_e = R_d \int_{\text{LFC}_e}^{\text{LNB}_e} (\theta_e^* - \theta_{e,\text{sfc}}) d\ln p \quad (3)$$

$\text{LFC}_e$  is the level of free convection,  $\text{LNB}_e$  is the level of neutral buoyancy,  $\theta_e$  is the equivalent potential temperature.  $\theta_e^*$  and  $\theta_{e,\text{sfc}}$  are the saturation equivalent potential temperature and the surface equivalent potential temperature, respectively. The variable  $p$  is the pressure (in Pascal) and  $R_d$  is the specific gas constant for dry air ( $287 \text{ J kg}^{-1} \text{ K}^{-1}$ ). Positive parcel buoyancy occurs at levels where  $\theta_{e,\text{sfc}}$  exceeds the local  $\theta_e^*$  (i.e. between  $\text{LNB}_e$  and  $\text{LFC}_e$ , Petersen and Rutledge, 2001).

### 3. Results and discussion

#### 3.1 Diurnal variability in the characteristics of precipitating storms

In West Africa and adjoining areas of eastern Atlantic Ocean strong convection occurs during

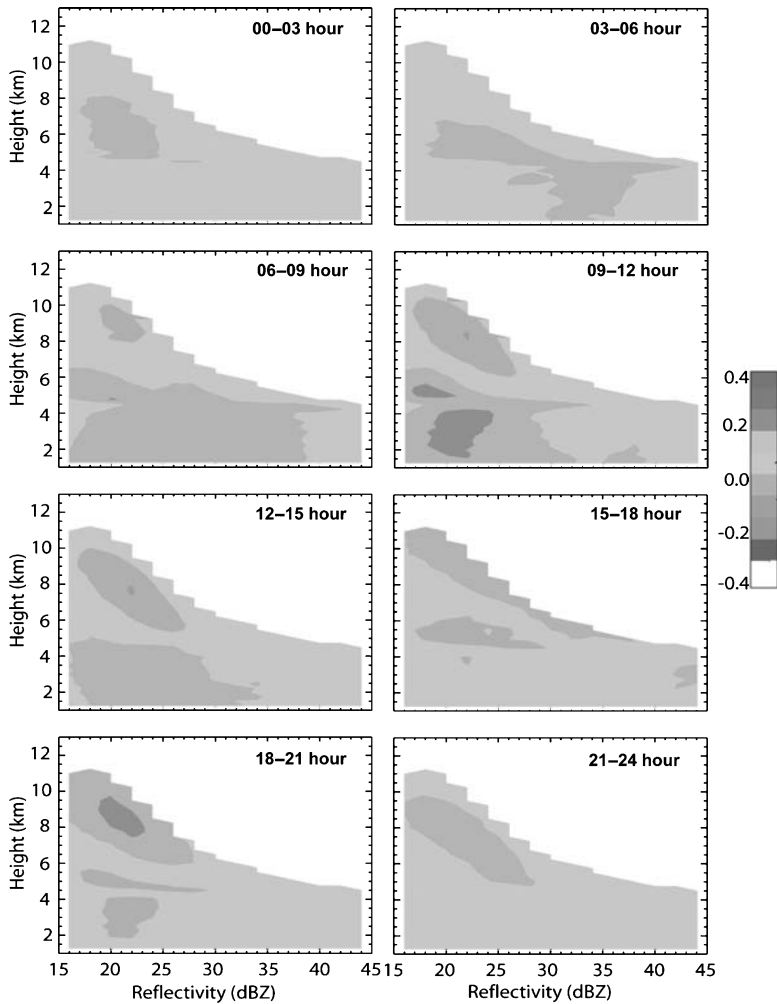


**Fig. 2.** Diurnal variation of frequency distribution of reflectivity for continental West Africa [units  $(2 \text{ dBZ})^{-1} (250 \text{ m})^{-1}$ ]. The normalized frequencies are expressed as a difference from the normalized 24 h mean values. The bar on the right hand side of the figure provides the scale for the estimated frequencies

the months of June to September, especially along the latitudinal belt of the Inter-tropical Convergence Zone (ITCZ) (Fontaine and Janicot, 1996). The dynamics of precipitating systems are locally invigorated by diurnally varying surface energy fluxes and lower tropospheric wind shear. The horizontal and vertical extent of the identified storms and their duration varied depending on factors such as proximity to the moisture sources, heat capacity of the location, and presence of the African Easterly Jet. Thus, to investigate the evolution of precipitating systems in the transition region from continental West Africa to eastern Atlantic Ocean, we first analyzed the diurnal variability of the vertical attributes of precipitating storms over the three study regions. A diurnal delay (relative to local solar noon) in the vertical radar reflectivity of the identified storms was evident in all three regions (Figs. 2, 3 and 4). A time lag in the changes of the reflectivity pro-

file was observed along the transect going from continental to oceanic regions. Strong and deep echoes occurred mostly during 15–21 h (local time, LT) over continental West Africa (Fig. 2). Over coastal West Africa, the maximum reflectivity values took place during 18–24 LT (Fig. 3). On the other hand, over the eastern Atlantic Ocean, the diurnal precipitation cycle had a smaller amplitude and deep echoes occurred mostly during 06–12 LT (Fig. 4). The peaks in the low-level (shallow) convection also showed a time lag from continental West Africa to eastern Atlantic Ocean. Shallow convection was most frequent during 9–12 LT, 12–15 LT and 15–18 LT over continental West Africa, coastal West Africa and eastern Atlantic Ocean, respectively. The deeper storms over continental and coastal West Africa were most likely triggered by daytime surface heating and water vapor transport over the continental regions. In the summer, water vapor advection from

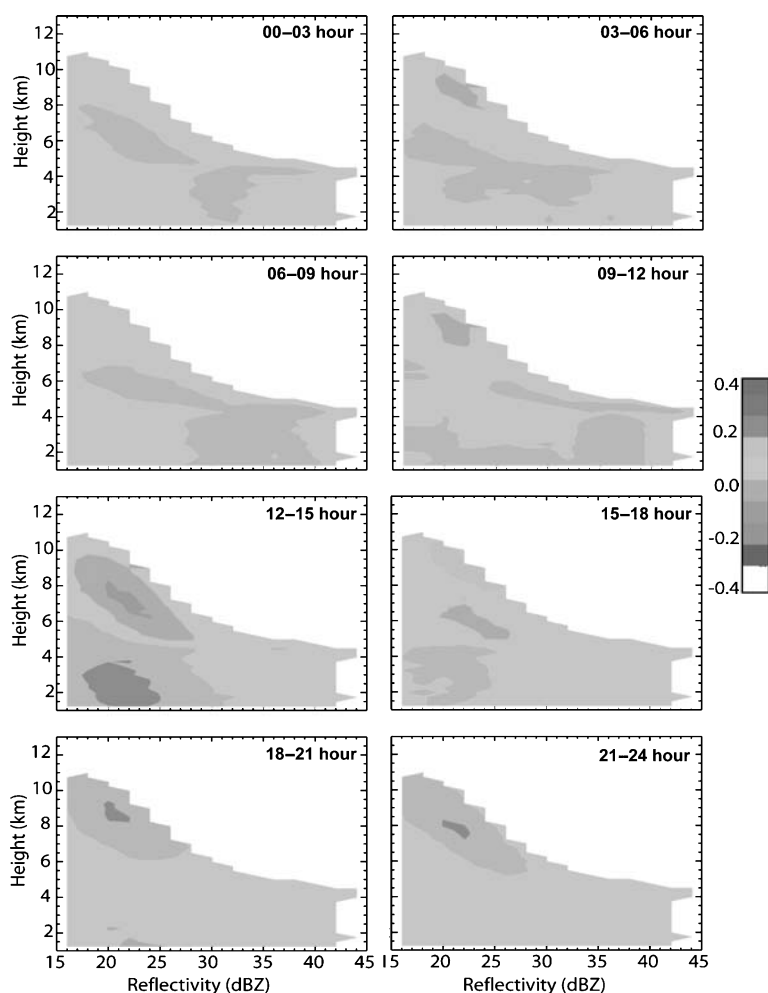


**Fig. 3.** As Fig. 2, but for coastal West Africa

the south peaks at night in West Africa (Cook, 1999; Paeth and Friederichs, 2004). Additionally, there might be distinct differences in the cloud microphysical properties between the continental and maritime atmospheres of West Africa. Over the continental areas terrigenous materials may provide the necessary cloud condensation nuclei. In contrast, over the central Atlantic Ocean sea-salt aerosols and dust act as the principal nucleation agents. The early morning maximum of deep echoes over the ocean (Fig. 4) is consistent with results from previous studies (Geerts and Dejene, 2005; Schumacher and Houze, 2006). Offshore MCSs often form near midnight and reach their maximum intensity in the morning (Hodges and Thorncroft, 1997). Furthermore, the present results suggest that storm systems that develop over coastal West Africa in the evening period are frequently sustained by the favorable nocturnal marine environment after exiting the coast.

### 3.2 Regional variability of the vertical storm characteristics

Regional differences in the vertical structure of precipitating storms were evident along the established transect from the continental region of West Africa to the eastern Atlantic Ocean. For stratiform-type precipitation, the frequency distribution for all regions exhibited similar patterns (Fig. 5), and the average reflectivity profiles in stratiform precipitation were remarkably similar in the three regions (Fig. 6). Schumacher and Houze (2006) also found similar patterns in the same region during a different time period. A signature of stratiform precipitation is the presence of a bright band which was observed at an altitude of about 4.5 km in all three regions (Fig. 6). Compared to continental West Africa, echo tops were about 1 km lower over the eastern Atlantic Ocean. Additionally, the isolines below the freezing level were shifted to lower reflectivities for

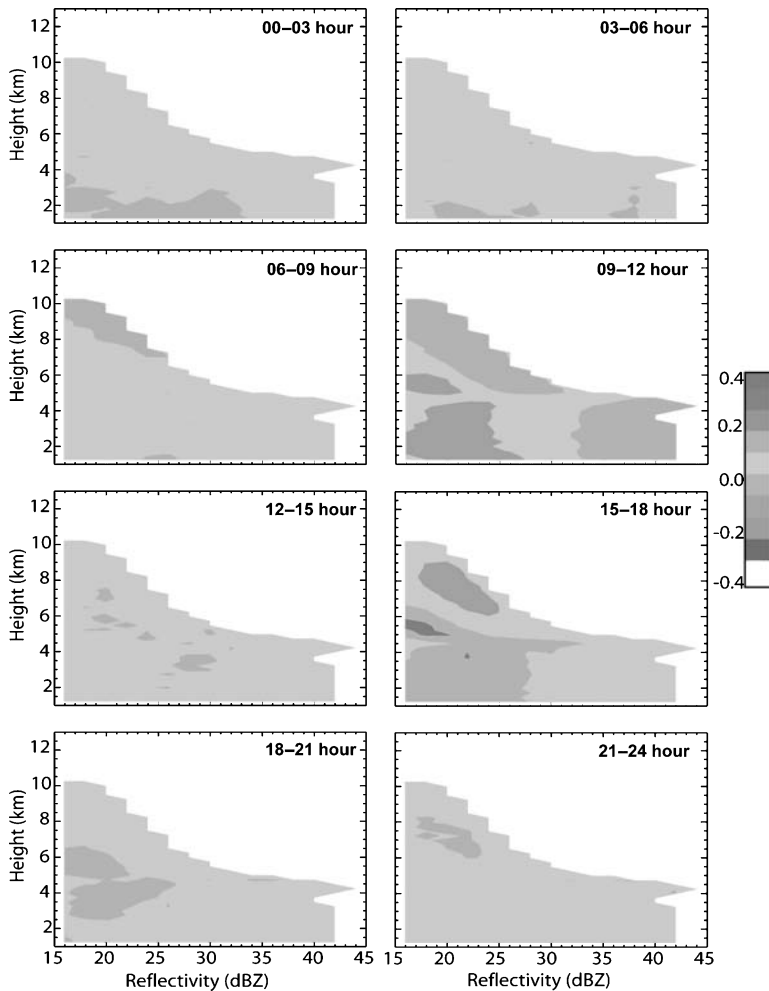


**Fig. 4.** As Fig. 2, but for eastern Atlantic Ocean

the stratiform-type precipitation over continental West Africa, suggesting low-level evaporation over the region (Hirose and Nakamura, 2004; Geerts and Dejene, 2005). Low-level evaporation was deduced from the more frequent occurrence of higher reflectivities near the 4-km level as compared to closer to the ground. The angle of tilt was systematic such that it was almost vertical (with no much tilt) for coastal West Africa and the tilt to higher reflectivities significantly increased for eastern Atlantic Ocean, indicating low-level raindrop growth or dominance of warm rain processes over the region.

Convective storms became less deep and less intense over the ocean (Figs. 5 and 6). The implication is that maritime convection had a lower hydrometeor content above the freezing level than continental storms in West Africa. The reflectivity frequency occurrences of convective storms over the three regions (Fig. 5) show that shallow convection progressively became more

common from continental West Africa to the eastern Atlantic Ocean, consistent with the TRMM-PR study reported by Schumacher and Houze (2006). The high frequency occurrence of reflectivities ranging from 20 to 30 dBZ at low elevation suggested that light convective rain, for instance from cumulus congestus, was relatively common over the eastern Atlantic Ocean. As a result, the mean reflectivity profile for oceanic convection exhibited lower values compared to that over the adjacent continent (Fig. 6). In order to further define and contrast the vertical variations of reflectivity, the mean profile and the frequency distribution for reflectivities exceeding certain threshold levels (i.e. 17, 27, and 37 dBZ) were determined (Fig. 7). The mean profiles were calculated by taking the mean of all reflectivities (in Z units) for each level. Note that the reflectivity profiles present the probabilities, varying with height, that at least a certain reflectivity value (exceeding 17, 27, or 37 dBZ) can be found

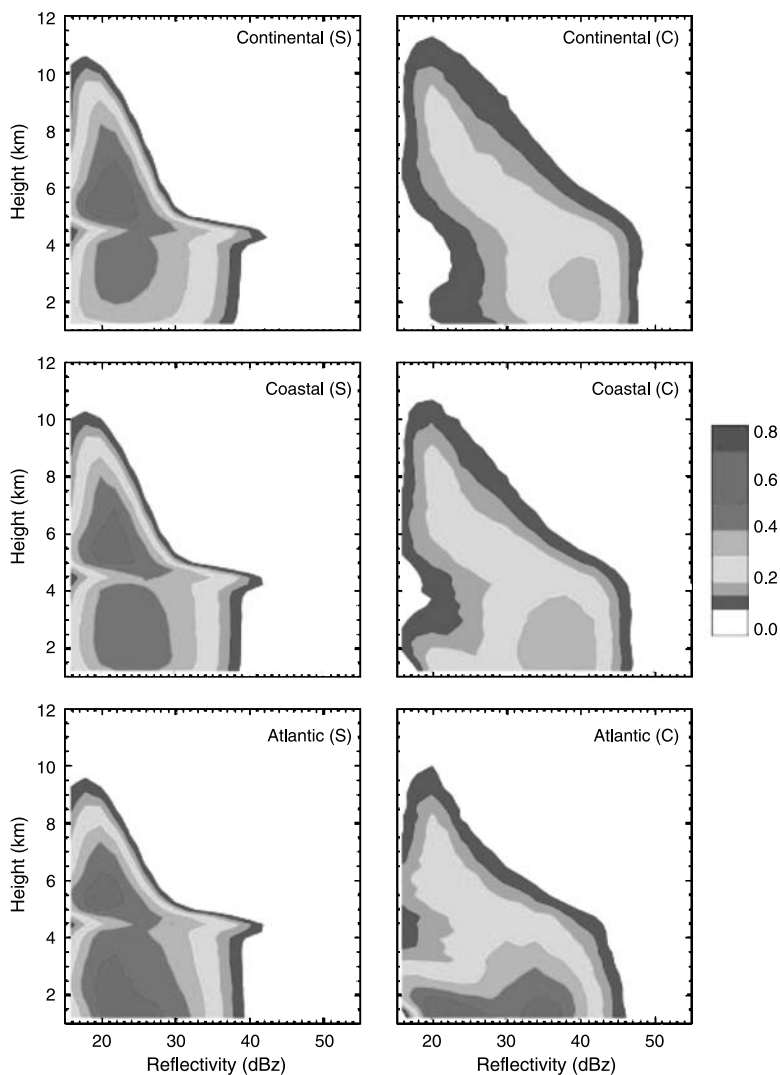


**Fig. 5.** Ensemble probability density functions estimated based on the relationship of reflectivity as a function of altitude for the regions identified in Fig. 1. The left and right panels of figures report result for stratiform (S)- and convective (C)-type precipitation, respectively, during June to September (1998–2004). The results are based on the TRMM 2A25 data (1998–2004). The bar on the right hand side of the figure provides the scale for the estimated probabilities

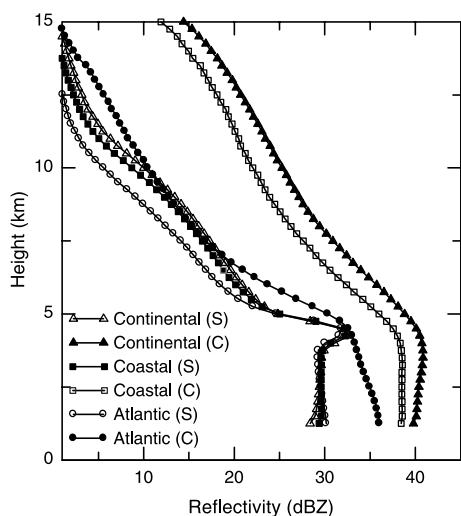


**Fig. 6.** Ensemble average reflectivity as a function of altitude for the regions identified in Fig. 1 during June to September (1998–2004)

when it rains on the ground (the 17 dBZ threshold includes all measurable intensities of precipitation, 27 dBZ includes moderate and heavy precipitation, and 37 dBZ includes only heavy precipitation; the profiles depict the typical vertical structure of precipitating systems). The frequency of the lowest reflectivity threshold at low levels was much greater over the eastern Atlantic Ocean, and the rapid decay of this threshold with height indicates that many systems were shallow. The echo frequency over continental West Africa decreased towards the ground for all threshold reflectivity levels, suggesting evaporation or break-up of raindrops (Fig. 7). In contrast, the echo frequency (reflectivity count) over coastal West Africa and eastern Atlantic Ocean increased from just below the freezing level down to near the ground. This indicated that raindrops grow as they

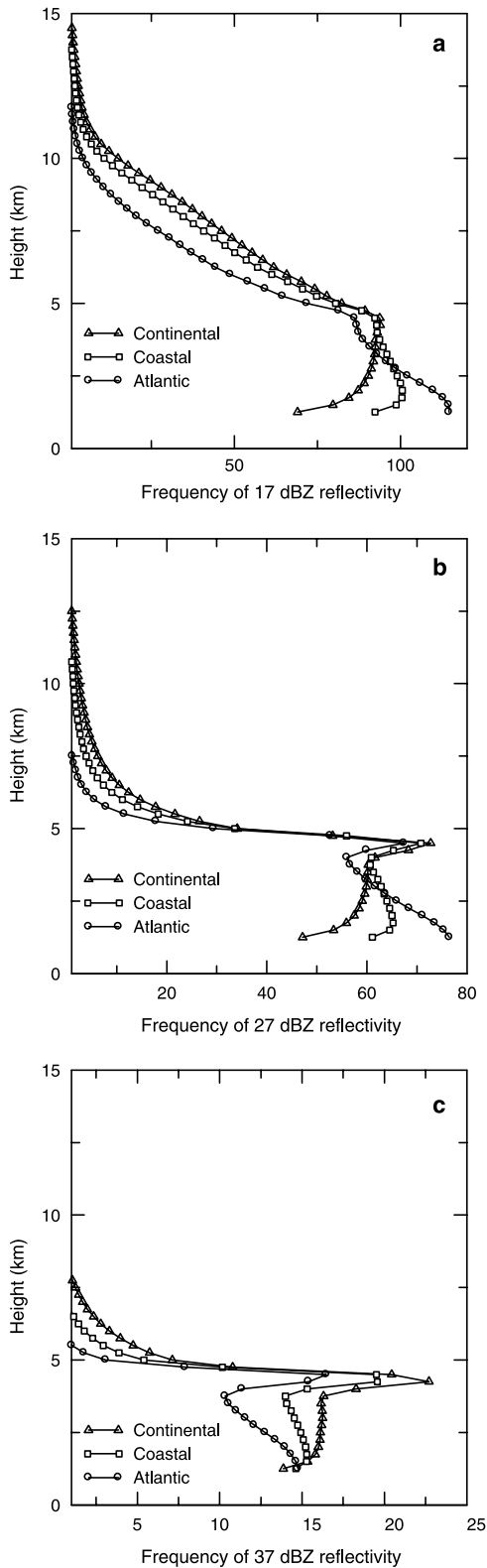


**Fig. 7.** Frequency distribution of reflectivity values plotted against altitude. Three thresholds reflectivity values chosen for the analyses included (a) 17, (b) 27 and (c) 37 dBZ. The frequencies were normalized by the number of rain profiles in each region

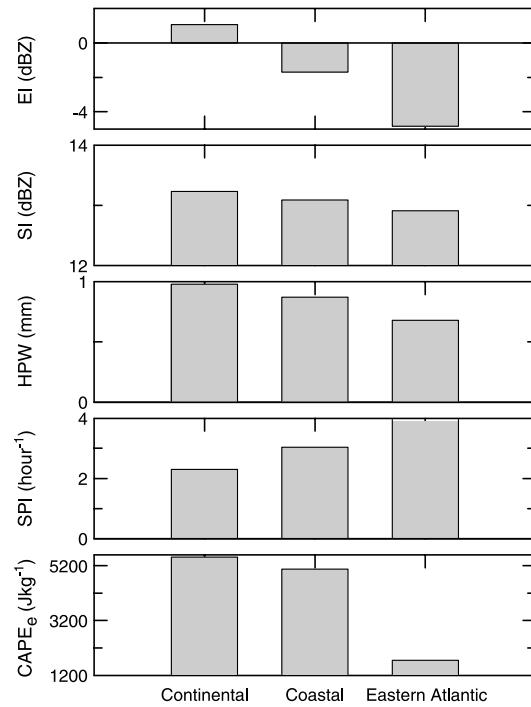


**Fig. 8.** Average values of the indices estimated to define the characteristics of precipitating systems in West Africa. The SI is the evaporation index (in dBZ), SI is the stratiform index (in dBZ), HPW is the hydrometeor precipitable water (in mm), and  $CAPE_e$  is the equivalent convective available energy (in  $J kg^{-1}$ )

move towards ground, implying a dominance of warm-rain processes and low-level cloud base over the eastern Atlantic Ocean.

Key differences were also revealed in various precipitation indices estimated for the three regions (Fig. 8). Precipitation systems over continental West Africa had the higher evaporative index (EI) compared with the east Atlantic Ocean, indicating higher evaporation of water drops before reaching the ground. The EI decreased substantially along the land-to-ocean transect, with the lowest value over the eastern Atlantic Ocean. The negative EI there is likely due to the low-level growth of raindrops by the collision-coalescence process. The stratiform signature (SI) was high in all regions with less regional variability, suggesting that a high proportion of stratiform precipitation exists in all the regions. Continental West Africa tended to have deeper storms with higher HPW, and therefore also had a low SPI value (i.e. a relatively high water volume aloft for a given surface rain rate). On the other hand, storms over the eastern Atlantic Ocean were more efficient rain producers (higher SPI) due

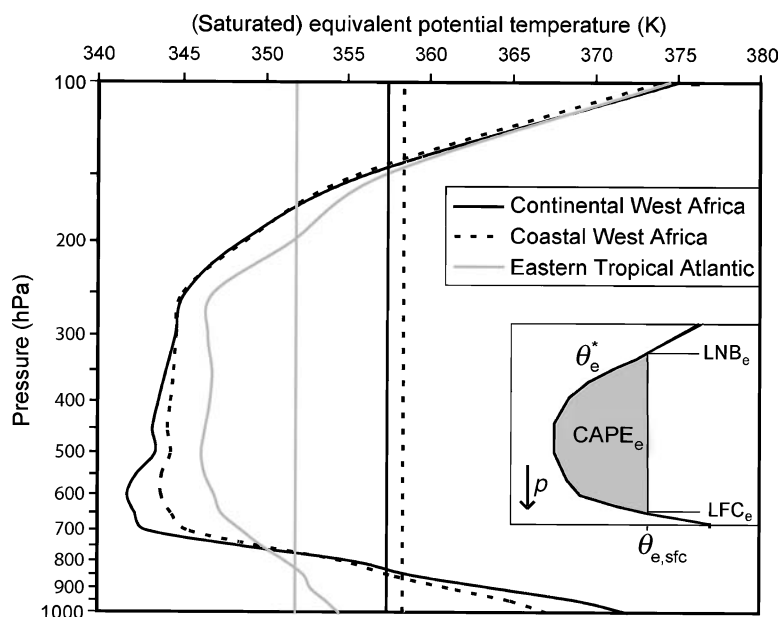


**Fig. 9.** Vertical profiles of  $\theta_c^*$  (curved lines) plotted as a function of pressure (log coordinate) for various regions. The vertical lines are corresponding values of  $\theta_e$  derived from the temperature and specific humidity at 1000 hPa. Data are based on NCEP–NCAR re-analysis data

to lower HPW associated with shallow precipitating systems.

The highest  $CAPE_e$  values were estimated for the continental West Africa, followed closely by coastal West Africa (Fig. 9). On average, the eastern Atlantic Ocean had much lower  $CAPE_e$  values. The differences in the CAPE values are mostly associated with the higher values of  $LNB_e$  for continental and coastal West Africa. The continental and coastal West Africa regions had higher  $LNB_e$  levels (150 hPa) than for the eastern Atlantic Ocean (200 hPa). These  $CAPE_e$  results are consistent with the more frequent occurrences of PR echoes recorded at the upper levels in those regions (Figs. 5 and 7). In general, the relatively weaker storms and higher warm-rain fraction over the eastern Atlantic Ocean were consistent with the lower values of  $CAPE_e$  compared with the continental and coastal West Africa.

#### 4. Discussion and conclusions

This study described the regional and diurnal variability of the vertical attributes of precipitating systems along the continental-maritime transition region in West Africa. The diurnal peak in maximum vertical storm structure occurred between 15 and 21 LT in continental West Africa, and 12–15 h later over the eastern Atlantic Ocean. Shallow convection over these regions also showed a westward time lag, peaking at 9–12 LT, 12–15 LT and 15–18 LT over continental

West Africa, coastal West Africa and eastern Atlantic Ocean, respectively.

In West Africa, organized convection generally moves westward. From the TRMM data source it is not clear whether the MSCs, peaking in the evening over land, were the same as those observed into the early morning over water. However, such offshore storm travel has been previously documented (Hodges and Thorncroft, 1997). Convective storms exhibited different attributes along the investigated land-to-ocean transect. For example, in the eastern Atlantic Ocean storms were shallower and had lower integrated hydrometeor content (Fig. 8). This difference applies mostly to those parts of storms classified as convective. Over continental West Africa, the stratiform precipitation did not differ much from those over the adjacent ocean (Fig. 5).

Furthermore, the echo strength from 4 km down to the ground increased for the eastern Atlantic Ocean and decreased for continental West Africa (Fig. 6). These profiles can be explained by low-level evaporation and/or raindrop break-up over continental West Africa as opposed to low-level drop size growth over the eastern Atlantic Ocean due to a much lower cloud base there. The higher cloud base, more intense low-level evaporation, and deeper convection observed over the continent likely result from surface-atmosphere interactions, specifically the high sensible heat fluxes over land. Over land, such interactions affect the surface energy and moisture balance with a con-

sequent impact on the availability of energy to enhance convection. In addition, the occurrence of raindrop break-up, as suggested by the decrease in echo-frequency towards the ground, may be caused by the differences in cloud condensation processes resulting from the different aerosol types prevailing over land and ocean (e.g. Williams et al., 2002). Warm-rain processes likely dominated over the eastern Atlantic Ocean as a result of the growth or increase in hydrometeor content at low elevation. The frequency isolines of reflectivity below the freezing level tilted to lower reflectivity values over continental West Africa, indicating a low proportion of shallow precipitation clouds, and/or low-level evaporation. The isolines gradually tilted to higher reflectivity values towards the surface from coastal to eastern Atlantic Ocean, suggesting low-level rain drop growth. Over the eastern Atlantic Ocean purely warm rain clouds were more likely to occur than over land (Fig. 5).

The intensity and depth of convective storms systematically decreased from continental West Africa to the eastern Atlantic Ocean. The regional changes in the vertical characteristics of precipitating storms, observed using the TRMM PR 2A25 data, are consistent with the changes in  $CAPE_e$  of the basic environment estimated from NCEP–NCAR re-analysis data.

#### Acknowledgments

TRMM is a project cosponsored by NASA and NASDA, the Japanese space agency. This research was supported by NASA grant NAG5-13778. Courtney Schumacher of Texas A&M University provided excellent suggestions to improve the manuscript. Two reviewers are thanked for providing comments that considerably improved the quality of the manuscript.

#### References

- Adeyewa ZD, Nakamura K (2003) Validation of TRMM radar rainfall data over major climatic regions in Africa. *J Appl Meteor* 42: 331–347
- Awaka J, Iguchi T, Kumagai H, Okamoto K (1997) Rain type classification algorithm for TRMM Precipitation Radar. Proc. of the IEEE 1997 Intl. Geoscience and Remote Sensing Sym., Aug. 3–8, Singapore, pp 1633–1635
- Battán LJ (1973) Radar observations of the atmosphere. University of Chicago Press, 324 pp
- Boccippio DJ, Goodman SJ, Heckman S (2000) Regional differences in tropical lightning distributions. *J Appl Meteor* 39: 2231–2248

- Cecil DJ, Zipser EJ (2002) Reflectivity, ice scattering, and lightning characteristics of hurricane eyewalls and rainbands. Part II: Intercomparison of observations. *Mon Wea Rev* 130: 785–801
- Cook K (1999) Generation of the African Easterly Jet and its role in determining West African precipitation. *J Climate* 12: 1165–1184
- Diedhiou A, Janicot S, Viltard A, de Felice P, Laurent H (1999) Easterly wave regimes and associated convection over West Africa and tropical Atlantic: results from the NCEP/NCAR and ECMWF reanalyses. *Clim Dynam* 15: 795–822
- Durden SL, Haddad ZS, Kitiyakara A, Li FK (1998) Effects of non-uniform beam filling on rainfall retrieval for the TRMM precipitation radar. *J Atmos Oceanic Technol* 15: 635–646
- Fontaine B, Janicot S (1996) Sea surface temperature fields associated with West African rainfall anomaly types. *J Climate* 9: 2935–2940
- Geerts B, Dejene T (2005) Regional and diurnal variability of the vertical structure of precipitation systems in Africa based on spaceborne radar data. *J Climate* 18: 893–916
- Halverson J, Rickenbach T, Roy B, Pierce H, Williams E (2002) Environmental characteristics of convective systems during TRMM-LBA. *Mon Wea Rev* 130: 1493–1509
- Heymsfield GM, Geerts B, Tian L (2000) TRMM precipitation radar reflectivity profiles as compared with high-resolution airborne and ground-based radar measurements. *J Appl Meteor* 39: 2080–2102
- Hirose M, Nakamura K (2004) Spatiotemporal variation of the vertical gradient of rainfall rate observed by the TRMM precipitation radar. *J Climate* 17: 3378–3397
- Hirose M, Oki R, Shimizu S, Kachi M, Higashiuwatoko T (2007) Fine-scale diurnal rainfall statistics refined from 8 years. *J Appl Meteor Climatol* (Accepted)
- Hobbs PV, Politovich MK, Radke IF (1980) The structures of summer convective clouds in eastern montana. 1. Natural clouds. *J Appl Meteor* 19: 645–663
- Hodges KI, Thorncroft CD (1997) Distribution and statistics of African mesoscale convective weather systems based on the ISCCP Meteosat imagery. *Mon Wea Rev* 125: 2821–2837
- Houze RA Jr (1997) Stratiform precipitation in regions of convection: a meteorological paradox? *Bull Amer Meteor Soc* 78: 2179–2196
- Houze RA Jr, Betts AK (1981) Convection in GATE. *Reviews Geophys Space Phys* 19: 541–576
- Iguchi T, Meneghini R (1994) Intercomparison of single-frequency methods for retrieving a vertical rain profile from airborne or spaceborne radar data. *J Atmos Oceanic Technol* 11: 1507–1516
- Iguchi T, Kozu T, Meneghini R, Awaka J, Okamoto K (2000) Rain-profiling algorithm for the TRMM Precipitation Radar. *J Appl Meteor* 39: 2038–2052
- Kalnay E, Kanamitsu M, Kistler R, Collins W, Deaven D, Gandin L, Iredell M, Saha S, White G, Woollen J, Zhu Y, Chelliah M, Ebisuzaki W, Higgins W, Janowiak J, Mo KC, Ropelewski C, Wang J, Leetmaa A, Reynolds R, Jenne R, Joseph D (1996) The NCEP/NCAR 40-year reanalysis project. *Bull Amer Meteor Soc* 77: 437–471

- Kozu T, Kawanishi T, Kuroiwa H, Kojima M, Oikawa K, Kumagai H, Okamoto K, Okumua M, Nakatsuka H, Nishikawa K (2001) Development of precipitation radar onboard the Tropical Rainfall Measuring Mission (TRMM) satellite. *IEEE T Geosci Remote* 39L: 102–116
- Kummerow C, Barnes W, Kozu K, Shiue J, Simpson J (1998) The Tropical Rainfall Measuring Mission (TRMM) sensor package. *J Atmos Oceanic Technol* 15: 809–817
- Kummerow C, et al (2000) The status of the Tropical Rainfall Measuring Mission (TRMM) after two years in orbit. *J Appl Meteor* 39: 1965–1982
- Laing AG, Fritsch JM (1997) The global population of mesoscale convective complexes. *Quart J Roy Meteor Soc* 123: 389–405
- Lebel T, Diedhiou A, Laurent H (2003) Seasonal cycle and interannual variability of the Sahelian rainfall at hydrological scales. *J Geophys Res-Atmospheres* 108: Art. No. 8389
- Lin JL, Mapes B, Zhang MH, Newman M (2004) Stratiform precipitation, vertical heating profiles, and the Madden-Julian oscillation. *J Atmos Sci* 61: 296–309
- Mohr KI (2004) Interannual, monthly, and regional variability in the wet season diurnal cycle of precipitation in sub-Saharan Africa. *J Climate* 17: 2441–2453
- Negri AJ, Bell TL, Xu L (2002) Sampling of the diurnal cycle of precipitation using TRMM. *J Atmos Oceanic Technol* 19: 1333–1344
- Nesbitt SW, Zipser EJ (2003) The diurnal cycle of rainfall and convective intensity according to three years of TRMM measurements. *J Climate* 16: 1456–1475
- Nicholson SE, Some B, McCollum J, Nelkin E, Klotter D, Berte Y, Diallo BM, Gaye I, Kpabeba G, Ndiaye O, Noukpozoukou JN, Tanu MM, Thiam A, Toure AA, Traore A (2003) Validation of TRMM and other rainfall estimates with a high-density gauge dataset for West Africa. Part I: validation of GPCC rainfall product and pre-TRMM satellite and blended products. *J Appl Meteor* 42: 1337–1354
- Paeth H, Friederichs P (2004) Seasonality and time scales in the relationship between global SST and African rainfall. *Clim Dynam* 23: 815–837
- Petersen WA, Rutledge SA (2001) Regional variability in tropical convection: observations from TRMM. *J Climate* 14: 3566–3586
- Petersen WA, Fu R, Chen MX, Blakeslee R (2006) Intra-seasonal forcing of convection and lightning activity in the southern Amazon as a function of cross-equatorial flow. *J Climate* 19: 3180–3196
- Reed RJ (1977) Structure and properties of African wave disturbances as observed during phase III of GATE. *Mon Wea Rev* 105: 317–333
- Redelsperger JL, Diongue A, Diedhiou A, Ceron JP, Diop M, Gueremy JF, Lafore JP (2002) Multi-scale description of a Sahelian synoptic weather system representative of the West African monsoon. *Quart J Roy Meteor Soc* 128: 1229–1257
- Rotunno R, Klemp JB, Weisman ML (1988) A theory for strong, long-lived squall lines. *J Atmos Sci* 45: 463–485
- Roux F (1988) The West-African squall line observed on 23 June 1981 during COPT-81: Kinematics and thermodynamics of the convective region. *J Atmos Sci* 45(3): 406–426
- Rowell DP, Milford JR (1993) Generation of African squall lines. *J Climate* 6: 1181–1193
- Sauvageot H, Mesnard F, Tenorio RS (1999) The relation between the area-average rain rate and the rain cell size distribution parameters. *J Atmos Sci* 56: 57–70
- Sealy A, Jenkins GS, Walford SC (2003) Seasonal/regional comparisons of rain rates and rain characteristics in West Africa using TRMM observations. *J Geophys Res-Atmospheres* 108 (D10): Art. No. 4306
- Schumacher C, Houze RA Jr (2003) Stratiform rain in the tropics as seen by the TRMM Precipitation Radar. *J Climate* 16: 1739–1756
- Schumacher C, Houze RA, Kraucunas I (2004) The tropical dynamical response to latent heating estimates derived from the TRMM precipitation radar. *J Atmos Sci* 61: 1341–1358
- Schumacher C, Houze RA Jr (2006) Stratiform precipitation production over sub-Saharan Africa and the tropical east Atlantic as observed by TRMM. *Quart J Roy Meteor Soc* 132: 2235–2255
- Simpson J, Adler RF, North GR (1988) A proposed Tropical Rainfall Measuring Mission (TRMM) satellite. *Bull Amer Meteor Soc* 69: 278–295
- Steiner M, Houze RA Jr (1997) Sensitivity of the estimated monthly convective rain fraction to the choice of Z-R relation. *J Appl Meteor* 36: 452–462
- Stith JL, Dye JE, Bansemmer A, Heymsfield AJ, Grainger CA, Petersen WA, Cifelli R (2002) Microphysical observations of tropical clouds. *J Appl Meteor* 41: 97–117
- Toracinta ER, Cecil DJ, Zipser EJ, Nesbitt SW (2002) Radar, passive microwave, and lightning characteristics of precipitating systems in the Tropics. *Mon Wea Rev* 130: 802–824
- Weisman ML, Rotunno R (2004) A theory for strong long-lived squall lines revisited. *J Atmos Sci* 61: 361–382
- Williams E, et al (2002) Contrasting convective regimes over the Amazon: Implications for cloud electrification. *J Geophys Res-Atmospheres* 107: D20 8082 (doi: 10.1029/2001JD000380)
- Yuter SE, Houze RA (1995) 3-Dimensional kinematic and microphysical evolution of Florida cumulonimbus. Part 1: spatial-distribution of updrafts, downdrafts, and precipitation. *Mon Wea Rev* 123: 1921–1940

Authors' addresses: Jose D. Fuentes (e-mail: jf6s@virginia.edu), Teferi Dejene, Paolo D'Odorico, Department of Environmental Sciences, University of Virginia, 291 McCormick Road, Clark Hall, Charlottesville, VA 22904, USA; Bart Geerts, Department of Atmospheric Science, University of Wyoming, Laramie, WY 82071, USA; Everette Joseph, Department of Physics, Howard University, Washington, DC 20059, USA.

